**Exploring the Role of Primary Mass and Star-forming Environment on the Formation of Stellar and Sub-stellar Multiple Systems**

by

Matthew C. De Furio

A dissertation submitted in partial fulfillment
of the requirements for the degree of
Doctor of Philosophy
(Astronomy and Astrophysics)
in the University of Michigan
2023

Doctoral Committee:

Professor Michael Meyer, Chair
Professor Fred Adams
Professor Kaitlin Kratter, University of Arizona
Professor John Monnier
Associate Professor Keren Sharon

Matthew C. De Furio
defurio@umich.edu
ORCID iD: 0000-0003-1863-4960

To Sylvia A. Figueroa, always and forever.

# ACKNOWLEDGEMENTS

In contemplating the last six years of my graduate studies, there are many people who have played significant roles that allowed me to attain a Doctor of Philosophy in Astronomy & Astrophysics.

I would like to first thank my wife, Sylvia, for always believing in me since the moment we met in high school, just sixteen years old. She is the embodiment of a soulmate, my favorite person in the known and unknown universe, and the person with whom I want to share each and every day. Sylvia has stuck by my side, providing infinite support, through all the challenges and obstacles of my undergraduate and graduate studies. I know that I am incapable of being the person I am today without her, and am eternally grateful for the love of the most caring, loyal, exciting, and strong person I have ever known. I am honored to call myself her husband.

I would like to thank my parents, Cathryn and James De Furio, who always supported my pursuit of scientific interests and provided the crucial background necessary to make it this far. Their love and sacrifice is foundational in allowing me to achieve all that I have in life. They worked so hard and did so much in order for my siblings and myself to be where we are today. I would also like to thank my siblings Laura, Anthony, Michael, and Nicholas for being such an influential part of my life. In addition, I would like to thank mis suegros, Claudia Acosta and Luis Figueroa, and my second sister Laura for welcoming me into their family all these years.

I would like to give special thanks to my advisor, Prof. Michael R. Meyer, for all of the encouragement, long discussions, and opportunities for me to grow into the scientist I am today. Michael's advice and mentorship were fundamental in overcoming the often challenging and seemingly insurmountable tasks of graduate school. Leading projects and working with the Hubble and James Webb Space Telescopes were unimaginable before my time at UM, but are now a reality thanks to Michael's help and trust in me. I hope that I can live up to the expectation of "peer".

Additionally, I would like to thank my many collaborators (too many to individually name), especially Megan Reiter, Adam Kraus, Alexandra Greenbaum, Charles Beichman, John Monnier, Trent Dupuy, Tyler Gardner, Kaitlin Kratter, Graça Rocha, Marie Ygouf, Trent Dupuy, Per Calissendorff, and all others who contributed to this work. I would like to particularly note my undergraduate research mentors Elizabeth Lada and Stephen Hagen who both sparked my interest in all things science. I would like to thank my thesis committee members (Michael Meyer, John Monnier, Kaitlin Kratter, Keren Sharon, and Fred Adams) for their contributions to forming my thesis project and suggested improvements with which I am extremely happy.

Lastly, I would like to thank all the other graduate employees with whom I have had the pleasure of working alongside these last six years, particularly my cohort of Nicolás Trueba, Kevin Whitley, Larissa Markwardt, and Xi Meng. Many of them likely had to hear my many complaints, arguments, and rants so I thank all for dealing with me and anyone who argued with me (Nic). To my fellow Florida astronomers, Sarik and Stephanie, our long nights on physics homework finally paid off. To the Cosmic Rays, especially Cam, Gillen, Kate, and Rory, we did it. Special thanks to all graduate employees in the decades preceding me whose never-ending struggle won countless benefits and salary increases for myself and others they did not know. To all future graduate employees, solidarity forever.

# TABLE OF CONTENTS

# LIST OF FIGURES

FIGURE

# LIST OF TABLES

TABLE

# ABSTRACT

Multiplicity is a common outcome of the star formation process that occurs across orders of magnitude in primary mass and orbital separation, from brown dwarfs to O-stars and out to thousands of au. Initial companion properties depend on the mass and specific angular momentum of molecular cloud cores, and are further modulated by continued accretion and orbital migration. Dynamical processes likely sculpt the companion population based on cluster environment. In this thesis, we explore crucial regimes of star-forming environment and primary mass to understand their impact on the formation and evolution of companion populations which are valuable inputs to a predictive star and planet formation theory.

We investigated the companion population to known low-mass stellar and sub-stellar members of the Orion Nebula Cluster (ONC), a high-density star-forming region, for comparison to results in low-density star-forming regions. With data from the Hubble Space Telescope, we created a double point-spread function fitting routine to detect companions beyond $0.5\lambda$/D, 10au at the distance to the ONC. We detected fifty-one companions (twenty-four are new) and characterized companion demographics using Bayesian analyses. We demonstrate that cluster dynamics are likely important at early times, shaping the companion population of the ONC to resemble the Galactic field, unlike low density associations. We argue that low binding-energy brown-dwarf binaries in the ONC can still be disrupted. We also find evidence for initial companion formation processes which do not depend on stellar density, but are dynamically processed depending on local stellar density.

Utilizing similar detection techniques, we explored the multiplicity of Y-dwarfs, the lowest temperature ($<$ 500 K) known free floating objects, with JWST. We probe the low-mass limit of companion formation around the lowest primary masses explored to date. We demonstrated the ability to recover companions beyond 0.05" in the NIRCam long wavelength channel, $0.5\lambda$/D. We show that WISE1828+2650, a peculiar low-mass brown dwarf, has no companion beyond 0.5 au. Either one exists at closer separations or this object has a more complex atmosphere than can be currently modeled. We report the first detection of a Y-Y dwarf binary system, WISE0336-0143, with a separation=1 au, primary mass=8.5-18 $M_J$, and companion mass=5-11.5 $M_J$ assuming ages from 1-5 Gyr. This result confirms that multiplicity occurs through the star formation process even approaching the opacity limit of fragmentation. These data and future JWST observations will allow us to fully characterize the companion population near the fragmentation limit and constrain

their formation processes.

Lastly, we probed the close companion population to A-type stars (1.5-2.5 $M_{\odot}$) using long-baseline interferometry with MIRC-X/MYSTIC at the Center for High Angular Resolution Astronomy Array. We detected seven companions across 0.29-8.86 au with mass ratios=0.21-0.96. We find no evidence for a difference between the companion frequency of A-type and solar-type (0.7-1.3 $M_{\odot}$) stars over 0.01-27.54 au and mass ratios of 0.1-1.0. However, we find tentative evidence for a difference in the companion frequency between A-type and more massive B-type stars. This result is potentially indicative of an increase in circumstellar disk fragmentation for higher mass primaries that produces more close companions.

All together, these results identify key features of the companion population based on star-forming environment and primary mass that will further our understanding of star formation processes and how companions impact the early conditions of disk evolution and planet formation.

# CHAPTER 1

# Introduction

## 1.1 General Background on Stellar Multiplicity

### 1.1.1 History of Stellar Multiplicity

For thousands of years, people observed stars and tracked their motions in the sky. Before long, astronomers noticed that some stars appeared close to others, referring to these observed phenomena as "double stars". Giovanni Battista Riccioli, an Italian Jesuit priest, first observed stars in close proximity to each other in 1650 (Niemela, 2001). For decades, these were considered to be chance projections of stars, not physically associated to each other. However, the concept of a gravitationally bound system of two stars was first proposed statistically by John Michell using observed separations and magnitudes to conclude some stars must be associated, hence the reality of multiple systems (systems with two or more stellar or sub-stellar components) and star clusters (Michell, 1767). Within the same era, William Herschel began monitoring the stars to observe their parallaxes, and soon found many double star systems although he was not yet convinced of their mutual attraction (Herschel and Watson, 1782). After almost twenty-five years of observations, Herschel was able to present the apparent motion of the components of binary systems around a common center of mass that was not attributable to their parallax, the first of which was Castor ($\alpha$ Geminorum) (Herschel, 1803). Such observations continued for decades, some led by his son John Frederick William Herschel, generating a list of over one thousand physically associated multiple systems (Herschel and South, 1824; Herschel, 1829). Decades later, the first spectroscopic binaries, Mizar ($\zeta$ Ursae Majoris) and Algol ($\beta$ Persei), were detected at about the same time in 1889 by Edward Charles Pickering and Carl Vogel (e.g. Vogel, 1890a,b). Today, we know that multiplicity is a frequent outcome of the star formation process, and with these first measurements a new area of exploration was opened.

### 1.1.2 Early Significance of Stellar Multiples

As the prevalence of multiplicity became clear, it also became evident that their formation and evolution were important pillars to understand stellar structure and evolution. The Hertzsprung-Russell (HR) diagram became a common fixture in studying stellar evolution within stellar populations, tracing the luminosity of stars as a function of effective temperature or the apparent magnitude as a function of observed color (Russell, 1914). With the discovery of binary systems, the masses of stars could be precisely measured. These estimates were crucial as stellar structure and evolution strongly depends on mass.

Other puzzling features of the HR-diagram were readily explained by the presence of multiple systems. Cluster members that were elevated above the main sequence (i.e. brighter than expected given their color) were discovered to be the result of unresolved multiple systems, counting the combined flux as that of a single star (Schlesinger, 1975). After resolving the flux of each component, they are well placed on the main sequence of the rest of the population as expected given their similar ages. Another mystery of the HR-diagram was a small population of stars that appeared to not evolve off the main sequence with the rest of the population. They remained on the main sequence with bluer colors than the turn-off point of the observed population, hence blue stragglers (Sandage, 1953). Eventually, these objects were discovered to be multiple systems at very close separations where either mass was transferred from the primary expanding star onto the companion or the two stars merge to create a higher mass star effectively with a younger age than the counterparts in the same population, e.g. primary expands enclosing the companion in a common envelope followed by the companion inward spiral (Ferraro et al., 2006; Di Stefano, 2011). In the history of astronomy, multiple star systems played a prominent role in many ways. With the improved ability to detect these systems, we can begin to more thoroughly understand their formation in our quest for a comprehensive theory of star formation.

### 1.1.3 Common Detection Techniques

Many methods have been utilized to detect and characterize multiple systems. These techniques each have their advantages and disadvantages and apply to specific regimes of companion separations and mass ratios ($M_{companion}/M_{primary}$). Some of the most common and historically important methods to find companions are described here.

The radial velocity technique utilizes the spectrum of the primary star and our knowledge of orbital mechanics to detect companions to stars (Struve, 1952). In the case of a companion orbiting the common center of mass of a binary system, the orbital velocity modulated by inclination is measured through the Doppler effect. Double-lined spectroscopic binaries are systems where both spectra of the components of the system can be extracted within the combined spectrum where the

change in radial velocity will move each spectrum along the course of its orbit (Tomkin and Tran, 1987). Single-lined spectroscopic binaries are systems where the companion spectrum can not be extracted from the combined spectrum due to its low signal, and therefore motion of particular spectral features of the primary star will uncover the presence of a companion. We can measure the radial velocity of a star with a sufficient resolution and signal-to-noise spectrum and a stable spectrograph. With multiple measurements over the course of a companion's orbit, the orbital parameters (e.g. eccentricity, period, semi-major axis, M*sini* etc.) can be estimated by fitting various models to the radial velocity curve. Due to the necessity of measurements throughout a significant fraction of the orbit, the radial velocity technique is limited to close companions usually $\lesssim 5$ au. However, this technique is commonly applied in the search for exoplanets with the ever increasing resolving power of modern day instruments, and even led to the first discovery of an exoplanet around a Sun-like star, 51 Peg b (Mayor and Queloz, 1995).

The eclipse method also depends on the orbit of the companion passing in front of the primary star. This technique utilizes photometric data observed frequently over a period of time, searching for changes in the estimated flux of the system (Grison et al., 1995). Before the companion transits the primary, the combined flux of the system serves as the baseline measurement. As the companion passes in front of the star, the light from the primary is blocked by the companion with respect to the observer, thus reducing the total flux. As the companion passes behind the primary, the flux of the system also reduces as the companion is now occulted by the primary. The signal of the decrease in flux over the course of the orbit can be used to determine the physical parameters of the system, most importantly the radius of the companion. In conjunction with the radial velocity technique, these measurements can be used to estimate the mass and radius of the companion, yielding a mean density. As with the radial velocity technique, this method depends on the orbit of the companion and therefore is most useful for companions at separations $\lesssim 1$ au. This technique is also a common approach to detecting exoplanets (Charbonneau et al., 2000). Typical ground-based photometric precision to detect companions through the eclipse method is roughly one in a thousand (Mallonn et al., 2022) while sub-Mercury sized objects have been detected with a transit depth of one in fifty thousand (Barclay et al., 2013).

Directly imaging companions is also commonly used with higher attainable contrast and angular resolution as telescopes increase in size and go to space and post-processing techniques improve. This technique requires the components of a multiple system to be individually resolved (Ghez et al., 1993). From the ground, this is limited by the atmospheric seeing of the night in question for a companion's flux to be isolated from the primary (Fried, 1965). With the advent of adaptive optics, direct imaging can reach the theoretical diffraction of the telescope where the point-spread function (PSF) of each component is not limited solely by atmospheric seeing (Fusco et al., 2006; Hugot et al., 2012). From space, the stability of the PSF allows the observer to attain similar diffraction limited

imaging as adaptive optics instruments from the ground (Rhodes et al., 2007). These imaging data can be better explored through various post-processing techniques that all attempt to optimally model the PSF of the primary and search for faint companions either simultaneously in the image or within the residuals of the subtracted primary PSF. This technique is also being utilized to observe exoplanets, placing constraints on the physical and atmospheric properties of the planets (Marois et al., 2006). This technique can detect companions beyond roughly the canonical diffraction limit of the telescope, depending on telescope diameter and observed wavelength ($\lambda$/D). This method is best applied to more widely separated companions, complementary to RV and eclipses, where recent coronagraphic observations with JWST/NIRCam and VLT/SPHERE achieve contrasts of 15-16 mag beyond 1-2 arcseconds (Greenbaum et al., 2023; Carter et al., 2023).

Optical and near-infrared long-baseline interferometry (LBI) is an observing mode that enables the detection of very close companions. This technique is based on the premise that one can use multiple telescopes separated by some baseline distance to achieve angular resolution equivalent to a telescope with the diameter of the longest baseline (Monnier et al., 2006). Light from the target in question is observed simultaneously with each telescope in the array and combined to produce an interferogram that is the result of positive and negative interference of the light from each telescope. From this interferogram, interferometric observables which describe the astrophysical scene (e.g. squared visibilities and closure phases) are derived over all sets of closed triangles (i.e. combinations of three telescopes) (Jennison, 1958; Rogers et al., 1974; Monnier, 2000; Monnier et al., 2004). Unresolved single sources will produce closure phases equal to zero and squared visibilities equal to one, while resolved sources or multiple point sources will cause these values to deviate. Models can then be fit to the interferometric observables over all baselines to identify the signal of a companion (Gallenne et al., 2015), e.g. non-zero closure phases. Typical contrasts limits with LBI are 5-7 mag at separations beyond $\lambda$/B where B is the longest baseline of the array. Nulling interferometry (Velusamy and Beichman, 2001) is another interferometric observing technique used to detect faint companions close to their primary stars. It relies on the concept of destructive interference whereby stellar light from one telescope is delayed in order to destructively interfere with the same stellar light from another telescope, effectively removing the signal of the star. Light from other point sources within the field of view (e.g. stellar companions or planets) will not be destructively removed because it enters the telescope at an angle, and will therefore be reinforced after the artificial delay allowing for sensitivity at very close separations. Other types of interferometric analysis include aperture-masking interferometry (AMI) (Tuthill et al., 2000). Instead of using multiple telescopes, AMI uses a mask that is placed within the image plane of a telescope which converts the normal PSF into an interferogram over which this same analysis can be applied. AMI is most useful at close separations, below the diffraction limit, often improving resolution over typical direct imaging post-processing techniques (Greenbaum et al.,

2015). This type of observation bridges the gap between RV/transit methods and that of direct imaging while achieving contrasts of ~ 7 mag at the diffraction limit with JWST (Kammerer et al., 2023).

Another common technique that uses imaging data is the common proper motion technique (Caldwell et al., 1984). This relies on having images of the resolved components of the system over a long period of time. If the components share a common proper motion, then they are likely physically associated to one another as unassociated sources should have random motion relative to each other. Common proper motion detections must be sufficiently separated so that their orbital motion around the center of mass of the system is not detectable over the time baseline. Therefore, this is best applied to much wider companions in nearby stellar systems over a long period of time (Ward-Duong et al., 2015).

Companions can also be detected through astrometric signals over an extended period of time (Danby, 1988). Stars with measurable proper motions will exhibit a "wobble" or periodic change in its motion if a companion is present (Morais and Correia, 2008). Since both components of the system orbit its center of mass, the motion of the observable primary star will exhibit this wobble which is dependent on the separation and mass of the companion. As with radial velocity and eclipse techniques, this method is dependent on an orbit. The maximum astrometric signal resulting from a companion is highest at larger separations due to the amount of motion the companion induces on the primary. However, widely separated companions have long orbits and the astrometric signal produced from the companion may not be observationally feasible due to the time require for that motion to occur. At very close separations, the primary moves much less as a result of the companion thereby reducing the astrometric signal. Detections through astrometric signal require a significant amount of the orbit observed to produce a strong enough signal and an orbit amenable to produce significant astrometric motion given the achievable astrometric precision of the observations. Tertiary components and higher order components of multiple systems can also be detected astrometrically. Gardner et al. (2021) showed the ability to detect the "wobble" induced by a tertiary component by tracking the relative astrometry of visually resolved binaries. Such analyses can be done with direct imaging and LBI observing as long as the astrometric precision is good enough to resolve the orbit of the higher order component. All together, these techniques and others can cover a broad range of companion properties, allowing for the exploration of multiplicity.

Example limits in separation and mass ratio are shown for various detection techniques in Fig. 1.1. For all techniques, we assume the primary is a 1 $M_\odot$ star at a distance of 100 pc and with an age of 2 Myr. For the astrometric technique, we assume the companion has a 10 yr orbit (twice the lifetime of the Gaia mission) and achievable precision of 10 micro-arcseconds, the expected precision of the Gaia mission for a G=10 mag star. For the radial velocity technique, we assume a 0.1 km/s achievable precision and a period of 2 years. For long-baseline interferometry, the

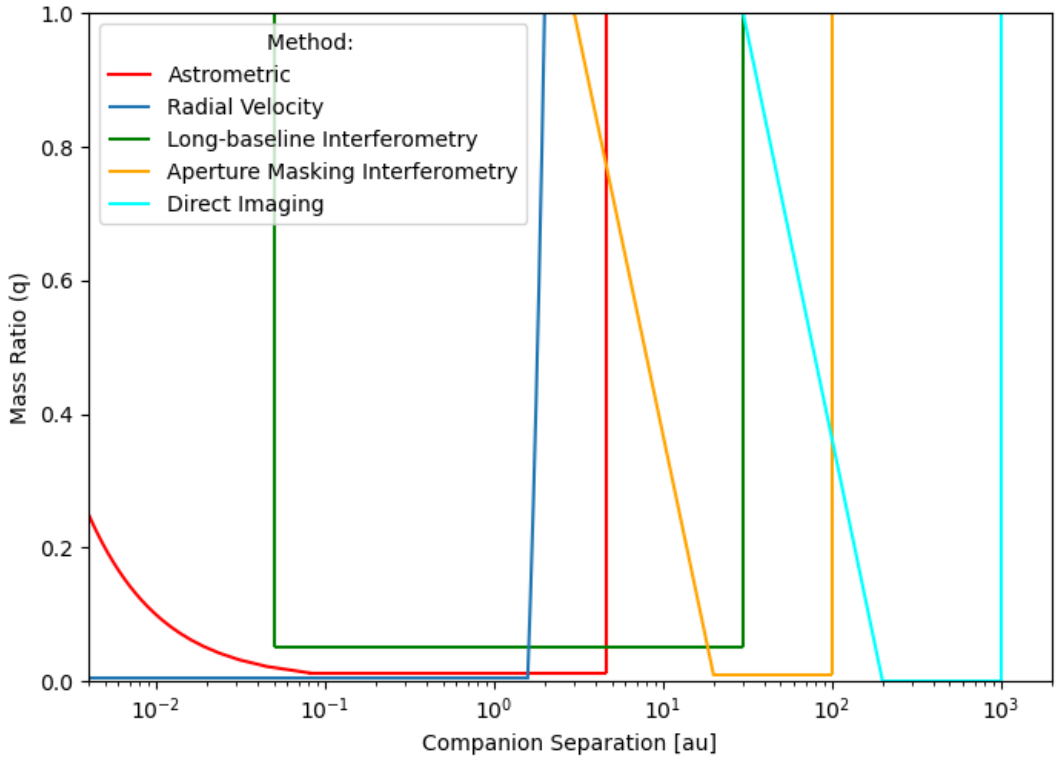


Figure 1.1: Various detection limits are displayed for different techniques. These show the ability to recover companions across a broad range of separations and mass ratios. Mass ratios are derived based on either the expected signal (for radial velocity and astrometric signal) or the attainable contrast and using the BT-Settl 2 Myr isochrone (Allard et al., 2012).

assumed primary has expected K = 7 mag (the limit for the CHARA array) where contrast of 5 mag is achievable over 0.5-300 milli-arcseconds. For AMI and direct imaging, we assume achievable contrasts of 7 and 15 mag respectively in the background limit. We estimate that AMI is sensitive to equal mass companions down to $\sim$ 0.03" and achieves the background limit near 0.2", c.f. JWST/NIRISS and KeckII/NIRC2. We estimate that direct imagining is sensitive to equal mass companions down to $\sim$ 0.3" and achieves the background limit near 2".

## 1.2 Theoretical Foundations in the Formation of Stellar and Sub-stellar Multiple Systems

Multiple systems are a frequent outcome of star formation, and their origin poses significant challenges for star formation theory. Companions are thought to be originally produced through two dominant channels, disk fragmentation (at separations $\leq$ the size of the disk, $\sim$ 100 au) and

turbulent fragmentation (out to 1000s of au) each with distinct mass-ratio distributions (Adams et al., 1989; Goodwin et al., 2004a; Offner et al., 2023). A third mechanism, capture, has been shown to occur in simulations of both young protostars due to gas friction and the migration of initially unbound protostars as well as within decaying star forming regions, as rare sets of cluster members become gravitationally bound at 1000s of au (Moeckel and Bate, 2010).

The formation of stellar and sub-stellar multiple systems through turbulent fragmentation of molecular cloud cores requires gravitational fragmentation of a sub-region of a cloud combined with the inclusion of gas turbulence, rotation, and magnetic fields to produce proto-stellar cores (Chen et al., 2019; Offner et al., 2022). Turbulence can be introduced to a gaseous medium through various sources, such as differential Galactic rotation in spiral arms, supernova explosions, stellar feedback, shocks, and more (Mac Low and Klessen, 2004; Falceta-Gonçalves et al., 2015). This turbulence will produce density fluctuations (von Weizsäcker, 1951; Padoan et al., 1997; Goodwin et al., 2004b) that can be represented on a continuum from less structured gas clouds to filamentary structures (Pineda et al., 2015). Within local increases in density, gas efficiently cools which can then produce a dense self-gravitating core (Jijina et al., 1999). As gravity overcomes the thermal pressure of the gas (i.e. the Jeans instability), an interior portion of the core collapses producing a protostellar core which continues to accrete and make a star (Shu et al., 1987). Two or more dense cores may form independently, but be bound through their mutual gravitation. Unbound cores can become bound if migration through gaseous material positions them close enough to another potential well, e.g. a dense core, where their mutual gravity is greater than the gravity provided by the cluster (Offner et al., 2023). Multiple fragmentation events can occur within a single prestellar dense core where the protostellar cores are expected to initially form at larger separations out to 1000s of au as the initial size of the prestellar core is roughly 0.1 pc (Arzoumanian et al., 2011). The initial mass ratios of systems produced from this formation mechanism are expected to follow random sampling from the initial mass function (IMF), e.g. preferentially lower masses for primaries with masses > the peak of the IMF, around 0.2-0.3 $M_\odot$ (Bastian et al., 2010).

Disk fragmentation is another formation mechanism to produce companions to stars. First, it requires the formation of a single protostellar core surrounded by a protostellar envelope. The central core has low angular momentum, but as more material is accreted from the envelope, more angular momentum is being transported requiring the formation of a circumstellar disk (Kuznetsova et al., 2019). Material continues to be accreted from the disk onto the star where the disk flattens and extends to conserve angular momentum. Other processes like outflows also serve as a way to conserve angular momentum. The gravitational instability within a circumstellar disk can be simply modeled by the Toomre criterion where the gravity of local portions of the disk overcomes the rotation and thermal pressure (Toomre, 1964):

$$Q = \frac{c_s \Omega}{\pi G \Sigma} \leq 1 \tag{1.1}$$

However, this model assumes a thin disk (Adams et al., 1989) which is not representative of the protostellar environment. In the case of a Class 0 protostar (young protostars where the majority of the final stellar mass is within the envelope yet to be accreted), the disk is being replenished by the envelope and instabilities will arise with an increase in local surface density. This occurs when more material is moving from the envelope to the disk than is being accreted by the star and the increased surface density is not counteracted by an increase in temperature from the central star (Kratter et al., 2010). This can also occur through late infall of gaseous material onto the disk (Kuffmeier et al., 2021). If instabilities occur early when the primary core is still small, the companion is able to build up more mass due to the large gas reservoir available and its preferential accretion within the disk, i.e. increase the initial mass ratio ($q \leq 1.0$). If disk fragmentation occurs at later times, the primary has already accreted a significant amount of mass and the companion has a smaller reservoir from which to accrete, producing smaller mass ratios. These two cores then continue to evolve and draw from the protostellar envelope and disk, where the companion likely preferentially draws material from the disk compared to the primary (Bate, 2000). Companions produced from this mechanism are expected to have initial separations on the order of the size of the disk $\lesssim$ 100 au. Masses of the companions are less predictable as they strongly depend on the gaseous reservoir available in the envelope, their separation from the companion, and the initial mass ratio of the system.

Companion formation from either channel can be impacted by subsequent processes that alter the companion properties. Companion migration through a gaseous disk can occur for objects resulting from disk fragmentation which continue to preferentially accrete from the disk. This has been known to drive mass ratios toward one if the process can begin at early times and drive the companion to close separations. Wider companions made through turbulent fragmentation out to 1000s of au can also migrate inward, some to < 10 au (Bate et al., 2002, 2003), and preferentially grow, increasing their mass ratio away from randomly drawing from the IMF. In these cases, companions $\lesssim$ 1 au likely form from disk fragmentation and subsequent evolution, those between $\sim$ 1-100 au likely form from either disk or turbulent fragmentation with the necessary migration and evolution, and those at $\gtrsim$ 100 au are likely formed through turbulent fragmentation.

All these processes and associated separation and mass ratio estimates could also depend on primary mass. In the extreme case, high-mass stars can form disks of 1000s of au (Preibisch et al., 2011; He and Ricotti, 2023), greatly increasing the ability to form companions at such wide separations (Kratter and Matzner, 2006; Ilee et al., 2018), although little is known about those companion populations due to their very high contrasts (e.g. Reggiani et al., 2022). Brown dwarf primaries also form disks whose dust sizes appear much smaller than those of high-mass stars, but

perhaps more similar to T-Tauri stars (e.g. 70-140 au, Ricci et al., 2014). These disks are typically very low mass, and simulations show that low-mass stars should be stable to disk fragmentation (Boley et al., 2007; Offner et al., 2010), although can fragment if the disk exceeds 50% the mass of the primary (Kratter et al., 2010), likely during the Class 0 protostellar phase.

High order multiple systems are also a common occurrence, particularly for high mass primaries (Gravity Collaboration et al., 2018). These can result from any combination of the formation channels. Many triples systems often show a wide outer companion where the distribution of mass ratios for these objects is consistent with random drawing from the IMF (Moe and Di Stefano, 2017), i.e. turbulent fragmentation. Often, very close binary systems have an outer tertiary component which can be partially explained through Kozai-Lidov cycles (Tokovinin et al., 2006; Moe and Kratter, 2018). Triple systems typically have the wide companion orbiting the primary star as opposed to a tight binary orbiting a higher mass primary. Quadruple systems, tend to form with two widely bound binary systems, i.e. a close binary system bound to another close binary system, as opposed to a primary with three companions on stable orbits (Raghavan et al., 2010).

Further, three-body interactions within dense star forming regions can destroy multiple systems, harden tight binaries, and soften wide binaries (Parker and Goodwin, 2011). The impact of such interactions depends on the binding energy of the multiple system which is a function of the separation and masses of the components within the system. We can expect very wide, very low mass ratio, or low mass primary systems to be preferentially disrupted due to interactions with other cluster members. Dense star clusters may experience a cold collapse phase that temporally increases the stellar density of the region by an order of magnitude, exacerbating this effect (Allison et al., 2009, 2010). Low density, unbound stellar associations do not experience this phase and likely never have significant processing of companion populations. Bound clusters and globular clusters that remain relatively high density over their lifetimes can have significant amounts of processing that alter their companion populations relative to their unbound counterparts (Kroupa et al., 2001a). The sum of these interactions over the course of the cluster lifetime will sculpt the companion population of the region. Therefore, differences in companion properties may be crucial factors into understanding the dominant environments in which stars form, as these environments imprint their properties on the companion population (Patience et al., 2002). All told, a predictive theory of star formation requires a complete understanding of the multiple formation process over orders of magnitude in separation, mass ratio, and primary mass.

## 1.3 Impact of Stellar Multiplicity on Other Astrophysical Phenomena

Multiple systems are known to form during the embedded protostellar phase and can persist through the stellar remnant phase of the sources within the system. Due to their presence throughout the stellar life cycle, they have significant impacts on a wide variety of astrophysical phenomena. Wide companions (> 100s au) have disks that evolve independent of effects from the primary and vice versa (Tobin et al., 2015). Companions that form during the protostellar phase can attain separations $\lesssim$ 100 au through either disk fragmentation or turbulent fragmentation with migration (Tokovinin and Moe, 2020). As these companions are at separations on the order of the size of the circumstellar disk, they can rapidly accrete material from the disk which causes the disk to dissipate at a much faster rate and reduces its lifetime (Cieza et al., 2009). They can also truncate disks to radii ~ 0.1-0.5 of the orbital separation of the companion (Artymowicz and Lubow, 1994). Companions at separations $\lesssim$ 40 au have been shown to allow for the presence of a circumbinary disk within which planets can form and have previously been detected (e.g. Doyle et al., 2011; Welsh et al., 2012). Kraus et al. (2012) found that the disk frequency for multiples with solar-type primaries in Taurus-Auriga increases with the separation of the companion, including a drastic transition from ~40% to 85% for primaries with companions < 40 au and those > 40 au. With shorter disk lifetimes, the ability to form planets is also hampered due to the lack of material to draw from in the disk. Studies of known planet hosts find that companions at separations 1 - 200 au significantly suppress the probability of finding a transiting planet (Kraus et al., 2016; Moe and Kratter, 2021). A recent multiplicity study targeting TESS planet candidate hosts, supports these findings for solar-type stars while also finding preliminary evidence for the same effect in M-type stars (Ziegler et al., 2021). Additionally, wide companions can scatter planets out of their previously stable orbits, impacting allowable planetary architectures (Kaib et al., 2013). Planets at > 10 au can be dynamically ejected even with companions at $\gtrsim$ 100 au (Marzari et al., 2005). Moe and Kratter (2021) estimate that $\eta_{\oplus}$, the frequency of Earth-sized planets in the habitable zone of a single Sun-like star, increases by a factor of 2.1 ± 0.3 after accounting for multiplicity. This is particularly important when designing missions and programs searching for Earth-like planets to the nearest stars (Bowens et al., 2021), many of which are in binary and higher order multiple systems, e.g. Alpha Cen, Sirius, Gliese 65, and Procyon. Observations point to an intricate relationship between host star mass, multiplicity, disk lifetime, and the formation of planets.

As stars age and lose their disks, wide companions no longer impact the evolution of astrophysical phenomena related to these systems. However, companions at close separations can continue to affect stellar evolution processes, sometimes until the end of the object itself. High-mass stars (M $\gtrsim$ 8 $M_{\odot}$) frequently have companions at close separations (Sana et al., 2012; Moe and Di Stefano,

2017). Once such a massive star evolves, it can become a black hole or neutron star (Celotti et al., 1999, and references within). If a close companion exists to these high mass stars, they can remain gravitationally bound to the stellar remnant. If the companion is close enough, the stellar remnant may then draw mass from the companion, resulting in an X-ray binary (Trueba et al., 2020). These come in many flavors depending on the mass of the companion and the amount of material being drawn, i.e. high-mass and low-mass X-ray binaries. High mass stars with high mass close companions are the progenitors to black hole-black hole, neutron star-black hole, and neutron star-neutron star binary systems. If the components within these systems merge, they produce very strong gravitational waves that have been recently detected by the Laser Interferometer Gravitational-Wave Observatory (LIGO) (Abbott et al., 2016). If a neutron star is a part of these very close binary systems, they produce a kilonova event which also creates a significant amount of gamma ray energy in the form of one class of gamma ray burst (Li and Paczyński, 1998; Abbott et al., 2016). When lower mass stars ($\lesssim 8$ $M_\odot$) evolve, they shed off their outer layers and eventually become white dwarfs, a degenerate core of helium/carbon/oxygen/neon depending on the mass of the progenitor star (Schatzman, 1958; Gil-Pons and García-Berro, 2001). If a close companion exists to these stellar remnants, they may be able to draw mass in the same way neutron stars and black holes can, governed by the Roche limit (Chandrasekhar, 1963). Hot white dwarf surfaces heat up the extracted Hydrogen, eventually resulting in a burst of fusion termed a nova (Darnley et al., 2012). If enough material is accreted onto the white dwarf, i.e. 1.44 $M_\odot$ the Chandrasekhar limit, the temperature of the core reaches that necessary for carbon fusion (Whelan and Iben, 1973). As carbon fusion begins, a cascade of nuclear reactions occur throughout the white dwarf. This produces enough energy to overcome the electron degeneracy pressure holding the white dwarf together and the object is blown apart in a rapid nuclear reaction event, a Type Ia supernova. These events can also occurs if two white dwarfs merge and overcome the same Chandrasekhar mass limit (Webbink, 1984). Type Ia supernova are useful distance measures to calibrate cosmological distances (Phillips, 1993). They also contribute significantly to the total amount of iron, nickel, and manganese among others to the universe, created in the expanding explosion after carbon detonation. Kilonova events produce a majority of the r-process (rapid neutron capture), heavy metal elements in the universe (Domoto et al., 2021). Kilonovae also inject energy into the interstellar medium as gamma ray bursts and contribute to the chemical evolution of galaxies through nucleosynthesis. Understanding their formation, particularly with respect to multiplicity, has crucial implications on many other astrophysical phenomena.

## 1.4 Observations of Stellar and Sub-stellar Multiple Systems Based on Primary Mass

Many multiplicity surveys of stellar and sub-stellar populations have been carried out in the Galactic field. The Galactic field population is an amalgamation of all stars produced in star-forming regions that have either completely dissolved or ejected portions of their populations into the field population. Stars in the field are formed in regions that span a broad range of properties, from low-density associations to high-density globular clusters. Therefore, we can treat the Galactic field population itself as the average outcome of the star formation process. Surveys in the Galactic field are typically best performed on an unbiased volume-limited (if not volume-complete) sample using a combination of observing techniques to cover the range of possible separations. Although some surveys have significant incompleteness over some parameter spaces, we are still able to draw general conclusions about the field companion population and its implications for star formation if the data are carefully analyzed to account for completeness.

Recent surveys of O and B stars ($M \gtrsim 2.5\ M_{\odot}$) have explored the companion population of high mass stars through radial velocity techniques, transits, long-baseline interferometry, sparse aperture masking, and direct imaging. Since they evolve quickly, these stars do not survive into the Galactic field population, so their multiplicity must be explored at early times in star-forming environments. These studies find that nearly all O and B stars are in multiple systems over the mass ratios and separations sampled, with a large portion existing in triple or higher order systems. Sana et al. (2012, 2013) performed spectroscopic surveys of O-stars in the Tarantula Nebula and nearby open clusters, finding multiplicity frequencies > 0.5 for periods $\lesssim$ 1000 days. Sana et al. (2014) performed a long-baseline interferometry, sparse aperture masking, and direct imaging survey for O-stars within 3.5 kpc in the Southern Hemisphere and found a multiplicity frequency of 0.91 and a companion frequency of 2.2 across $\sim$ 2-16,000 au (0.001-8" assuming the average distance of 2 kpc). Here we define multiplicity frequency as the fraction of primaries with at least one companion, and we define companion frequency as the average number of companion per primary star. More recently, Lanthermann et al. (2023) observed a small sample of Northern Hemisphere O-stars with long-baseline interferometry at the CHARA Array and found a multiplicity frequency of 0.59 over 1-110 au, or 0.5-55 milli-arcseconds assuming the typical distance of 2 kpc. Moe and Di Stefano (2017) characterized multiplicity for high mass stars, compiling statistics over many surveys and correcting for survey incompleteness finding that O-type stars have a multiplicity frequency of $\sim$ 0.90 over mass ratios > 0.1 and 0.2 < log(period) [days] < 8. They found similar results for B-type primaries after compiling statistics from Abt et al. (1990), Shatsky and Tokovinin (2002) and Rizzuto et al. (2013). They also found that the separation distribution peaks at $\sim$ 10 au with tentative evidence for a secondary peak at 0.5 au. They describe the mass ratio distribution as

a function of separation changing from flat to one biased towards lower mass ratios as separation increases, likely highlighting the enhanced prevalence of disk fragmentation for companion at close separations and turbulent fragmentation at wide separations.

Intermediate mass stars (A-type stars) have masses $\sim$ 1.5-2.5 $M_\odot$ and represent the bridge between the most common types of stars and the most massive, rare types of stars. Their multiplicity has been studied previously, although less thoroughly than most types of stars. Historically, they are bad candidates for radial velocity surveys due to their fast rotation that broadens absorption lines, and their lack of metal lines. A small spectroscopic survey by Abt (1965) found a population of companions to A-type stars, but there were no significant attempts to characterize their companion population for the decades following. Curiously, the radial velocity surveys of Am stars (chemically peculiar A-stars with small rotational velocities) by Abt and Levy (1985) and Carquillat and Prieur (2007) found a significant population of very close companions with a mean period of 5 days ($\sim$ 0.1 au), and a lower limit to the companion frequency of 0.64. While close companions could drive the decreased rotational velocity of Am stars and thus their peculiar chemical composition, they only make up a small fraction of all A-type stars. It is still unknown if such a close companion population with a significant fraction of companions at $\sim$ 0.1 au exists around typical A-type stars. De Rosa et al. (2014) carried out the first adaptive optics survey searching for companions to A-type stars within 75 pc, finding a companion frequency of 0.34 over $q > 0.1$ and $30 < a < 10^4$ au. They find a peak in the separation distribution at $\sim$ 390 au, but suffer from incompleteness to low mass ratios below 100 au, and are unable to resolve most companions below 30 au. Moe and Di Stefano (2017) attempt to correct for incompleteness, finding a flat separation distribution for A-type stars in log-period space for $q > 0.3$ for separations $> 30$ au. At closer separations, Murphy et al. (2018) used a phase modulation technique to identify companions to $\delta$ Scuti AF stars, and were sensitive over periods of 100-1500 days ($\sim$ 0.6-3.6 au), identifying a companion frequency of 0.14 for $q > 0.1$. While this program probed unexplored parameter space, the companion population to A-type stars at closer separations $< 0.6$ au and wider separations $3.6 < a < 30$ au is still underexplored and in need of a full characterization.

Understanding the formation processes of solar-type stars ($\sim$ 0.7-1.3 $M_\odot$) is crucial as they are so far the only type of star known to host life. Raghavan et al. (2010) is the quintessential multiplicity survey of solar-type stars, following Duquennoy and Mayor (1991). They performed a volume-limited survey within 50 pc to characterize the companion population using a wide variety of techniques, many of which are mentioned above, and compiling additional results from the literature. They found that the multiplicity frequency of solar-type primaries is 0.44 with a companion frequency of 0.58 over $q > 0.1$ and $a < 10^5$ au. They found that the separation distribution peaks at 50 au, and is well-fitted by a log-normal distribution while the mass ratio distribution is flat for $q > 0.1$.

M-type stars (low-mass and very low-mass stars with masses $\sim$ 0.08-0.7 $M_\odot$) dominate the stellar population in total number and mass with the most common star having a mass of 0.2 $M_\odot$. In order to have a comprehensive theory of the star formation process, it is crucial to understand M-type stars. Janson et al. (2012) carried out an imaging survey of hundreds of M-type primaries within 52 pc. They were sensitive to companions between $\sim$ 3-227 au and q $\gtrsim$ 0.5, and found a companion frequency of 0.27. Similarly, Winters et al. (2019) performed a volume-limited survey within 25 pc of M-type primaries, finding a companion frequency of 0.32. They state that they suffer from incompleteness for q < 0.5 and are sensitive to companions down to 30 au for 50% of their sample. Ward-Duong et al. (2015) also performed an AO survey to early-M primaries within 15 pc, finding a companion frequency of 0.24 over 3-10,000 au and q > 0.2. While these surveys have differing incompleteness, they each find a large population of companions around 5-20 au and speculate that the separation distribution is well-fitted with a log-normal with a peak at closer separations than solar-type primaries. The mass ratio distribution appears consistent with a flat distribution for q > 0.5, where incompleteness begins to impact statistics for Janson et al. (2012) and Winters et al. (2019), a result consistent with Reggiani and Meyer (2013), while Ward-Duong et al. (2015) finds that a flat mass ratio distribution extends to q=0.2 for their early-M star sample. Importantly, Susemiehl and Meyer (2022) synthesized these analyses of M-type primaries and estimated the best fit log-normal to the separation distribution as well as the companion frequency. They find a peak in the log-normal around 50 au (consistent with FGK-type primaries, but not that of these other M-star surveys), and a companion frequency of 0.229 $\pm$ 0.028 over q=0.6-1.0 and a=0-10,000 au, similar to that of solar-type and A-type primaries over the same range of separation and mass ratio. These results demonstrate the potential uncertainty in the known companion population to M-type primaries in the Galactic field.

Brown dwarfs (sub-stellar objects with masses $\sim$ 0.003-0.08 $M_\odot$) represent the limit of the star formation process at the low mass end of the initial mass function (IMF), governed by the opacity limit for fragmentation (Goodwin et al., 2004c). A robust accounting of the IMF down to Jupiter masses is currently in progress with the JWST, but even with the uncertainty at the low mass end, brown dwarfs contribute a sizable fraction of the stellar population, roughly one brown dwarf for every five stars with masses < 1 $M_\odot$ (Andersen et al., 2008). The formation of companions to brown dwarfs also represents the lower mass limit to companion formation properties and is required to develop a predictive theory of star formation. Several surveys have been carried out using ground based AO or space-based diffraction-limited imaging to characterize the companion population to brown dwarf primaries. Typically, samples are small ($\lesssim$ 100) due to the faintness of the primaries and the expense associated with long exposures to observe individual targets. These studies (e.g. Close et al., 2003; Gizis et al., 2003; Reid et al., 2006; Fontanive et al., 2018) in the Galactic field reveal companions at close separations, < 10 au, with a paucity of wide companions, > 20 au. They

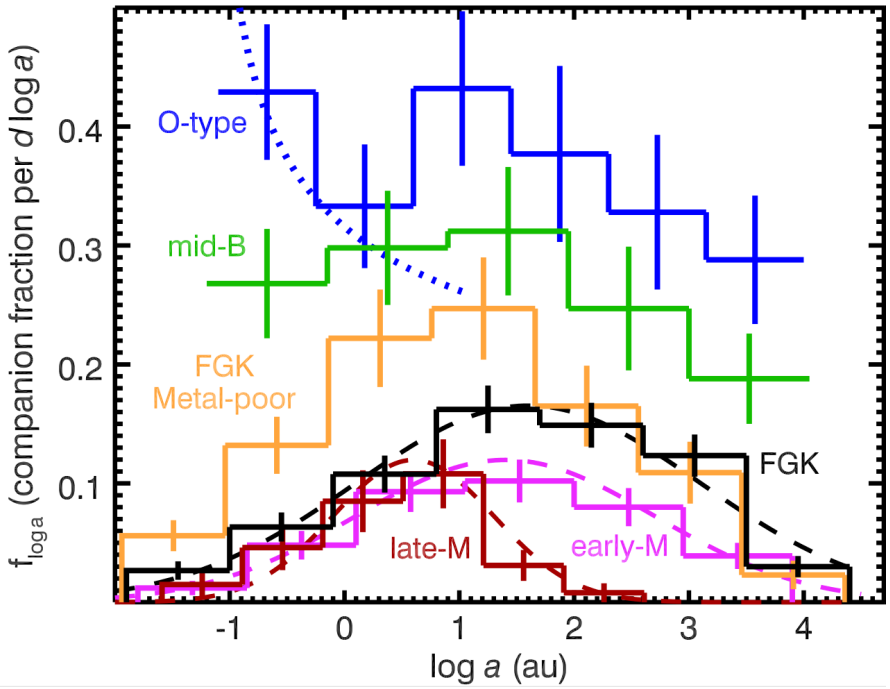


Figure 1.2: Image Credit: Offner et al. (2023). Companion frequency per decadal bin in orbital separation for various primary masses in the Galactic field. Different colored lines correspond to different primary masses of the multiple systems from late-M type primaries to O-type primaries. Stellar companion frequency appears to increase with primary mass as does typical separations of companions. From late-M to FGK-type primaries, separation distributions are consistent with a log-normal distribution, while O-type and B-type primaries have roughly flat distributions.

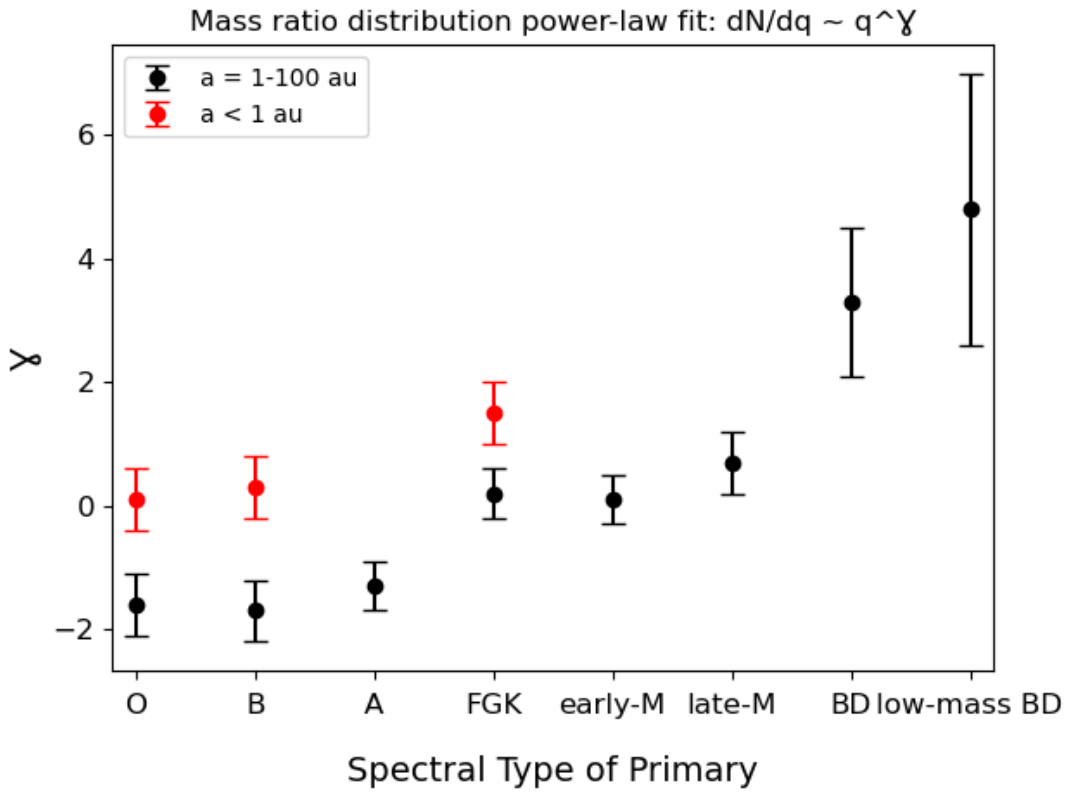


Figure 1.3: Adapted from Offner et al. (2023). Power-law indices of the mass ratio distribution model across primary masses from O-stars to low mass brown dwarfs in the Galactic field for a < 1 au and a = 1-100 au. The power law index increases as primary mass decreases over 1-100 au. Power law index also increases for FGK-, B-, and O-type primaries for companions with separations 1-100 au and those < 1 au, indicative of additional processes that alter the mass of the companion at separations < 1 au.

estimate companion frequencies of $\sim$ 0.15-0.24 beyond a few au and q $\gtrsim$ 0.2-0.4, showing that the separation distribution can be modeled by a log-normal distribution with a narrow peak somewhere between 3 and 10 au and a mass ratio distribution biased toward equal mass companions, e.g. power-law index of 3.6 for L-dwarfs (Reid et al., 2006) and 6.1 for T-dwarfs (Fontanive et al., 2018). Importantly, separations < a few au are underexplored for brown dwarf primaries and may harbor a population of companions undetected to date. Even colder objects, Y-dwarfs (Teff < 500 K), are so faint in the optical and near infrared that ground-based large telescopes with adaptive optics cannot obtain high signal-to-noise data. These objects represent the absolute limit of fragmentation, and are the oldest and/or lowest mass free floating objects in the field. With larger telescopes and observations in the thermal infrared ($\sim$ 3-5 microns), characterizing the multiplicity of Y-dwarfs is an essential test of formation at the limit of fragmentation.

From these many multiplicity surveys, we can conclude that the separation distribution is well-fit with a log-normal peaking at 3-10 au for brown dwarf primaries, $\sim$ 20 au for M-star primaries, and 50 au for solar-type primaries. A recent review (Offner et al., 2023) explored these multiplicity statistics further and show that higher mass O, B, and A stars appear to have separation distributions flat in log-space, with high frequencies of companions across all separations, see Fig. 1.2. They also describe the distribution of mass ratios with a power law which becomes more heavily weighted towards equal mass companions as the primary mass decreases, i.e. power-law index increases as primary mass decreases, see Fig. 1.3,

$$\frac{dN}{dq} \propto q^{\gamma} \tag{1.2}$$

Importantly, they find that mass ratios also appear to depend on orbital separation. Companions at wider separations ($\gtrsim$ 100 au) are skewed toward lower mass ratios, similar to being drawn from the IMF. Companions at close separations ($\lesssim$ 1 au) are skewed toward equal mass ratios due to competitive accretion processes, and those between 1-100 au have a mass ratio distribution in between these two which likely results from preferential accretion from the circumstellar disk. These differences point to the various formation channels and evolutionary processes within the natal cloud and circumstellar disk that dominate specific ranges of parameter space in terms of primary mass, mass ratio, and orbital separation. While many of these surveys are comprehensive, significant incompleteness exists in our understanding of multiplicity in the Galactic field particularly for intermediate mass stars and at the fundamental limit of fragmentation. In this thesis, we probe these primary masses to place strong constraints on the formation of stellar and sub-stellar multiple systems as a function of primary mass.

## 1.5 Observations of Stellar and Sub-stellar Multiple Systems in Star-forming Regions

Stars are created in many, varied environments that enable the fragmentation of molecular gas. After the dissociation of these regions, their stellar content will become a part of the Galactic field. Even high density, bound clusters will expel a majority of their stellar content over the course of its lifetime (e.g. the Pleiades, Kroupa et al., 2001a). Companions to stars in the field with orbital separations < 100 au are thought to be tightly bound, and will likely conserve their companion properties regardless of Galactic dynamics (Parker and Meyer, 2014). However, dynamics within star-forming regions at early times, and particularly high density, can disrupt multiple systems thus modifying the primordial companion population. Therefore, differences in the companion population of particular types of star-forming regions may be an indication of which regions contribute the most to the Galactic field over the course of the lifetime of the Galaxy, i.e. which regions are most common and typical locations for the formation of most stars.

There have been many multiplicity studies in young, star-forming regions of various environments. Spectroscopic surveys within many varied star-forming environments, 35% complete out to 1 au and 20% complete out to 4 au, find a consistent companion frequency relative to the field in all types of regions (Kounkel et al., 2019). These separations are rarely affected by dynamical interactions with other cluster members due to the high binding energy of these multiple systems, and therefore should not vary across star-forming environments if formation mechanisms are universal. Imaging surveys in Taurus-Auriga, a nearby low-mass low-density stellar association, found a companion frequency to low-mass and solar-type stars of $\sim 0.70$, roughly twice that of the Galactic field, across all mass ratios and separations of 3-5000 au (Kraus et al., 2011). A similar excess of companions had been previously identified in this and other low-density nearby stellar associations (e.g. Ghez et al., 1993; Leinert et al., 1993; Reipurth and Zinnecker, 1993; Simon et al., 1995; Brandner et al., 1996; Ghez et al., 1997). Other studies in Upper Scorpius (Tokovinin and Briceño, 2020), a high-mass OB association with low stellar density, identified a companion frequency to early M-stars and solar-type stars of 0.33 and 0.35 respectively over q > 0.3 and a = 9-2800 au, and claim an excess relative to the field for separations between 10-100 au. Duchêne et al. (2018) explored the companion population to 0.3 - 2.5 $M_{\odot}$ stars in the Orion Nebula Cluster (ONC), the closest high-mass high-density region with active star formation, and claim an excess relative to the field over 10-60 au. Importantly, this survey had a small sample size of 42 stars to which they found 13 companions and spans a broad range of primary masses to which companion properties strongly depend. Therefore, the ONC is a highly underexplored region below $\sim 100$ au for primaries $< 2.5$ $M_{\odot}$. If dynamical effects are important in shaping the companion population, a thorough multiplicity survey within a high density cluster like the ONC is necessary at these intermediate

separations. See Gravity Collaboration et al. (2018) for a long-baseline interferometry survey of O and B stars in the ONC.

Many earlier multiplicity surveys targeted wider companions, and attempted to statistically differentiate between observed objects that were chance alignments and those that were bound companions. Simon (1997) and Kraus et al. (2008) performed such analyses and found that low density regions likely have bound companions out to thousands of au in separations, while high density regions (e.g. the ONC) only have bound companions below $\sim$ 400 au. Scally et al. (1999) explored the wide companion population in the ONC using proper motion analyses and found an upper limit of three companions to 894 stars between 1000-5000 au. Reipurth et al. (2007) report a significantly reduced companion frequency in the ONC relative to the field for separations 150-675 au, although their detections in $H_\alpha$ make a direct comparison to the field over common mass ratios difficult. Köhler et al. (2006) similarly report a lower companion frequency relative to the field for companions out to 600 au. Offner et al. (2023) again compiled many statistics from various surveys and see a difference between the prevalence of wide companions beyond $\sim$ 300 au to stars in the ONC and those in lower density regions. Taurus and Upper Sco are more like the field beyond $\sim$ 300 au, but the ONC has a significantly lower companion frequency likely due to dynamical interactions at early times that disrupt companions at hundreds of au in separation. Multiplicity surveys targeting other star-forming regions like the embedded cluster NGC 2024 (Liu et al., 2003), and the OB associations Orion OB1a and Orion OB1b (Tokovinin et al., 2020) each found a companion frequency consistent with the field for wide companions $>$ 200 au. Intermediate separations ($\sim$ 10-200 au) are unexplored in many star-forming regions due to their far distances ($\sim$ 150-400 pc). However, we now have the ability to achieve high angular resolution with ground-based AO systems and space-based imaging to detect such systems.

Importantly, Galactic dynamics may impact the end state of a multiple system with separation $>$ a few hundred au. Therefore, wide companions are not a practical tracer of the origin of the field population. Similarly, close companions $<$ 10 au are hard multiple systems that will remain unaffected by cluster dynamics and Galactic dynamics, and are not good tracers of the dominant contributor to the field population. Intermediate separation multiples ($\sim$ 10-200 au) can be impacted by cluster dynamics but are mostly unaffected by Galactic dynamics, making them the optimal tracer for the origin of the field population. While studies in Taurus find an excess of companions for both the low-mass and solar-type stars, similar studies covering intermediate separations have not been performed in high density regions, mostly due to the distance and angular resolution required. In this thesis, we present a multiplicity survey in the ONC sensitive down to 10 au for low-mass stellar and sub-stellar primaries that allows us to explore the potential impact of dynamics on intermediate separation scales. As low mass stars dominate the stellar population in total number and mass and typically have companions at 20 au in the field, such a survey will probe the largest number

of possible companions for the most common type of star in a unique star-forming environment. With the analysis of these intermediate separation companions, we can explore how high stellar density within a star-forming environment promotes dynamical interactions to sculpt its companion population, whether these dynamical processes result in a companion population similar to the Galactic field, and the likely formation channels that dominate to produce companions to low mass stars.

## 1.6 Overview of Thesis

In my thesis, I first explore the companion population of low-mass stars and brown dwarfs across 10-200 au within the Orion Nebula Cluster using the Hubble Space Telescope as a test of the effect of cluster dynamics on the formation of multiple systems. Described in Chapter 2 are the results of this survey and a comparison to other star-forming regions and the Galactic field population. Then in Chapter 3, I explore the potential multiplicity of a peculiar Y-dwarf (WISE1828+2650) in the Galactic field using the James Webb Space Telescope, and report the first ever detection of a Y-Y dwarf binary system as a part of a larger program exploring the multiplicity of a small sample of these low mass brown dwarfs which represent the limit of fragmentation. In Chapter 4, I present and report the results of an ongoing multiplicity survey, targeting A-type intermediate mass stars within 80 pc using long-baseline interferometry. This survey searches the highly unexplored companion population of typical A-type stars as a probe of star formation processes as a function of primary mass. In Chapter 5, I discuss the implications of this work in the broader field of star formation, both its processes and the environments in which it occurs. Then, I present future programs that could answer the still outstanding questions uncovered or unaddressed in this work. I present my concluding remarks in Chapter 6. Finally, I present an additional project that I led in Appendix A where I explored the ability to perform high-contrast imaging on JWST/NIRISS data for full aperture and aperture-masking observing modes using information from the phase calibration of the telescope as priors to a theoretical point-spread function model.

# CHAPTER 2

# Binary Formation in the Orion Nebula Cluster: Investigating the Low-mass Stellar and Sub-Stellar Population

The work presented in this chapter was originally published in the Astrophysical Journal over a series of three papers: De Furio et al. (2019, 2022b,a). I led the data analysis, statistical interpretations, and the manuscript writing. These data were observed by the Hubble Space Telescope during Cycle 13 as a part of "The Hubble Space Telescope Treasury Program on the Orion Nebula Cluster" (ID: 10246, PI M. Robberto). Thank you to my co-authors: Michael R. Meyer (University of Michigan), Megan Reiter (Rice University), John Monnier (University of Michigan), Adam Kraus (University of Texas - Austin), Trent Dupuy (University of Edinburgh), Alexandra Greenbaum (IPAC), and Christopher Liu (University of Michigan). Special thanks to Christopher Liu for analyzing data in De Furio et al. (2022a).

## 2.1 Abstract

We present results constraining multiplicity demographics for the stellar and sub-stellar population of the Orion Nebula Cluster (ONC), across primary masses 0.012 - 0.7 $M_{\odot}$. Our study utilizes archival Hubble Space Telescope (HST) data obtained with the Advanced Camera for Surveys(ACS) using multiple filters (PID: 10246, PI M. Robberto). Studying the companion populations of young, star-forming regions provides valuable constraints of how the birth environment affects multiple formation and evolution. Previous multiplicity surveys in low-mass, low-density associations like Taurus-Auriga identify an excess of companions to low-mass primary stars roughly twice that of the Galactic field, over all mass ratios and for separations of 3-5000 au, and even trends in the companion properties as a function of primary mass (some seemingly consistent with the field population). Our study investigates the companion population of the ONC (a high-mass, high density star-forming region) where dynamical interactions are more likely to occur and modify the companion

population. We implement a double point-spread function (PSF) fitting algorithm sensitive beyond separations of 10 au (0.025", 0.5$\lambda$/D at 555nm) using empirical, position-dependent PSF models. We have identified 44 companions to low-mass stars and 7 companions to very low-mass stellar and sub-stellar primaries. We found: 1) the companion frequency (CF) of low-mass stars in the ONC is consistent with the Galactic field over all mass ratios and orbital separations of 10-200 au, in contrast to the higher CF found in low-density regions like Taurus, 2) the power-law fit to the mass ratio distribution of low-mass primaries in the ONC is consistent with that in the field and Taurus, similar to results from N-body simulations and potentially indicative of a formation mechanism independent of stellar density, and 3) the CF to brown dwarfs with separations > 20 au in the ONC is in excess of the field, requiring further dynamical evolution to destroy binaries with low binding energy and resemble the field.

## 2.2 Introduction

Multiplicity is a common outcome of star formation that impacts stellar evolution, planet formation, and the eventual makeup of the Galactic Field population. Developing a predictive theory of star formation requires an explanation for the formation of low-mass stars ($\sim$ 0.1 - 0.7$M_{\odot}$), very low mass stellar ($\sim$ 0.08-0.1 $M_{\odot}$), and sub-stellar objects ($<$ 0.08 $M_{\odot}$). Low-mass stars dominate stellar populations in total number and mass, and sub-stellar objects represent a limiting case of the star formation process, accounting for roughly one object for every five stars with masses $<$ 1 $M_{\odot}$ (Andersen et al., 2008). Multiple systems are thought to be created through two dominant mechanisms, turbulent fragmentation (Goodwin et al., 2004a; Offner et al., 2010) and disk fragmentation (Adams et al., 1989; Bonnell and Bate, 1994; Kratter et al., 2008). Their properties (e.g. separation, mass ratio, and eccentricity) can be altered by various processes. The mass ratio can increase due to an inwardly migrating companion preferentially accreting material from the circumstellar disk (Mazeh et al., 1992; Kroupa, 1995b; Bate and Bonnell, 1997; Bate, 2000). Wide companions can migrate to closer separations through interactions with infalling gas from the protostellar cloud or circumstellar disk (Bate et al., 2002, 2003; Offner et al., 2010; Bate, 2012). Other processes, like dynamical interactions between a multiple system and other cluster members, can even cause the complete dissolution of the multiple system (Kroupa et al., 2001a). Stars tend to form in clusters or associations which will eventually dissolve into the Galactic field (Carpenter, 2000). By studying young, star-forming regions, we can identify the properties of primordial binary populations which can help us put constraints on how binaries form as well as how they evolve with time. By studying diverse star forming regions, we can search for differences in binary populations as a function of various environmental properties such as stellar density.

Previous multiplicity surveys in the Galactic field have characterized the companion population

as a function of primary mass (Duchêne and Kraus, 2013; Offner et al., 2023). They find a separation distribution well-fitted with a log-normal where the mean separation appears to increase with primary mass: $\sim$ 3-6 au for very-low mass star ($\sim$ 0.08 - 0.1 $M_\odot$) and brown dwarf primaries ($<$ 0.08 $M_\odot$ Reid et al., 2006; Fontanive et al., 2018), 20 au for stellar M-type primaries ($\sim$ 0.1-0.7 $M_\odot$ Janson et al., 2012; Winters et al., 2019), and 50 au for solar-type primaries ($\sim$ 0.7-1.3 $M_\odot$ Raghavan et al., 2010). Higher mass O and B stars appear to have separation distributions flat in log-space, with high frequencies of companions across all separations. The distribution of mass ratios can be described by a power law ($dN/dq \propto q^\gamma$), weighted towards equal mass companions as the primary mass decreases, e.g. flat for solar-type primaries ($\gamma$= 0, Raghavan et al., 2010) and peaked toward unity for TY-dwarf ($\sim$ 20 $M_{Jup}$) primaries ($\gamma$= 6.1, Fontanive et al., 2018).

Multiplicity surveys in young, nearby associations find an excess of companions to low-mass primary stars relative to the Galactic field (Ghez et al., 1993; Leinert et al., 1993; Reipurth and Zinnecker, 1993; Simon et al., 1995; Brandner et al., 1996; Ghez et al., 1997). One such survey in the Taurus-Auriga dark cloud found a companion frequency of $0.79^{+0.12}_{-0.11}$ over all mass ratios and for separations of 3-5000 au for stars with primary masses of 0.25 - 0.7 $M_\odot$, roughly twice that of the Galactic field (Kraus et al., 2011). Other studies targeting very low-mass stellar and sub-stellar primaries in young, stellar associations such as Upper Sco, Chamaeleon I, TW Hydrae, and Ophiuchus have identified companions to brown dwarfs at separations $>$ 20 au (e.g. Chauvin et al., 2004; Luhman, 2004; Close et al., 2007; Ahmic et al., 2007), where similar types of companions are exceptionally rare in the field. These binary excesses for low-mass primaries and detections of wide companions to brown dwarf primaries have led to the speculation that many stars and brown dwarfs could form as multiple systems where a large fraction of these binaries could be destroyed through dynamical evolution (Horton et al., 2001; Kroupa, 1995a). Importantly, regions like Taurus have low stellar densities ( $\sim 10^0$ - $10^1$ $pc^{-3}$, see Liu et al., 2003) which could allow for an excess in wide binaries that are not destroyed through dynamical evolution. These regions could be examples of more uncommon locations for star formation to occur, contributing only a small fraction of the Galactic field population.

The Orion Nebula Cluster (ONC) is the nearest high mass, high density star forming region at $\sim$ 400 pc (Großschedl et al., 2018), and thus the ideal location to study the primordial binary population over a broad range of separations in a more dense environment than the nearby young associations. It has also been extensively observed through the Hubble Space Telescope Treasury Program (Robberto et al., 2013) using the Wide Field Channel (WFC) on the Advanced Camera for Surveys (ACS), granting us access to a large survey area with high angular resolution (a diffraction limit of $\sim$ 0.05" at 555 nm, or $\sim$ 20 au at 400 pc the distance to the ONC).

An adaptive optics (AO) survey of the ONC achieved an inner working angle of 60 au and was sensitive to mass ratios down to 0.4 for separations 160-500 au (Köhler et al., 2006). The most

recent survey of the ONC was carried out by Duchêne et al. (2018) with AO and is sensitive over separations 10 - 60 au. Their sample of 42 sources mostly consisted of solar-type stars, and had 11 M-stars, low-mass stars with masses 0.1-0.7 $M_{\odot}$. Low mass stars dominate the stellar population of the ONC in both total mass and number, and therefore play an important role in dynamical evolution. It follows that a much larger sample of low-mass stars is necessary to determine if an excess in companion frequency is typical of most star forming regions as seen in Taurus-Auriga and other low density associations which are also dominated by low mass stars. The HST Treasury Program of the ONC has the sensitivity to observe low-mass stars and, with point-spread function (PSF)-fitting, e.g. Garcia et al. (2015), identify companions at separations down to 10 au, a parameter space previously unexplored and incomplete for low mass stars and brown dwarfs.

In Section 2.3, we describe the HST data in the ONC. In Section 2.4, we describe our double PSF-fitting technique. In Section 2.5, we describe our sample of low-mass stellar, very low-mass stellar, and sub-stellar objects. In Section 2.6, we describe how we characterized the sensitivity of our survey and the procedure of identifying high confidence detections. In Section 2.7, we present our discovered multiples as well as the characterization of the companion population and its comparison to other populations. In Section 2.8, we discuss the implications of our survey. In Section 2.9, we summarize our conclusions.

## 2.3 Data

We downloaded archival HST data taken with ACS on the Wide Field Camera (WFC) from GO program 10246 (PI: M. Robberto, Robberto et al., 2013). The data analyzed in this chapter were obtained from the Mikulski Archive for Space Telescopes (MAST) at the Space Telescope Science Institute, and can be accessed via DOI [1]. This program captured a large mosaic of the ONC, covering 627 arcminutes, with four broadband filters and one narrow band filter: F435W, F555W, F658N, F775W, and F850LP. Each of the 104 pointings had an integration time of 420s, 385s, 340s, 385s, and 385s respectively and a field of view of 202" x 200", with no dithering or CR-SPLITing in order to preserve the true astrophysical scene and implement empirical PSF model fits. The plate scale of ACS/WFC is 0.05"/pixel, undersampled across the visible spectrum (e.g. $\lambda$/D = 0.037" for F435W). We used empirical PSFs to fit the data and accurately estimate the centroid of the primary PSF and any potential companion. We use the _flt data products from the HST pipeline, which have been bias-subtracted and flat-fielded. These are the images specified by Anderson and King (2006), hereafter AK06, for which the empirical PSFs apply. Within these long exposures, many images suffered from severe saturation which prevented us from performing PSF-fitting to many known members. A more thorough description of the data can be found in Robberto et al. (2013).

[1] http://dx.doi.org/10.17909/5w65-rr60

## 2.4 Fitting Empirical PSF Models

Anderson and King (2006), hereafter AK06, developed 90 empirically-derived, position-dependent PSFs per filter for both detectors on ACS/WFC, which enable accurate astrometry of $\sim$ 0.5 mas (0.01 pixels). AK06 produced a PSF library for each filter which describes the shape of the PSF as a function of location on the ACS detector. These PSFs are 4x super-sampled where the 100x100 pixel array of each PSF corresponds to a 25x25 pixel array on the ACS detector, or a 12.5 pixel radius. To construct a model PSF at a given location on the detector, we first identify the four nearest empirical PSFs. For each pixel within a 21x21 pixel stamp centered on the target, we perform a bi-cubic interpolation of each of the four nearest empirical PSFs based on the distance of that pixel to the center of the stamp. Then, we linearly interpolate those resulting four pixel values based on the proximity of each of the nearest empirical PSFs to the location of the target on the detector. This results in a detector-sampled PSF. AK06 also provide a function to perturb the PSF models based on the brightest PSFs within a given image to account for changes in focus and pointing instability which can cause the PSF to deviate from the average over time. We applied the perturbation to the PSF library of each filter for each image, effectively generating slightly different PSFs for each image.

We used the interpolation method of AK06 to make a double-PSF model (constructed from two detector-sampled PSFs) with their position-dependent empirical PSFs. The companion PSF is defined by its relative location from the center of the primary source and the difference in brightness between the two sources. Our complete binary model has six parameters: x and y position of the center of the primary, combined magnitude of the binary, pixel separation between the centers of the primary and companion PSFs, position angle between the centers of the primary and companion PSFs, and the difference in magnitude between the primary and companion.

Before fitting the model to the data, we subtract off the mean background around the source inside an annulus with an inner radius of 10 pixels and an outer radius of 15 pixels. To determine a best fit binary model to any input source, we fit the binary model to the background-subtracted 21x21 pixel stamp of the data where our algorithm first uses a coarse grid search to identify a region of parameter space where our model returns the best fit. Then by defining this result plus some random noise as the initial guess, we use the IDL downhill simplex function, AMOEBA (Press et al., 2007), which incorporates a series of reflections, expansions, and contractions, to sample the parameter space and identify the best-fit six parameter model by minimizing the chi squared test statistic. This process is repeated 200 times to adequately sample the parameter space and then derive errors for each variable. This process is performed individually for each image of all targets across all filters in which the targets appear. Each filter used in our data has its own PSF library generated by AK06 except for F555W. Instead, we use the F606W PSF library as the differences in

PSF structure between these two filters are negligible (J. Anderson, private communication). We calculated the reduced chi squared test statistic of each source by summing the chi squared statistic over each pixel in a 21 x 21 pixel stamp:

$$\chi^2_\nu = \frac{1}{\nu - 1} \sum_{i=1}^{N} \frac{(\text{data}_i - \text{model}_i)^2}{\sigma_i^2} \tag{2.1}$$

Here, the total error per pixel was the summed in quadrature errors of the source photon noise, the standard deviation in the background, the error in the mean of the background, the dark current, and the read noise as seen in Eq. 2. We added an additional 2% noise floor, defined as 2% of the flux in a given pixel, to the source photon noise in order to account for the error in the PSF models.

$$\sigma^2 = \sigma^2_{Source} + \sigma^2_{Bkgd} + \sigma^2_{\overline{Bkgd}} + \sigma^2_{DC} + \sigma^2_{RN} \tag{2.2}$$

Our algorithm will always find a "best fit" to any source. Whether the source in question is truly a binary depends on the sensitivity of our model for the particular S/N of the source. Our algorithm can converge to a fit that has large differences in magnitude between the primary and potential companion which would correspond to a companion indistinguishable from background noise or residuals in the primary PSF core. To determine if a given double-PSF fit is a true detection of a binary system, we calculate the false detection probability for each source in each image of each filter based on our sensitivity tests and metrics as stated in Sec. 2.6.2.

## 2.5 Sample

### 2.5.1 Low-mass stars

The target list was constructed from Da Rio et al. (2016). They used the Sloan 2.5m telescope and the APOGEE spectrograph (R ~ 22,500) to obtain multi-object spectroscopy in the H-band of roughly 2700 sources in the ONC. With these data, they were able to estimate the $T_{eff}$, log $g$, $v$ sin$i$, and extinction.

We searched through each of the 104 images in the five filters and identified which of the members exist within the data. Then, we determined whether or not the central pixel value was above 55,000 counts, to exclude sources affected by saturation (AK06). Finally, we ran the double-PSF fitting algorithm on each target in each image in which it was detected. We set a chi squared threshold to indicate a reasonable fit where the data are likely described by the six-parameter double-PSF model, here a p-value of 0.1, $\chi^2_\nu$ = 1.774. Nebulosity is the key factor for poor fits within these data as spatially variable extended emission is not factored into the model and results

in high $\chi^2_\nu$ values. This process left us with 198 sources in F435W, 143 sources in F555W, 226 sources in F658N, 11 sources in F775W, and 5 sources in F850LP. Source counts are very low in F775W and F850LP due to saturation. In total, we have 276 unique sources throughout all filters, and 245 sources among the broadband filters with which we can estimate masses of the multiple systems.

### 2.5.2 Very Low-mass Stars and Brown Dwarfs

We adopted our input target list of M6 - M9.5 objects ($\sim$ 0.012 - 0.1$M_\odot$ at 2 Myr from Allard et al. (2001) evolutionary models) from Hillenbrand et al. (2013) who identified ONC members with medium resolution, red optical spectroscopy. They classified low mass objects by measuring the depth of TiO and VO lines that are mainly temperature sensitive (Riddick et al., 2007). We also included M6 - M9.5 members that were previously spectroscopically confirmed in other surveys (e.g. Lucas et al., 2001; Slesnick et al., 2004; Lucas et al., 2006; Riddick et al., 2007; Weights et al., 2009) with optical spectra using TiO and VO band indices or near infrared spectra using $H_2O$ band indices and aggregated by Hillenbrand et al. (2013) in their Table 3. Some of these targets had been observed in multiple surveys with different molecular indices. For these targets, we preferentially assign the optical spectral type over IR spectral type due to the larger uncertainty in IR data associated with variability in young stars as described in Simon (2020). For the 15 targets with a range of spectral types listed, we use the median spectral type, e.g. for M6-M7 we adopt M6.5. This results in a total target list of 103 very low mass star (0.08 - 0.1 $M_\odot$) and brown dwarf (< 0.08 $M_\odot$) ONC members.

From the list of ONC members with spectral types M6 - M9.5, we first limited our source list to those that appeared in the area covered by the HST Treasury Program of the ONC, resulting in 94 sources remaining. Then, we limited our source list to those above a signal-to-noise (S/N) minimum of 15 (the equivalent to a few hundred counts) as it is challenging to detect companions around faint primaries. This minimum was set for each broadband filter meaning that as long as a target had a S/N of at least 15 in all its images in a single filter, it was included as a target in the sample (84 sources remaining). Lastly, we limited our source list to objects with a maximum pixel value below 55,000 counts, which excludes sources affected by saturation, analogous to the procedure of AK06. These filtering processes left the sample with 79 sources that were within the field of view and had sufficient S/N in at least one broadband filter to be analyzed with the double-PSF fitting tool.

For a source with the maximum pixel value equal to 55,000 counts, the entire PSF contains $\sim$ 250,000 counts. This flux corresponds to a 0.2 $M_\odot$ and a 0.03 $M_\odot$ object in the F435W and F850LP filters respectively with no extinction, and a 0.07 $M_\odot$ object in the F850LP filter with a

moderate amount of extinction (e.g. $A_v$ = 3). The lower bound of our sample cut-off (S/N = 15, $\sim$ 500 total counts) corresponds to a 0.017 $M_\odot$ and a 0.005 $M_\odot$ object in the F435W and F850LP filters, respectively, with no extinction and a 0.05 $M_\odot$ object and a 0.007 $M_\odot$ object with a moderate amount of extinction. Therefore, higher mass and low extinction brown dwarfs are more likely found in the bluer filters while lower mass and higher extinction brown dwarfs are more likely found in redder filters, see Fig. 2.16.

We then ran the double-PSF binary algorithm on our sample and set a chi squared threshold to indicate a reasonable fit to that in which a six-parameter model has a p-value equal to 0.1, $\chi^2_\nu$ = 1.774. Below this value, we do not reject the null hypothesis that the data could have come from our model. This resulted in a sample of 75 members found with S/N $\geq$ 15 and $\chi^2_\nu \leq 1.774$ in at least one broadband filter. Sources can be excluded from the sample based on goodness of fit criteria due to either the presence of a higher order companion or due to high differential nebulosity. In our sample, only four sources were excluded due to either being within a proplyd (one target) or in a region of high nebulosity (three targets).

## 2.6 Characterizing our Sensitivity

### 2.6.1 Completeness

First, we will characterize the ability of our binary PSF-fitting method to recover known binary systems before explaining how we determine whether or not a given double-PSF fit is representative of a true binary detection. The sensitivity of this method is a function of the S/N of the target, the separation between primary and companion, the difference in magnitude between the two, and the filter in which the data were taken. The S/N of a target is dependent on both the mass of the target and the interstellar extinction to the target. For two objects of the same mass, the object with higher extinction will have a correspondingly lower S/N, and it will be more difficult to recover faint companions around that source. Conversely, it will be easier to recover faint companions around the source with less extinction because the source is brighter and therefore there is a larger contrast where we can see fainter objects between the source and the background limit, see Fig. 2.1.

In order to distinguish between a real binary and a false positive result from our algorithm, we had to first determine the sensitivity of our method. This is a function of separation and difference in magnitude, as well as S/N of each source. We created artificial binaries from the PSF models of AK06 based on the location of the source. To create the companion source, we add another PSF at the defined location and with the specified flux ratio relative to the primary. To mimic a photon-noise limited observation (like expected from our data), we add Poisson noise to each pixel until the artificial binary was at the desired S/N. Since the data on ACS/WFC is under-sampled,

interpolation of the data to create sub-pixel shifts in the PSF would change the distribution of flux in each pixel and introduce more error. The PSF models of AK06 are super-sampled, and we can create artificial binaries at sub-pixel separations from the models instead of re-sampling the data. This allows us to accurately replicate the PSF of a binary system without losing information about the PSF if we interpolated the real data. We created binaries at multiple separations, random position angles, and differences in magnitude depending on the desired S/N of the sample.

The S/N ratio of each source was calculated with the following equation over all pixels in the 21x21 pixel stamp that encompassed each source where the error is the same as described in Sec. 2.4:

$$S/N = \frac{\sum_{i=1}^{N} (\mathrm{data}_i - \overline{\mathrm{bkgd}})}{\sqrt{\sum_{i=1}^{N} \sigma_i^2}} \tag{2.3}$$

The magnitude bins we sampled were dependent on the S/N. For higher S/N artificial binaries, we sampled integer (1.0-5.0) pixel separation binaries with Δmag down to 6.0 mags and sub-pixel (0.4, 0.6, and 0.8) separation binaries with Δmag down to 4.0 mags. For lower S/N artificial binaries, we sampled in a similar fashion, but down to lower contrast (e.g. 4.5 mags for integer pixel separation binaries of S/N = 30). This is again due to the fact that the range in Δmag space in which we can detect companions is directly related to the S/N of the target. We created 500 binaries in each bin for each S/N and ran the double-PSF code on these sources.

In our double-PSF fitting code, the AMOEBA routine samples the six binary parameter space as described in Sec. 2.4. We save each step taken by AMOEBA and its corresponding $\chi^2_\nu$ value. Because we created these artificial binaries, we know the true binary parameters values for each binary. Therefore, we can evaluate the goodness of fit of the double-PSF model at the exact value of the known binary parameters. If that $\chi^2_\nu$ value is > some critical value, then we can consider that binary not recovered by our method. We select a critical value for the $\chi^2_\nu$ distribution corresponding to a certain probability that the known binary parameter values come from the model that was fit. Here, we select the critical value ($\chi^2_\nu$ = 1.21) where there is a 99% probability that a $\chi^2_\nu$ value less than this critical value for a given set of parameters could be drawn from distribution of our model fit parameters. If the double-PSF fitting routine is complete for binaries of a given separation and Δ mag, we expect to recover 99% of the 500 binaries within that bin, showing that our method can accurately recover these binaries. We evaluate this metric for every artificial binary created within each bin in separation and Δmag space for all S/N values of all filters. When the method begins to become incomplete, this recovered fraction will drop below 99%. This cutoff value of 99% ensures that we expect to have failed to recover < 1 binary within both the stellar sample (276 unique

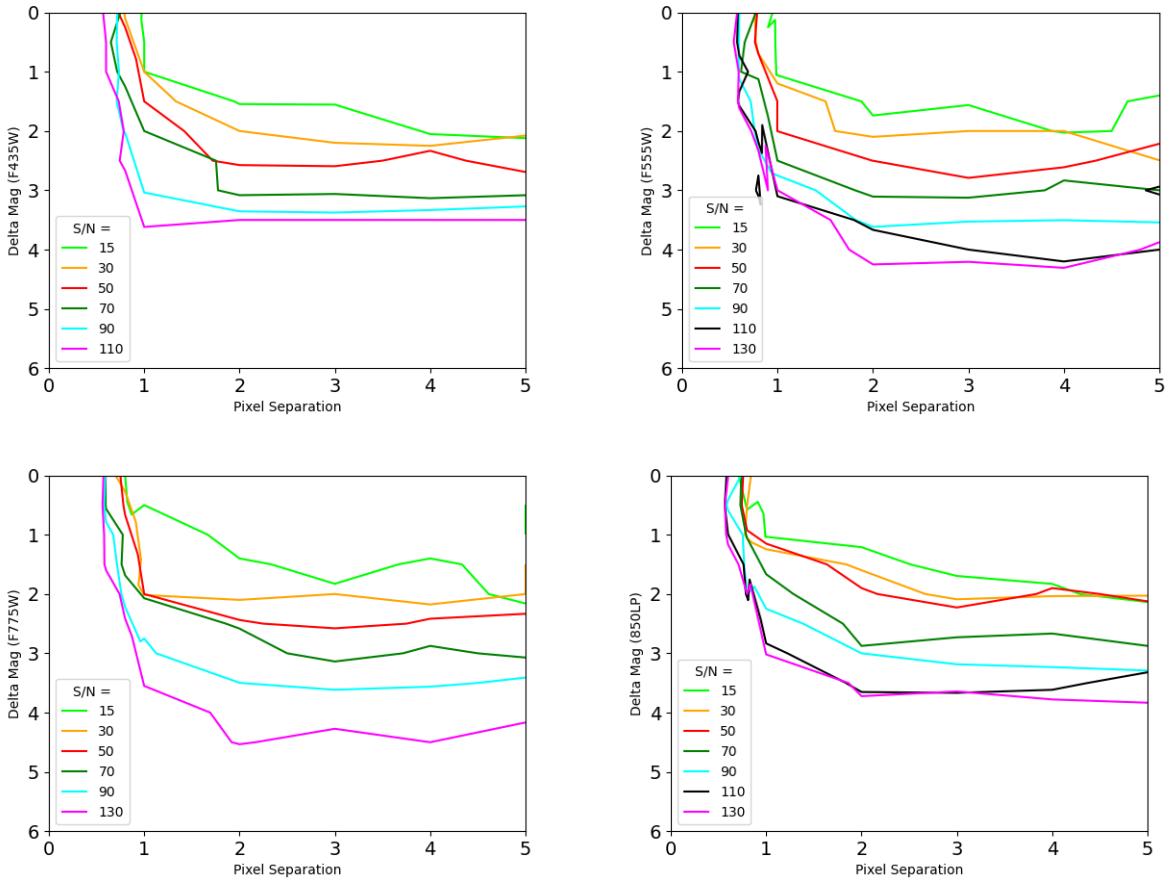


Figure 2.1: 99% recovery lines for all S/N tested in the four broadband filters of ACS used in the HST Treasury Program of the ONC. The different colors represent the recovery ability of our code for various S/N values. As expected, our code can recover fainter and closer companions around brighter targets. The angular resolution of our algorithm also improves as the S/N of the target increases. Above this line, we are confident that our double-PSF fitting algorithm is recovering nearly all binaries and our method is complete. From left to right and top to bottom: F435W, F555W, F775W, and F850LP.

sources) and the very-low mass stellar and sub-stellar sample (75 unique sources). Fig. 2.1 shows the 99% recovery line for each S/N tested for each filter used. This curve serves to define where we are confident our sample is complete. Importantly, the completeness of this method varies for different S/N values. A companion separated from the primary by three pixels with a $\Delta$mag of three mags will be detectable for all targets with S/N $\geq$ 90 in all filters, but will be undetectable around targets with S/N $\leq$ 70 in all filters.

### 2.6.2 False Positive Analysis

In addition to characterizing our completeness, we must also investigate the reliability of our fitting code. We can utilize false positive information to define the region of high probability detections. A false positive occurs when our binary fitting code converges on a binary fit to a single star, but with a $\chi^2_\nu \leq 1.774$ (as detailed in Sec. 2.5). We use the separation and $\Delta$mag values from the binary fits to artificial singles in order to determine the region in which our algorithm converges on a best-fit binary model, but the source is not a true binary.

The AMOEBA routine samples the six dimensional binary parameter space, fitting various binary models each with a calculated $\chi^2_\nu$, until converging. When fitting to a single, our double-PSF fitting code will fit the primary PSF accurately while the secondary PSF is fit to the residuals of the primary PSF or to the background pixels. Similar to the recovery of artificial binaries, the location in separation vs. $\Delta$mag space of false positive fits depends on the S/N of the source and the filter used, e.g. fitting to background pixels occurs at lower contrast around lower S/N targets.

We created 1000 artificial single stars built from the models in the AK06 PSF libraries for each filter and specified S/N, adding Poisson noise to simulate a generic observing scene. Then, we ran our double PSF-fitting routine on each of the artificial single stars, using the best fit from a coarse grid search in the six dimensional binary parameter space as an input to the downhill simplex algorithm (same process as for fitting binaries).

We use all steps and their associated $\chi^2_\nu$ within each fit to all 1000 single stars of a given S/N and filter in order to characterize the distribution of expected fits to single stars of the given S/N and filter. First, we calculated the chi squared probability, P($\chi^2$), for each fit AMOEBA makes to each artificial single while stepping to reduce the $\chi^2$:

$$P(\chi^2) \propto \chi^{2^{(\mathrm{dof}/2)-1}} e^{-\chi^2/2} \tag{2.4}$$

where dof is the degrees of freedom equivalent to the number of data points (i.e. pixels) minus the number of free parameters in the model (the six binary parameters). From the P($\chi^2$) equation, we calculate the P($\chi^2$) of each step while fitting to each artificial single star.

Then, we define the region of interest where the code is likely to fit the binary model to the data

(whether it is fitting to a real companion, the background, or the residuals of the primary) in terms of separation, centered on the primary, from 0 - 10 pixels and Δmag from 0 - 10 mags with bin sizes of 0.1 pixels and 0.1 mags. Within each bin, we select the best fit to each single, i.e. highest P($\chi^2$), and normalize the resulting distribution to one. This creates a probability distribution in separation and Δmag space for the double-PSF fitting routine to an artificial single star. We repeat this process for all 1000 artificial single stars for a given S/N and filter, which results in 1000 separate probability distributions of binary fits to artificial single stars. We sum all of these 1000 distributions, normalizing the result to one, which results in one distribution of all of the binary fits to single stars with the same S/N and in the same filter. This process samples the entire region of interest and allows us to determine where in separation and Δmag space the code is likely to converge if it is in fact fitting to a single star. Lastly, we sum vertically in Δmag space for each separation bin to find the value below which a certain percentage of the false positive fits will lie. This process is performed for all filters and all S/N values.

In Fig. 2.2, we show two examples of this in the F435W filter for S/N = 30 and 130. The color scale corresponds to the false positive probability of any given separation bin below which the corresponding fraction of the false positive fits will lie. We plot the 0.1% false positive probability in both figures to show the value below which 99.9% of false positive fits lie. The binary best fit to a single star will only converge 0.1% of the time above this value. Black circles represent the best fit binary parameters to the 1000 artificial singles, all of which lie below the 0.1% false positive probability line. The mean $\chi^2_\nu$ of the 1000 best fits to these single stars of a given S/N and filter is 0.99, indicative of no unmodeled noise terms. Binary fits above this value are likely binary detections. We define this as the reliability of our method, where fits with a false positive probability > 0.1% are unreliable. The corresponding curves are shown in Fig. 2.3 for each filter and S/N.

Fig. 2.4 gives an example of the 0.1% false positive probability curve for a S/N=90 target in the F435W with the completeness line for binaries of the same S/N in the F435W filter overplotted. It is evident that the completeness limit from Sec. 2.6.1 and the 0.1% false positive probability curve are overlapping. This is the case across all S/N values and filters. These results lead us to conclude that our sample is complete down to the 0.1% false positive probability line, and we do not expect to miss any real binaries above this limit. Therefore, we do not have to correct for incompleteness over the sensitivity of our survey.

Additionally, we compared the results of binary fits to artificial singles to binary fits to real singles within one filter and one S/N as an example of our method. We identified sources within the data that had a S/N ~ 30 in the F435W filter that were well fit with a single PSF. Each source was run through the binary-fitting code, and we repeated the process above to derive the false positive maps similar to Fig. 2.2. In Fig. 2.5, we show the 0.1% false positive probability line when fitting

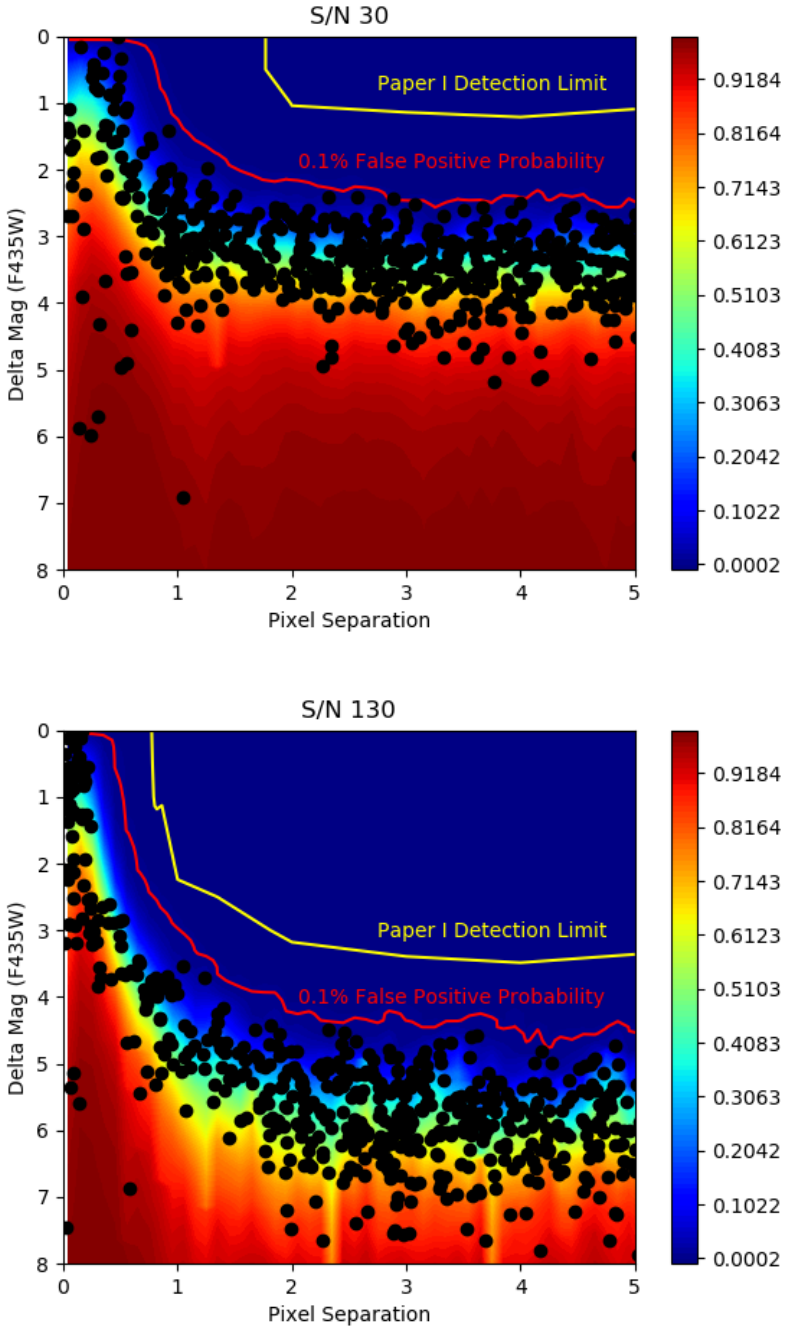


Figure 2.2: False positive probability maps in separation and Δmag space. The color scale represents the false positive probability where larger differences in magnitude correspond to a higher likelihood of a false positive fit. We show two examples in the F435W filter with low S/N (30) and high S/N (130). Over-plotted are the 0.1% false positive probability lines and a preliminary completeness limit from a more conservative approach detailed in (De Furio et al., 2019). The black circles represent the best fit binary parameters from the double PSF-fitting algorithm to the 1000 artificial single stars. All 1000 best fits fall below the 0.1% positive probability line, indicating that fits above this line are inconsistent with a single source.

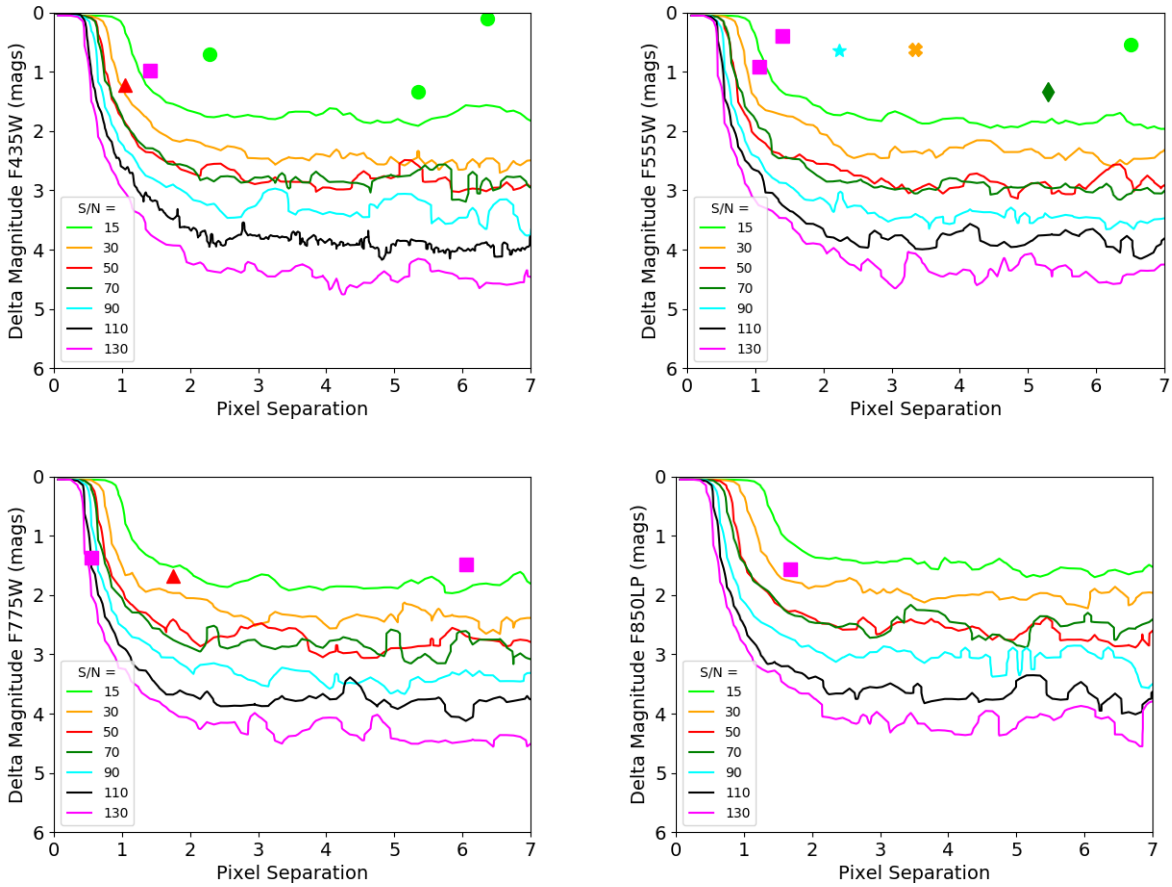


Figure 2.3: The 0.1% false positive probability curves for all specified S/N values and the four broadband filters as described in Sec. 2.6.2. The point estimates represent the detected companions to brown dwarf primaries that are listed in Tables 2.3 and 2.4 and are color-coded based on S/N to match the corresponding reliability limit of the source.

our binary PSF model to real singles and artificial singles. Their overlap, particularly at small separations, indicates that the empirical PSFs of AK06 accurately model the data.

From the false positive maps, we can then calculate a false positive probability for each target based on its resulting chi squared probability distribution in separation and Δmag space from the binary fitting routine. As above, we create a probability distribution in separation and Δmag space from all the steps taken within the double-PSF fitting routine to a given source. We multiply this probability distribution by the corresponding false positive distribution of the same S/N (as exemplified in the heat map in Fig. 2.2) and take the sum to derive the false positive probability of the fit to the data (here one image of one source). Most of our targets appear in multiple images of the Treasury Program data as well as in multiple filters. To calculate the false positive probability of a source with multiple images within a filter, we combine the false positive probabilities within

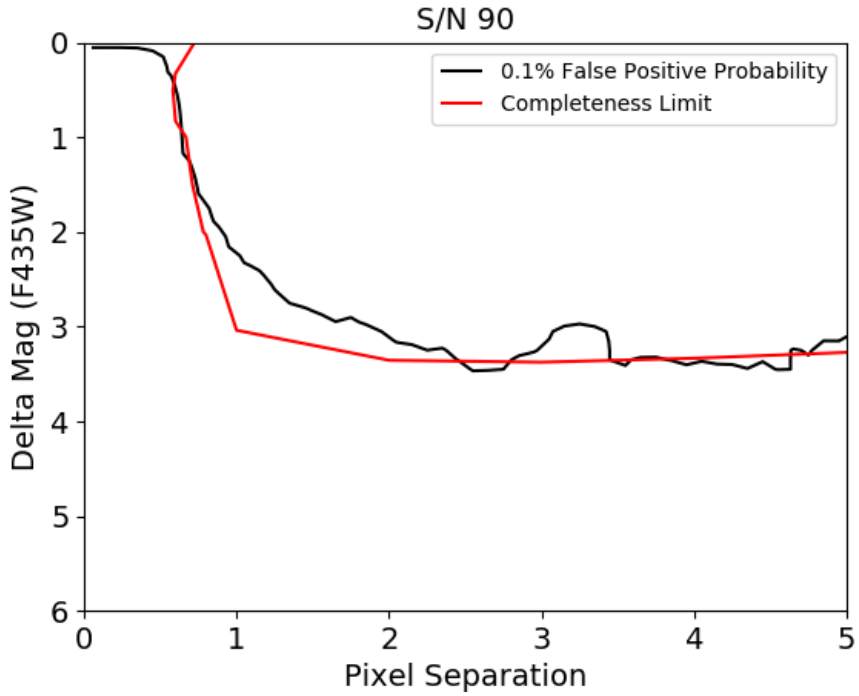


Figure 2.4: Plotted are the completeness limit and 0.1% false positive probability curve associated with targets of S/N=90 in the F435W filter.

each image of the filter:

$$FP_{filter1} = FP_i \times FP_{i+1} \times ... \times FP_N \tag{2.5}$$

where $\mathrm{FP}_{filter1}$ is the false positive probability of one target within filter1 and $\mathrm{FP}_i$ is the false positive probability of one image of that target within the same filter. We then use the false positive probability derived from all images within the filter, $\mathrm{FP}_{filter1}$, to determine whether or not that target has a detected companion or if it is classified as a single. Here, we define sources as detected binaries if the false positive probability is $\leq 0.1\%$.

If the target appears in multiple images within multiple filters, we can also combine those false positive probabilities for a global false positive probability across all filters:

$$FP_{total} = FP_{filter1} \times FP_{filter2} \times ... \times FP_{filterN} \tag{2.6}$$

where $\mathrm{FP}_{total}$ is then used to determine whether or not that target has a detected companion.

This combination of false positive probabilities requires the code to be fitting to the same feature within all images and in all filters. Therefore, we must confirm that we are identifying the same feature in all the binary fits to every image of the same source. We can verify this by measuring

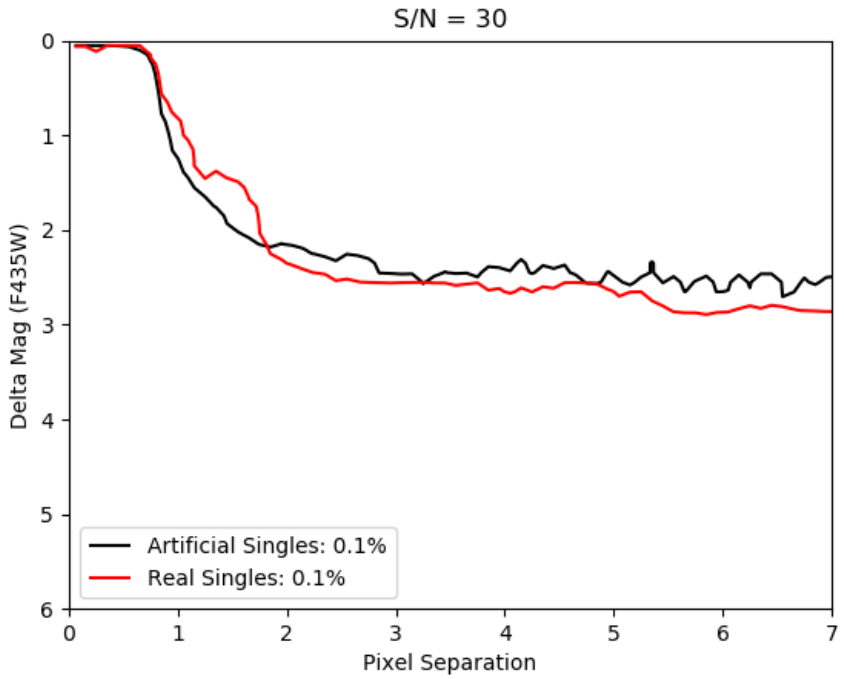


Figure 2.5: 0.1% false positive probability lines for actual single stars and artificial singles built from the empirical PSFs of AK06 for S/N = 30 targets.

the similarity between the chi squared probability distributions that result from the binary fits to a given target in multiple images. We measure this similarity through the Bhattacharyya coefficient (BC). This statistic quantifies the amount of overlap between any two distributions, and is defined as:

$$BC = \sum_{i=1}^{N} \sqrt{p_i \times q_i} \tag{2.7}$$

where there are N bins in our multivariate parameter space and p and q are the two probability distributions in question for the two different images.

This metric is bound between 0 and 1 where 0 indicates no overlap, and 1 indicates complete overlap. We tested the extent to which this metric would distinguish between two distributions by creating two identical normal distributions and varying their centers, moving them further apart. Then, we calculated both the Bhattacharyya coefficient and the sigma difference between the two distributions. We found that at a $3\sigma$ difference, the Bhattacharyya coefficient equals 0.1. Therefore, there is 99.7% confidence that a Bhattacharyya coefficient below 0.1 is indicative of two distinct distributions. We use this critical value to confirm the similarity between probability distributions in two images (if BC $>$ 0.1) in order to combine their false positive probabilities for a global false

positive probability. When a Bhattacharyya coefficient < 0.1 occurs, we select the image with the lowest $\chi^2_\nu$ to calculate the false positive probability and ignore the other image.

This is done among all images of the same source in the same filter where we calculate the BC between images in the three dimensions associated with the companion: separation, position angle, and difference in magnitude. The false positive probability of that target within a filter ($FP_{filter1}$) will then be used to assess whether or not there was a detection, where we define a false positive probability > 0.1% as a non-detection. If that source appears in multiple filters we calculate the BC in the two dimensions that are consistent across all filters: separation and position angle. The false positive probability $FP_{total}$ is then used to assess binarity in the same way that $FP_{filter1}$ is used to assess binarity if the target appears in one filter.

### 2.6.3 Limitations of the Model

We recognize that there are limits to the application of this code for multiplicity surveys. The most obvious and important limitation is that our model cannot detect triple or higher order systems. A true visual triple system would produce high residuals when fit with our model. Such systems are outside the scope of our study, but also rare for low-mass stellar, very low-mass stellar, and sub-stellar primaries.

An additional complication of our model comes in regions of high, structured background. The residual background in the data will decrease the S/N and can potentially mask the existence of a companion. This is especially important in the centers of young, star-forming regions. Future work refining our model will include fitting a 2D surface to local background in order to mitigate the effects of nebulosity, resulting in better fits for those particular sources in structured background environments.

Lastly, some of the sources in our sample were only found in one frame. It is possible that a cosmic ray could have hit the detector at the same location as the source or the candidate companion. This effect would result in a poor fit because the observed structure of the PSF would be altered by the cosmic ray and poorly fit with the PSF models. However, this is unlikely to have impacted our survey as it was also rare.

## 2.7 Results

In this section, we present the results of our multiplicity analysis from the samples of low-mass stellar and very low-mass stellar plus sub-stellar primaries. We also describe the comparison of these multiple populations to those of the Galactic field and various star-forming regions of differing environment.

### 2.7.1 Low-mass Stellar Primaries

#### 2.7.1.1 Detections

We made 76 detections of 44 unique companions across all filters from the sample of 276 cluster members. Twenty-one detections were made in the F435W filter, 24 in the F555W filter, 29 in the F658N filter, 2 in the F775W filter, and 0 in the F850LP filter. Three detections were made only in the F435W filter, five in only F555W, ten in only F658N, and two in only F775W. Thirteen detections were made in both the F435W and F555W filters, 13 in both the F435W and F658N filters, 14 in both the F555W and F658N filters, and 8 in the F435W, F555W, and F658N filters. Twenty-five of the companions were previously detected (Köhler et al., 2006; Reipurth et al., 2007; Robberto et al., 2013; Duchêne et al., 2018; Strampelli et al., 2020). The redder filters had fewer detections due to saturation effects. The F658N filter enabled the detection of the most companions because the narrow bandpass decreases the number of saturated sources. In Table 2.1, we present the photometry: the combined magnitude of the system and the difference in magnitude between the primary and companion. We constructed a color-magnitude diagram (Fig. 2.6) for all of the sources in our sample that were observed in the F435W and F555W filters, where both components of binary detections are shown. Figures 2.7 - 2.12 show an image of each detection made in every filter in which it was found.

The estimated projected separations range from 14 - 196 au (0.034"-0.49" or 0.68 - 9.8 ACS/WFC pixels) assuming a distance of 400 pc (Großschedl et al., 2018), and mass ratios range from 0.3 - 0.97. We estimate masses using the isochrones produced from the BT-Dusty evolutionary models (Chabrier et al., 2000; Allard et al., 2001, 2011, 2012) as they have updated opacities (Barber et al., 2006). We assume a cluster age of 2 Myr, the average age of the stellar population (Reggiani et al., 2011), and the extinction to each source as derived from Da Rio et al. (2016). They used their estimated effective temperature of each source to derive the intrinsic *(J-H)* color of the system and the observed *(J-H)* 2MASS color to estimate the extinction, assuming a 2 Myr isochrone. With these extinction values and the 2 Myr BT-Dusty isochrone, we estimate masses for the primary and companion of each binary system from the color information of Table 2.1, assuming the same extinction to both components. In Table 2.2, we present the estimated physical parameters of each binary system along with essential values from the double-PSF fitting process.

We investigated whether excess disk emission could impact the derivation of extinction for our binary detections. We took the 2MASS JHK photometry and created a color-color plot comparing to the observed colors of known pre-main sequence stars (Pecaut and Mamajek, 2013a). Significant disk emission would cause the observed near-IR photometry to be in excess of that expected from the photosphere, where the reddest photometry has a larger difference, causing motion toward the right in Fig. 2.6. With the inclusion of the reddening vector (Cardelli et al., 1989) and the classical

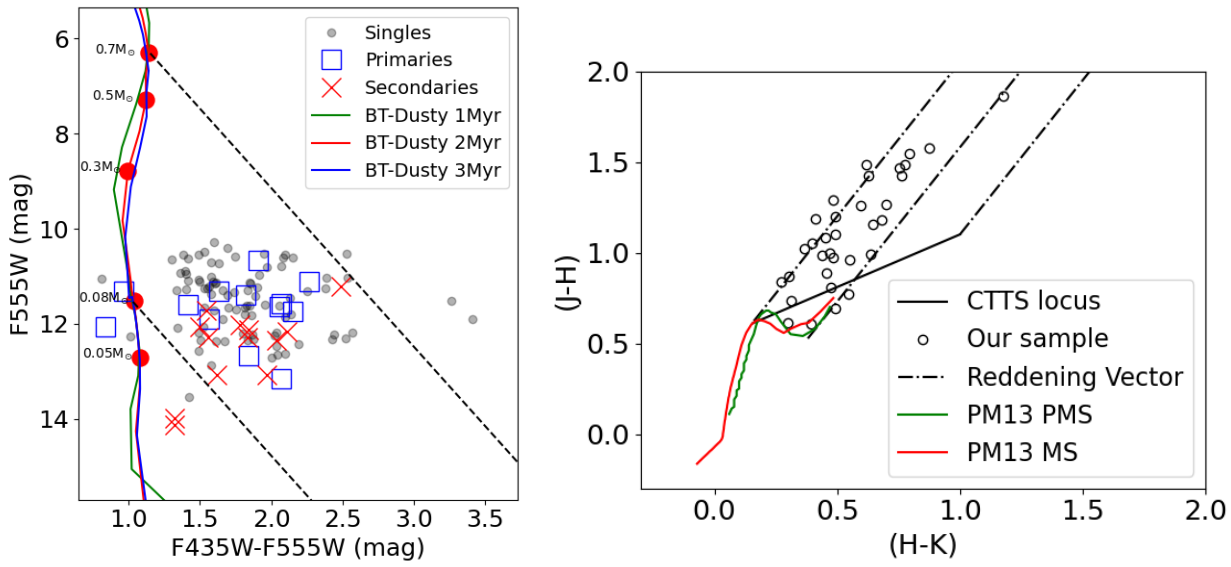


Figure 2.6: Left: Color magnitude diagram for all the sources that were included in our sample with F435W and F555W data. The detected binaries are plotted with both the primary and secondary components. The solid lines are the BT-Dusty 1-3 Myr isochrones with specific masses chosen for reference. The black dashed line represent the extinction vector derived from Cardelli et al. (1989). Right: The J-H vs. H-K color-color plot for the sources with detected companions within our survey (black circles), showing no obvious signs of disk excess. Over-plotted are the observed pre-main sequence (PMS) and main-sequence (MS) colors of Pecaut and Mamajek (2013a), PM13, the reddening vector (Cardelli et al., 1989), and the classical T-Tauri star (CTTS) locus from Meyer et al. (1997).

T-Tauri locus (Meyer et al., 1997), we show that there is no large near infrared excess observed.

Because sources were found in multiple filters, we used the data from the reddest filter in which they were found to estimate masses as excess emission from accretion shocks may impact blue/UV photometry (Azevedo et al., 2006). We do not use data from the F658N ($H_\alpha$) filter to calculate masses as it will not be representative of the flux from the photosphere.

#### 2.7.1.2 Chance Alignments

In order to perform a statistical analysis of our results, we must determine the probability that our candidates are not physically associated with their primaries, i.e. chance alignments. There are three potential sources of contamination in binary surveys of star clusters: 1) foreground stars, 2) other cluster members, and 3) background sources. We used the source list from Robberto et al. (2013) which contains all targets within the field of view (not just members) in each broadband filter to estimate the stellar surface density. First, we define the center of the cluster at the location of Theta 1 Ori C, the most massive star in the cluster. Then, we create 10 successive circular annuli

Table 2.1: We list the observed magnitude information of each binary system. In each set of two columns, we present the total magnitude of each system and the difference in magnitude between the primary and companion. These values are the weighted mean calculated from all exposures of the target where the error is the 68% confidence interval.

| Source # | Total Mag (F435W) | Δ mag (F435W) | Total Mag (F555W) | Δ mag (F555W) | Total Mag (F658N) | Δ mag (F658N) | Total Mag (F775W) | Δ mag (F775W) |
|---|---|---|---|---|---|---|---|---|
| 1 | - | - | - | - | 16.96 ± 0.01 | 1.1 ± 0.1 | - | - |
| 2 | 19.49 ± 0.01 | 0.57 ± 0.15 | - | - | 15.97 ± 0.01 | 0.46 ± 0.15 | - | - |
| 3 | - | - | - | - | 15.39 ± 0.01 | 0.04 ± 0.04 | - | - |
| 4 | - | - | - | - | 15.84 ± 0.01 | 0.20 ± 0.02 | - | - |
| 5 | 21.32 ± 0.02 | 0.38 ± 0.15 | 19.18 ± 0.01 | 0.42 ± 0.04 | - | - | - | - |
| 6 | - | - | 20.79 ± 0.01 | 0.51 ± 0.3 | - | - | - | - |
| 7 | - | - | - | - | 16.32 ± 0.01 | 0.25 ± 0.02 | - | - |
| 8 | 20.51 ± 0.02 | 2.88 ± 0.04 | 18.63 ± 0.01 | 3.46 ± 0.01 | 15.99 ± 0.01 | 2.58 ± 0.02 | - | - |
| 9 | - | - | - | - | 14.91 ± 0.01 | 1.10 ± 0.01 | - | - |
| 10 | 20.60 ± 0.01 | 1.22 ± 0.03 | 19.42 ± 0.01 | 0.22 ± 0.02 | - | - | - | - |
| 11 | - | - | 18.61 ± 0.01 | 0.77 ± 0.15 | 16.46 ± 0.02 | 0.8 ± 0.15 | - | - |
| 12 | - | - | 21.56 ± 0.03 | 0.3 ± 0.2 | 18.20 ± 0.02 | 0.61 ± 0.09 | - | - |
| 13 | 20.56 ± 0.01 | 0.9 ± 0.3 | 18.96 ± 0.01 | 0.95 ± 0.3 | - | - | - | - |
| 14 | - | - | 20.45 ± 0.01 | 0.2 ± 0.2 | - | - | - | - |
| 15 | 22.00 ± 0.02 | 0.54 ± 0.06 | 20.11 ± 0.02 | 0.41 ± 0.02 | 17.67 ± 0.02 | 0.52 ± 0.03 | - | - |
| 16 | - | - | - | - | 14.65 ± 0.01 | 1.56 ± 0.01 | - | - |
| 17 | - | - | - | - | 15.44 ± 0.01 | 1.84 ± 0.02 | - | - |
| 18 | 21.06 ± 0.01 | 0.30 ± 0.14 | 19.08 ± 0.01 | 0.5 ± 0.2 | 16.46 ± 0.02 | 0.4 ± 0.2 | - | - |
| 19 | 19.15 ± 0.01 | 0.01 ± 0.01 | - | - | 15.33 ± 0.01 | 0.22 ± 0.01 | - | - |
| 20 | - | - | 21.74 ± 0.05 | 0.48 ± 0.08 | - | - | - | - |
| 21 | - | - | - | - | 15.62 ± 0.01 | 0.04 ± 0.02 | - | - |
| 22 | 19.92 ± 0.01 | 0.99 ± 0.09 | 18.76 ± 0.01 | 0.41 ± 0.03 | - | - | - | - |
| 23 | 19.81 ± 0.01 | 0.43 ± 0.04 | - | - | - | - | - | - |
| 24 | - | - | 19.48 ± 0.02 | 1.54 ± 0.15 | 16.53 ± 0.02 | 1.7 ± 0.3 | - | - |
| 25 | - | - | 20.36 ± 0.01 | 0.87 ± 0.03 | 17.91 ± 0.04 | 0.8 ± 0.15 | - | - |
| 26 | 20.98 ± 0.01 | 1.46 ± 0.11 | 19.20 ± 0.01 | 1.66 ± 0.05 | 16.71 ± 0.02 | 1.27 ± 0.07 | - | - |
| 27 | 20.89 ± 0.01 | 0.34 ± 0.02 | 19.22 ± 0.01 | 0.12 ± 0.02 | 16.83 ± 0.02 | 0.42 ± 0.02 | - | - |
| 28 | 19.63 ± 0.02 | 0.23 ± 0.02 | - | - | - | - | - | - |
| 29 | 20.79 ± 0.01 | 0.33 ± 0.03 | 18.43 ± 0.01 | 0.10 ± 0.01 | 16.40 ± 0.01 | 0.28 ± 0.02 | - | - |
| 30 | - | - | 20.45 ± 0.01 | 2.2 ± 0.1 | - | - | - | - |
| 31 | 18.64 ± 0.01 | 1.43 ± 0.01 | - | - | - | - | - | - |
| 32 | 18.87 ± 0.01 | 2.23 ± 0.02 | - | - | 15.45 ± 0.01 | 1.79 ± 0.02 | - | - |
| 33 | 19.17 ± 0.01 | 0.19 ± 0.02 | - | - | 15.49 ± 0.02 | 0.17 ± 0.02 | - | - |
| 34 | - | - | 22.12 ± 0.03 | 0.62 ± 0.06 | - | - | - | - |
| 35 | - | - | 21.36 ± 0.03 | 1.33 ± 0.03 | 18.41 ± 0.03 | 0.27 ± 0.04 | - | - |
| 36 | - | - | - | - | - | - | 19.49 ± 0.02 | 0.16 ± 0.02 |
| 37 | 19.22 ± 0.01 | 0.86 ± 0.02 | - | - | 15.34 ± 0.02 | 0.94 ± 0.03 | - | - |
| 38 | - | - | - | - | - | - | 17.61 ± 0.01 | 0.27 ± 0.01 |
| 39 | 22.53 ± 0.02 | 0.09 ± 0.07 | 20.76 ± 0.01 | 0.8 ± 0.2 | 18.11 ± 0.02 | 0.20 ± 0.08 | - | - |
| 40 | 21.24 ± 0.04 | 0.7 ± 0.2 | 19.19 ± 0.02 | 0.71 ± 0.03 | 16.92 ± 0.05 | 0.62 ± 0.08 | - | - |
| 41 | - | - | - | - | 17.08 ± 0.02 | 0.08 ± 0.03 | - | - |
| 42 | - | - | 20.51 ± 0.02 | 1.12 ± 0.03 | 17.83 ± 0.01 | 0.88 ± 0.04 | - | - |
| 43 | 20.51 ± 0.02 | 0.6 ± 0.2 | 19.06 ± 0.01 | 0.5 ± 0.3 | - | - | - | - |
| 44 | - | - | - | - | 15.45 ± 0.01 | 1.96 ± 0.02 | - | - |

Table 2.2: Candidate binaries with masses ($M_\odot$), mass ratios (q), projected separations in arcseconds, physical separation in au, and position angles in degrees. To estimate masses, we used the 2 Myr BT-Dusty isochrone and the $A_v$ estimates from Da Rio et al. (2016). We assumed a distance of 400 pc (Großschedl et al., 2018). Binary parameters are the weighted mean calculated from all exposures of the target where the error is the 68% confidence interval. We also show the S/N of the target for the filter within which it is brightest along with the $\chi^2_\nu$ associated with that filter.

| Source # | 2MASS ID | $M_{prim}$ ($M_\odot$) | $M_{sec}$ ($M_\odot$) | q | $A_v$ (mag) | Projected Sep. (arcseconds) | Physical Sep. (au) | PA (deg) (E of N) | $\chi^2_\nu$ | S/N |
|---|---|---|---|---|---|---|---|---|---|---|
| 1 | J05341202-0524196 | - | - | - | - | 0.05 ± 0.001 | 20.2 ± 0.4 | 254.91 | 1.19 | 164 |
| 2 | J05342650-0523239 | 0.20 | 0.15 | 0.78 | 1.14 | 0.054 ± 0.001 | 21.68 ± 0.4 | 283.21 | 1.37 | 370 |
| 3 | J05342753-0528284 | - | - | - | - | 0.050 ± 0.002 | 20.0 ± 0.4 | 236.64 | 1.72 | 517 |
| 4 | J05344083-0528095 | - | - | - | - | 0.210 ± 0.001 | 83.0 ± 0.4 | 45.22 | 1.63 | 350 |
| 5 | J05344878-0517464 | 0.30 | 0.26 | 0.87 | 2.93 | 0.063 ± 0.002 | 25.2 ± 0.8 | 96.16 | 1.52 | 389 |
| 6 | J05345009-0517121 | 0.14 | 0.10 | 0.72 | 2.68 | 0.034 ± 0.002 | 13.6 ± 0.8 | 294.44 | 0.92 | 100 |
| 7 | J05345099-0517565 | - | - | - | - | 0.250 ± 0.001 | 100.0 ± 0.4 | 49.8 | 1.22 | 195 |
| 8 | J05345120-0516549 | 0.78 | 0.24 | 0.30 | 4.7 | 0.346 ± 0.001 | 137.2 ± 0.4 | 91.09 | 1.52 | 554 |
| 9 | J05345265-0529452 | - | - | - | - | 0.398 ± 0.001 | 159.0 ± 0.4 | 176.86 | 1.00 | 670 |
| 10 | J05345483-0525125 | 0.14 | 0.12 | 0.88 | 1.48 | 0.202 ± 0.001 | 80.8 ± 0.4 | 323.6 | 1.18 | 250 |
| 11 | J05345683-0521363 | 0.81 | 0.63 | 0.78 | 5.16 | 0.048 ± 0.002 | 19.0 ± 0.6 | 101.49 | 1.27 | 414 |
| 12 | J05350121-0521444 | 0.10 | 0.084 | 0.84 | 3.03 | 0.067 ± 0.003 | 27 ± 1 | 283.57 | 0.91 | 38 |
| 13 | J05350160-0524101 | 0.09 | 0.06 | 0.67 | 0.0 | 0.042 ± 0.003 | 16 ± 1 | 196.84 | 1.42 | 307 |
| 14 | J05350161-0533380 | 0.64 | 0.59 | 0.92 | 6.47 | 0.035 ± 0.003 | 14 ± 1 | 52.59 | 0.93 | 190 |
| 15 | J05350207-0518226 | 0.28 | 0.24 | 0.86 | 3.66 | 0.125 ± 0.001 | 49.8 ± 0.3 | 107.5 | 1.22 | 148 |
| 16 | J05350243-0520465 | - | - | - | - | 0.350 ± 0.001 | 140.2 ± 0.4 | 118.82 | 1.53 | 605 |
| 17 | J05350274-0519444 | - | - | - | - | 0.292 ± 0.001 | 116.8 ± 0.4 | 241.55 | 1.07 | 301 |
| 18 | J05350309-0522378 | 0.32 | 0.26 | 0.83 | 2.93 | 0.044 ± 0.002 | 17.5 ± 0.8 | 46.22 | 0.99 | 255 |
| 19 | J05350476-0517421 | - | - | - | - | 0.270 ± 0.001 | 110.0 ± 0.2 | 196.11 | 0.97 | 373 |
| 20 | J05350617-0522124 | 0.36 | 0.30 | 0.84 | 5.99 | 0.43 ± 0.005 | 172 ± 2 | 185.79 | 0.70 | 37 |
| 21 | J05350642-0527048 | - | - | - | - | 0.177 ± 0.001 | 70.8 ± 0.4 | 148.61 | 1.37 | 264 |
| 22 | J05350739-0525481 | 0.13 | 0.10 | 0.76 | 0.56 | 0.070 ± 0.001 | 28.0 ± 0.4 | 240.08 | 0.75 | 238 |
| 23 | J05350985-0519339 | 0.79 | 0.69 | 0.87 | 5.29 | 0.085 ± 0.001 | 34.0 ± 0.4 | 325.1 | 1.35 | 163 |
| 24 | J05351021-0523215 | 1.20 | 0.69 | 0.57 | 6.87 | 0.080 ± 0.005 | 32 ± 2 | 200.74 | 0.98 | 153 |
| 25 | J05351188-0521032 | - | - | - | - | 0.440 ± 0.005 | 176 ± 2 | 110.15 | 0.98 | 84 |
| 26 | J05351227-0520452 | 0.55 | 0.31 | 0.56 | 4.39 | 0.093 ± 0.002 | 37.2 ± 0.8 | 113.23 | 1.16 | 166 |
| 27 | J05351270-0527106 | 0.20 | 0.19 | 0.95 | 2.1 | 0.233 ± 0.001 | 93.2 ± 0.2 | 230.86 | 0.99 | 265 |
| 28 | J05351365-0528462 | 0.66 | 0.61 | 0.92 | 4.64 | 0.329 ± 0.001 | 131.5 ± 0.2 | 62.82 | 1.15 | 314 |
| 29 | J05351445-0517254 | 0.50 | 0.49 | 0.98 | 3.85 | 0.297 ± 0.001 | 118.6 ± 0.4 | 255.47 | 1.45 | 664 |
| 30 | J05351475-0534167 | 1.02 | 0.47 | 0.46 | 7.34 | 0.067 ± 0.003 | 27 ± 1 | 143.29 | 0.97 | 193 |
| 31 | J05351491-0536391 | 0.40 | 0.24 | 0.58 | 1.88 | 0.387 ± 0.001 | 150.6 ± 0.4 | 73.38 | 1.50 | 690 |
| 32 | J05351534-0519021 | 0.18 | 0.062 | 0.34 | 0.0 | 0.157 ± 0.001 | 63.0 ± 0.4 | 252.44 | 1.68 | 400 |
| 33 | J05351547-0527227 | 0.59 | 0.55 | 0.94 | 3.87 | 0.117 ± 0.001 | 47.0 ± 0.4 | 218.2 | 1.69 | 366 |
| 34 | J05351624-0528337 | 0.42 | 0.34 | 0.81 | 6.76 | 0.167 ± 0.003 | 67 ± 1 | 355.36 | 0.87 | 25 |
| 35 | J05351676-0517167 | 0.13 | 0.064 | 0.51 | 2.86 | 0.265 ± 0.002 | 105.8 ± 0.8 | 118.05 | 0.97 | 75 |
| 36 | J05351789-0518352 | - | - | - | - | 0.280 ± 0.001 | 111.8 ± 0.4 | 99.38 | 1.27 | 211 |
| 37 | J05351794-0525338 | 0.36 | 0.26 | 0.72 | 2.26 | 0.167 ± 0.003 | 67 ± 1 | 332.53 | 0.65 | 213 |
| 38 | J05351884-0522229 | 0.04 | 0.03 | 0.9 | 0.0 | 0.226 ± 0.001 | 90.6 ± 0.4 | 124.72 | 1.25 | 449 |
| 39 | J05351986-0531038 | 0.65 | 0.49 | 0.75 | 6.64 | 0.061 ± 0.001 | 24.2 ± 0.4 | 168.32 | 1.04 | 162 |
| 40 | J05352017-0523085 | - | - | - | - | 0.232 ± 0.005 | 93 ± 2 | 194.32 | 0.74 | 215 |
| 41 | J05352032-0536394 | - | - | - | - | 0.099 ± 0.001 | 39.6 ± 0.2 | 324.78 | 1.68 | 179 |
| 42 | J05352190-0515011 | 0.36 | 0.24 | 0.67 | 4.52 | 0.103 ± 0.001 | 41.4 ± 0.4 | 90.65 | 1.06 | 166 |
| 43 | J05352534-0525295 | 0.16 | 0.12 | 0.77 | 1.24 | 0.035 ± 0.003 | 14 ± 1 | 89.78 | 1.02 | 203 |
| 44 | J05352543-0521515 | - | - | - | - | 0.489 ± 0.001 | 195.6 ± 0.2 | 64.46 | 1.48 | 242 |

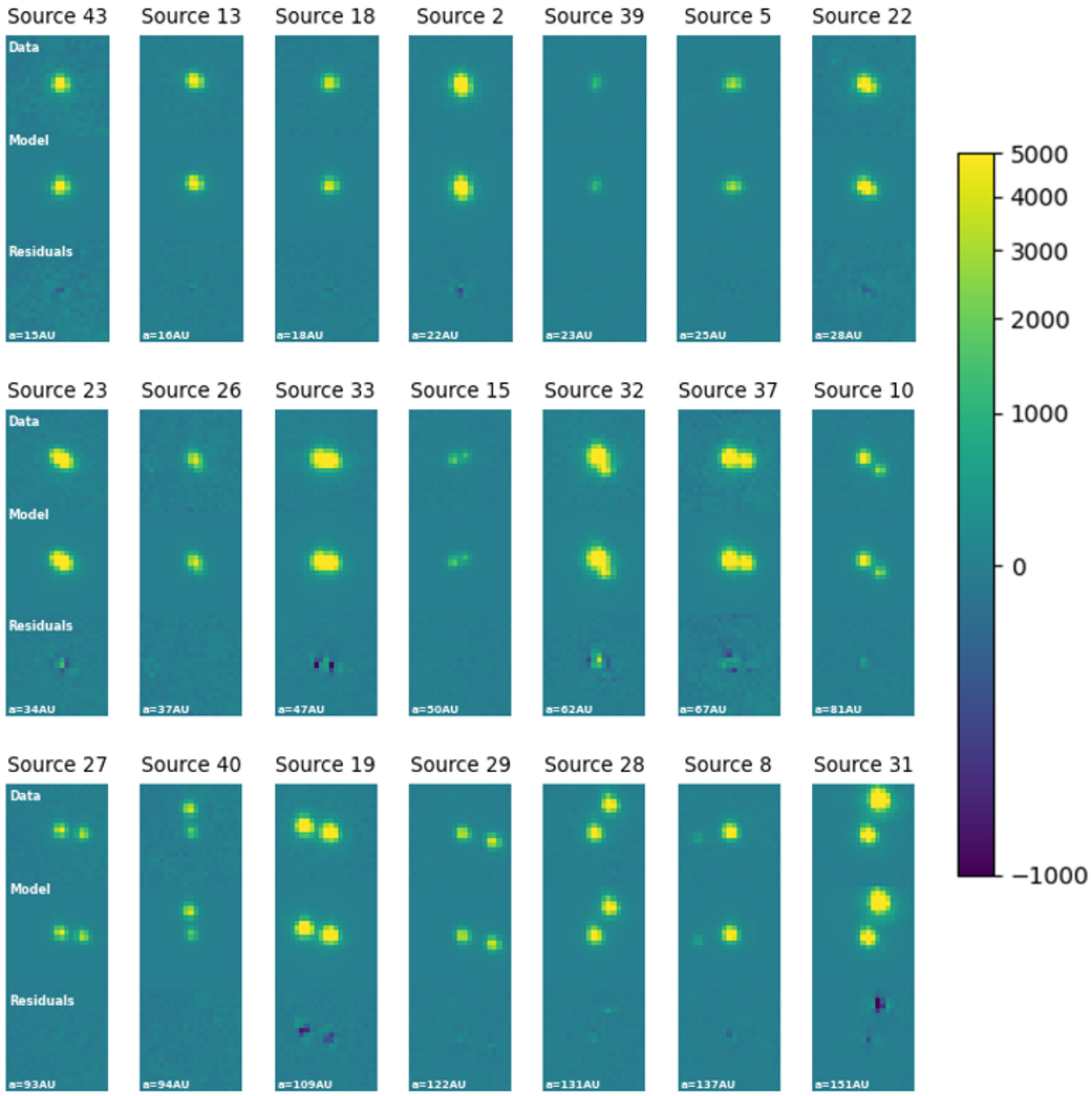


Figure 2.7: We display all the binary detections made in the F435W filter, showing one image per detection. The top panel shows the 21x21 pixel postage stamp cutout of the HST/ACS data, the middle panel shows our double-PSF model, and the bottom panel shows the residuals. Each binary is labeled with their Source # that corresponds to a 2MASS ID listed in Table 2.2 and the estimated separation is given at the bottom of each image. Sources are listed left to right and top to bottom in order of increasing orbital separation. The colorbar shows the dynamic range of all the images in units of detector counts.

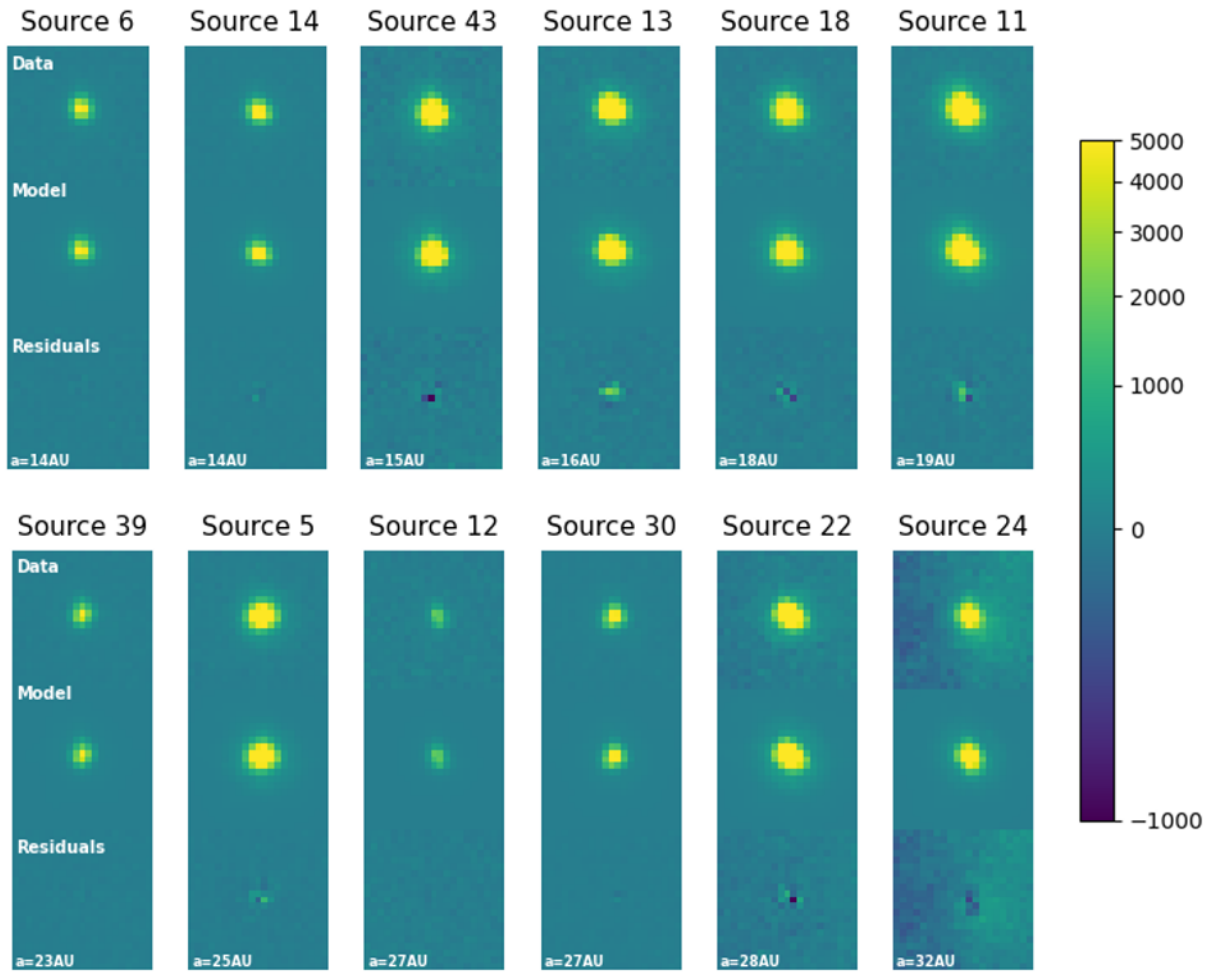


Figure 2.8: Same as Fig. 2.7 but for the F555W filter.

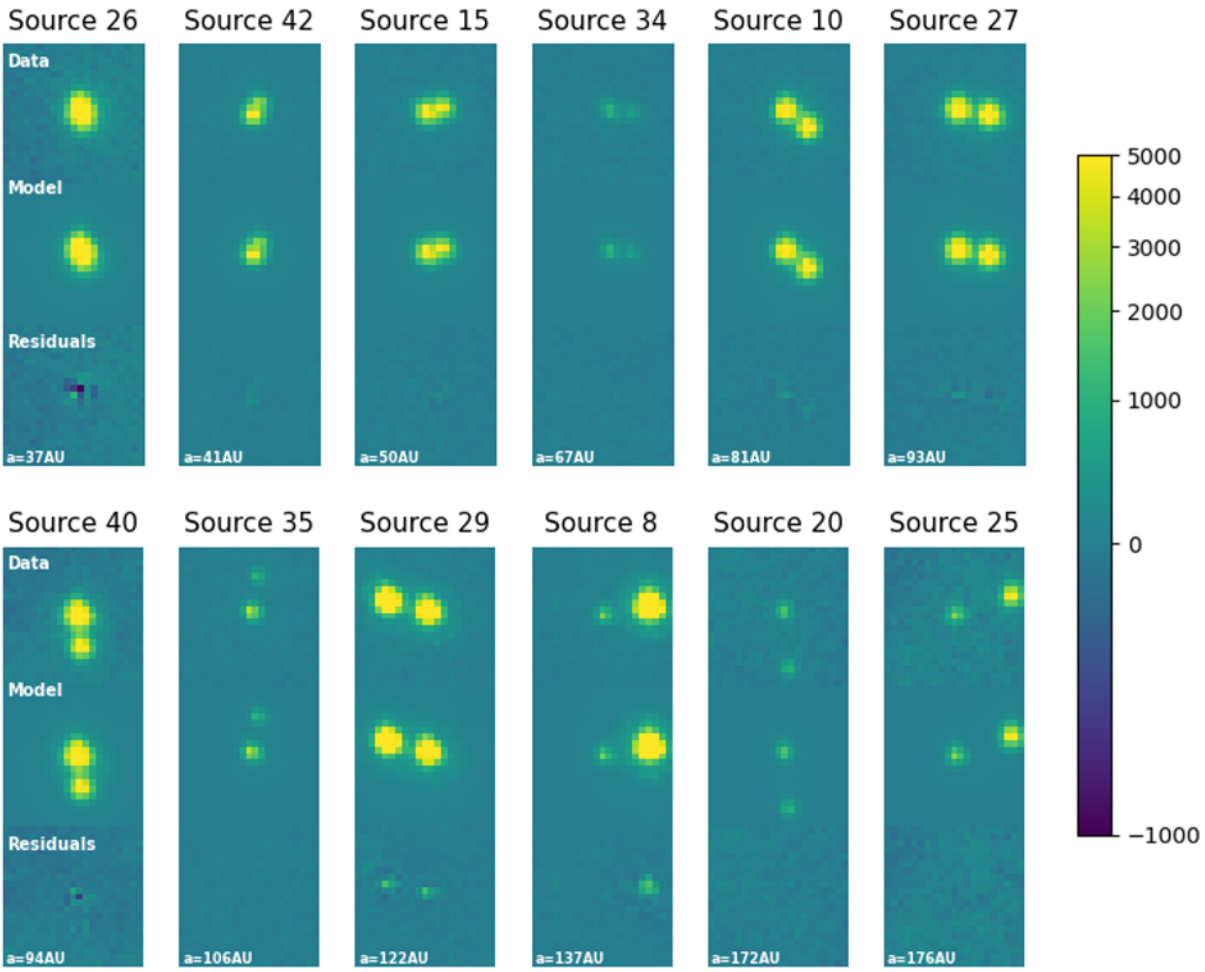


Figure 2.9: Continuation of Fig. 2.8.

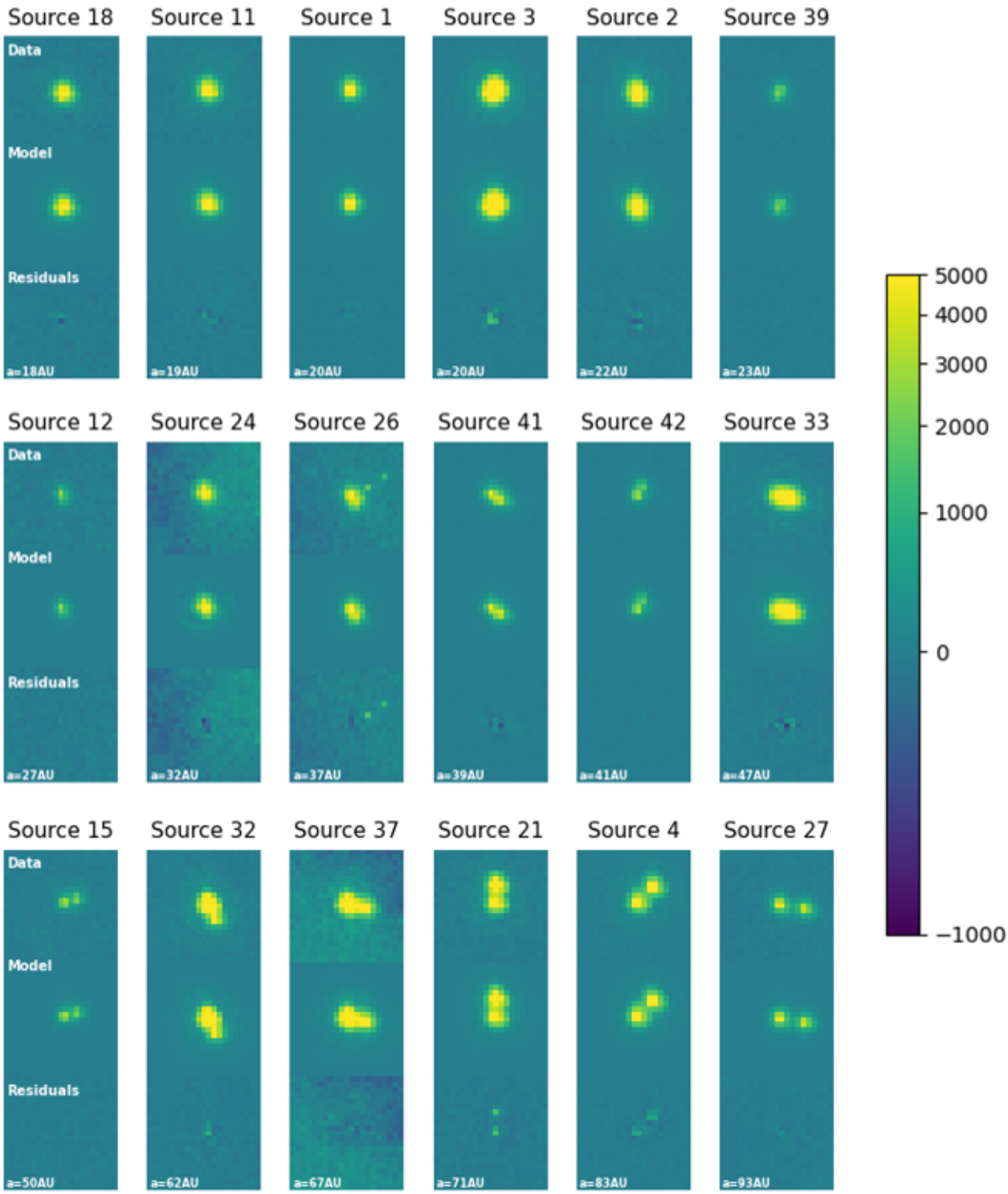


Figure 2.10: Same as Fig. 2.7 but for the F658N filter.

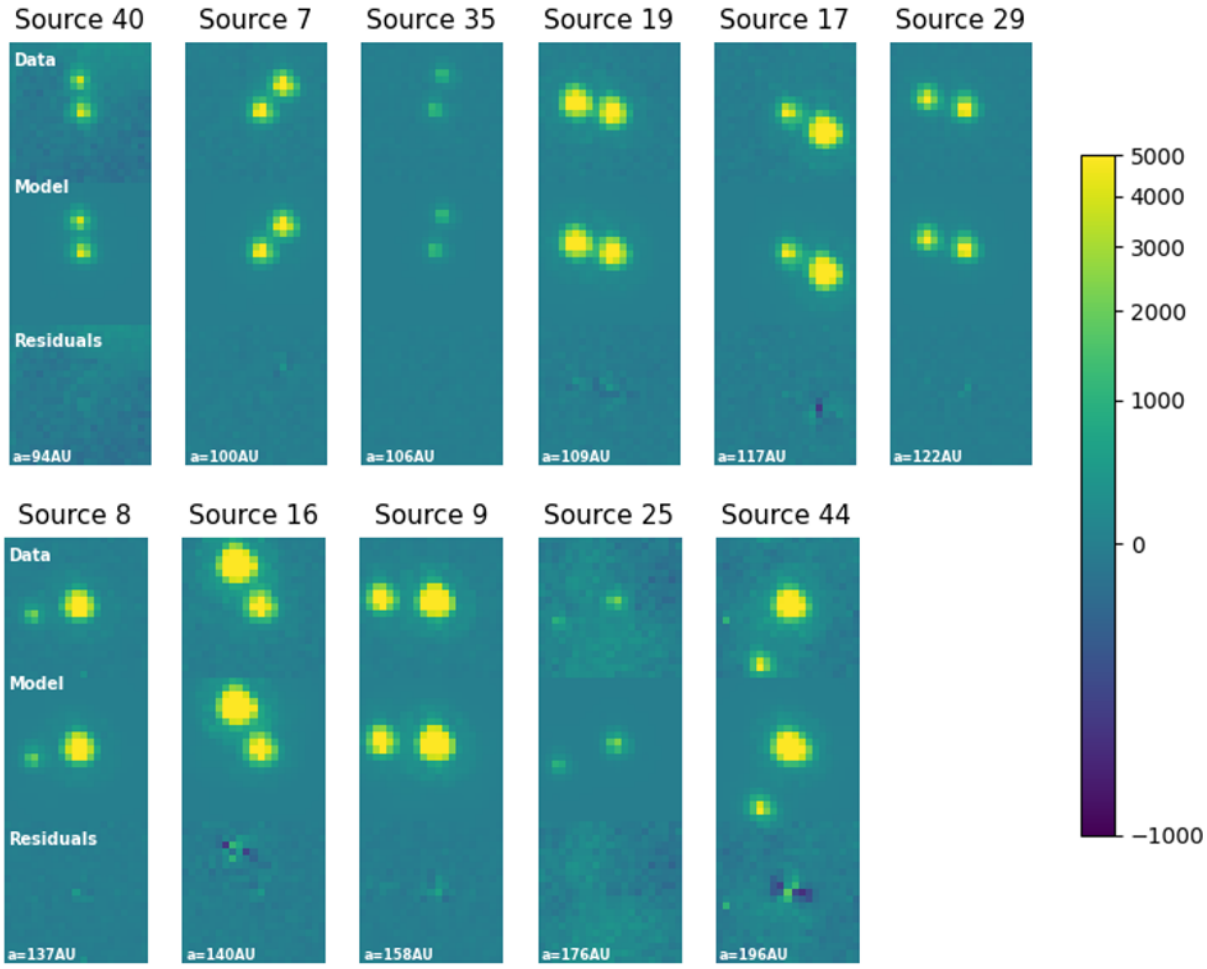


Figure 2.11: Continuation of Fig. 2.10.

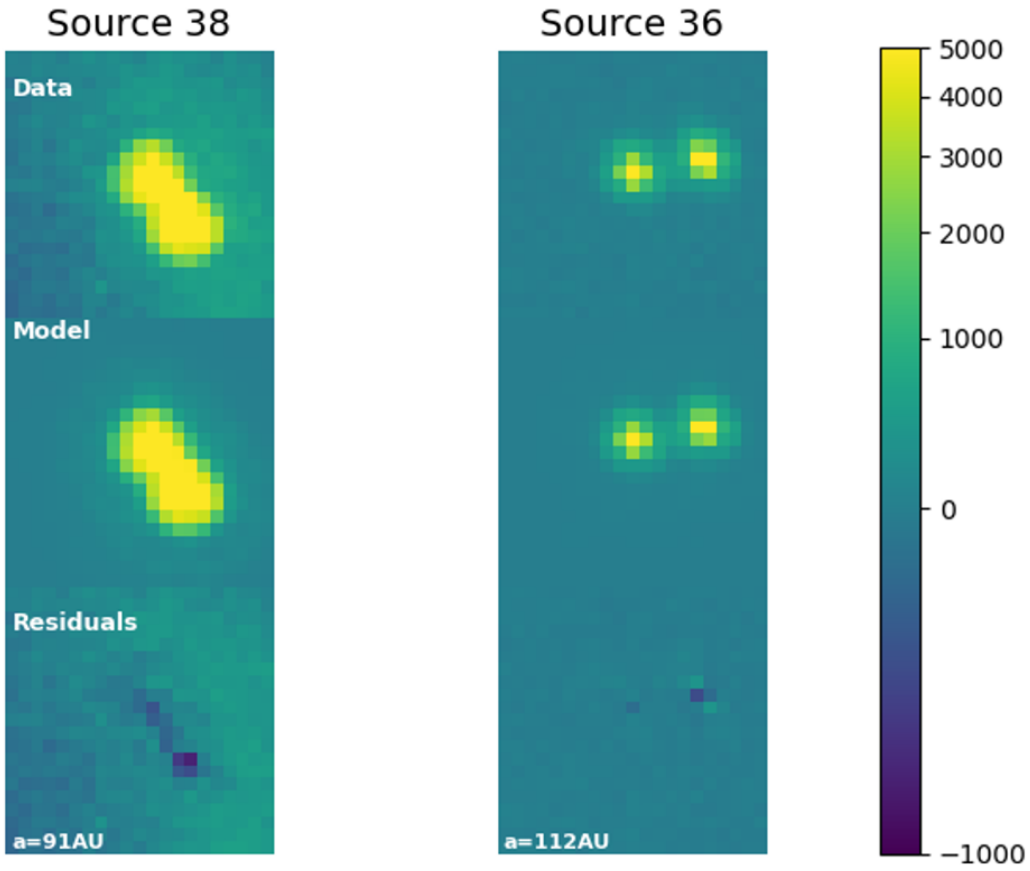


Figure 2.12: Same as Fig. 2.7 but for the F775W filter.

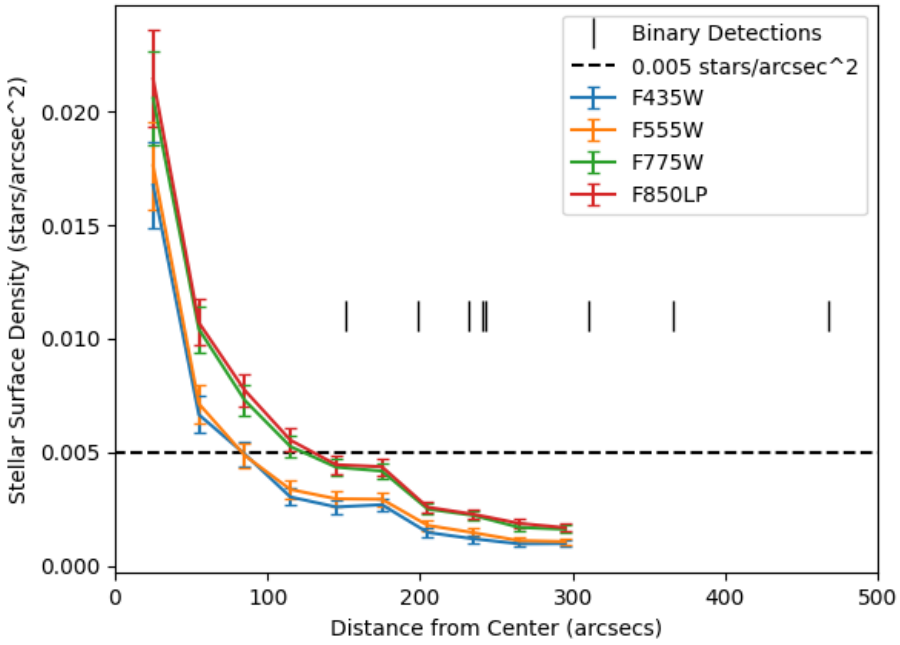


Figure 2.13: Stellar density as a function of angular distance from Theta 1 Ori C. We plot the stellar density for all four broadband filters used in this study, over-plot the 0.005 stars/arcsec$^2$ line, and over-plot the distance from each brown dwarf binary detection to Theta 1 Ori C. Included are $1\sigma$ error bars assuming the number of sources within each annulus is Poisson distributed.

each 30" further from the center than the last. Within each annulus, we calculate the number of sources identified in Robberto et al. (2013) in the specified filter and calculate the stellar surface density. We take the midpoint of the annulus as its distance from Theta 1 Ori C and plot the stellar density in each filter as a function of distance from the center of the ONC, as seen in Fig. 2.13.

As expected, the stellar density is highest near the center, but flattens out around 0.001 stars/arcsec$^2$ after $\sim$ 250". This result is consistent across all four broadband filters, with the redder filters having a higher density around 0.002 stars/arcsec$^2$. In our survey, we search for companions within a 10 pixel radius from each target. At a distance of 115" from the cluster core (as defined by distance from Theta 1 Ori C), the stellar surface density is 0.0034 stars/arcseconds$^2$ for the F435W and F555W filters, beyond which a vast majority of our sources for which we can estimate masses appear. We expect to have 0.74 chance alignments given this stellar surface density, a search radius of 0.5", and 276 sources in total. Since we used the entire catalog of sources from Robberto et al. (2013) without membership information, this includes foreground and background contaminants. Therefore, we conclude that all of the detections are likely physical binaries with no expected chance alignments.

#### 2.7.1.3 Characterizing the Companion Population

For our stellar primary sample, we use a Bayesian approach in order to characterize the companion population in terms of its mass ratios, separations, and overall companion frequency. This approach preserves all information of the survey by including the contrast limits for each individual source in the sample, and does not lose information by excluding true detections at close separations or higher contrasts that are inaccessible to fainter sources in the sample. To do this, we first defined the detection limit for each source given the 0.1% false positive probability curves associated with their S/N, e.g. Fig. 2.3. At each separation, there is an associated achievable contrast. This contrast value is converted into a companion mass using the 2 Myr BT-Dusty isochrones, as described in Sec. 2.7.1.1, and the minimum mass ratio that can be detected at each separation. For sources that appear in multiple filters, we assign the mass ratio limit based on the lowest achievable mass ratio between filters. We then sum over mass ratios and orbital separations to construct a combined detection probability of the entire sample, see Fig. 2.14, where each value of mass ratio and orbital separation has a corresponding fraction of the sample over which we are complete to companions.

We carry out a Bayesian analysis similar to the approach of Fontanive et al. (2018, 2019) to fit models of the companion population to our data without the known biases of fitting binned histogram data (e.g. Allen, 2007; Kraus et al., 2011; Kraus and Hillenbrand, 2012). Bayes' theorem

$$P(\theta|D) \propto P(D|\theta)P(\theta) \tag{2.8}$$

is based on the concept that we can evaluate the likelihood function, P(D|$\theta$), given the observed data (D) and some initial model distribution or prior, P($\theta$), which then informs the model ($\theta$) and produces a posterior distribution P($\theta$|D) giving the probability that the model reproduces the data. From the posterior distribution, we can then derive the values of the model parameters that best fit the data with their associated errors as this gives a probability density function (PDF) for each variable of the model.

We assume simple functional forms for the mass ratio and projected orbital separations distributions guided by previous work. We define the mass ratio distribution as a power-law:

$$\frac{dN_1}{dq} \propto \begin{cases} q^{\beta} & \text{if } \beta \geq 0 \\ (1-q)^{-\beta} & \text{if } \beta < 0 \end{cases} \tag{2.9}$$

where $\beta$ is the power-law index, and the piecewise function ensures symmetry about q=0.5 as defined in Fontanive et al. (2019). We define the projected orbital separation distribution as a log-normal:

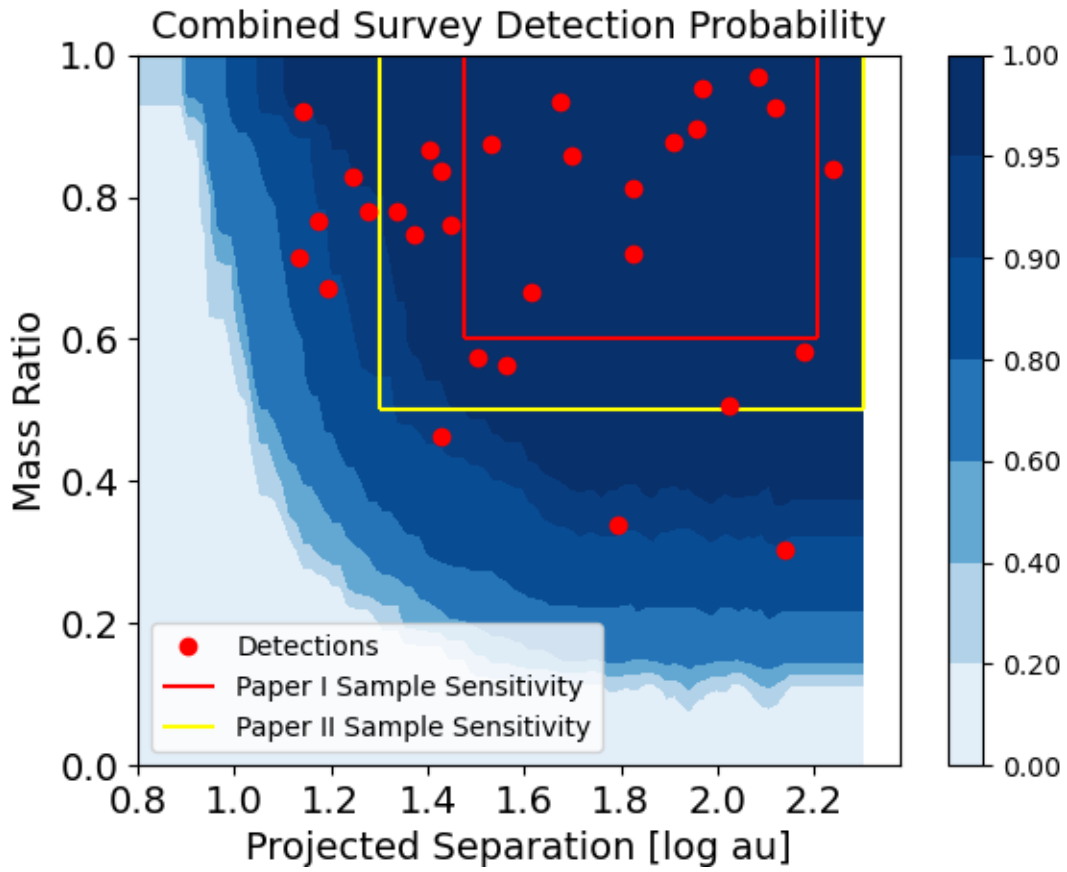


Figure 2.14: Summed detection probabilities for all the 245 sources in our survey in which we can calculate masses. Red circles show the projected separation and estimated mass ratios for all detected companions. Red and yellow lines show the detection limits from our past surveys in De Furio et al. (2019, 2022b), respectively. We use this map in Sec. 2.7.1.3 to model the separation and mass ratio distribution of the companion population in the ONC.

$$\frac{dN_2}{da} = \frac{1}{\sqrt{2\sigma^2_{loga}}} e^{-\frac{(log(a)-log(a_o))^2}{2\sigma^2_{loga}}} \tag{2.10}$$

where $\log(a_o)$ is the mean and $\sigma_{loga}$ is the standard deviation of the distribution.

We use the python module PyMultiNest (Buchner et al., 2014a) that performs the Nested Sampling Monte Carlo analysis using MultiNest (Feroz et al., 2009a) to adequately sample our parameter space and estimate the best fitting model to our observations. Importantly, PyMultiNest also calculates the evidence of the model tested by integrating eq. 2.8 over all parameters which can then be used to compare different models. Nested sampling is based on generating a user-defined large number of live points that are sampled directly from the prior distribution with

their likelihoods evaluated and sorted. Then, points are sampled again from the priors until a point reaches a likelihood greater than the lowest likelihood of the original set of live points. This process continues to maximize the likelihood until the effect of sampling becomes negligible. Buchner et al. (2014a) describe this as a "scan vertically from the least probable zones to the most probable".

We define our likelihood function used in the sampling routine based on Poisson statistics and the physical parameters of our detected companions (Fontanive et al., 2018). First, the Poisson likelihood is calculated with:

$$\mathcal{L}_p = \frac{k^d e^{-k}}{d!} \tag{2.11}$$

where $k$ (mean of the Poisson distribution) is the expected number of companion detections given the model and $d$ is the number of detections observed in the data. We evaluate the expected number of detections with

$$k = \sum_{i=1}^{n} p_i \times CF \times \frac{N}{n} \tag{2.12}$$

where $CF$ is the companion frequency of the sample (mean number of companions per primary star) over all mass ratios and 10-200 au (our survey sensitivity in projected separation), $N$ is the total number of sources in our sample (here, 245), $n$ is the number of generated companions in the sampling process, and $p_i$ is the probability that the $i$ generated companion will be detected given our survey sensitivity. We assign $p_i$ based on the physical parameters of the generated companions and the probability that they would be detected in our survey, see Fig. 2.14. A companion generated with q = 0.01 and log(a) = 1.0 would result in $p_i$ = 0.0, but a companion with q = 1.0 and log(a) = 1.8 would result in $p_i$ = 1.0.

Each time we evaluate the likelihood of a model, we sample the prior distribution for $\beta$, $\log(a_o)$, $\sigma_{loga}$, and $CF$. For our case, we do not have informed priors on the free parameters, so we generate flat distributions with $-5.0 < \beta < 5.0$, $0.0 < \log(a_o) < 4.0$, $0.1 < \sigma_{loga} < 5.0$, and $0.0 < CF < 1.0$. Priors for $\log(a_o)$ and $\sigma_{loga}$ are log-flat, so that each au is equally weighted. Then, we generate the mass ratio and projected orbital separation distributions of eqs. 2.9 and 2.10 based on those sampled values. From each model, we generate n = $10^4$ companions, with mass ratios = 0 - 1 and projected orbital separations = 10 - 200 au, and determine the detection probability $p_i$ for each based on Fig. 2.14. We sum over all $n$ generated companions to derive the expected number of detections $k$, and then compute the Poisson likelihood where $CF$ is a free parameter.

We then calculate the total likelihood given the information from the model and our real detections. As done in Fontanive et al. (2018), we use the sampled parameters to generate the model. We then multiply the model by the combined survey detection probability in mass ratio and projected

orbital separation space. This produces a joint distribution that gives the expected companion distribution based on the sensitivity of the survey. Then, we calculate the joint probability of each true detection from our survey given that sampled model distribution and our detection limits, $p_j$. The total likelihood is then calculated as:

$$\mathcal{L} = \mathcal{L}_p \times \prod_{j=1}^{d} p_j \tag{2.13}$$

We use our list of detected multiple systems with estimated primary masses of 0.08-0.7 $M_\odot$ (24 in total) to represent the low-mass stellar population as the companion properties can depend on primary mass. Stars with masses > 0.7 $M_\odot$ were only observable in F435W or F555W due to their high extinctions, typically $A_v > 5$ mag.

From our sample of 24 low-mass binaries in the ONC, we estimated the following four parameters over all mass ratios and projected orbital separation 10-200 au with $1\sigma$ errors (68% confidence interval): $\beta = 2.01^{+0.99}_{-0.80}$, $CF = 0.13^{+0.04}_{-0.03}$, $\log(a_o) = 1.71^{+1.47}_{-2.17}$, and $\sigma_{loga} = 3.03^{+1.32}_{-1.42}$. As shown in Fig. 2.15, the parameters of the projected orbital separation distribution are unconstrained, likely due to our sensitivity between 10 - 200 au (only 1.3 orders of magnitude). Unless the distribution was very narrow, this search radius limited our ability to fit a log-normal distribution to the detected companions.

We then re-ran our fitting code assuming the separation distribution is flat in order to compare to our best fit from the four parameter model. We estimated the following two parameters with $1\sigma$ errors: $\beta = 2.08^{+1.03}_{-0.85}$, $CF = 0.13^{+0.05}_{-0.03}$. The estimated mass ratio power law index and companion frequency were consistent between both models.

One of the useful features of nested sampling is calculating the Bayesian evidence of a particular model to which other models can be compared. The log-evidence of the four parameter model is -81.0 while the log-evidence of the two parameter (flat separation distribution) model is -80.8. Trotta (2008a) show that when comparing two models a difference in the log-Bayesian evidence < 1 is inconclusive and therefore no distinction can be drawn between the two models. This allows us to conclude that the observed companion population is not better modeled by a log-normal distribution fit.

#### 2.7.1.4 Comparison to the Galactic field

Many studies in the Galactic field have characterized the companion population and estimated the companion frequency as a function of primary mass. We can compare our results to those surveys in order to search for differences based on environmental impacts within the ONC.

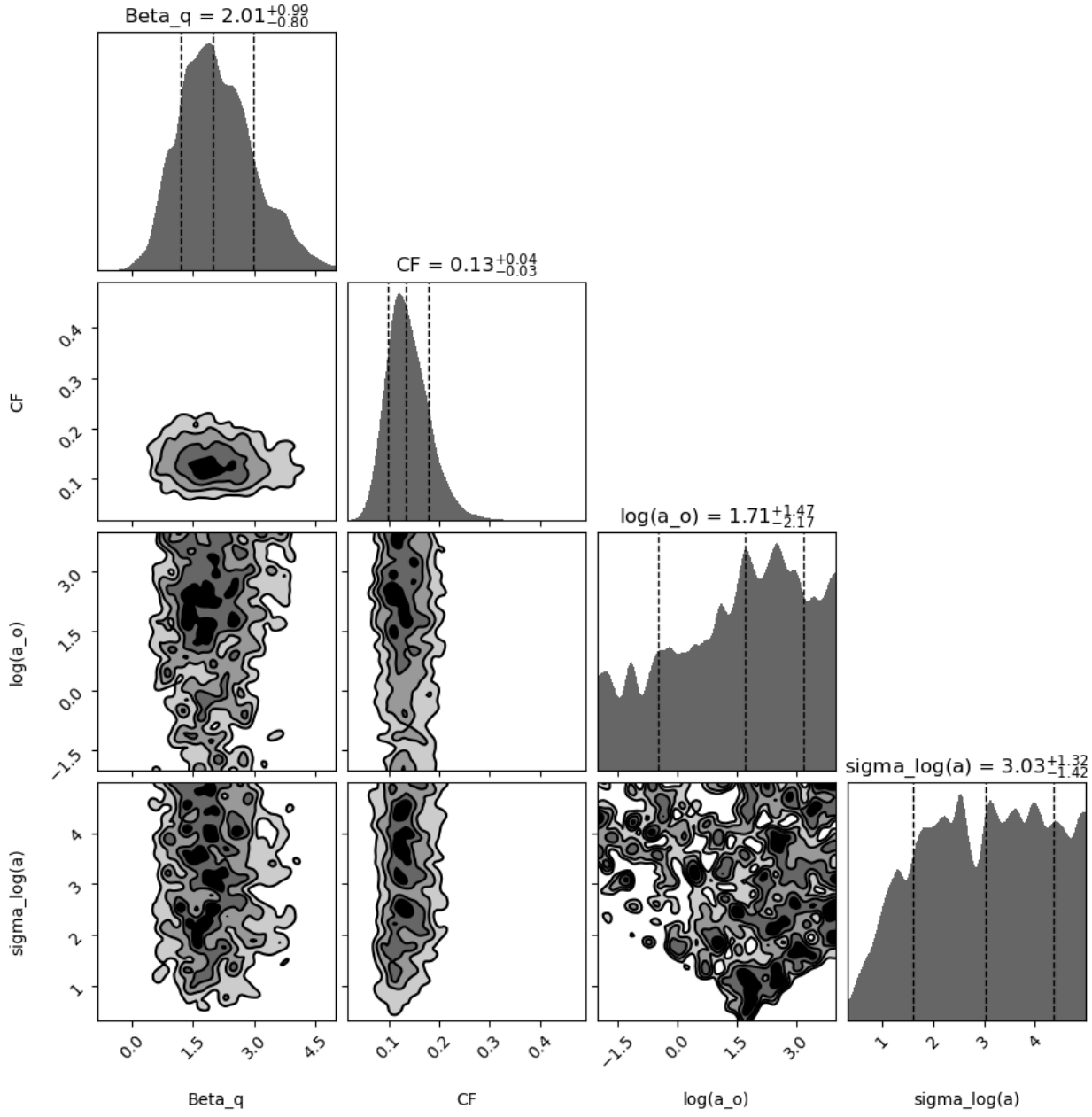


Figure 2.15: Corner plots representing the posterior distributions of the companion population model used in our fit. Beta_q is the exponent to the power law model of the mass ratio distribution, CF is the companion frequency over q=0-1 and a=10-200 au, log(a_o) is the mean of the log-normal separation distribution, and sigma_log(a) is the standard deviation of the log-normal separation distribution. The separation distribution is unconstrained with a log-normal, likely due to the limited range of our survey.

Reggiani and Meyer (2013) analyzed two Galactic field multiplicity surveys to characterize the mass ratio distributions of solar-type (Raghavan et al., 2010) and M-type (Janson et al., 2012) stars. They found the distributions of mass ratios between the two surveys consistent, and therefore combined the data and fit a power-law using the maximum-likelihood estimation of Feigelson and Babu (2012), resulting in $\beta = 0.25 \pm 0.29$. Using the results of our model, we see a $2.1\sigma$ difference between our fitted power-law exponent and that of Reggiani and Meyer (2013).

The sample of primary stars in the Janson et al. (2012) survey to which they detected companions had a significant portion of masses > 0.3 $M_\odot$. A significant portion of the sources in our sample however have a mass < 0.3 $M_\odot$ (see Fig. 2.6) potentially indicative of a difference in the mass ratio distribution of mid-late M-stars from our sample and early M-stars. Offner et al. (2023) performed a similar analysis as Reggiani and Meyer (2013) where they fit a power-law to the mass ratio distribution of the results from the Winters et al. (2019) field M-star survey. For primary masses 0.3 - 0.6 $M_\odot$, they find a power-law index of 0.1 ± 0.4, also a $2.1\sigma$ difference compared to our model. However, they also found a power-law index of 0.7 ± 0.5 for primary masses 0.15 - 0.3 $M_\odot$ (more similar to our sample, a difference of $1.4\sigma$). We can also compare our results to the brown dwarf multiplicity study of Fontanive et al. (2018) who found a power law index of $6.1^{+4.0}_{-2.7}$ to their companion population. This results in a $1.7\sigma$ difference compared to our survey.

In our survey, we were also able to constrain the companion frequency of our sample over mass ratios = 0 - 1 and projected separations 10 - 200 au. We can compare these results to those of Susemiehl and Meyer (2022) who constrain the orbital separation distribution and companion frequency of low-mass stars in the Galactic field using a combination of multiple surveys that extend to primary masses of 0.13 $M_\odot$, more similar to our sample, see Fig. 2.6. We take eqs. 2.9 and 2.10 to define a new equation to characterize the companion frequency of a survey given the detection limits:

$$CF = C_n \times \int_{q_1}^{q_2} \frac{dN_1}{dq} \int_{a_1}^{a_2} \frac{dN_2}{da} \tag{2.14}$$

where $C_n$ is an integration coefficient and CF is the companion frequency.

Susemiehl and Meyer (2022) model the semi-major axis distribution as a log-normal resulting in a peak $\log(a_o) = 1.68^{+0.14}_{-0.16}$ and $\sigma_{loga} = 0.97 \pm 0.19$, having corrected projected separations to physical separations using a multiplicative factor of 1.26 (Fischer and Marcy, 1992). They estimate the companion frequency over $0.6 \leq q \leq 1.0$ and $0 \leq a \leq 10{,}000$ au assuming the mass ratio distribution from Reggiani and Meyer (2013), resulting in CF= 0.229 ± 0.028. Taking those bounds as the bounds of the integrals in eq. 2.14, we can solve for the constant $C_n$. We then integrate over the bounds of our own results ($0.0 \leq q \leq 1.0$ and $12.6 \leq a \leq 252$ au after converting to physical separations with their same multiplicative factor) and arrive at an expected companion

frequency of the Galactic field over the sensitivity of our survey. We repeated this process $10^4$ times, sampling the companion parameters given their errors from Reggiani and Meyer (2013) and Susemiehl and Meyer (2022), evaluating the expected companion frequency each time. We estimate a companion frequency of $0.244^{+0.076}_{-0.053}$ over mass ratios 0-1.0 and semi-major axes 12.6-252 au, $1.5\sigma$ difference compared to our estimate in the ONC.

#### 2.7.1.5 Comparison to Taurus-Auriga

Kraus et al. (2011) performed a multiplicity survey in Taurus, sensitive to companions between 3-5000 au. In order to directly compare our results to their companion population, we must restrict their sample of primary stars over a similar mass range and restrict the companion detections over a common separation and mass ratio to which our survey and theirs is sensitive. Therefore, we restricted their sample to sources with primary masses $\leq 0.45$ $M_\odot$, where the mean primary mass of the sample is 0.31 $M_\odot$ compared to 0.29 $M_\odot$ in our ONC sample. Our Bayesian analysis evaluates the companion frequency over all mass ratios and projected separations = 10-200 au. Of the 34 stars in their sample with masses $< 0.45$ $M_\odot$, 12 had companions between projected separations of 10-200 au. To determine how this compares to our survey, we converted these results to a binomial distribution following the formalism of Burgasser et al. (2003). Then, we sampled the results of our companion frequency distribution and integrated the binomial distribution of the results of Kraus et al. (2011) from 0 to the sampled ONC companion frequency to determine the posterior probability that our ONC results resemble the observed Taurus results. Taking the mean of all the samples, we arrive at a probability of 0.002 that our ONC model can describe the Taurus observations.

### 2.7.2 Very Low Mass Stellar and Sub-stellar Primaries

#### 2.7.2.1 Detections

Our sample consists of 75 ONC members that meet the selection criteria defined in Sec. 2.5.2 and are all classified as M6-M9.5. After analyzing each source in all images and filters, we detected 8 candidate binaries with false positive probabilities $< 0.1\%$ and binary fits with $\chi^2_\nu < 1.774$. Two of these candidate companions were only identified in one filter (one in F555W and one in F775W). Six of these candidate companions were identified in at least two filters in all images in which they appeared. All detections were found in at least two images.

In general, there are three potential outcomes from the analysis in Sec. 2.6.2: 1) a well-detected binary with a false positive probability $<< 0.1\%$; 2) a binary fit with a false positive probability $>> 0.1\%$; and 3) a fit with a false positive probability near 0.1% and binary parameters poorly constrained due to the influence of the primary PSF residuals or the background. Of the eight

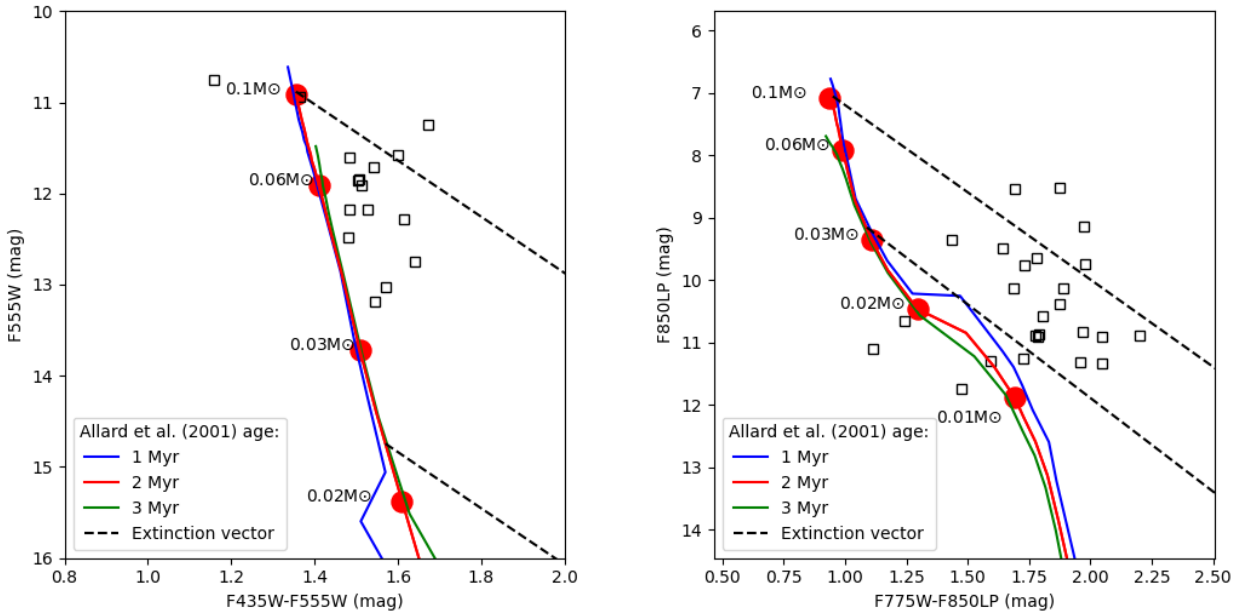


Figure 2.16: Color-magnitude diagrams for the targets (open black squares) in our sample that have S/N $\geq$ 30 in both filters represented in either diagram, corrected for distance (400 pc). The solid lines denote the 1, 2, and 3 Myr isochrones from Allard et al. (2001), the dashed black lines denote the effect of interstellar extinction. The effective wavelength of each filter is used to calculate extinction with the procedure of Cardelli et al. (1989) Filled red circles are included to note parts of the isochrone corresponding to specific masses, 0.02 - 0.1 $M_{\odot}$ on the left, 0.01 - 0.1 $M_{\odot}$ on the right.

detections, seven were well-detected binaries in at least one filter in which they appeared, well above the completeness limit and reliability threshold. Only one detection (J05350957-0519426 at 0.028") was observed near the 0.1% false positive probability for a single image in a single filter with poorly constrained binary parameters. In all cases where the companion was bright enough to detect above the reliability threshold and the images were unsaturated, we detected the companion in all images of all filters. For the companion only identified in the F555W filter (J05351624-0528337), the primary was too faint to observe in the F435W filter, and the images were saturated in F775W and F850LP. For the companion only identified in the F775W filter (J05350957-0519426), the primary was too faint to detect in F435W and F555W, and the companion was too close in separation to detect in the F850LP filter (assuming the $\Delta$ mag in F850LP corresponded to the estimated mass ratio of the binary).

The projected separations of the candidate companions range from 11 - 121 au (0.028" - 0.30", or 0.55 - 6.06 pixels on ACS). Two of these candidate companions, both with separations > 100 au, were previously detected by Reipurth et al. (2007), and one of these same two was identified in stellar sample where the primary mass estimate has been corrected based on the Hillenbrand et al. (2013) spectral type. One other candidate companion (J05351624-0528337) was previously identified in the stellar sample, but because this target only appeared in one filter, we could not estimate our own extinction value so we used the extinction estimate from the most recent spectroscopic observation. We adopt $A_v$ = 4.5 from Kounkel et al. (2018), which, combined with the spectral type of Hillenbrand et al. (2013), resulted in a primary mass of 0.15 $M_\odot$, larger than the upper limit of our target sample. Therefore, this target was excluded from our sample, leaving us with 7 candidate very low mass star and brown dwarf binaries. The remaining five detections are new.

In Table 2.3, we present the observed color information derived for each source, i.e. the combined magnitude of the system and difference in magnitude between the primary and secondary in each filter. All binary detections have a $\Delta$ mag < 2 mag across all filters, shown in Table 2.3 and Fig. 2.3. Our method is sensitive to companions at 4 mags in contrast, although this is only the case for high S/N targets. For lower S/N targets, we are sensitive to lower contrast companions. See Sec. 2.7.2.3 for a discussion on the sensitivity of a large sub-set of the sample and Sec. 2.7.2.4 for our statistical approach in determining that we do not have a bias against low mass ratio binaries. We also display the photometric information in two color-magnitude diagrams (CMDs) shown in Fig. 2.16. We limit the sources included to those with S/N $\geq$ 30 in both filters that the CMDs cover. Included in the plots are the 2 Myr isochrone of Allard et al. (2001) and extinction vectors. These plots show that higher mass and/or lower extinction objects are more often found in the bluer filters while lower mass and/or higher extinction objects are more often found in the redder filters. In Table 2.4, we present the physical parameters of each binary (masses, separation, and position angle) and the measured values from our analysis (e.g. S/N and $\chi^2_\nu$).

Table 2.3: We list the observed magnitude information of each binary system. In each set of two columns, we present the total magnitude of each system in each filter followed by the difference in magnitude between the primary and companion. These values are the weighted mean calculated from all exposures of the target where the error is the 68% confidence interval. We use these values to estimate masses in Table 2.4. Where values are not listed, they did not fulfill the requirements listed in Sec. 2.5.2.

| Source # | Total Mag (F435W) | Δ mag (F435W) | Total Mag (F555W) | Δ mag (F555W) | Total Mag (F775W) | Δ mag (F775W) | Total Mag (F850LP) | Δ mag (F850LP) |
|---|---|---|---|---|---|---|---|---|
| 1 | 23.07 ± 0.04 | 0.09 ± 0.06 | 22.10 ± 0.03 | 0.52 ± 0.05 | 18.74 ± 0.01 | 1.48 ± 0.02 | - | - |
| 2 | 23.10 ± 0.04 | 0.71 ± 0.07 | 21.20 ± 0.02 | 0.62 ± 0.03 | - | - | - | - |
| 3 | 19.92 ± 0.02 | 0.90 ± 0.04 | 18.76 ± 0.01 | 0.39 ± 0.04 | - | - | - | - |
| 4 | 23.55 ± 0.03 | 1.31 ± 0.09 | 21.35 ± 0.01 | 1.33 ± 0.02 | - | - | - | - |
| 5 | 20.92 ± 0.02 | 1.12 ± 0.25 | 19.24 ± 0.01 | 0.94 ± 0.08 | - | - | - | - |
| 6 | - | - | - | - | 20.67 ± 0.02 | 1.68 ± 0.05 | 18.89 ± 0.02 | 1.57 ± 0.05 |
| 7 | - | - | - | - | 18.80 ± 0.01 | 1.37 ± 0.57 | - | - |
| 8[a] | - | - | 22.3 ± 0.03 | 0.72 ± 0.06 | - | - | - | - |

NOTE— a) This target is excluded from the final sample, see Sec. 2.7.2.1.

We estimate the extinction of each source with multi-filter data using the observed flux of the primary with ACS, the intrinsic model flux of the primary derived from Allard et al. (2001) based on the spectral type of the target, and the extinction law of Cardelli et al. (1989). For one target (J05350739-0525481), the estimated extinction is -1.4. This target was observed to have Ca II triplet emission lines in Hillenbrand et al. (2013) which are indicative of accretion. Shocks from accretion onto an object along magnetic field lines will cause excess emission in blue/UV wavelengths (Azevedo et al., 2006). This could cause a source to have higher flux in bluer filters, and could account for the negative extinction estimate. Since this negative extinction is non-physical, we assume an extinction of zero similar to the treatment of Herczeg and Hillenbrand (2014) and Kounkel et al. (2018).

We calculate masses using the isochrones of Allard et al. (2001), assuming that the derived extinction is the same for both the primary and secondary components of the binary. The ONC has an observed age spread of $\sim$ 1-3 Myr (Reggiani et al., 2011; Beccari et al., 2017). If we assume ages of 1, 2, and 3 Myr, our mass estimates vary by $< 20\%$ while the mass ratio estimates vary by $< 0.1$. Because we do not have individual age estimates of our detected binaries, we derived masses using the 2 Myr isochrone, the mean age estimated by Reggiani et al. (2011). If instead we use the COND models of Allard et al. (2001), all mass estimates change by $< 25\%$ while the mass ratio estimates vary by $< 0.15$.

The physical separation is calculated assuming a distance of 400 pc to each target (Großschedl et al., 2018) and applying a correction factor of 1.16 to convert from projected to physical separation in a statistical sense (Dupuy and Liu, 2011). Fig. 2.17 shows one image of each detection in the F435W and F555W filters in order of separation. Fig. 2.18 shows the same but for the F775W and

Table 2.4: Candidate binaries with masses ($M_\odot$), mass ratios (q), projected separations in arcseconds, physical separation in au, and position angles in degrees. To estimate masses, we used the 2 Myr isochrone of Allard et al. (2001). We assumed a distance of 400 pc (Großschedl et al., 2018) and applied a correction factor of 1.16 to convert from projected separation to physical separation (Dupuy and Liu, 2011). Binary parameters are the weighted mean calculated from all exposures of the target where the error is the 68% confidence interval. We also show the S/N of the target for the filter within which it is brightest along with the $\chi^2_\nu$ associated with that filter.

| # | 2MASS ID | $M_{prim}$ ($M_\odot$) | $M_{sec}$ ($M_\odot$) | q | $A_v$ (mag) | Projected Sep .(arcsec) | Physical Sep. (au) | PA (deg) (E of N) | S/N | $\chi^2_\nu$ |
|---|---|---|---|---|---|---|---|---|---|---|
| 1 | J05350136-0524132 | 0.044 ± 0.002 | 0.036 ± 0.002 | 0.82 | 1.9 | 0.318 ± 0.009 | 148 ± 4 | 114 ± 0.5 | 335 | 1.12 |
| 2 | J05345805-0529405 | 0.046 ± 0.002 | 0.037 ± 0.002 | 0.80 | 1.1 | 0.113 ± 0.006 | 52 ± 2 | 64 ± 0.8 | 167 | 0.94 |
| 3 | J05350739-0525481 | 0.079 ± 0.003 | 0.065 ± 0.002 | 0.82 | 0.0[a] | 0.070 ± 0.003 | 32 ± 1 | 153 ± 0.8 | 307 | 0.75 |
| 4 | J05351676-0517167 | 0.093 ± 0.006 | 0.050 ± 0.003 | 0.54 | 2.6 | 0.270 ± 0.006 | 124 ± 2 | 265 ± 1.2 | 87 | 0.94 |
| 5 | J05351404-0525499 | 0.10 ± 0.015 | 0.063 ± 0.007 | 0.63 | 0.8 | 0.052 ± 0.009 | 24 ± 4 | 280 ± 1.6 | 197 | 0.91 |
| 6 | J05350313-0525364 | 0.023 ± 0.001 | 0.012 ± 0.001 | 0.52 | 1.1 | 0.086 ± 0.005 | 40 ± 2 | 58 ± 1.0 | 141 | 1.01 |
| 7 | J05350957-0519426 | 0.033 ± 0.005 | 0.021 ± 0.004 | 0.63 | 1.2[b] | 0.027 ± 0.007 | 13 ± 3 | 129 ± 2.8 | 263 | 0.98 |
| 8[d] | J05351624-0528337 | 0.15 ± 0.010 | - | - | 4.5[c] | 0.17 ± 0.006 | 67 ± 2 | 183 ± 0.9 | 32 | 0.86 |

NOTE— a) Our extinction estimate using photometry from the F435W and F555W filters was -1.4. As explained in Sec. 2.7.2.1, this estimate is non-physical and instead we assume an extinction of 0.0 following the procedure of Herczeg and Hillenbrand (2014) and Kounkel et al. (2018). b) Extinction estimate taken from the source paper of the spectral classification (Riddick et al., 2007) due to the identification of the companion in only one filter. This value was used in order to derive mass estimates. c) Extinction estimate taken from most recent spectral observation (Kounkel et al., 2018) due to the identification of the companion in only one filter. This value was used in order to derive mass estimates. d) This target is excluded from the final sample used to calculate the companion frequency of the ONC as its estimated mass of 0.15 $M_\odot$ is above the upper bound to be included.

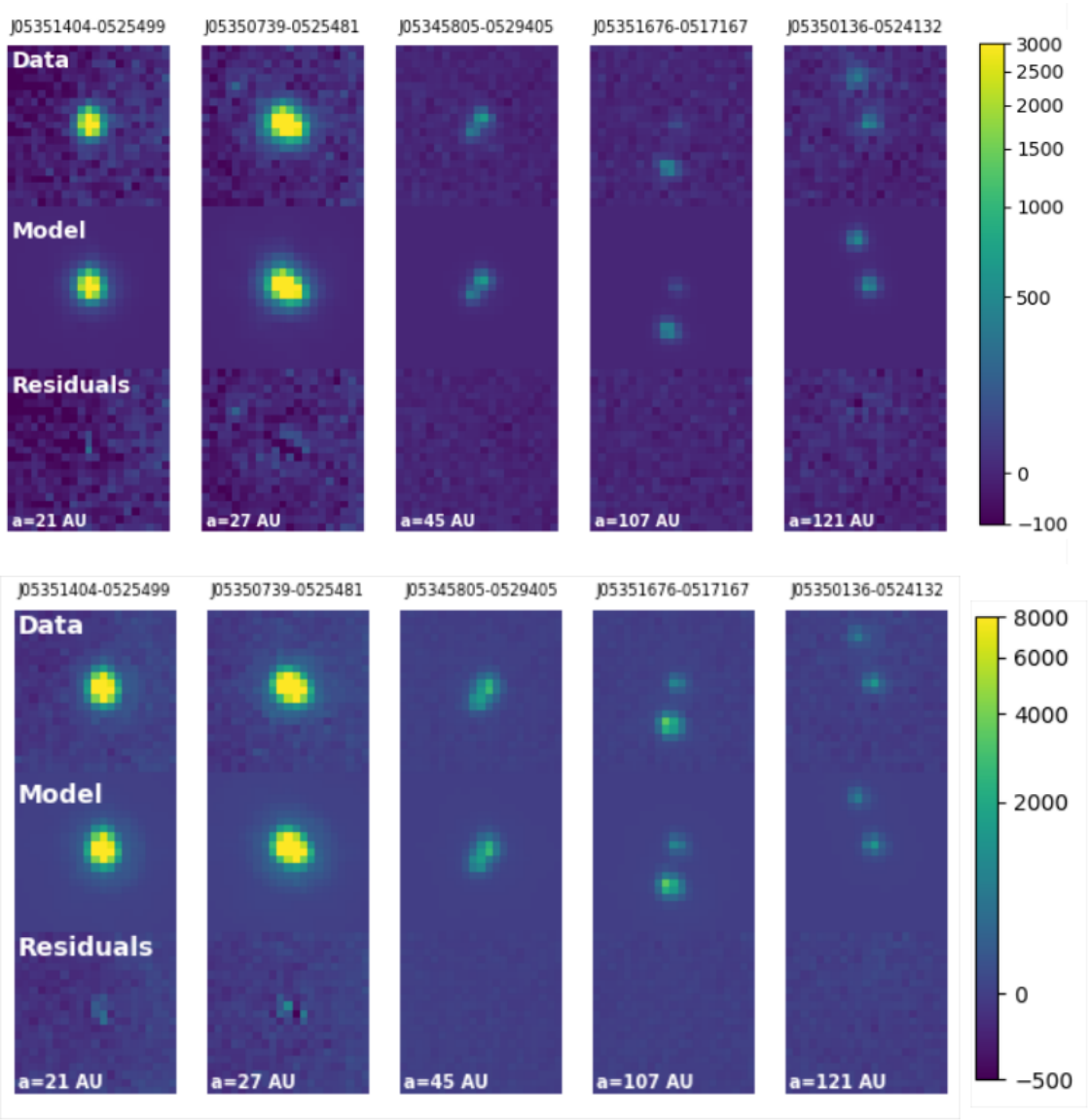


Figure 2.17: We show the binary detections of our survey in the F435W and F555W filters. For each panel, the top image is the postage stamp of the *HST* data, the middle image is our binary PSF best-fit model, and the bottom image is the residual. The binaries are listed from left to right in order of increasing projected separation. Each postage stamp is 21x21 pixels across, an angular size of 1.05"x1.05". The images are displayed with an inverse hyperbolic sine stretch and the units are in counts.

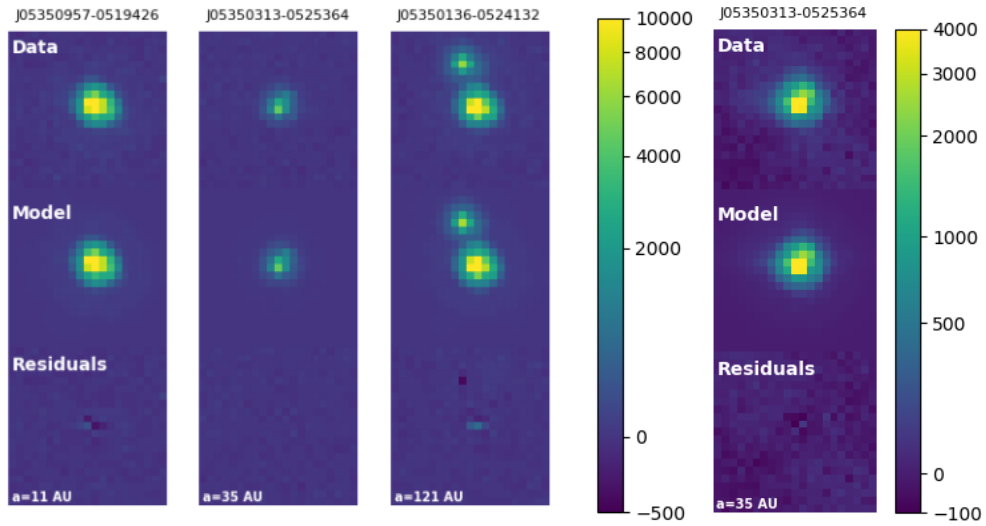


Figure 2.18: Same as Fig. 2.17 but for the F775W and F850LP filters.

F850LP filters.

#### 2.7.2.2 Chance Alignments

In order to perform a statistical analysis of our results, we must determine the probability that our candidates are not physically associated with their primaries, i.e. chance alignments. This can occur from foreground stars, background stars, and other cluster members along the line of sight. As in Sec. 2.7.1.2, we used the photometric list of Robberto et al. (2013) to derive the stellar surface density as a function of radius from the cluster core that takes into account any object within the region regardless of its membership. We search for companions within a 10 pixel radius from each target. The detected binary closest to Theta 1 Ori C is 151" away. The highest stellar density of all broadband filters in our survey at 150" from Theta 1 Ori C is 0.0045 stars/arcsec$^2$. Using this stellar density as the upper limit to the expected density within the cluster, we expect 0.0035 chance alignments per target within this search radius and 0.26 chance alignments for all 75 targets in our sample. Although we searched a radius of 0.5" from the target, the widest detection was found at 0.3". We expect to find 0.1 chance alignments to all 75 targets in the sample within a 0.3" radius. Since we used the entire catalog of sources from Robberto et al. (2013) without membership information, this includes foreground and background contaminants. Therefore, we conclude that all of the detections are likely physical binaries with no expected chance alignments.

#### 2.7.2.3 Calculating the Companion Frequency to Brown Dwarf Primaries

Before we can calculate a model independent companion frequency for 0.012 - 0.1 $M_{\odot}$ primaries in the ONC, we must define the common parameter space over which the detection method is sensitive to companions for a large sub-set of the sample, e.g. mass ratio and separation. The initial sample is defined in Sec. 2.5.2, but the sensitivity to companions depends on the S/N of the targets and the filters in which those targets meet the requirements laid out in Sec. 2.5.2. To calculate the achievable contrast within an image for a given source, we take the value from the 0.1% false positive line shown in Fig. 2.3 at some specified separation. Then, we calculate the mass of a companion corresponding to that highest achievable contrast from the Allard et al. (2001) evolutionary models, assuming the primary has the mass associated with the defined spectral types of Hillenbrand et al. (2013), an age of 2 Myr, and the extinction of the companion is the same as the primary. For any given source that appears in multiple images in one filter, we calculate the S/N of the target in each image and use the minimum S/N to determine the achievable contrast for that source within all images of that filter. If the source appears in other filters, we repeat the S/N calculations as before and determine the achievable contrast within each filter. Then, we select the lowest detectable companion mass achievable in a single filter as the companion detection threshold for a given target. Lastly, we calculate the mass ratio, $m_{comp}/m_{prim}$, for each source to determine the common mass ratio range for most of the sample at a given separation.

As shown in Fig. 2.3, the sensitivity of this method becomes background limited beyond about 2 pixels (0.1") in separation. At the distance of the ONC ($\sim$ 400 pc), this corresponds to a projected separation of 40 au. Many past surveys of field brown dwarfs (e.g. Close et al., 2003; Gizis et al., 2003; Reid et al., 2006; Fontanive et al., 2018) show that the separation distribution can be modeled by a log-normal distribution with a peak somewhere between 3 - 10 au, depending on primary mass and resolution limits. Additionally, the companion mass ratio distribution (CMRD) of field binaries with brown dwarf primaries is strongly peaked at one (e.g. Reid et al., 2006). Because the separation distribution peaks at small separation and half of our detections are within 40 au, we want to compare our detections to as much of the expected field population as possible and opt for a closer separation for common sensitivity. We also opt for a moderate mass ratio limit to maximize the number of targets included in the sub-sample since the field surveys are not sensitive to companions at low mass ratios and to include as many detected companions as possible.

Taking all of this into account, we define the range of common sensitivity for projected separations 20 - 200 au and from a mass ratio of 0.5 - 1.0 which is applicable to 50 targets out of our initial sample of 75. We are assured that the double-PSF fitting routine can detect all companions to these 50 targets (defined as the sub-sample) over mass ratios of 0.5-1.0 and projected separations of 20-200 au. Six of the seven detections in this survey had estimated mass ratios > 0.5 and projected separations > 20 au as well as high enough S/N for the code to detect companions above a mass

ratio of 0.5 at 20 au. One detection was at a projected separation of 11 au and therefore excluded from this analysis. Out of this analysis, we calculate a companion frequency of $0.12^{+0.06}_{-0.032}$ for brown dwarf primaries ($M_{prim} \leq 100\ M_{Jup}$) in the ONC over projected separations 20 - 200 au and mass ratios 0.5 - 1.0. Errors on the companion frequency are estimated from binomial statistics where we define the upper and lower bounds based on the 68% confidence range of the binomial distribution (Burgasser et al., 2003).

#### 2.7.2.4 Comparison to the Galactic Field

We next compare the observed companion frequency in the ONC to that of the Galactic field over the common sensitivity range of our sample, described in Sec. 2.7.2.3 . Reid et al. (2006) carried out an L-dwarf multiplicity survey in the Galactic field using the Near-Infrared Camera and Multi-Object Spectrometer (NICMOS). Their sample consists of field objects with masses $\sim$ 0.04 - 0.09 $M_{\odot}$, where higher order multiples are very rare, making it an appropriate sample to compare to the binary results of our ONC survey, where $M_{prim}$ = 0.012 - 0.1 $M_{\odot}$. We characterize the binary population of the Galactic field using functional forms of the observed binary parameters: the CMRD modeled as a power law (eq. 2.9) and the physical separation distribution modeled as a log-normal (eq. 2.10). Reid et al. (2006) used a Bayesian analysis to estimate the values of the functional form variables that describe the observed field L-dwarf binary population: 1) companion frequency ($C_n$), 2) mean of the physical separation distribution ($\overline{a}$), 3) width of log-normal physical separation distribution ($\sigma$), and 4) power-law index ($\beta$) of the CRMD. Their Fig. 7 shows the posterior probability distributions of this four-parameter model with best fits: $C_n = 0.24^{+0.06}_{-0.02}$, $log(\overline{a}) = 0.8^{+0.06}_{-0.12}$, $\sigma$ = 0.28 $\pm$0.4, and $\beta$ = 3.6 $\pm$ 1.

We estimated the expected brown dwarf binary fraction of the Galactic field using eq. 2.14. First, we sampled each of the four posterior distributions of Reid et al. (2006) $10^6$ times. Then, we integrated eq. 2.14 over the common mass ratio and physical separation limits, 0.5 < q < 1.0 and 23 < a < 230 au to determine the companion frequency of each sample. We took the mean of this result as the expectation value for the companion frequency. To approximate error bars, we defined the upper and lower bounds as the 68% confidence interval of this resultant companion frequency distribution. We derive the inner and outer bound of the separation by converting projected separation to physical separation (Dupuy and Liu, 2011). These calculations result in an expected field companion frequency of 0.009$\pm$0.006.

In order to compare the companion frequency of the Galactic field to that of the ONC, we took the binomial distribution formalism of Burgasser et al. (2003), described in Sec. 2.7.2.3, and integrated from 0 to the resulting companion frequency from each sampling above. This statistic determines the posterior probability of the field companion frequency being the real frequency of binaries in the ONC population, i.e. the probability that Galactic field binary population comes

from this ONC binary population. Then, we took the mean probability of all the sampling as the expectation value that the field sample companion frequency derived by Reid et al. (2006) is consistent with our ONC results. This procedure resulted in a mean probability of $10^{-6}$. This is evidence for an excess of very low mass star and brown dwarf binaries in the ONC compared to the Galactic field over $0.5 < q < 1.0$ and $23 < a < 230$ au.

Reid et al. (2006) calculate a strong preference for high mass ratio binaries for very low mass star and brown dwarf primaries in the Galactic field with a CMRD power-law of 3.6. We sought to determine whether we could statistically differentiate the observed mass ratio distribution of the ONC from that of the model of the Galactic field. To investigate this possibility, we sampled the Reid et al. (2006) posterior probability distribution of the power law index for the mass ratio distribution $10^4$ times, each time producing a companion mass ratio distribution that represent the Galactic field distribution. For every mass ratio distribution that we produced, we sampled it $10^6$ times, and then performed a two sample Kolmogorov–Smirnov test (KS test) against the observed mass ratios of the binaries in the ONC with separations > 20 au. The mean p-value resulting from this process is 0.02, likely ruling out that the observed ONC population and the Galactic field CMRD come from the same parent distribution. We also tested the observed ONC population against a flat CMRD ($\beta = 0.0$) in the same manner as above, producing populations of $10^6$ binaries $10^4$ times. This results in a mean p-value of 0.42, meaning we cannot rule out that the observed ONC population is drawn from a flat CMRD.

#### 2.7.2.5 Comparison to Other Star-forming Regions

The Galactic field is an amalgamation of all the stars, brown dwarfs, and planetary mass objects that are produced within star-forming regions (SFRs) over the lifetime of the Galaxy. While the original environment of individual field objects is unknown, the binary populations within SFRs and older star clusters provide important information about the effects of environment and age on binary formation and evolution.

There have been many binary surveys of nearby SFRs and star clusters targeting brown dwarf primaries. In the following comparisons, we focus on four SFRs and star clusters of various sizes and ages: Taurus-Auriga (Taurus), Chamaeleon I (Cha I), Upper Scorpius (Upper Sco), and the Pleiades. To compare their very low mass star and brown dwarf binary populations to that of the ONC, we require that each primary have a mass $\leq 0.1$ $M_\odot$ ($\geq$ M6 at 1 Myr) and that the survey is sensitive to binary systems of $q \geq 0.5$ at projected separations $\geq 20$ au, except where specified.

In Taurus, a $\sim$ 1 Myr old low-mass stellar association, we combine the results of four surveys: Kraus et al. (2006); Konopacky et al. (2007); Kraus and Hillenbrand (2012); Todorov et al. (2014). Restricting their sample to members $\geq$ M6, there are two detections out of a total sample of 60 objects, a companion frequency of $0.033^{+0.041}_{-0.011}$. In a similar manner to the comparison of the field

to the ONC, we sampled a binomial distribution that describes the companion frequency of Taurus and again integrated the ONC binomial distribution from 0 to the companion frequency of each iteration of the sampling procedure. Each integration returns the probability that the observed Taurus companion frequency is consistent with our results in the ONC. The p-value is 0.05, and therefore we do not find any strong evidence for an excess of very low mass star and brown dwarf binaries in the ONC compared to Taurus over projected separations 20 - 200 au and mass ratios 0.5 - 1.0.

In Cha I, a $\sim$ 2 Myr (Luhman, 2004) low-mass stellar association, we combine the results of Ahmic et al. (2007), Lafrenière et al. (2008), and Todorov et al. (2014). Restricting their sample to members $\geq$ M6, there are zero detections out of a total sample of 24 sources. We use the same procedure described above to calculate the probability that this companion frequency is consistent with our results in the ONC. We obtain a p-value of 0.05, and therefore we find no strong evidence for an excess of very low mass star and brown dwarf binaries in the ONC compared to Cha I over separations and mass ratios sampled. Additionally, Luhman (2004) made a serendipitous detection of a 240 au separation and q = 0.5 brown dwarf binary in Cha I, a potential indicator of the existence of wide brown dwarf binaries in this particular stellar association, analogous to our findings in the ONC.

Upper Sco is the nearest OB association that likely contains over 2000 stars (Preibisch and Mamajek, 2008) and at 5 Myr old, could be an example of the future structure of the ONC, i.e. unbound, less dense and expanding outward (cf. Hillenbrand and Hartmann, 1998). Combining the results of Biller et al. (2011) and Kraus and Hillenbrand (2012), there is one detection (projected separation of 21 au) out of a total sample of 40 targets. Repeating the method from above, we calculate a p-value of 0.06 that the Upper Sco companion frequency is consistent with our results for the ONC over separations and mass ratios sampled. If the ONC is unbound and evolves in a manner that resembles Upper Sco, then the brown dwarf binary population of the ONC does not need to be disrupted through additional processing mechanisms, but may still lose some binaries as the cluster dissolves into the field, resulting in more statistically similar populations. It is expected that Upper Sco will directly contribute to the field as it expands.

Lastly, we compare the brown dwarf binary population of the ONC to the Pleiades, a 125 Myr old open cluster which likely contains over 1000 stars (Adams et al., 2001). An ONC-like cluster has been suggested as a potential precursor to the Pleiades through N-body simulations (Kroupa et al., 2001a). Combining the samples of Martín et al. (2000) and Garcia et al. (2015), there are zero detections out of a sample of 45 targets. Importantly, Martín et al. (2000) are sensitive to companions down to 27 au in projected separation, and therefore we must constrain the ONC sample to the same projected separation. Over projected separations 27 - 200 au and mass ratios 0.5 - 1.0, the ONC has a companion frequency of $0.10^{+0.058}_{-0.028}$. Following the method from above,

we calculate a p-value of 0.02 that the companion frequency of the Pleiades is consistent with the companion frequency of the ONC population over separations and mass ratios sampled. It is likely that the ONC will require further processing for its binary population to resemble that of the Pleiades at a comparable age. However, larger sample sizes in both clusters will help determine the level of similarity between these binary populations.

## 2.8 Implications

Our analysis of the companion population of low-mass stars in the ONC identified 44 companions and constrained the mass ratio distribution with a power law fit with exponent $\beta = 2.08^{+1.03}_{-0.85}$ and a companion frequency = $0.13^{+0.05}_{-0.03}$ over 10-200 au and q=0-1. Due to our limited sensitivity in separation, we could not place meaningful constraints on the separation distribution.

We identified a $2\sigma$ difference between the power-law exponent of the mass ratio distribution for stars with masses $\geq$ 0.3 $M_\odot$ in the Galactic field from the studies of Reggiani and Meyer (2013) and Offner et al. (2023) and the results of our Bayesian analysis in the ONC for primary stars down to the hydrogen burning limit. Importantly, we find a $1.4\sigma$ difference between the mass ratio distribution of our results and those of Offner et al. (2023) for primary mass 0.15-0.3 $M_\odot$ and a $1.7\sigma$ difference compared to the results of Fontanive et al. (2018) for brown dwarf primaries (likely due to their large errors), see Fig. 2.20.

Kraus and Hillenbrand (2012) searched for companions at separations = 7 - 5000 au to stars with masses 0.07 - 0.5 $M_\odot$ in Taurus and Upper Sco, and found a trend in the mass ratio distribution similar to the field where $\beta = 0.18^{+0.33}_{-0.3}$ for 0.3 - 0.5 $M_\odot$ primaries and $\beta = 1.02^{+0.59}_{-0.52}$ for 0.15 - 0.3 $M_\odot$ primaries, see Fig. 2.20. Although these results are over a wider range of separations, the mass ratio distribution appears consistent with the Galactic field population for the same primary masses and also consistent with our results in the ONC for lower mass primaries ($1\sigma$ difference). These results are potentially indicative of a primordial mass ratio distribution that is an outcome of the star formation process and mostly unaffected by dynamical interactions (Parker and Reggiani, 2013), over the separations sampled.

Previous studies have identified preferential circumbinary disk accretion onto the companion as a mechanism to drive mass ratios toward unity (Young and Clarke, 2015; Satsuka et al., 2017). These companions can be produced through turbulent fragmentation or disk fragmentation, and can migrate inward through interactions with the circumstellar disk or gas from the natal cloud, producing separations like those seen in our survey (Bate et al., 2002, 2003; Offner et al., 2010). Bate (2012) simulated a turbulent molecular cloud using a radiation hydrodynamical simulation, and found the distribution of mass ratios to stars with masses 0.1-0.5 $M_\odot$ weighted towards equal masses with 63% of these multiple systems with q > 0.6, and only 50% for stars > 0.5 $M_\odot$. These

processes may be applicable to our observations within the ONC as we see a mass ratio distribution weighted towards equal masses for low-mass primaries.

In addition, we do not find a difference between the companion frequency of the ONC and that of the Galactic field (Susemiehl and Meyer, 2022) for low-mass stars over q=0-1.0 and semi-major axes = 12.6-252 au, see Fig. 2.19. However, we find a probability of 0.002 that the companion frequency of the ONC can describe the observations of the low-mass T-association Taurus-Auriga.

High stellar density has been linked to lower companion frequency due to increased dynamical interactions that can disrupt a multiple system (Kroupa, 1995a; Kroupa et al., 2001a). The ONC is a high density star-forming region, n $\sim 10^{3.5-4.5}$ stars pc$^{-3}$ (Hillenbrand and Hartmann, 1998; Marks and Kroupa, 2012), that is thought to have experienced a cool-collapse phase which temporarily increases the density by roughly a factor of 10 followed by relaxation and expansion (Allison et al., 2009, 2010; Parker et al., 2011). Within temporary states of higher density, dynamical interactions become significant over 10-200 au and could have disrupted many stellar multiple systems resulting in the present day configuration of the companion population differing from the initial state. Based on the present day density of the ONC, most stellar multiple systems with separations of 10-200 au are not expected to disrupted in many 10s of Myr (Weinberg et al., 1987). Taurus-Auriga, is a low-mass, T-association, that has a low stellar density of 1-10 stars pc$^{-3}$ (Marks and Kroupa, 2012; King et al., 2012; Parker, 2014). This region is not expected to have had a period of intense dynamical interactions, leaving the present day companion frequency likely very similar to the initial population. Additionally, the current state of the low-mass star companion population with separations $\lesssim$ 200 au in Taurus will remain unchanged in the future, in excess of the Galactic field population.

Higher density regions like Westerlund 1 ($10^5$ M$_\odot$ pc$^{-3}$) and Arches ($10^{5.5}$ M$_\odot$ pc$^{-3}$, Clark et al., 2005), would experience an even higher level of dynamical processing, likely destroying many multiple systems with separations between 10-200 au. All types of star-forming regions will contribute to the Galactic field population, potentially with an equal number of stars over order of magnitude bins in total cluster stellar mass (Gieles, 2009). If the star-forming regions within the same stellar mass bin experienced roughly equal density states, it is possible that regions that do not experience very high density states (like Taurus) will contribute an excess of companions, ONC-like clusters will contribute a comparable number of companions, and even higher density regions like Arches will contribute a paucity of companions relative to the Galactic field population over these orbital separations. In this case, the ONC would be representative of a companion population averaged over all star-forming regions commensurate with the Galactic field population.

Interestingly, our analysis of the ONC very low mass star and brown dwarf binary population reveals an excess of wide (a = 23 - 230 au) binaries relative to the Galactic field over q = 0.5 - 1.0, unlike our results for low-mass stellar primaries, see Fig. 2.19. In comparison to other star-forming

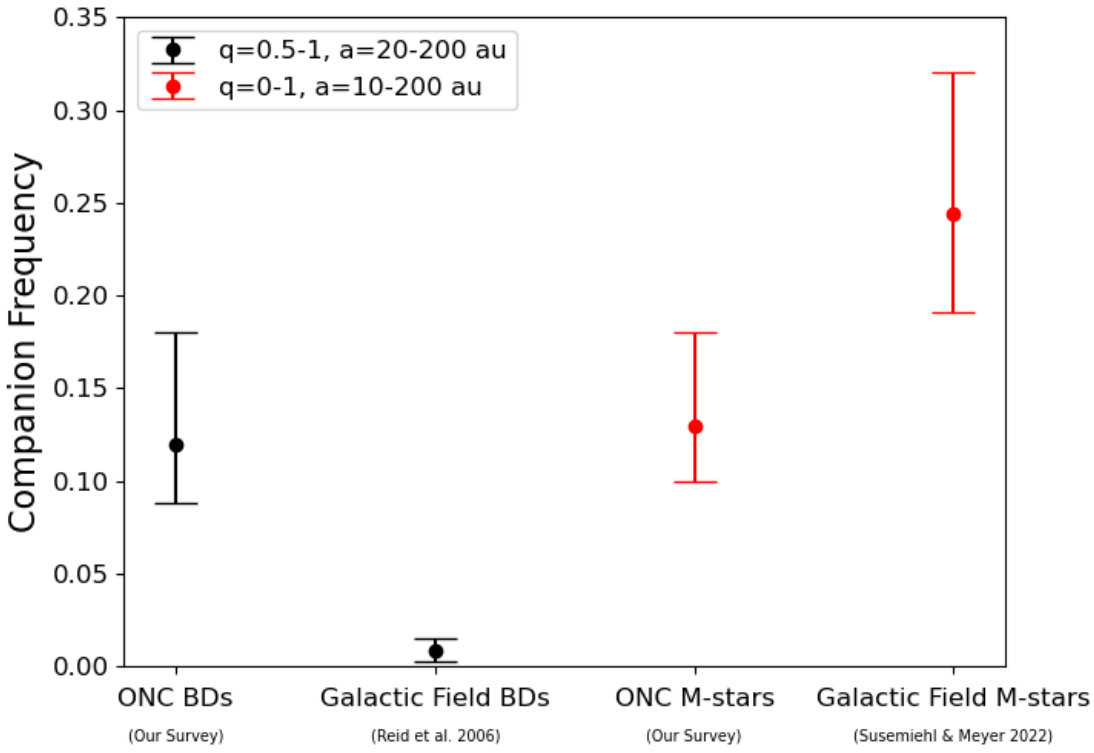


Figure 2.19: Companion frequencies based on primary mass in the ONC and the Galactic field. Companion frequencies for the very low mass star and brown dwarf (BD) primaries are calculated over mass ratios = 0.5 - 1.0 and separations (a) = 20 - 200 au, those for low-mass stellar primaries are over mass ratios = 0 - 1 and a 10 - 200 au. The companion frequency for BD primaries in the field is derived from the model of Reid et al. (2006), and M-type primaries in the field from the model of Susemiehl and Meyer (2022). We see an excess of companions to very low mass star and brown dwarf primaries in the ONC relative to the Galactic field. We find the companion frequency to low-mass stellar primaries is consistent with the Galactic field within the errors.

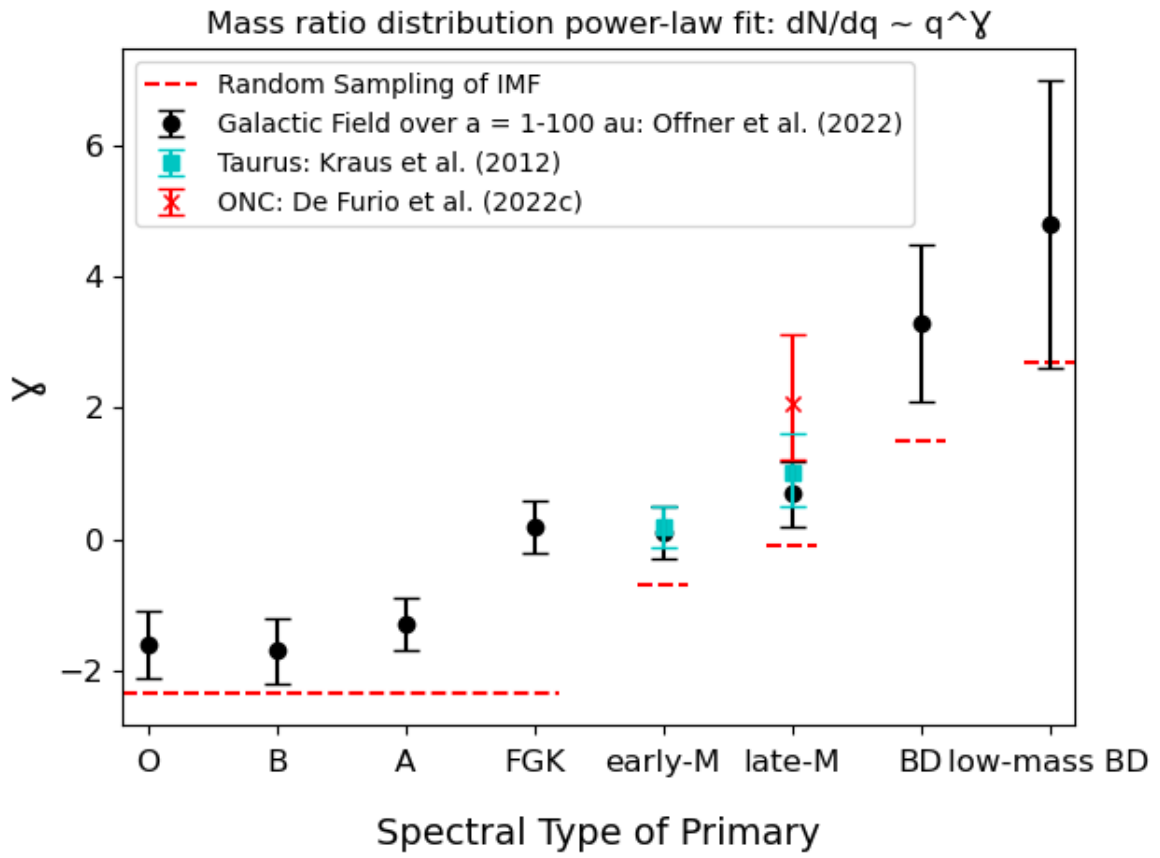


Figure 2.20: Adapted from Offner et al. (2023). Black points show the power-law indices of the mass ratio distribution model across primary masses from O-stars to low mass brown dwarfs in the Galactic field for a = 1-100 au. Over-plotted in cyan and red are the power-law fit results of the mass ratio distribution for low mass stars in Taurus (Kraus et al., 2011) and the ONC (this chapter) respectively. We see no difference in the mass ratio distribution among the ONC, Taurus, and the field for late-M primaries. This is indicative of initial formation mechanisms invariant of stellar density. Over-plotted in red dashed lines are the expected power-law indices for q > 0.3 for mass ratio distributions that are the result of random sampling from a log-normal ($\mu$ = 0.22, $\sigma$ = 0.33) initial mass function (Chabrier, 2003) for M-type and brown dwarf primaries and the Salpeter power-law for FGK- through O-type primaries (Salpeter, 1955). All observational results are roughly consistent with expectations from randomly drawing from the IMF within the errors (with some potential need for preferential accretion to increase the mass of the companion) except for solar-type primaries which may require significant processes to modify the companion mass.

regions, we find no strong evidence for an excess of very low mass star and brown dwarf binaries in the ONC relative to low mass stellar associations (e.g. Taurus and Cha I), but find a potential excess relative to the Pleiades.

Dynamical interactions have been invoked to explain how the companion frequency could decrease as unbound clusters dissolve into the Galactic field. If the ONC is unbound and all its stellar components become a part of the Galactic field population, dynamical interactions may reconcile the discrepancy we observe between its very low mass star and brown dwarf binary population and that of the Pleiades. On the other hand, if the ONC remains bound, it could ultimately resemble an open star cluster like the Pleiades (as suggested by Kroupa et al., 2001b), and still most likely would require a small amount of further processing.

Weinberg et al. (1987) explored how effectively encounters with other stars and giant molecular clouds (GMCs) can disrupt wide binaries. Using these calculations, Burgasser et al. (2003) determined that neither stellar nor GMC encounters in the Galactic field are likely to break up brown dwarf binaries with separations $< 10^4$ au, highlighting the potential need for encounters with other cluster members.

We can calculate the typical lifetime of a specific binary within an ONC-like environment from eq. 28 of Weinberg et al. (1987). First, we approximate the stellar density in the region of the ONC in which these binaries exist, between 0.3 - 0.9 pc from the cluster center. Da Rio et al. (2014) measured the stellar mass density distribution of the ONC (their eq. 3) as follows:

$$\rho_{stars}(r) = 70 M_{\odot} pc^{-3} (\frac{r}{1pc})^{-2.2}, r < 3pc \tag{2.15}$$

We then approximate the number density in this region by dividing the stellar mass density by the characteristic mass of 0.3 $M_{\odot}$ (Da Rio et al., 2012). For a binary of total mass 0.1 $M_{\odot}$ and separation of 100 au at 0.3 pc, the approximate stellar number density is 3.7 x $10^3$ stars $pc^{-3}$ and the characteristic lifetime is 5 Myr. The mean age of the ONC is estimated to be 2.2 Myr (Reggiani et al., 2011), so these observed binaries may not have existed long enough to be disrupted but they may not ultimately survive the current dense environment of the ONC. Importantly, Reggiani et al. (2011) and Beccari et al. (2017) find an age spread in the ONC stellar population. This leaves open the possibility that these wide binaries formed after the cool collapse phase and did not encounter an environment of significantly higher density that would almost assuredly destroy such low binding energy binaries. Instead, the disruptions may occur over the next several Myr and could explain both the discrepancy in the companion frequency and the CMRD of the brown dwarf primaries in the ONC relative to the Galactic field.

This scenario is consistent with that of Kroupa et al. (2003) who shows that dynamical interactions of wide (> 20 au) very low mass star and brown dwarf binaries in an ONC-like cluster can

happen in ~ 1 Myr. Parker and Goodwin (2011) also show that clusters represented by virialized Plummer spheres of initial density comparable to the current density in the ONC (half-mass radius = 0.8 pc, see McCaughrean and Stauffer, 1994; Hillenbrand and Hartmann, 1998) can disrupt some wide very low mass star and brown dwarf binaries at separations > 10 au, although most of these binaries remain unaffected. While the ONC may already be significantly dynamically mixed, these simulations leave open the possibility for further dynamical interactions.

Conversely, we considered the possibility that these wide binaries will be hardened to the smaller separations seen in the Galactic field instead of disrupted through dynamical interactions. Many simulations of star clusters that account for dynamical interactions show that wider binaries are preferentially destroyed due to their low binding energy. Kroupa and Burkert (2001); Kroupa et al. (2001b); Parker et al. (2011); Parker and Goodwin (2012) all arrive at a decrease in wide binaries with no subsequent increase in small separation binaries after dynamical processing, indicative of the fact that wide binaries are not likely to harden.

Importantly, an excess of very low mass star and brown dwarf binaries is not inconsistent with our results for the stellar primaries. We found that the low-mass stellar companion frequency was consistent with the Galactic field, leaving no need for further dynamical interactions. Although these stellar binaries have similar separations to the very low mass star and brown dwarf binaries, the total binding energy of stellar binaries is significantly higher than that of the very low mass star and brown dwarf binaries. Additionally, the characteristic lifetime of the stellar binaries is between 4-20 times longer than that calculated for the very low mass star and brown dwarf binaries, using the Weinberg et al. (1987) derivation. If the ONC continues to expand and eventually expel most of its population into the Galactic field, the stellar binaries are very unlikely to be disrupted while the very low mass star and brown dwarf binaries are significantly more likely to be disrupted before large changes in the density. Even if the ONC remains bound, a large majority of its stellar content will be ejected to the field before the impact of further dynamical interactions would affect the stellar population as opposed to the likely impact on the very low mass star and brown dwarf binaries population.

On the other hand, Parker and Goodwin (2012) stress the potential of stochasticity in the destruction of binaries within ONC-like star clusters. They show that over separations 62 to 620 au the number of stellar binaries destroyed after 1 Myr can vary by a factor of > 2, with a statistically significant difference, after only 10 realizations of the same cluster. Any apparent statistical difference of an observed young binary population of one star cluster could be a result of stochasticity in the destruction of binaries rather than evidence for a distinct formation mechanism or environmental impact, highlighting the necessity for an expansion of surveys in many environments.

## 2.9 Conclusions

We performed a multiplicity survey of low-mass stars and very low-mass stellar plus sub-stellar primaries in the ONC using a double-PSF fitting routine with empirical PSFs with archival *HST/ACS* data. To summarize the results of our survey:

1) Our binary detection routine is capable of identifying companions at 0.025" for high S/N sources, below the diffraction limit of HST. This resolution limit is competitive with that attained through the aperture masking interferometry technique with ground-based adaptive optics on 8m telescopes, e.g. Duchêne et al. (2018), and kernel phase interferometry with HST, e.g. Pope et al. (2013).

2) We detected 7 candidate companions from our total sample of 75 very low-mass star and brown dwarf primaries ($M_{prim} \leq 0.1 M_{\odot}$), two of which were previously found by Reipurth et al. (2007). We detected 44 companions out of the 276 low-mass stellar members in our sample. Twenty-five of the 44 were previously detected in other multiplicity surveys, leaving a total of 24 new companions found to the observed primaries. The closest companion detection is at a projected separation of 11 au (0.027").

3) For our sample of $M_{prim} \leq 0.1 M_{\odot}$, over physical separations of 23 - 230 au and mass ratios of 0.5 - 1.0, we observed a companion frequency of $0.12^{+0.06}_{-.032}$ in the ONC. This result is distinct from the Galactic field over the same sensitivity range, 0.009±0.006, with a probability of the field companion frequency being the true ONC companion frequency equal to $10^{-6}$.

4) Using a Bayesian analysis, we estimate the companion frequency as $0.13^{+0.05}_{-0.03}$ for low-mass stars in the ONC and the exponent of the power law to the mass ratio distribution as $2.08^{+1.03}_{-0.85}$ over projected separations of 10-200 au and all mass ratios. We find that the companion frequency of low-mass stars in the Galactic field is consistent with that of the ONC. However, we find a significant excess in Taurus relative to the ONC, with a probability of 0.002 that the companion frequency of the ONC can describe the observations in Taurus.

5) We find a $1.4\sigma$ difference in the mass ratio distribution power law exponent derived for low-mass stars in the ONC ($2.08^{+1.03}_{-0.85}$) compared to low-mass primaries (0.15 - 0.3 $M_{\odot}$) in the field (0.7 ± 0.5), a result consistent with that identified for low-mass primaries in Taurus and Upper Sco ($1.02^{+0.59}_{-0.52}$, Kraus and Hillenbrand, 2012). These results are supportive of the hypothesis that the mass ratio distribution is mostly unaffected by dynamical processes and is the result of the star formation process itself (Parker and Reggiani, 2013), cf. companion frequency.

6) Based on the current high density environment of the ONC, dynamical interactions over the next few Myr could destroy very low mass star and brown dwarf binaries with low binding energies

(e.g. lower mass ratios, wider separations), but leave the wide stellar binaries mostly unaffected. If this is an important process within ONC-like clusters (as suggested by Weinberg et al., 1987; Burgasser et al., 2003), dynamical interactions could sculpt the very low mass star and brown dwarf binary population of the ONC to resemble that of the Galactic field or the Pleiades, while the current stellar population remains intact.

7) Our findings suggest that early dynamical processing of multiple systems in high density star-forming regions is important in sculpting the companion frequency, and that the ONC may be a more representative star-forming region that will contribute to the Galactic field than low-density regions like Taurus-Auriga.

We would like to thank Jay Anderson for many productive discussions on PSF modeling and the implementation of his PSF code, as well as Megan Kiminki for contributions to the construction of our code. We thank anonymous referees for careful and helpful reports which improved the presentation of this chapter. Megan Reiter received funding from the European Union's Horizon 2020 research and innovation programme under the Marie Skĺodoska-Curie grant agreement No. 665593 awarded to the Science and Technology Facilities Council. Trent J. Dupuy acknowledges research support from Gemini Observatory. This work is based on observations made with the NASA/ESA Hubble Space Telescope obtained from the data archive at the Space Telescope Science Institute, which is operated by the Association of Universities for Research in Astronomy, Inc., under NASA contract NAS 5–26555. These observations are associated with program GO-10246. Support for this work was provided by NASA through grant number HST-AR-15047.001-A from the Space Telescope Science Institute.

# CHAPTER 3

# Multiplicity in the Galactic Field: Probing the Low Mass Limit of Formation with Y-dwarf Primaries

The work presented in this chapter was originally published in the Astrophysical Journal and the Astrophysical Journal Letters. I am the first author of a paper (De Furio et al., 2023) presented in the second section on WISE J182831.08+265037.8 as a part of the *James Webb Space Telescope (JWST)* NIRCam Guaranteed Time Observations (GTO) team. The techniques and the Python code to determine multiplicity that I developed and used in the second section were later applied to a *JWST* Cycle 1 GO program (ID: 2473, PI: L. Albert, M. Meyer) of which I am a co-I. In this program, I supervised the application of the code to a sample of field Y-dwarfs which led to the discovery of a companion to WISE J033605.05-014350.4, a result published in Calissendorff et al. (2023) to which I also contributed to manuscript writing as second author. I would like to thank all those who contributed to the planning, development, and implementation of *JWST* and the NIRCam instrument in particular, without which none of this analysis could have been performed. Additionally, I would like to acknowledge all co-authors who contributed to the success of these programs. I would like to especially thank Charles Beichman, Ben Lew, and David Ciardi who performed spectral model fitting, Keck imaging analysis, and distortion characterization, searched for field brown dwarfs, and contributed to manuscript writing in the second section. In the third section, I would like to especially thank Per Calissendorff who used the companion detection techniques from the second section to detect W0336B and led manuscript writing.

## 3.1 Introducing Studies of Y-dwarfs

The star formation process produces objects over many orders of magnitude in mass. On the high mass end, stars form with masses over 100 $M_{\odot}$, while on the low-mass end brown dwarfs can be formed from star formation process down to $\sim M_{Jup}$ ($0.001 M_{\odot}$). Many studies are currently ongoing to explore the fundamental lower limit of the star formation process in young star-forming

regions using the *JWST* due to their increased luminosity at young ages. Importantly, previous mid-infrared space telescopes (e.g. Wide-field Infrared Survey Explorer, WISE) have identified isolated planetary mass objects within the Galactic field population with masses estimated between 5-20 $M_{Jup}$, although highly uncertain due to their unknown ages and the degeneracy between age and luminosity for these objects. The lowest temperature field objects identified to date have Teff $<$ 500 K, the lowest temperature of which WISE 0855-0714 has Teff $\sim$ 250 K, and are classified as Y-type brown dwarfs. These objects are approaching the temperature of Jupiter (130 K) and serve as a test case for both the lower limit to star formation and planetary analogs with similar atmospheric physics. Importantly, as Y-dwarfs are a relatively newly observed phenomena, their formation is highly important in understanding the physics of star formation at low mass scales.

A frequent outcome of the star formation process across orders of magnitude in mass is multiplicity. However, little is known about the multiplicity of low-mass brown dwarfs, particularly at the lowest temperatures, i.e. the lowest masses. *JWST* offers an unprecedented opportunity to observe these objects and characterize their multiplicity due to its sensitivity in the thermal infrared, 3-5 microns (covering the peak emission for Y-dwarfs), and highly stable point-spread function allowing for diffraction limited imaging.

Previous multiplicity analyses of brown dwarfs in the Galactic field have identified a peak in the separation distribution of companions around 3-7 au with a mass ratio distribution weighted towards equal mass binaries. However, many of these studies are unable to resolve companions at separations within a few au, meaning the presence of companions to brown dwarfs at separations $\lesssim$ 3 au is highly uncertain. Therefore, multiple programs on *JWST* have been devoted to searching for close, faint companions to the lowest mass brown dwarfs known in the Galactic field which would place strong constraints on star formation processes and possible mechanisms to produce multiples. In this chapter, I highlight two such programs on which I worked to explore field Y-dwarf multiplicity.

## 3.2 The Case of WISE J182831.08+265037.8

### 3.2.1 Abstract

The Y-dwarf WISE 1828+2650 is one of the coldest known Brown Dwarfs with an effective temperature of ~300 K. Located at a distance of just 10 pc, previous model-based estimates suggest WISE1828+2650 has a mass of ~5-10 $M_J$, making it a valuable laboratory for understanding the formation, evolution and physical characteristics of gas giant planets. However, previous photometry and spectroscopy have presented a puzzle with the near-impossibility of simultaneously fitting both the short (0.9-2.0 $\mu$m) and long wavelength (3-5 $\mu$m) data. A potential solution to this

Table 3.1: JWST NIRCam Observing Parameters (PID:#1189)

| Instrument | Filter Pair | Readout | Groups/Int | Ints/Exp | Dithers | Total Time (sec) |
|---|---|---|---|---|---|---|
| NIRCam | F115W & F335M ($CH_4$) | MEDIUM | 4 | 10 | 4 | 1632 |
| NIRCam | F140M ($H_2O$, $CH_4$) & F360M | MEDIUM | 4 | 10 | 4 | 1632 |
| NIRCam | F162M (ref for F140M) & F470N ($H_2$) | MEDIUM | 4 | 10 | 4 | 1632 |

problem has been the suggestion that WISE 1828+2650 is a binary system whose composite spectrum might provide a better match to the data. Alternatively, new models being developed to fit JWST/NIRSpec and MIRI spectroscopy might provide new insights. This article describes JWST/NIRCam observations of WISE 1828+2650 in 6 filters to address the binarity question and to provide new photometry to be used in model fitting. We also report Adaptive Optics imaging with the Keck 10 m telescope. *We find no evidence for multiplicity for a companion beyond 0.5 au with either JWST or Keck.*

### 3.2.2 Introduction

The WISE mission (Wright et al., 2010a) identified cool brown dwarfs (BDs) using their very red ([3.4]–[4.6] or hereafter W1-W2) colors (Kirkpatrick et al., 2011). The most extreme of these objects, with effective temperatures $T_{\rm eff}$ <500 K, have been typed as Y dwarfs (Cushing et al., 2011; Kirkpatrick et al., 2012). With W1-W2>4.2 mag, WISEP J182831.08+265037.8 (hereafter WISE 1828+2650) was identified as one of the reddest of this small group of only two dozen Y dwarfs. Follow-up photometry and spectroscopy with the Hubble Space Telescope (HST), the Spitzer Space Telescope, and various ground-based facilities found weak emission between 1.0-1.7 $\mu$m marked by absorption due to $H_2O$, $CH_4$ and $NH_3$ (Cushing et al., 2011), extremely weak emission in the $K$ band (2.2 $\mu$m), followed by a sharp rise out to 5 $\mu$m.

Astrometry from Keck, Spitzer and HST determined distances to the WISE Y dwarf sample ranging from 5-15 pc (Beichman et al., 2013; Martin et al., 2018; Kirkpatrick et al., 2019). With distances serving to constrain the absolute luminosity and typical ages of 3-10 Gyr inferred from their transverse motions, it was possible to fit the photometry and spectroscopy to evolutionary models to estimate masses from 5-10 $M_{\rm J}$. Beichman et al. (2014) and Kirkpatrick et al. (2019) put WISE 1828+2650 at a distance of of 9.93±0.23 pc and suggested an effective temperature of 400K and a mass around 5 $M_{\rm J}$.

WISE 1828+2650 has proven to be exceptional even within the unusual class of Y dwarfs. Its extreme W1-W2 color, the difficulty in simultaneously fitting models to the 1-2 and 3-5 $\mu$m photometry, and WISE 1828+2650's position at least 1 mag above the Y/T dwarf locus in the H-W2 color-magnitude diagram (Kirkpatrick et al., 2019, Figure 8) highlighted the challenges of

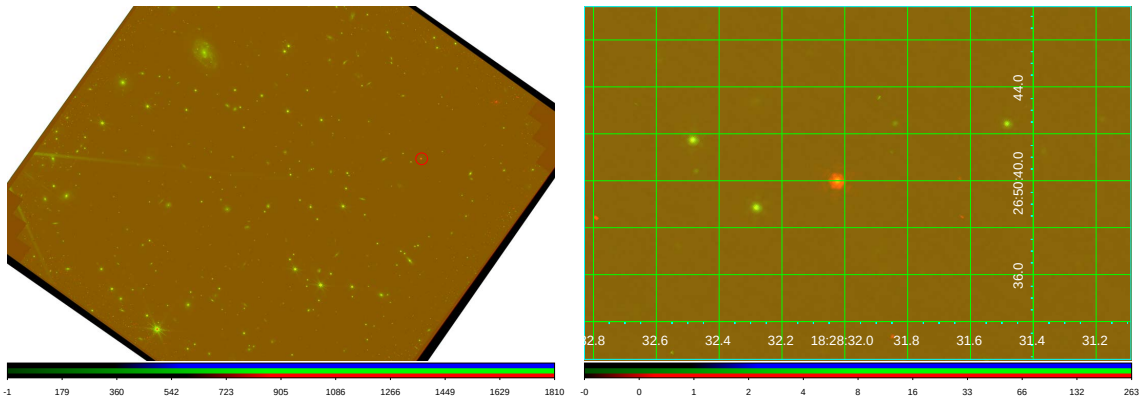


Figure 3.1: left) A color-composite image of 3 NIRCam filters, F162M, F335M and F470N showing one extremely red object at the expected position of WISE 1828+2650. right) a zoom-in on the position of WISE 1828+2650. Colorbar in MJy/sr.

making satisfactory models for such cold objects. Leggett et al. (2013, 2017) suggested that WISE 1828+2650 might be a binary system which would account for at least 0.75 mag of its separation from the Y/T locus. Most recently, Cushing et al. (2021) used 0.7-1.7 $\mu$m HST spectroscopy and a new generation of models (Marley et al., 2021a, the Sonora Bobcat models) to bolster the idea that WISE 1828+2650 is an unresolved binary consisting of roughly equal mass objects with $T_{\rm eff}$~275-350 K. However, there remain challenges with the model ages (<1 Gyr for a single object) and the subsolar values of [M/H] $\sim -0.5$ and [C/O] $\sim -0.6$ required to fit the existing data (Cushing et al., 2021).

With the expectation that JWST would help resolve these theoretical difficulties, we set out a program of imaging and spectroscopy, particularly in the key 3-10 $\mu$m region. The JWST NIRCam imaging data permit a search for faint companions at separations and sensitivity levels not previously possible as well as anchoring the fluxes of the higher-spectral resolution NIRSpec data. The spectroscopy provides critical diagnostics of physical conditions, composition, the presence or absence of clouds, and surface gravity in the 3-5 $\mu$m region where Y dwarfs emit most of their energy.

This section describes NIRCam imaging in six filters spanning 1-5 $\mu$m undertaken by the NIRCam Guaranteed Time Observation (GTO) team under PID#1189. Companion studies will give results from NIRSpec and MIRI spectroscopy, and from a deep NIRISS search for a close companion. Section 3.2.3 describes the observations and Section 3.2.4 the data reduction procedures and results. Section 3.2.5 addresses the search for and limits to the presence of a close companion to WISE 1828+2650 while Section 3.2.6 presents fits to the spectral energy distribution of WISE 1828+2650 and estimates of derived physical parameters. The section ends with a search for wide field companions (Section 3.2.7) and concluding remarks.

Table 3.2: NIRCam Photometry. [1] First quoted uncertainty reflects only photometric accuracy based on aperture photometry. Values in parenthesis include an average 10% calibration uncertainty at all wavelengths estimated from the average of successive iterations of the calibration values (PHOTMJYSR and PIXAR_SR) available at MAST. The values listed here use image files created on 2022-11-11 using calibration software version 11.16.14 and photometric reference data from jwst_nircam_photom_0114.fits. Values below the solid line come from ground and space missions as given in (Martin et al., 2018; Liu et al., 2016; Kirkpatrick et al., 2019, 2021). [2]Observation obtained using the NIRISS instrument.

| Filter | $F_\nu$ ($\mu$Jy)[1] | Magnitude |
|---|---|---|
| F090W | 0.078±0.005(0.015) | 26.16±0.20 |
| F115W | 0.311±0.005(0.03) | 24.39±0.10 |
| F162M | 1.29±0.009(0.13) | 22.25±0.10 |
| F335M | 2.41±0.013(0.24) | 20.23±0.10 |
| F360M | 34.2±0.05(3.4) | 17.19±0.10 |
| F470N | 340.4±0.62(34) | 14.16±0.10 |
| F480M[2] | 326±0.14(32) | 14.21±0.10 |
| J (1.25 $\mu$m) | 0.65±0.23 | 23.48±0.23 |
| H (1.65 $\mu$m) | 0.83±0.21 | 22.73±0.13 |
| K (2.16 $\mu$m) | 0.27±0.08 | 23.48±0.36 |
| Spitzer/IRAC (3.55 $\mu$m) | 48.1±1.0 | 16.92±0.02 |
| Spitzer/IRAC (4.55 $\mu$m) | 335.5±6.71 | 14.32±0.02 |
| WISE W2 (4.62 $\mu$m) | 310±14 | 14.35±0.05 |

### 3.2.3 Observations and Data Reduction

Table 3.1 describes the observing parameters for this program, using the long and short wavelength modules of NIRCam to observe WISE 1828+2650 simultaneously in a combination of narrow, medium and wide filters between 0.9 and 4.7 $\mu$m. Data were obtained on 2022-07-28 UTC. The NIRISS full frame imager was used to obtain a long exposure in the F480M filter in a deep search for a close companion. The NIRISS results will be presented separately, but the photometry at that wavelength is presented here for comparison with models. NIRSpec and MIRI spectroscopy were also obtained at this time and are discussed separately.

NIRCam images in the six wavelength bands and the single NIRISS band were downloaded from the Mikulski Archive for Space Telescopes (MAST) at the Space Telescope Science Institute, specifically the "...i2d.fits" files which are the result of mosaicing the four dither positions obtained at each wavelength. The specific observations analyzed can be accessed via DOI [1]. Figure 3.1 shows a three- color, full-frame NIRCam image of the field around WISE 1828+2650 and is composed of images obtained at F162M (blue), F335M (green) and F470M (red) with a close-up around the position of WISE 1828+2650. Only one object in the frame appears with the highly red color characteristic of a cool Y dwarf.

[1] https://archive.stsci.edu/doi/resolve/resolve.html?doi=10.17909/jxva-9x26

### 3.2.4 Analysis

#### 3.2.4.1 Photometry

Table 3.2 shows the results of standard aperture photometry using the astropy/photutils package (Astropy Collaboration et al., 2013, 2018, 2022; Bradley et al., 2020) with the image files created on 2022-11-11 and the calibration software version 11.16.14 with photometric reference data from jwst_nircam_photom_0114.fits. We selected an aperture size corresponding to 70% encircled energy and the appropriate aperture correction from the CRDS database[2]. The F090W filter was the weakest detection with the total flux dependent on the selected aperture due to the poorly defined Point Spread Function. For small apertures with encircled energy < 50%, the flux estimates in F090W were variable at the 20-30% level. Beyond encircled energy of 50%, the flux estimates were consistent at the 10% level, shown in the total uncertainty in Table 3.2. We adopted a large radius of 9.25 pixels encircling 85% of the total energy for the F090W filter. We also obtained photometry using the NIRISS imager in full frame mode (Willott et al., 2022) using the same procedure as described above.

Figure 3.2 shows the JWST results along with previous data from Spitzer, WISE, HST and Keck (Kirkpatrick et al., 2011; Leggett et al., 2015; Kirkpatrick et al., 2019; Cushing et al., 2021). WISE 1828+2650 is detected at high signal-to-noise (SNR) in all filters with statistical uncertainties of just a few percent. However, we adopt a higher level of uncertainty for the absolute calibration in the model fitting. Successive MAST releases of these data from August-November 2022 have shown significant variations in the absolute calibration of the NIRCam filters used here. We adopt a uniform 10% uncertainty for the absolute photometric calibration in all filters.

We note the consistency between the JWST data and previous observations although different passbands can be expected to yield significant differences given the highly structured nature of the SED of cool BDs. The close agreement between multiple facilities at the wavelengths of peak emission around 4-5 $\mu$m is consistent with the general lack of variability in the brightness of WISE 1828+2650. Brooks et al. (in preparation) investigated the variability of several hundred cold BDs observed in the Kirkpatrick et al. (2021) astrometric program using Spitzer. For WISE 1828+2650 they found a limit of 3% ($3\sigma$) to the variability in IRAC Ch2 ([4.5]) in 28 observations spanning almost 8 years. A model fit based on the cloudless Sonora-Bobcat models (Marley et al., 2021a) is also plotted and will be discussed in Section 3.2.6.

#### 3.2.4.2 Astrometry

As described in (Kirkpatrick et al., 2019),WISE 1828+2650 has a high proper motion (~1 arcsec/yr), mostly in right ascension, and a parallax corresponding to a distance of 9.93±0.23 pc. The

[2]https://jwst-crds.stsci.edu/

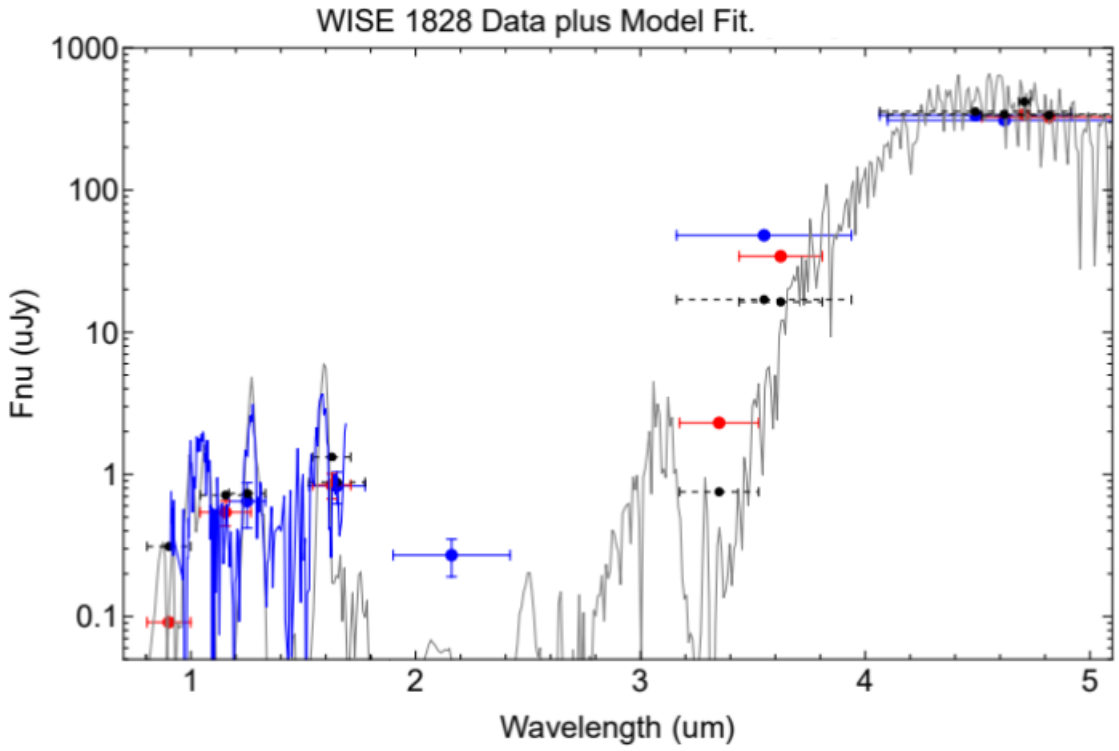


Figure 3.2: The figure shows a combination of the new JWST photometry (large red circles), previous ground- based and space-based observations (large blue circles) (Kirkpatrick et al., 2011; Leggett et al., 2015; Kirkpatrick et al., 2019), and in the 1-2 $\mu$m region the HST spectrum (Cushing et al., 2021, thin blue line). Horizontal bars denote the widths of the various filters. As discussed further in Section 3.2.6, we also plot as a thin grey line a cloudless Sonora (Bobcat) spectrum smoothed to R$\sim$3000 for the best fitting, binary object solution (Table 3.4). The black circles with dashed lines denote predicted fluxes as integrated over the relevant passbands for each filter (Marley et al., 2021a).

values listed in Table 3.3 were used to establish the pointing of the NIRCam, NIRSpec and MIRI observations in this program.

The F360M image was used to obtain the position of WISE 1828+2650. The high signal to noise ratio in this filter would imply a nominal positional accuracy of FWHM/(2×SNR) < 5 milli-arcseconds (mas) where FWHM is the Full Width at Half Maximum of the Point Spread function. We calculated both center-of-mass and 2-D Gaussian fits to obtain the image centroid which yielded nominal accuracy of <0.1 pixel or <6 mas. Information in the FITS header was used to convert the pixel location into celestial coordinates (J2000, 2022.5699) as given in Table 3.3[3]

A comparison of the NIRCam positions of 31 unsaturated, proper-motion corrected Gaia stars (20 mag > Gmag >14 mag) across the 4arcmin×4arcmin field showed a small offset of order the measurement uncertainty with dispersion of $(\Delta\alpha, \Delta\delta)$= 10±10, 7±6) mas, demonstrating that the reference frame is accurate to ∼5-10 mas. However, Figure 3.3 shows that there remains some coherent distortions across the field of view.

The predicted position of WISE 1828+2650 was calculated at the JWST epoch incorporating stellar parallax (Smart and Green, 1977) using the rectangular coordinates of JWST's location in the solar system as given in the FITS header (reversed to give the coordinates of the Sun). The uncertainty in the F360M position is the combination of the centroid uncertainty and the uncertainty in the reference frame derived from the Gaia stars, ±2 mas, for a combined uncertainty of ±4.4 mas. The difference in the predicted vs observed positions is within the uncertainties derived from a Monte Carlo run in which the Kirkpatrick et al. (2021) values were varied according to their quoted uncertainties. The Monte Carlo distribution yielded uncertainties at the JWST epoch of 6.4 mas in right ascension and declination. The Predicted-JWST position difference is consistent with the existing parallax and proper motion values for WISE 1828+2650.

### 3.2.5 Search for Close Companions

#### 3.2.5.1 Near-IR Observations

Previous observations with Keck and HST revealed no evidence for multiplicity at the level of 0.1" (Beichman et al., 2013), corresponding to orbital separations of >1 au for equal brightness components. However, the Keck observations were done with the 40 mas/pixel wide-field camera mode with a typical resolution of ∼ 0.16". New Keck observations were obtained 2022-Sep-08 UT with NIRC2 behind the laser guide star adaptive optics system (Wizinowich et al., 2000) in the narrow-field camera mode with a pixel scale of 0.009942".

Observations of WISE 1828+2650 were made in the $H$ filter ($\lambda_o = 1.633; \Delta\lambda = 0.296\ \mu$m) with an integration time of 300 seconds per frame in a standard 3-point dither pattern that is used with

[3]The astrometric distortion correction in the MAST processing used the file crds://jwst_nircam_distortion_0158.asdf

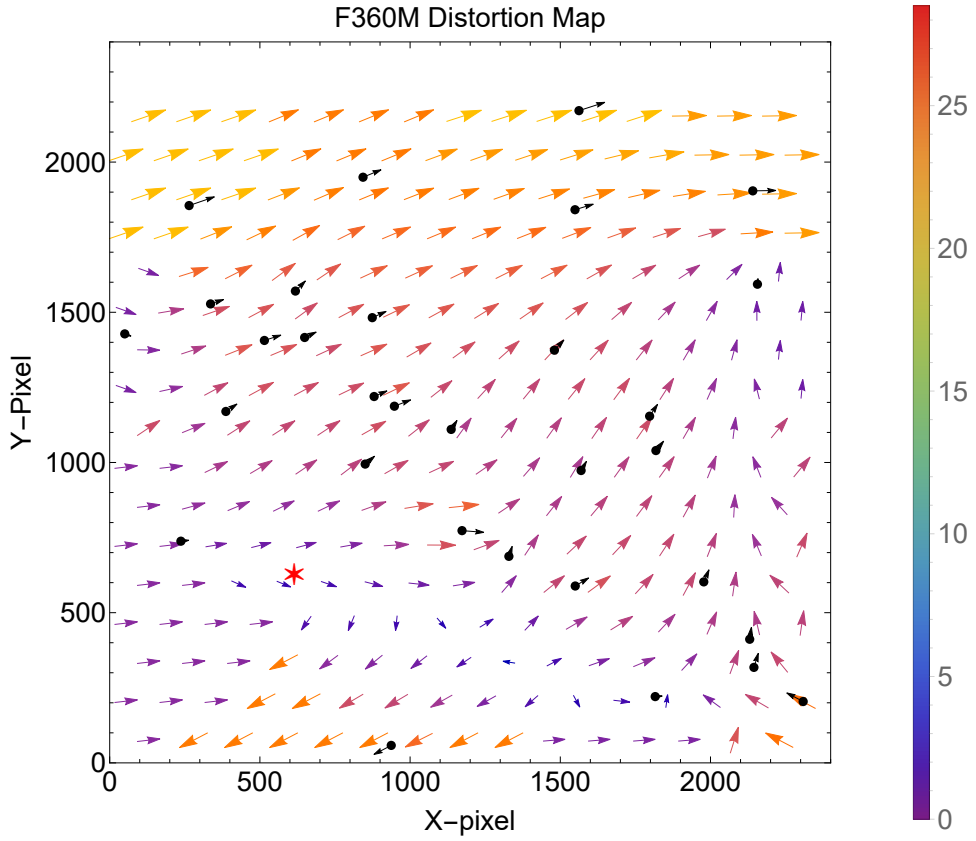


Figure 3.3: Differences in the positions of 31 Gaia DR3 stars (selected for negligible parallactic motions and corrected for proper motion) relative to the positions observed by JWST in F360M. Individual Gaia stars are shown as black symbols with the arrow showing the difference in pixels (63 mas), scaled by a factor of 200 for visibility. The position of WISE 1828+2650 is shown as a red star. The colors in the image and the color bar encode the magnitude of deviation in mas. The maximum Gaia-JWST difference is 27 mas with an average of 10 mas and dispersion of 10 mas.

Table 3.3: NIRCam Astrometry of WISE 1828

| Observatory | Epoch (MJD) | RA RA (Equinox=J2000) | Dec (Equinox=J2000) | Parallax (mas) | $\mu_{RA}$ (mas/yr) | $\mu_{DEC}$ (mas/yr) |
|---|---|---|---|---|---|---|
| Spitzer[1] | 57094.09 | 277.131096 (±2 mas)<br>18h28m31.463s | 26.844069(±2 mas)<br>+26°50'38.65" | 100.3±2 | 1016.5±0.8 | 169.3±0.8 |
| JWST (predicted) | 59788.5143 | 277.1334156 (±6 mas)<br>18h28m32.020s | 26.8444348 (±6 mas)<br>+26°50'39.965" | | | |
| JWST (F360M) | 59788.5143 | 277.1334164 (±10 mas)<br>18h28m32.020s | 26.8444334 (±10 mas)<br>+26°50'39.960" | | | |
| ΔSpitzer-JWST(pred) | | −7.45" | −1.32" | | | |
| ΔJWST (Pred-Obs) | | 2.5±12 mas | -5.1±8.2 mas | | | |
| Gaia-JWST differences[3] (mas) | | 10.4±10.2 (1.8) | 6.8±5.1 (0.9) | | | |

NOTE— [1]Kirkpatrick et al. (2019). [2]Absolute astrometric accuracy estimated by measurements of nearby Gaia stars. [3] Difference in positions between 31 proper-motion corrected Gaia stars and their JWST values. The value in parenthesis is $\sigma\_mean$ for the sample and represents an estimate of the overall precision of reference frame.

NIRC2 to avoid the noisier lower-left quadrant. The transparency and seeing during the night was highly variable and not all frames detected the BD. A total of 12 frames at 300 seconds each were acquired yielding a total on-source integration time of 3600 seconds.

The science frames were flat-fielded and sky-subtracted. The flat fields were generated from a median average of dark subtracted flats taken on-sky. The flats were normalized such that the median value of the flats is unity. The sky frames were generated from the median average of the dithered science frames; each science image was then sky-subtracted and flat-fielded. The reduced science frames were combined into a single combined image using a intra-pixel interpolation that conserves flux, shifts the individual dithered frames by the appropriate fractional pixels, and median-coadds the frames. The final resolutions of the combined dithers was determined from the full-width half-maximum of the point spread functions: 7.1 pixels = 0.071".

The sensitivity of the final combined AO image was determined by injecting simulated sources azimuthally around the primary target every 20° at separations of integer multiples of the central source's FWHM. The brightness of each injected source was scaled until standard aperture photometry detected it with $5\sigma$ significance. The resulting brightness of the injected sources relative to WISE 1828+2650 set the contrast limits at that injection location. The final $5\sigma$ limit at each separation was determined from the average of all of the determined limits at that separation, and the uncertainty on the limit was set by the rms dispersion of the azimuthal slices at a given radial distance. The Keck data have a sensitivity close-in of $\Delta H \approx 1.5$ mag at 0.071"; the final sensitivity curve for the Keck image is shown in (Figure 3.4). No close-in stellar companions were detected and the FWHM of the WISE 1828+2650 is consistent with the brighter nearby star to the southeast (Gaia DR3 4585337218702066560). WISE 1828+2650 is $\Delta H = 3.4 \pm 0.2$ mag fainter than Gaia DR3 4585337218702066560.

The $H$-band magnitude of WISE 1828+2650 as measured by the Keck data is $H = 22.9 \pm 0.2$

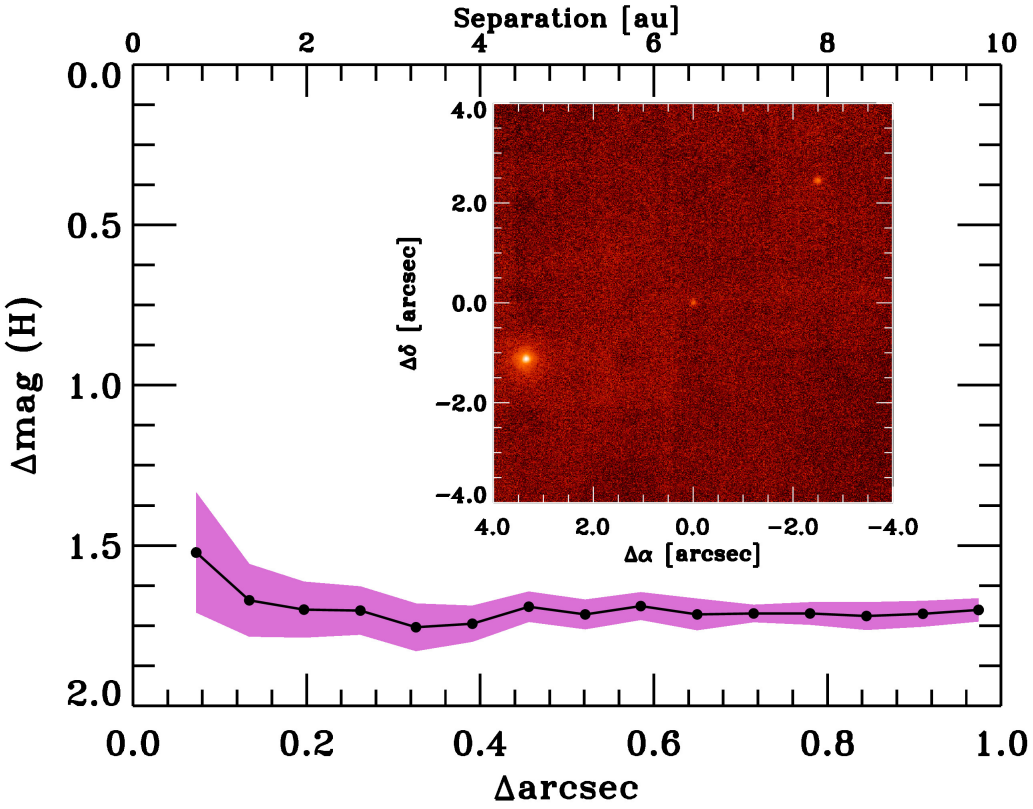


Figure 3.4: Keck NIR AO imaging and sensitivity curve for WISE 1828+2650 taken in the *H* filter. We can recover a companion at a contrast of $\sim$ 1.5 magnitudes relative to the BD at separations greater than 0.071". *Inset:* Image of the central portion of the NIRC2 image.

mag. Using the JWST F162M filter as a proxy for the H-band filter, this measurement is consistent with the infrared photometry determined directly from the JWST images (see Table 3.2).

#### 3.2.5.2 NIRCam Observations

Although the aperture of JWST is smaller than that of Keck, JWST offers a highly stable point spread function (PSF) and much greater sensitivity at wavelengths where cold BDs are brightest. For the JWST data reported here, the best combination of spatial resolution and SNR in the JWST data comes in the F360M filter. A simple Gaussian fit of the image of WISE 1828+2650 compared to fits of two nearby stars shows no evidence for extent: FWHM(WISE 1828+2650)= 0.150±0.001" compared with 0.153 ± 0.001" and 0.150 ± 0.001" for the two stars.

We explored the data further by constructing realistic models of the PSF and searching for a potential companion at all separations within 0.25". Anderson and King (2000) and Anderson (2016) developed a novel technique applicable to multiple instruments on HST where they construct an "effective" PSF (ePSF) from bright single stars within a given image. The ePSF is intended to describe the contemporaneous realization of the theoretical PSF on the detector pixels given the wavefront during the observation. They build the ePSF first by identifying a sample of many bright stars in the image that appear to be singles and without contamination from cosmic rays or other stars. These stars are all centered at various positions within their peak pixel, giving many samplings of the distribution of flux of the center of the PSF. The initial ePSF is then generated by interpolating each PSF by the factor of user-defined oversampling, and taking the median. Then, an iterative process begins, comparing the ePSF to all stars in the sample, evaluating the median residual, and adding that on to the ePSF model. For our case, we generated an ePSF model 4x oversampled, as recommended in Anderson (2016), after 20 iterations of the ePSF calculation, over 9x9 detector pixels. This analysis was performed using publicly available PSF building tools from the python package photutils (Bradley et al., 2020).

We chose the F360M data to perform this analysis as the number of bright sources in the F470N data was small which limits the production of a reasonable ePSF model. Also, the diffraction limit in F470N is 30% larger than in F360M, limiting the sensitivity to close companions. We also avoid the F335M filter due to the low signal to noise of WISE 1828+2650. Of the four pointings, two had reliable data for WISE 1828+2650 without nearby cosmic rays or bad pixels contaminating its flux. Within each integration, we constructed a separate ePSF model from 57 and 63 separate stars (integration number 2 and 4, respectively), excluding WISE 1828+2650 from the sample.

We then made a double-PSF fitting code that takes a cutout array of the data as input (here a 9x9 pixel array centered around WISE 1828+2650) and then fits the best-fit binary model using the ePSF, an approach similarly implemented on HST, see Section 2. We use the python module PyMultiNest (Buchner et al., 2014a) that performs the Nested Sampling Monte Carlo analysis

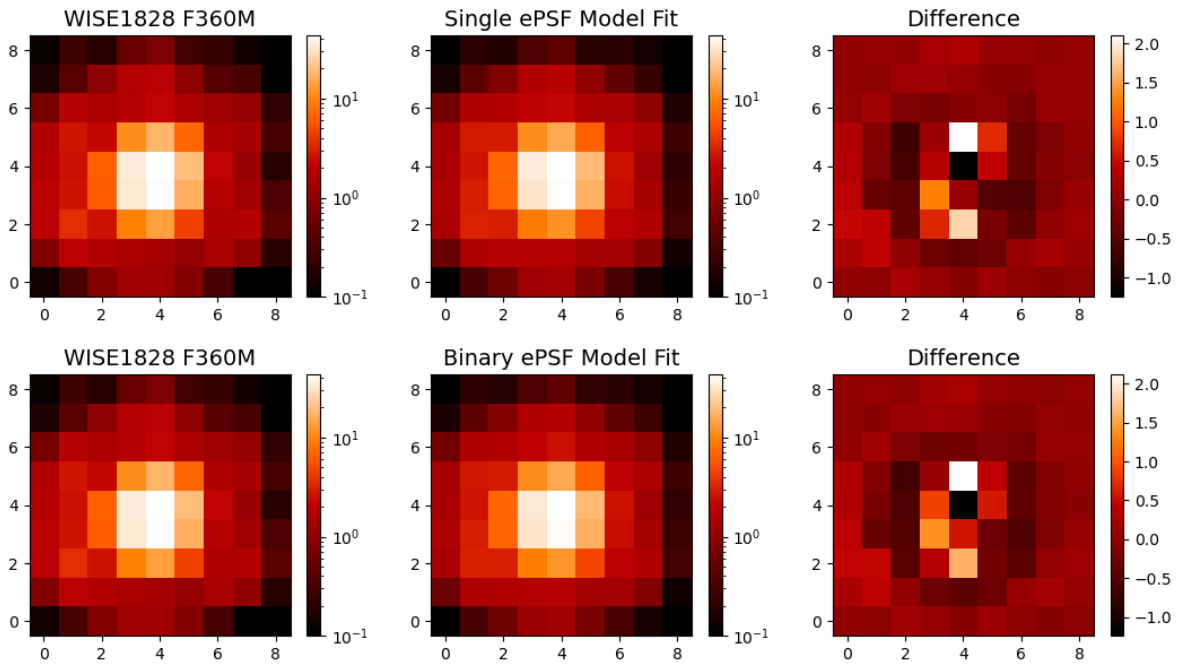


Figure 3.5: Top row: WISE 1828+2650 cutout in F360M filter on the left, ePSF single model in center, and residuals on the right. Bottom row: WISE 1828+2650 cutout in F360M filter on the left, ePSF binary model in center, and residuals on the right. Units are in DN/s and the axes are in detector pixels (0.063”/pixel). We used the level 2 pipeline product *cal.fits files to perform this analysis.

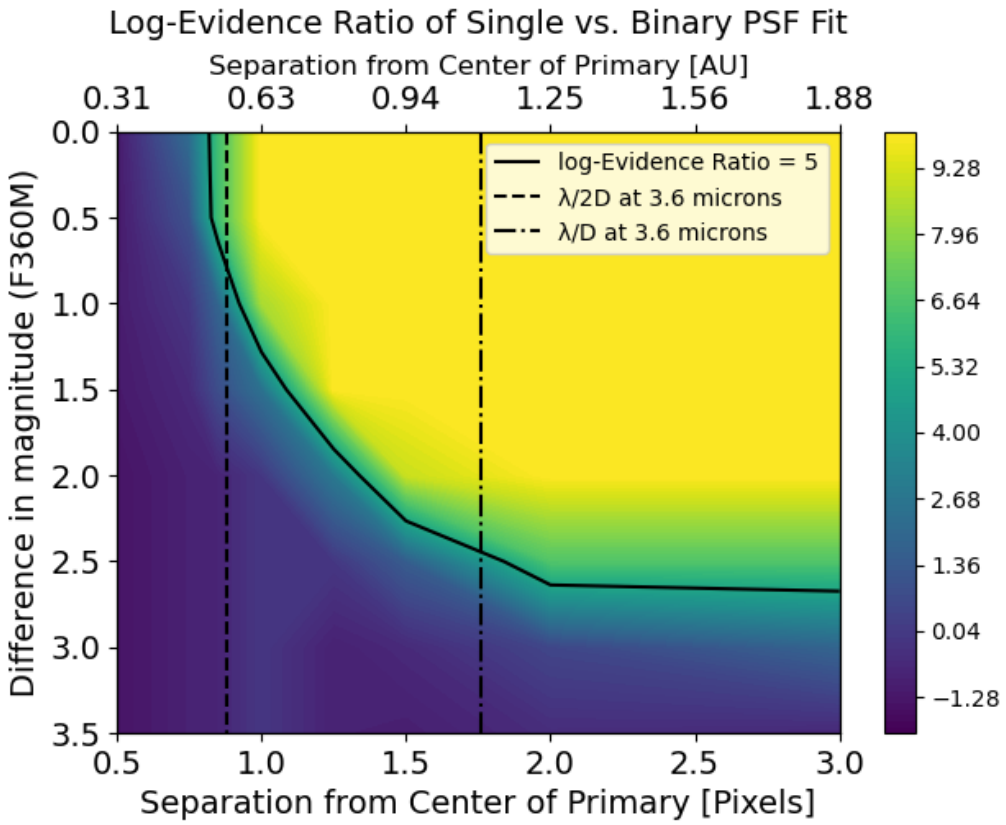


Figure 3.6: Shown is the difference in log-evidence between the binary-PSF model and single-PSF model performed on artificial binaries, made from the ePSF models. The threshold for strong evidence of the binary model fit over the single model fit is shown with a solid line (corresponding to a difference of 5). The diffraction limit and half the diffraction limit at 3.6 microns are shown for comparison as the vertical dash-dotted and dashed lines, respectively.

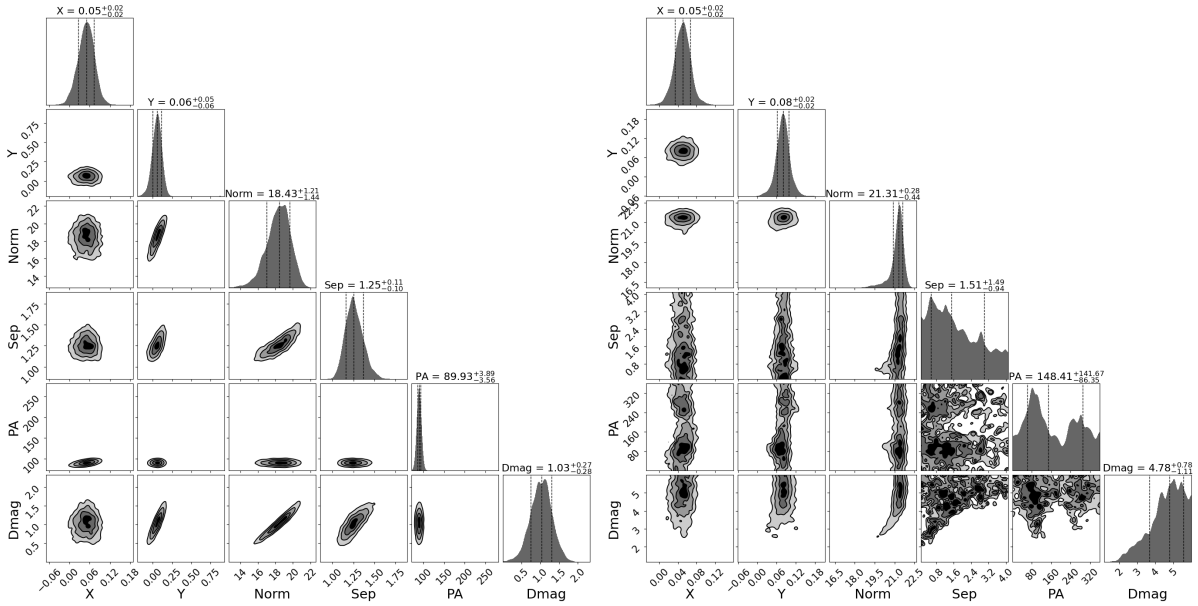


Figure 3.7: Binary model parameters from the recovery of a companion injected at 1.25 pixels in separation (Sep), a position angle (PA) of 90 degrees, and a contrast (Dmag) of 1.0 (left) and 3.5 (right) mag relative to the primary. These artificial binaries were constructed from empirical PSFs of NIRCam in the F360M filter. X and Y are the central pixel coordinates of the primary and Norm is the flux normalization of the primary.

using MultiNest (Feroz et al., 2009a) to derive the best-fit binary ePSF model to the data, by maximizing our chi-sqaured likelihood statistic. Our model consists of six parameters: x and y center of the primary, flux normalization of the primary, separation between the centers of the primary and secondary, the position angle of the center of the secondary relative to the primary, and the difference in magnitude between the secondary and primary. We define flat priors with -1.5 $\leq x_{cen} \leq$ 1.5, -1.5 $\leq y_{cen} \leq$ 1.5, 0.0 < flux normalization < 40.0, 0.01 $\leq$ separation $\leq$ 4.0 pixels, 0.0 $\leq$ position angle < 360.0, and 0.01 $\leq$ difference in magnitude $\leq$ 6.0 mag.

To both images of WISE 1828+2650 in F360M in question, the code converges to the edge of the prior in separation (4 pixels) and approaching that in difference in magnitude (5.6 and 5.8 mags in each), i.e. fitting to background noise. If instead we force the code to fit within the core of the PSF (0.01 $\leq$ separation $\leq$ 2.0 pixels) and exclude wide separations, the best fit converges to $0.14^{+0.04}_{-0.03}$ pixels in separation and $\Delta$mag=$2.44^{+0.34}_{-0.36}$ in Frame #2, and $0.28^{+0.13}_{-0.06}$ pixels in separation and $\Delta$mag=$3.06^{+0.74}_{-0.68}$ in Frame #4 (errors are 68% confidence interval). See Figure 3.5 for the comparison of our binary PSF model to the data.

However, our binary PSF-fitting code will always find a best fit binary solution regardless of whether a true binary is present. If the object in question is a single point source, the code will either fit a companion to the brightest residuals in the background (e.g. the 4 pixels in separation

and Δmag ~ 5.5-6 mag initial fit) or to the residuals in the core of the source as models are photon-noise limited and have uncertainties (e.g. the resulting best fit when forced to fit a companion at separations < 2 pixels).

In order to determine whether we can recover a companion with these values, we constructed many artificial binaries from the ePSF models at various separations and differences in magnitude with the same signal to noise as our F360M data. Then, we ran our double-PSF fitting code and a modified version that just fits a single PSF (3 variables: $x_{cen}$, $y_{cen}$, and flux normalization) on those same artificial binaries. PyMultiNest also calculates the evidence of the model in question by taking the integral of the likelihood times the prior over all parameters which allows us to test different models and determine which model is preferred given the data.

Trotta (2008b) define a difference in the log-evidence between two models of 5 as being strong evidence for one model over another (with a probability of 0.993 that the higher evidence model is preferred). For a given companion at some separation and difference in magnitude, we compare the log-evidence of the binary-PSF model to that of the single-PSF model.

In Figure 3.6, we show the log-evidence difference between the binary and single ePSF model fits based on separation and difference in magnitude of our artificial binaries. We define our sensitivity as the point where the difference in log-evidence between the binary and single PSF models equals 5. With our binary fitting tool and ePSF models, we can resolve companions down to ~ 0.8 F360M pixels (0.05") in separation for an equal brightness companion and are sensitive to companions at Δmag=2.5 beyond 2 F360M pixels (0.126"). See Figure 3.7 for the posteriors for a fit to a binary at 1.25 pixels in separation and Δmag=1.0 and 3.5 . For the Δmag=3.5 companion, the parameters (separation, position angle, and difference in magnitude) are unconstrained.

In addition, we fit a single PSF model to the WISE 1828+2650 data set. The difference in log-evidence between the single and binary PSF models is 3.5, less than the threshold for a detection. In Fig. 3.5, we show both the single and binary PSF models compared to the data, demonstrating how the binary fit does not significantly improve the residuals. *Therefore, we are confident that the best-fit binary model solution to WISE 1828+2650 in the F360M filter is not a true detection of a companion, and that we can rule out an equal mass companion beyond 0.5 au and a Δmag=2.5 companion beyond 1.25 au.* Fainter companions at larger separations can also be ruled out although these would not help resolve the problem of excess brightness of WISE 1828+2650 relative to model predictions. Such models generally require an equal mass system as discussed below (Section 3.2.6).

The incidence of binarity among BDs is generally low, 10%-30%, compared with higher mass stars (Burgasser et al., 2007; Raghavan et al., 2010). While less is known about the multiplicity of the coldest T/Y BDs, there is evidence that the incidence of binarity may be even lower than for warmer BDs, with Opitz et al. (2016) failing to find any companions in the range of 0.5-2 au among

the five Y dwarfs they examined with AO imaging. Similarly, Fontanive et al. (2018) estimated a companion frequency < 10% for T-Y dwarfs with separations tightly peaked at 3 au, e.g. Luhman 16 AB (Luhman, 2013). However, it should be noted that separations ≤ 3 au are not well explored. If indeed WISE 1828+2650 is a binary as inferred from the spectral modeling presented by Cushing et al. (2021), then high resolution JWST NIRSpec spectra may reveal a double lined system, given an appropriate orbital plane inclination. Furthermore, two 5-10 $M_J$ objects orbiting at 0.5 au would have a period of 3-5 years and a typical orbital velocity of ~5 km/s which might be discernible in multiple epochs of high SNR spectra to yield masses for the two objects.

### 3.2.6 The Spectral Energy Distribution and Model Fits

The broad wavelength coverage of JWST NIRCam photometry from 1 to 5μm is ideal for characterizing the spectral energy distribution (SED) and inferring the bulk atmospheric properties of BDs. We include thirteen ground- and space-based photometric points (i.e, Table 3.2) in our spectral energy distribution fitting. We considered a number of models for this comparison: Sonora Bobcat and Cholla (Marley et al., 2021a), ATMO (Phillips et al., 2020b) chemical-equilibrium (CEQ) models, ATMO chemical non-equilibrium models with strong vertical mixing (CNEQ-strong), and the Linder et al. (2019) models. We selected cloudless Sonora models[4,5] as the most up to date compared, e.g. with older COND models, or the recent Linder et al. (2019) models which are limited to low mass objects (<2 $M_J$). The Sonora Cholla models do not go to sufficiently low temperatures for this study and the ATMO 2020 models gave similar results but with higher reduced chi-squares than the Sonora Bobcat models.

We defer discussion of the new Leggett et al. (2021b) models to a companion study on the NIRSpec low and high resolution spectroscopy (Lew et al in preparation). Leggett et al. (2021b) noted that their new model failed to fit the total luminosity of WISE 1828+2650 as a single object and assumed an equal mass binary.

We used the Sonora model grid that comprises temperatures from 200 to 600 K, gravities from log(g) of 3.0 to 5.5 $ms^{-2}$, metallicities [M/H] from -0.5 to 0.5. The ATMO model grid assumes an atmosphere with solar metallicity and span a range of temperature from 100 K to 900 K and of gravity from $10^{2.5}$ $cms^{-2}$ to $10^{5.5}$ $cms^{-2}$. The ATMO chemical non-equilibrium models with strong vertical mixing assume an eddy diffusion coefficient of $10^6$ $cm^2s^{-1}$ at a gravity of $10^{4.5}$ $cms^{-2}$ and decreases with higher gravity (see Figure 1 in Phillips et al. 2020b). We linearly interpolated the models to construct a model spectra grid with a smaller spacing in temperature, gravity, and metallicity. We adopt a distance of 9.93 pc reported by Kirkpatrick et al. (2019).

[4]https://zenodo.org/record/1309035#.YwqSGbTMKUk
[5]https://zenodo.org/record/5063476#.YwqSTrTMKUk

In the model fitting process, we examined two cases: a single object or a binary with different temperatures. For the SED fitting, we performed the least-squares fit to the thirteen photometric points. For the binary case, we require the two objects to share the same age and metallicity. To enforce the equal-age constraints, we first calculate the age based on the free parameters temperature $T_1$ and gravity $g_1$ of one component of the binary using the Sonora evolution model. We then calculate the expected gravity $g_2$ of the second component based on the calculated age and sampled temperature $T_2$ of this object. Therefore, both components of the binary share the same age, where $g_2$ is thus a derived value based on $T_1, g_1, T_2$ and $M$. We calculate the chi-squared values of the binary models over the grid of temperature, gravity, metallicity, and radius of the binary components. We use the bootstrapping method to estimate the uncertainties of the fitted parameters. With the bootstrapping method, we randomly re-sample the thirteen photometric points for 10,000 times and refit the models to the resampled datapoints with the least squares method. We then calculate the 99.7 percentile range of the fitted parameters as the $3\sigma$ confidence ranges, as shown in Table 3.4.

In Table 3.4 and Figure 3.8, we show the best-fit parameters and display the corner plots associated with the fits to show the correlation between the parameters in our SED fitting. In the binary case, the chi-squared map suggests that the primary shares a similar temperature ($\Delta T$ <50K) to the secondary when both components have non-negligible radii ($R_1$ and $R_2 > 0$). We also calculate the combined radius, which is the square root of the sum of the two radii squared ($\sqrt{R_1^2 + R_2^2}$), for the binary case. The combined radius is moderately constrained, with a 99.7 percentile range of 1.15-2.83 $R_J$ and a median value of $1.67 R_J$, where the best-fit radius of the single model is $1.67 R_J$. Both the single and binary fits favor effective temperature of around 330K, low metallicity ([M/H = -0.5]), and low gravity ($\log(g) = 4$). However, the best fit models suggest that the single model requires a lower mass object ($2\,M_J$), while the binary model requires two higher mass objects ($\sim 4\,M_J$). Our single model has a lower reduced $\chi^2$ than the binary model, although both are too high to adequtely represent the data. We note that the best-fitted radius of 1.67 $R_J$ in the single BD case may be unphysically large, and that an equal-temperature binary may be preferred in this case, as suggested in previous studies of WISE 1828+2650 (e.g., Beichman et al., 2013; Leggett et al., 2013, 2017; Cushing et al., 2021; Leggett et al., 2021b)

A striking characteristic of the SED fits for both the single and binary cases is their predicted youth, with best-fit ages between 0.3-0.7 Gyr which is at odds with the likely dynamical age of WISE 1828+2650, although these young ages are not well constrained in our model. As previously noted (Beichman et al., 2014), WISE 1828+2650 is not associated with any known young cluster. This original conclusion is bolstered by application of the Banyan Σ tool[6] (Gagné et al., 2018) which puts the probability that WISE 1828+2650 is a field object at 99% independent of its as yet

[6]www.exoplanetes.umontreal.ca/banyan/banyansigma.php?

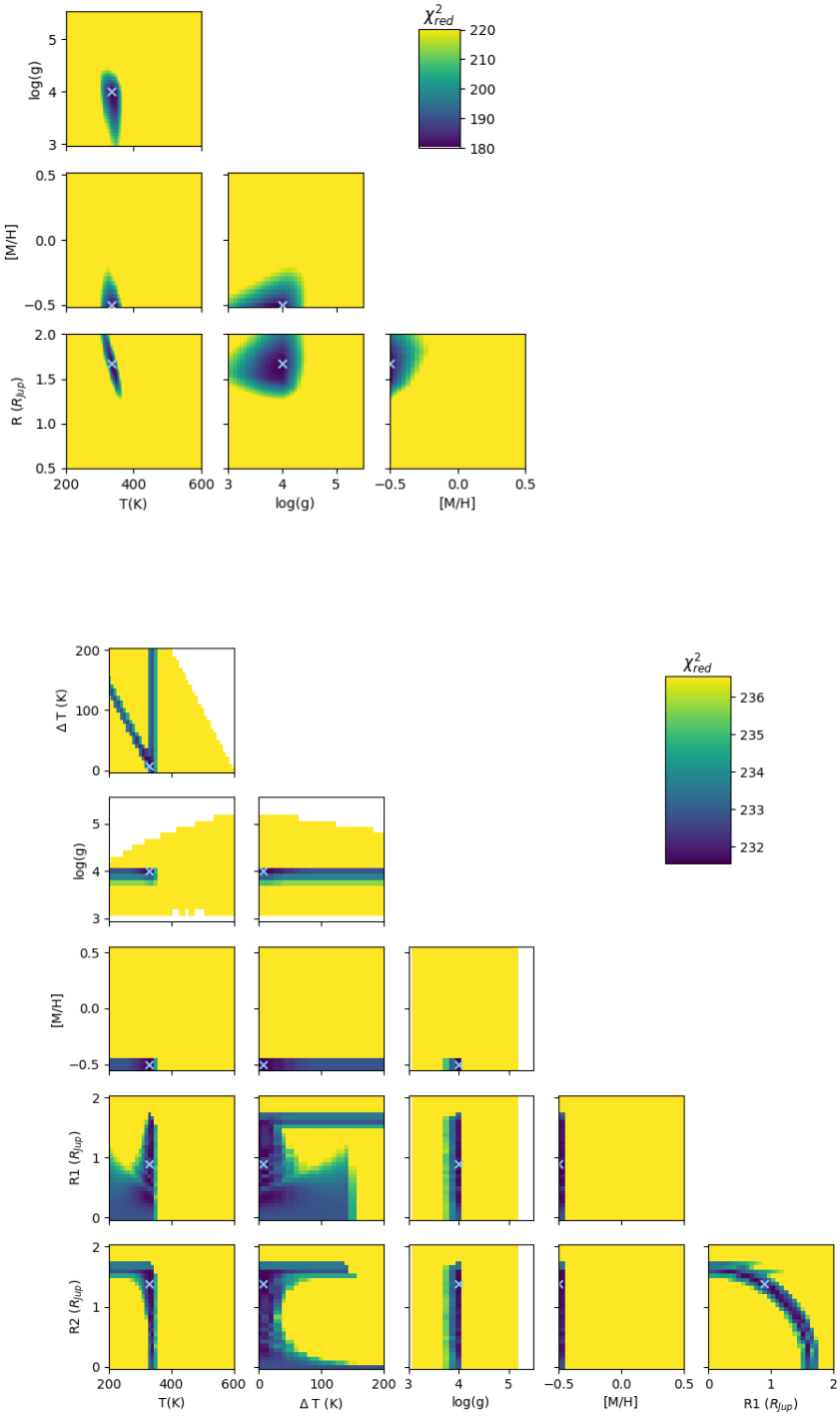


Figure 3.8: The $\chi^2_\nu$ maps of the photometry fitting results for both the single object case (top) and the binary case (bottom). Both models fitting results suggest WISE 1828+2650 has a temperature of around 330K, low metallicity, and low gravity. The blue crosses mark the location with the lowest $\chi^2_\nu$ that are listed in Table 3.4. The white regions are either outside of the considered temperature range (i.e., T + $\Delta T$ >600K) or incompatible with the Bobcat evolution model grid.

unknown radial velocity. We expect WISE 1828+2650 to have an age in the 2-4 Gyr range given its tangential velocity (Beichman et al., 2013), consistent with the mean age of 2.3 Gyr for a sample of BDs in the solar neighborhood (Dupuy and Liu, 2017), contrary to our modeling of the SED.

Based on the best-fit models, we extrapolate the flux density beyond the observed wavelength regions and estimate the bolometric luminosity. The estimated bolometric luminosity has $\log(L/L_{\odot})$ of around -6.5, as listed in Table 3.2. The bolometric luminosity of $\log(L/L_{\odot})$ = -6.5 is similar to the expected luminosity of a ~400K object at 1Gyr. Our calculations indicate that the JWST broadband photometry covers about 16% of the bolometric luminosity, while the composite photometry comprising JWST, 2MASS, WISE, and Spitzer photometry accounts for around 55% of the bolometric luminosity.

The discrepancy between models for cold BDs at long and short wavelengths is well known (Beichman et al., 2014) with models which fit well at long wavelengths failing to fit at short wavelengths and vice versa. This failure is prominent in our fits to the WISE 1828+2650 data, independent of metallicity or multiplicity. In all cases, the models, which fit reasonably at 4-5 $\mu$m, fail badly at 1 $\mu$m with the models being a factor of ~2 brighter than observed at 1 $\mu$m. Another striking feature is that both the F335M and F360M data points sit significantly above the predictions suggesting that the absorption in this part of the spectrum is less than expected. Further exploration of the possible temperature-pressure profile and atmospheric chemistry, such as those models in Leggett et al. (2021b), is essential to understand the atmospheric processes that drive the longstanding challenges in fitting the flux at near-IR and mid-IR wavelengths.

The SED fits to new JWST observations using two independent sets of models leave us in the uncomfortable position of either accepting a single object much younger than expected dynamically, or a near equal-mass binary system for which the NIRCam data finds no evidence at separations >0.5 au. Potentially the NIRSpec's high resolution spectroscopy will reveal a double-lined system which might resolve this problem. However, whether WISE 1828+2650 turns out to be a double, Figure 3.2 and the high $\chi^2$ values indicate significant deviations between the models and the emission of WISE 1828+2650.

At the fitted effective temperature of around 300K, it is possible that sulfide, chloride, and water clouds form near or within the photosphere and affect the emission spectra (e.g., Morley et al., 2012, 2014b,a). However, Cushing et al. (2021) SED fitting results with Morley et al. (2014b) cloud models at solar metallicity give a higher reduced chi square than that with Sonora bobcat cloudless models with subsolar metallicity. Further exploring cloudy models under various atmospheric chemistry and metallicity is essential to understand the role of clouds in shaping the SED of WISE 1828+2650. It is possible that the rotation rate and observed inclination of WISE 1828+2650 cause significant luminosity deviations from a typical BD of similar temperature. Deviations as high as 20% have been estimated in comparing pole-on vs. equator-on viewed BDs at

Table 3.4: Spectral Model Fits to Photometry

| | Primary | | | | Secondary | | | | | | | | |
|---|---|---|---|---|---|---|---|---|---|---|---|---|---|
| | $T_{eff}$ (K) | log g (cgs) | Mass ($M_J$) | Radius ($R_J$) | $T_{eff}$ (K) | log g (cgs) | Mass ($M_J$) | Radius ($R_J$) | Metallicity [M/H] | Age (Gyr) | $\chi^2_\nu$ | Degs. of Freedom | log ($L/L_\odot$) |
| Sonora Cloudless models | | | | | | | | | | | | | |
| best-fit single | 325 | 3.6 | 2 | 1.83 | | | | | -0.5* | 0.3 | 180 | 9 | -6.49± 0.03 |
| 99.7% CI | 309–405 | 3.0–5.5 | 0.6–13 | 1.1–2.0 | | | | | -0.5 | 0.01–7 | | | |
| best-fit binary | 337 | 4.0 | 4.4 | 1.38 | 330 | 4.0 | 4.1 | 0.90 | -0.5* | 0.7 | 231 | 7 | -6.49±0.04 |
| 99.7% CI | 316–413 | 3.0–4.8 | 0.6–20 | 0.4–2 | 268–395 | 3.5–4.8 | 0.6–20 | 0–2 | -0.5 | 0.03–10 | | | |
| ATMO Chemical Equilibrium models | | | | | | | | | | | | | |
| best-fit single | 300 | 4.0 | 3.7 | 2 | | | | | 0 (fixed) | 1.0 | 256 | 10 | -6.45± 0.06 |
| 99.7% CI | 287–359 | 3.0–5.1 | 0.5–13 | 2–2 | | | | | - | 0.02–8.5 | | | |
| best-fit binary | 300 | 3.6 | 1.5 | 1.9 | 300 | 3.6 | 1.7 | 1.4 | 0 (fixed) | 0.3 | 287 | 8 | -6.36±0.05 |
| 99.7% CI | 279–400 | 3.0–4.8 | 0.5–20 | 0.4–2 | 279–400 | 3.0–4.8 | 0.5–20 | 0–2 | - | 0.02–10 | | | |
| ATMO Chemical Non-equilibrium models with strong mixing | | | | | | | | | | | | | |
| best-fit single | 294 | 4.3 | 5.5 | 2.0 | | | | | 0 (fixed) | 2.4 | 303 | 10 | -6.46± 0.06 |
| 99.7% CI | 259–359 | 3.0–5.0 | 0.5–11 | 2.0–2.0 | | | | | - | 0.02–9.9 | | | |
| best-fit binary | 270 | 4.0 | 4.2 | 2 | 270 | 4.0 | 4.2 | 2 | 0 (fixed) | 2.1 | 320 | 8 | -6.38±0.09 |
| 99.7% CI | 253–340 | 3.0–4.6 | 0.5–13 | 2–2 | 253–340 | 3.0–4.6 | 0.5–13 | 2–2 | - | 0.03–9.9 | | | |

NOTE— [1] The fitted parameters and the corresponding 99.7% percentile ranges for the single and binary objects cases. The mass, radius, and the secondary object's gravity are derived from the fitted parameters using the Bobcat evolution models. *The fitted metallicity is at the lower bound of metallicity grid.

high rotation rates (Lipatov et al., 2022), but it is currently unknown if this effect occurs for WISE 1828+2650 . Important clues will come from the NIRSpec and MIRI spectroscopic observations spanning 1-12 $\mu$m at low and high resolution which are currently being analyzed.

### 3.2.7 A Search for Brown Dwarf Companions in the Field of View

The large field of view and great sensitivity of NIRCam are two of the instrument's great strengths. In addition to searching for a close companion we also looked for additional BD candidates which might or might not be associated with WISE 1828+2650. For example, Nonino et al. (2023) made a serendipitous discovery of a T dwarf ($T_{eff}$ ~600 K) at a distance of ~ 0.5 kpc in a deep survey field adjacent to Abell 2744.

We used the source catalogs provided by Level-3 processing from STScI for our 6 filters. We selected F360M unconfused point sources (the "is_extended" flag set to FALSE and the nearest neighbor distance ≥ 1") with SNR≥10. To avoid unreliable sources which appear at the edges of the field due to having less than the full coverage of 4 dither positions, we selected objects only within the central $2'x2'$ of the final F360M image. We selected sources in the other 5 filters (SNR≥5) in the same way and used the F360M objects as seeds for band merging using a radius of 0.2". We adopted the catalog values of aperture photometry based on 70% encircled value with pipeline-provided aperture correction. To enable a search for L,T and Y BDs we focused on filters optimized to find cold objects, requiring detections at F360M, F162M and F470N. Figure 3.9 shows 63 sources meeting these criteria. Sources around 0.5>[F360M]–[F470N]>0 and 0 < [F162M]–[F470N] < 2 mag are likely stars with spectral types as cool as M9 or galaxies (Pecaut and Mamajek, 2013b)[7].

[7] https://www.pas.rochester.edu/~emamajek/EEM_dwarf_UBVIJHK_colors_Teff.txt

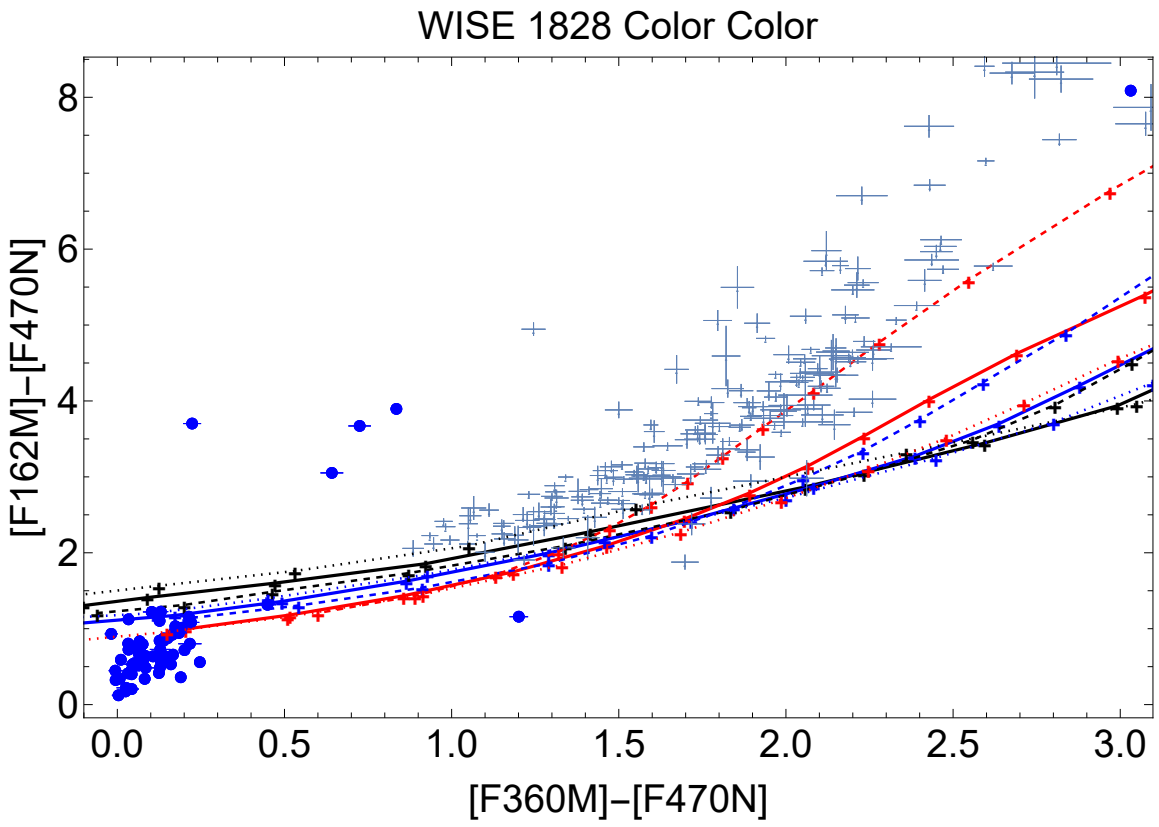


Figure 3.9: Color-Color plot for point sources detected in all three bands seeded with a high SNR detection in F360M. Blue circular symbols are sources in the WISE 1828+2650 field (WISE 1828+2650 is in the upper right corner), the light blue crosses represent the progression of BDs from Kirkpatrick et al. (2019) plotted in using H band, Spitzer IRAC Ch1 and Ch2 similar to the JWST filters. Visual examination of the F360M image shows that four JWST sources that lie above the BD locus are slightly extended, very red galaxies. The lines denote sequence of early L to late T dwarfs based on Sonora Models (Marley et al., 2021a). The colors denote values of log(g) (black, 3.0, blue, 4.0, red, 5.0). The line type denotes different values of [Fe/H]=(0,thick; -0.5,dashed; and +0.5 dotted).

Table 3.5: Highly Red Sources in WISE 1828+2650 Field. [1]Epoch 2022.5699, uncertainties in milliarcseconds in parentheses; [2]Top line is flux density in $\mu$Jy, the second line is corresponding Vega magnitude.[3]Full width at Half Maximum in F360M. This is to be compared with the FWHM of the WebbPSF of 0.17". [4]Source is WISE1828+2650. [5]Source to confusion with a nearby object.

| Label | RA2000[1] | DEC2000[1] | F090W[2] | F115W[2] | F162M[2] | F335M[2] | F360M[2] | F470N[2] | FWHM[3] |
|---|---|---|---|---|---|---|---|---|---|
| 1 | 277.138408(60.) | 26.8286435(55.) | 1.06±0.00769 | 4.08±0.00955 | 0.911±0.00908 | 6.23±0.0223 | 5.66±0.0218 | 4.24±0.0982 | 0.15" |
| | 18h28m33.22s | 26d49m43.12s | 23.33±0.0078 | 21.59±0.0025 | 22.62±0.011 | 19.2±0.0039 | 19.15±0.0042 | 18.92±0.025 | |
| 2 | 277.160802(20.) | 26.8420123(16.) | 0.172±0.00651 | 0.545±0.00633 | 0.975±0.00975 | 2.±0.0113 | 2.27±0.0122 | 2.5±0.0747 | 0.23" |
| | 18h28m38.59s | 26d50m31.24s | 25.3±0.04 | 23.78±0.013 | 22.55±0.011 | 20.43±0.0061 | 20.14±0.0058 | 19.5±0.032 | |
| 3[4] | 277.133408(26.) | 26.8444326(4.3) | 0.078±0.005 | 0.311±0.00446 | 1.29±0.00857 | 2.41±0.0132 | 34.2±0.0511 | 340.±0.619 | 0.15" |
| | 18h28m32.02s | 26d50m39.96s | 26.16±0.20 | 24.39±0.015 | 22.25±0.0072 | 20.23±0.0059 | 17.19±0.0016 | 14.16±0.002 | |
| 4 | 277.16172(24.) | 26.8470549(26.) | 0.0796±0.00708 | 0.323±0.00663 | 0.562±0.00985 | 1.93±0.0112 | 2.14±0.012 | 2.55±0.0752 | 0.44" |
| | 18h28m38.81s | 26d50m49.4s | 26.14±0.093 | 24.34±0.022 | 23.15±0.019 | 20.47±0.0063 | 20.2±0.0061 | 19.48±0.032 | |
| 5 | 277.138946(24.) | 26.8479253(5.9) | N/A | 0.23±0.0043 | 1.27±0.00946 | 4.85±0.0166 | 5.39±0.0176 | 7.1±0.098 | 0.18" |
| | 18h28m33.35s | 26d50m52.53s | N/A | 24.71±0.02 | 22.26±0.008 | 19.47±0.0037 | 19.2±0.0035 | 18.36±0.015 | |
| 6[5] | 277.152549(430.) | 26.8653645(380.) | 2.42±0.00887 | 3.94±0.0116 | 9.63±0.0276 | 6.41±0.0218 | 2.34±0.0225 | 4.31±0.0968 | 0.15" |
| | 18h28m36.61s | 26d51m55.31s | 22.44±0.004 | 21.63±0.0032 | 20.06±0.0031 | 19.17±0.0037 | 20.11±0.01 | 18.91±0.024 | |

Figure 3.9 shows only one object in the color space occupied by BDs, WISE 1828+2650 itself in the upper right corner of the plot. Finally, there are 4 other red objects with colors around [F162M]–[F470N] >2 mag (Table 3.5). A sixth source with [F360M]–[F470N]~ 1.2 lies below the BD locus and appears to be contaminated by confusion with a nearby object. Visual inspection and measured FWHM of the four red objects shows two to be extended (Table 3.5). A more detailed examination of the images and comparison with the predicted WebbPSF[8] image size shows that #2 and #4 have FHWM in the F360M image of 0.23" and 0.43", respectively, compared with other point sources in the field (0.15" in the mosaicked images) and the WebbPSF FHWM of 0.12-0.13" (Table 3.5). A third, #5, may be slightly extended 0.18". The other two, #1 and #6, are point-like or only very slightly extended. Source #3 is WISE 1828+2650. Extra-galactic objects with similar colors are being found in on-going deep imaging programs and are suggestive of a new class of highly dust obscured galaxy (Hainline et al, in preparation).

Figure 3.9 includes colors from a large sample of BDs from Kirkpatrick et al. (2021) using H-band, IRAC C1 and Ch2 as analogs for the JWST filters. The plot also includes loci of six different Sonora BD models evaluated in the JWST filters and ranging in surface temperature, gravity, and metallicity: $300 < T_{Eff} < 1700$ K, log(g) of (3,4,5), and [Fe/H] of (−0.5,0,+0.5). The comparison between the models and the Kirkpatrick sample show the well known problem that as the BDs become cooler, the models have a progressively harder time fitting the data.

The conclusion of this search and visual inspection of the six JWST images is that there are no obvious cool BD candidates in the WISE 1828+2650 field, but that there are a significant number of galaxies.

[8]https://webbpsf.readthedocs.io/en/latest/

### 3.2.8 Conclusion

This examination of the new 1-5$\mu$m NIRCam data for WISE 1828+2650 has confirmed what has been previously known about this source. It remains among the reddest and most challenging of the Y dwarfs to fit using existing models. Both the high SNR data at F360M and the data from the Keck telescope at 1.6 $\mu$m have failed to reveal a near-equal mass companion beyond 0.5 au. If, as has been suggested, a binary system offers a better chance of fitting the photometric models, the companion must orbit very close to WISE 1828+2650 itself, <0.5 au. Such a companion might reveal itself through double lines in the spectroscopy. However, even the binary model fails to provide an improved fit to the existing photometric data. Further insights into the properties of this enigmatic object will come with the analysis of the NIRCam and MIRI spectroscopic data forthcoming shortly in other publications.

We must first acknowledge the many years of effort by thousands of scientists, engineers and administrators who made JWST such a dramatic success, exceeding many of its most important requirements. This international collaboration should be an inspiration to us all. The NIRCam team at the University of Arizona and Lockheed Martin's Advanced Technology Center brought great skill, expertise and dedication to realize the full power of this instrument. This work was supported by NASA through the JWST NIRCam project through contract number NAS5-02105 (M. Rieke, University of Arizona, PI). This work is based in part on observations made with the NASA/ESA/CSA James Webb Space Telescope. The data were obtained from the Mikulski Archive for Space Telescopes at the Space Telescope Science Institute, which is operated by the Association of Universities for Research in Astronomy, Inc., under NASA contract NAS 5-03127 for JWST. These observations are associated with program #1189.

We wish to thank Davy Kirkpatrick for valuable discussions. Some of the research described in this publication was carried out at the Jet Propulsion Laboratory, California Institute of Technology, under a contract with the National Aeronautics and Space Administration. M. De Furio benefited from support from JPL's Strategic University Research Partnership (SURP). Doug Johnstone is supported by NRC Canada and by an NSERC Discovery Grant. L.A. acknowledges support by the Canadian Space Agency under contract 9F052-170914/001/MTB. T.R. would like to acknowledge the support of the NASA Science Mission Directorate under WBS 411672.07.05.05.03.01.

Some of the data presented herein were obtained at the W. M. Keck Observatory, which is operated as a scientific partnership among the California Institute of Technology, the University of California and the National Aeronautics and Space Administration. The Observatory was made possible by the generous financial support of the W. M. Keck Foundation. The authors wish to recognize and acknowledge the very significant cultural role and reverence that the summit of Maunakea has always had within the indigenous Hawaiian community. We are most fortunate to have the opportunity to conduct observations from this mountain.

## 3.3 The Case of WISE J033605.05-014350.4

### 3.3.1 Abstract

We report the discovery of the first brown dwarf binary system with a Y dwarf primary, WISE J033605.05−014350.4, observed with NIRCam on JWST with the F150W and F480M filters. We employed an empirical point-spread function binary model to detect the companion, located at a projected separation of 0.084", position angle of 295 degrees (E of N), and with contrast of 2.8 and 1.8 magnitudes in F150W and F480M, respectively. At a distance of 10 pc based on its Spitzer parallax, and assuming a random inclination distribution, the physical separation is approximately 1 au. Evolutionary models predict for that an age of 1-5 Gyr, the companion mass is 5-11.5 $M_J$ and the primary mass is 8.5-18 $M_J$, corresponding to a companion-to-host mass ratio of 0.61 ± 0.05. Under the assumption of a Keplerian orbit the period for this extreme binary is in the range of 5-9 years. The system joins a small but growing sample of ultracool dwarf binaries with effective temperatures of a few hundred Kelvin. Brown dwarf binaries lie at the nexus of importance for understanding the formation mechanisms of these elusive objects, as they allow us to investigate whether the companions formed as stars or as planets in a disk around the primary.

### 3.3.2 Introduction

Brown dwarfs are cool sub-stellar objects with masses below the $\approx 80\,M_{\rm Jup}$ hydrogen burning limit (e.g. Burrows et al., 2001). Studies of the initial mass function for stars extend far into the sub-stellar regime, even below 5 $M_{\rm Jup}$ (Kirkpatrick et al., 2019), which sets a tight boundary condition on the processes through which brown dwarfs can form. These formation processes may be similar to mechanisms that drive star formation like gravitational collapse of giant molecular clouds, or analogous to those of giant planets through planetesimal growth in a circumstellar disk. Brown dwarfs could also form through entirely other modes such as ejection from star forming aggregates (Reipurth and Clarke, 2001).

Studies of the multiplicity of these objects is an efficient approach to constrain theories of their formation. Those studies can measure and constrain fundamental trends such as the orbital separation of binaries and the mass ratio, $q = M_{companion}/M_{primary}$. For stars, the orbital separation distribution appears well-fitted by a log-normal distribution for M-stars through solar-type stars with the peak in the distribution increasing with primary mass (Winters et al., 2019; Raghavan et al., 2010). The companion mass ratio distribution also appears to change as a function of primary mass (Duchêne and Kraus, 2013), changing from a bottom heavy to top heavy power law for O-stars to brown dwarfs (Offner et al., 2023). Brown dwarf binaries appear to be consistent with the orbital separation trend observed for higher mass multiples and typically form tighter orbital

configurations. Burgasser et al. (2003, 2006) studied T0 to T8 spectral types for multiplicity, finding all identified systems to have separations <5 au and mass ratios > 0.8, thus confirming the trend. Those early studies were however limited by only being sensitive to mass ratios > 0.5 and did not probe the full range of mass ratios. More recent works have extending previous findings across a broader range of mass ratios and separations and support this trend, e.g. Fontanive et al. (2018) 50% complete to equal mass companions down to ∼ 2 au and q=0.3 beyond 10 au.

During the last decade we have seen an increase in the discoveries of brown dwarfs in the solar neighborhood, much to the efforts of deep imaging surveys and infrared missions such as the Wide-field Infrared Survey Explorer (WISE, Wright et al., 2010b). Cushing et al. (2011) discovered several brown dwarfs from WISE data to have spectral features which distinguished them from the previously known latest T-type dwarfs, providing a clear transition to the identified Y dwarf spectral class. These Y dwarfs represent an extreme in temperature among the field star populations of the Milky Way (Cushing et al., 2011; Kirkpatrick et al., 2019; Zalesky et al., 2019), and are used for probing the brown dwarf-exoplanet connection (Beichman et al., 2014). They have effective temperatures lower than 500 K, with some approaching that of Jupiter (130 K, Hanel et al., 1981). For brown dwarfs, Coulomb and electron degeneracy effects compete in the equation of state, dictating their structure so that typical radii are close to that of Jupiter (Burrows et al., 2011). Thus, the range of temperatures results in a range of luminosities.

Y dwarfs are much brighter at wavelengths > 4 $\mu$m than at shorter wavelengths, so for these objects the Near Infrared Camera (NIRCam) on JWST is orders of magnitude more sensitive than any other facility and the ideal tool for studying Y-dwarf multiplicity properties. Additionally, the 6.5m primary mirror diameter of JWST and the pixel sampling of NIRCam allows us to probe higher angular resolutions than previously available to ground-based 10m class telescopes (see Section 3.2.5.1) and HST in the near-IR. As part of a JWST Cycle 1 GO program (#2473, Albert et al., 2021)[9], we are conducting a survey of 20 Y dwarfs that is sensitive to companions beyond 1 au and down to 1 $M_{\rm Jup}$ given estimated sensitivity limits pre-launch (Ceau et al., 2019). This work will provide valuable information on the ability of low-mass brown dwarfs to form companions and place constraints on the specific processes that govern their formation.

Here we present our first discovery, a faint companion to the Y dwarf WISE J033605.05−014350.4 (hereafter W0336), the first Y+Y binary system.

[9] https://www.stsci.edu/jwst/phase2-public/2473.pdf

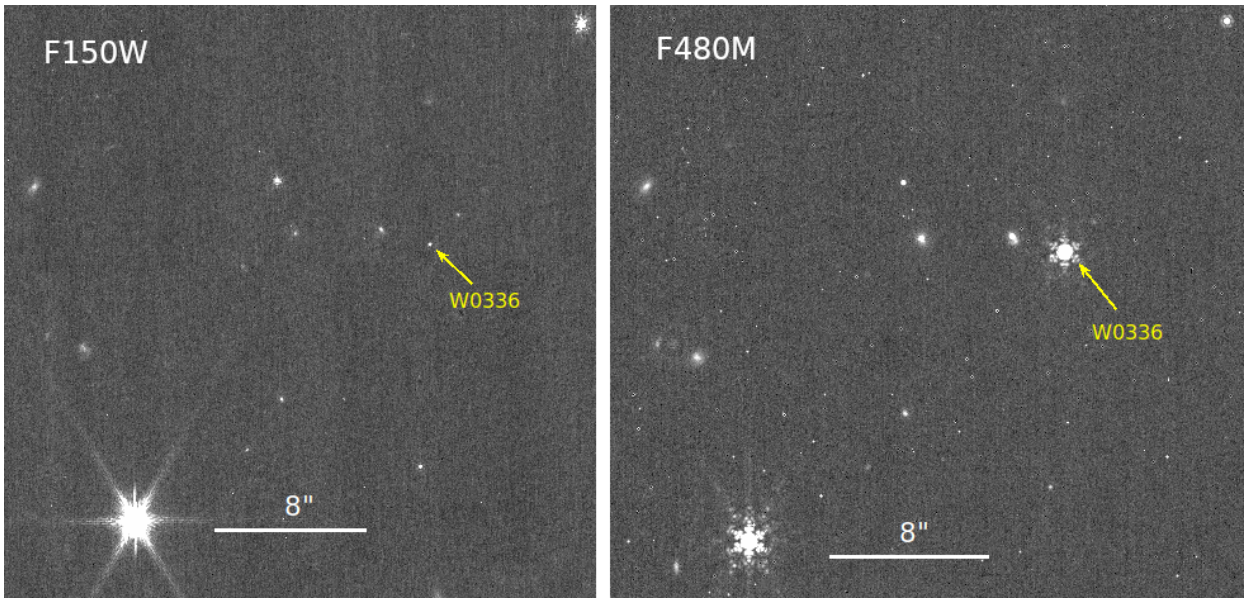


Figure 3.10: JWST/NIRCam images showing the aligned and scaled images of the target W0336 in each observed filter (left: F150W, right: F480M). North is up and East is to the left in the images. W0336 is identified with a yellow arrow.

### 3.3.3 Observations and Reduction

W0336 was first discovered by Kirkpatrick et al. (2012) using WISE data and the unresolved system has been classified as a Y0 dwarf (Martin et al., 2018)[10] with an estimated effective temperature of $T_{\rm eff}$ = 460 ± 79 K (Kirkpatrick et al., 2021). Spitzer (Werner et al., 2004) observations were used to measure the astrometry of the object (Martin et al., 2018; Kirkpatrick et al., 2019), and here we adopt the results from Kirkpatrick et al. (2021) with a parallax of $\pi$ = 99.8 ± 2.1 mas and proper motions of $\mu_{\rm RA} = -251.5 \pm 0.9$ mas/yr and $\mu_{\rm DEC} = -1216.1 \pm 0.93$ mas/yr.

We observed the target with JWST/NIRCam on 2022 September 22 at 12:49:44 UT, obtaining images in both F150W and F480M filters simultaneously. The source was observed with NIRCam imaging mode using a 5-point subpixel Small-Grid-Dither pattern for a total exposure time of 2630.509 seconds with the BRIGHT1 readout pattern. The data were reduced by the official JWST pipeline with the data processing software version 2022_3a, and downloaded from the MAST archive based on calibration software version 1.7.2[11]. The unresolved photometry of the system was estimated using the photoutils Python package (Bradley et al., 2020) and the JWST photometric reference data *jwst_nircam_photom_0114.fits*. An aperture size equal to 70 % encircled energy was adopted together with appropriate aperture corrections in accordance to the JWST Calibration

[10]Some discrepancies have been reported in the W0336 spectral type, likely related to a low signal to noise ratio of the observed spectrum (Mace et al., 2013; Martin et al., 2018).

[11]Using calibration reference data system version *11.16.14* with the reference file *jwst_1023.pmap*.

Reference Data System. We employed our analysis on the intermediate data reduction step, level 2 pipeline product **cal.fits* files, further described in Section 3.3.4. In addition to the standard calibrated images we performed our own background subtraction by fitting an annulus with 10–15 pixel radius centered upon the target.

We verified the positions of the target W0336 for the two bands by overplotting their respective images. The images from each band are shown in Figure 3.10, illustrating that W0336 appears brighter in the longer wavelength band F480M. The images have been rotated with respect to the instrument aperture positional angle (NIRCam APA) of 271.61° in the F150W band and 270.79° in the F480M band at the time of the observations, so that North is up and East is to the left in the images. We also cross-referenced the position of W0336 with publicly available Hubble Space Telescope images from GO-16229[12] in the F160W filter, verifying the position and motion of the system compared to background sources.

### 3.3.4 Empirical Point Spread Function Analysis

In order to search for companions at small separations, we applied a binary-PSF fitting routine using empirically derived PSF models, thoroughly described in Sec. 3.2.5.2. This analysis was based on the empirical PSF (ePSF) construction described by Anderson and King (2006) and has been applied to find close companions on sub-pixel scales using Hubble Space Telescope images, see Chapter 2.

We constructed the ePSF for each filter using three other Y-dwarfs which were observed close in time to W0336 (WISE J035934.06−540154.6, WISE J030449.03−270508.3, and WISE J041022.71+150248.4), within a 36 hour window. We used a pixel box size of $11 \times 11$ pixels centered upon the flux peak of the selected sources, and constructed a 4× oversampled PSF model. Each source was observed with a pattern of five sub-pixel dither positions, allowing for more detailed sub-pixel modeling of the ePSF. All dither positions were used in making of the ePSF for a total of $3 \times 5 = 15$ sources for the final combined ePSF in each filter. The PSF for a relatively wide bandpass can vary between objects if those objects have different spectral energy distributions through the filter. We therefore chose these sources to ensure consistent color and similar SNR to retain the integrity of the expected PSF of a Y-dwarf and to minimize wavefront error drifts over a short amount of time in order to optimize our estimation of the astrophysical scene.

We then used the ePSF to fit both single and double PSF models to the Y-dwarf data. We employed a Nested Sampling routine using the PyMultiNest Python package (Buchner et al., 2014a) that performs the Nested Sampling Monte Carlo analysis using MultiNest (Feroz et al., 2009a). Our single model consists of three parameters: $x$ and $y$ center position and flux normalization of

[12] https://www.stsci.edu/hst/phase2-public/16229.pdf

the target source. Our binary model consists of six parameters: $x$ and $y$ center of the primary, flux normalization of the primary, separation between the centers of the primary and secondary, the position angle of the center of the secondary relative to the primary, and the flux ratio between the secondary and primary ($f_r \equiv f_B/f_A$). The priors to the primary coordinates were set as flat over ±1.5 pixels from the centre of the pixel box. The companion parameter priors were set as flat over separations between 0.5-5.0 pixels, as we do not expect to be sensitive to companions closer in than half a pixel and we limited the search to the size of the pixel box. The positional angle prior was set to be flat between 0-360° and the flux ratio prior log-uniform over $10^{-4}$-1.

PyMultiNest calculates the Bayesian evidence of the model, which we used to determine whether a binary or single model fits the data better. We first fit each dither position individually to ensure that the companion was detected in every image, while also verifying consistency and check for possible bad frames. We then fit all dither positions simultaneously, treating the $x$- and $y$- positions of the primary as free parameters for each dither position while keeping the parameters for the secondary component the same for all dithers as they will be conserved between dithers, for a total of 14 parameters to be varied in the binary model fit. Figure 3.11 displays the data, the single and binary model fits, and their residuals in the F480M filter. The best fit values for both filters are presented in Table 3.6.

### 3.3.5 Results and Discussion

The empirical PSF analysis provides a compelling first look at these data. This is the only companion found with this method in our sample of 16 Y dwarfs observed to date, and the first companion ever discovered around a Y dwarf primary. Although these are small number statistics, the observed frequency of companions in our sample (1/16 = $6^{+12}_{-2}$%) is consistent with the companion frequency to late T-dwarfs (8%) over mass ratios of $q$ =0.2-1.0 and separations of $a$ =0.1-1000 au (e.g. Fontanive et al., 2018). Future work will characterize the companion population and estimate the companion frequency over mass ratios and orbital separations sampled across our entire survey.

Table 3.6 gives the angular separation and orientation of the resolved system. The values are estimated from the median of the probability density function obtained from PyMultiNest, with errors being the 16 % and 84 % percentiles. The separation measured in pixels is converted into milliarcseconds using the nominal plate scale from the JWST user documentation[13] of 63 mas/pixel and 31 mas/pixel for the F480M and F150W filters respectively. We adopt the angular separation of 0.084" measured in the F480M filter where the companion is brighter. Given the distance of 10.02 ± 0.21 pc from the Spitzer parallax, the estimated separation corresponds to a projected separation of $0.89^{+0.07}_{-0.10}$ au. This separation is consistent with what one would expect given the

[13] https://jwst-docs.stsci.edu/jwst-near-infrared-camera

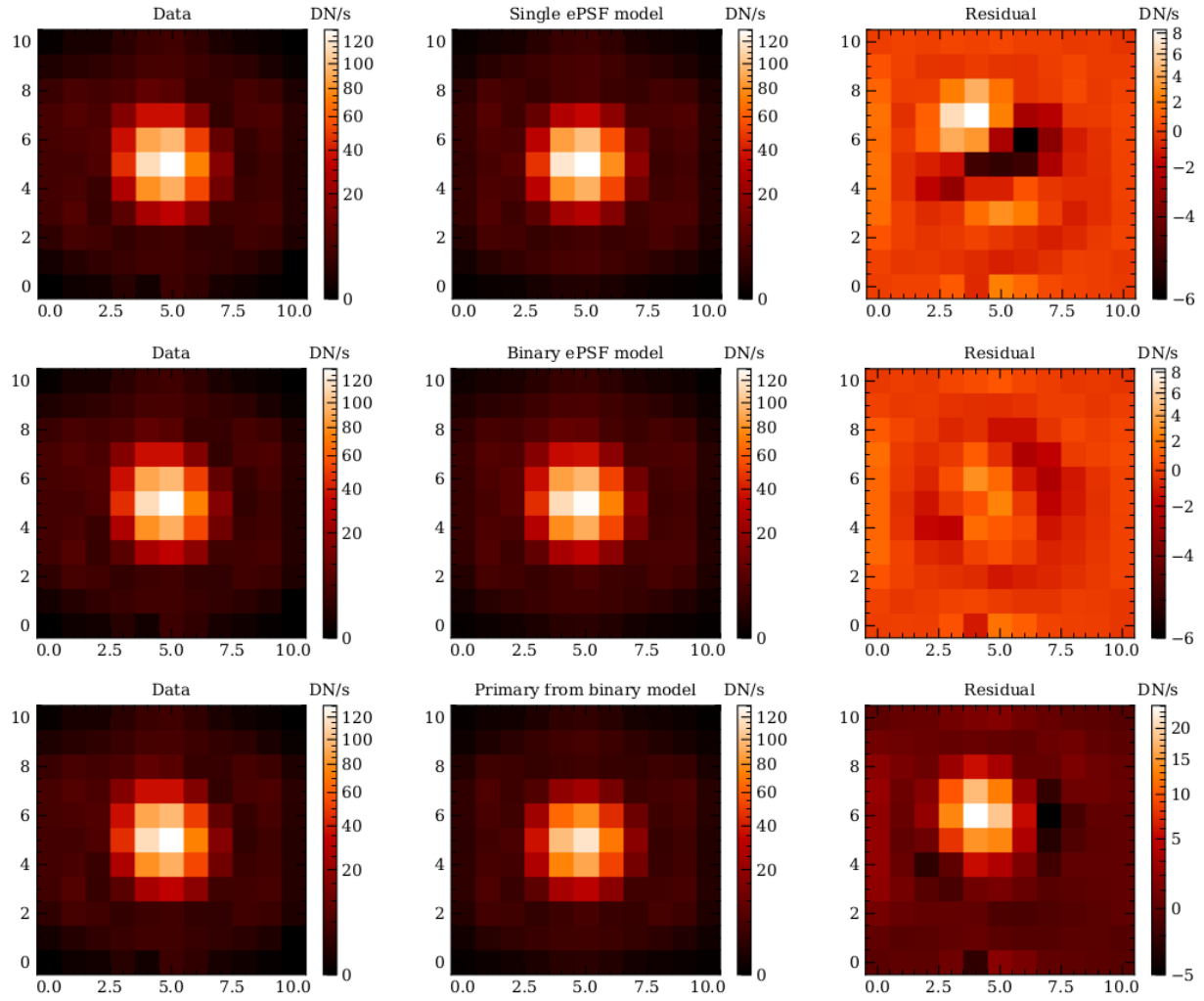


Figure 3.11: Images displaying the pipeline calibrated data of W0336 in the F480M band are in the left column, models are in the middle column, and their corresponding residuals when the models have been subtracted from the data are in the right column. The top row shows a single model fitted to the data, and the middle row shows a binary double ePSF model. The bottom row depicts the same binary model as the middle row, but only showing the primary component from that fit to better highlight the companion seen in the residuals after subtracting the primary component from the data. The units are in DN/s. The color scheme in the images are scaled to a power law with an exponent of 0.5, and the color bar for the binary model residual image has been scaled to match the single model residual image to better highlight the smaller residual and improved fit.

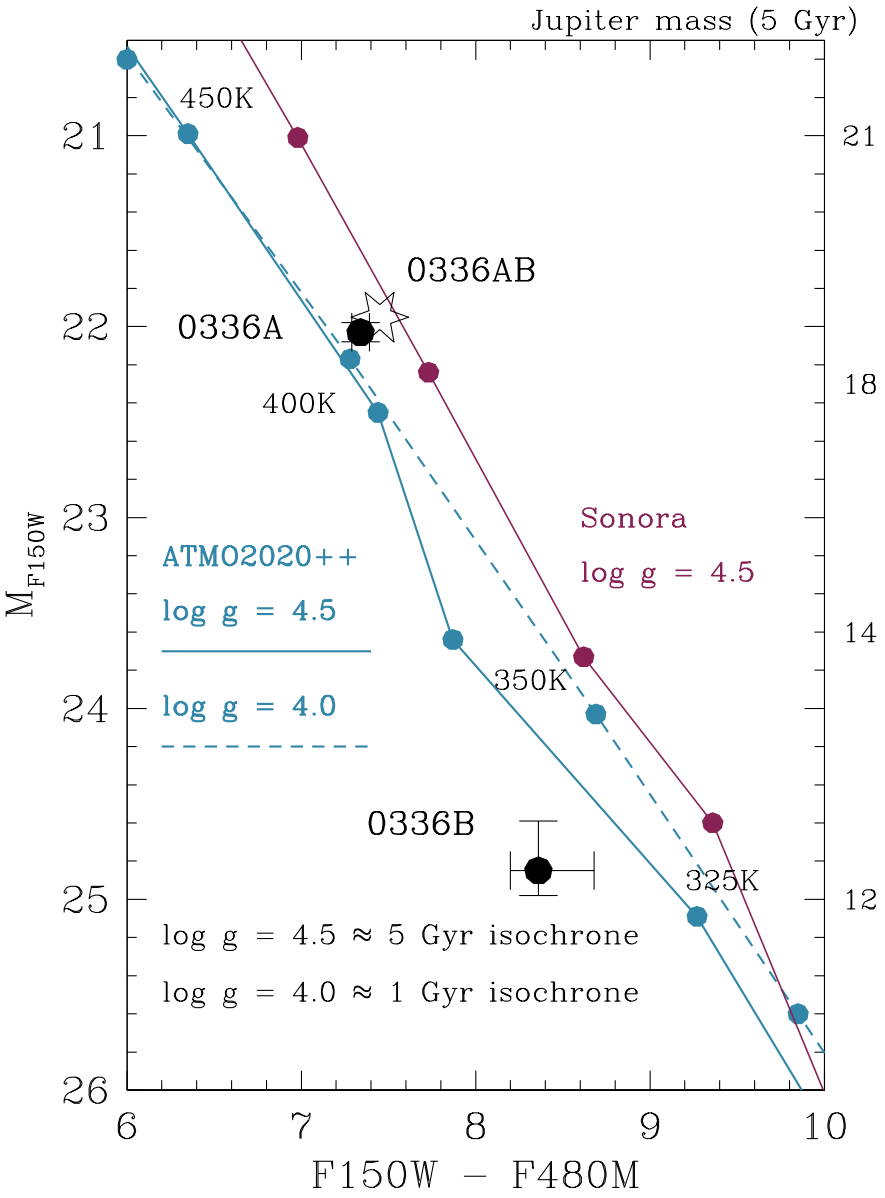


Figure 3.12: Color-magnitude diagram for W0336 in the NIRCam filters used in this work. The open star corresponds to the unresolved system, and black filled points indicate the resolved components. Model sequences are shown for effective temperatures and surface gravities indicated in the legend. All models are for cloud-free solar metallicity atmospheres, however the Sonora models (Marley et al., 2021b) are in chemical equilibrium, while the ATMO2020++ models (Phillips et al., 2020a; Leggett et al., 2021a) include disequilibrium chemistry and also an adjusted pressure-temperature profile. The masses along the right axis are taken from the Sonora evolutionary models of Marley et al. (2021b), for log g = 4.5 and the temperatures indicated along the sequences.

orbital separation distribution from Fontanive et al. (2018) for late T and early Y dwarfs with a peak at $2.9^{+0.8}_{-1.4}$ au in projected separation. The probability of the companion being a background contamination is extremely low given its proximity to the primary. Assuming a randomly uniform distribution of objects brighter than the companion W0336B in the field of view of our NIRCam images, we obtain a probability of $\sim 4x10^{-6}$ for a chance projection at the same separation as the discovered companion.

Table 3.6 also gives the measured F150W and F480M Vega magnitudes for the unresolved system and for the resolved components, where the resolved magnitudes are calculated from our contrast measurements of flux ratio between the components. Figure 3.12 shows a color-magnitude diagram for the system, together with model sequences. There are two recent model families which apply cloud-free atmospheres and cover the low luminosities of the W0336 system - the Sonora Bobcat models (Marley et al., 2021a) and the ATMO2020 models (Phillips et al., 2020b; Leggett et al., 2021b). The ATMO2020 models include disequilibrium chemistry and a physically-motivated empirical adjustment to the atmosphere's pressure-temperature profile (see discussion in Leggett et al., 2021b). Figure 3.12 shows that the two model sets predict very similar values of $M_{\rm F150W}$ for a given $T_{\rm eff}$ and gravity, although the F150W − F480M colors can differ. The models are thus expected to provide reliable estimates of $T_{\rm eff}$ for the W0336 system, given in Table 3.6. The uncertainties in $T_{\rm eff}$ have been estimated from the range of $M_{\rm F150W}$ values calculated by the models for plausible ranges in gravity and metallicity (Table 9 of Leggett et al., 2021b).

There are no constraints on age for this isolated system. However studies of the solar neighborhood, and of low mass stars and brown dwarfs in particular, suggest a likely age range for this system of 1-3 Gyr (e.g. Dupuy and Liu, 2017). The ATMO2020 models and Figure 3.12 on the other hand suggest that the age of the system may be older than 5 Gyr, and also that the system has approximately solar metallicity (not shown). However, the uncertainty in the measured F150W − F480M colors, and systematic differences in the models, means that surface gravity cannot be fully constrained, which would have constrained mass and age.

Nevertheless, Table 3.6 gives estimates of mass for the W0336 components for ages of 1 Gyr and 5 Gyr, derived from our absolute magnitude estimates and the Sonora evolutionary models (Marley et al., 2021a). The mass-estimates range from 8.5-18.0 $M_{\rm Jup}$ for the primary and 5.0-11.5 $M_{\rm Jup}$ for the secondary, and the mass ratio of the system is around $q = 0.6$, at the low end of the distribution found for low-mass binaries with masses $\leq 40\,M_{\rm Jup}$ inferred from Lyon/COND models (Fontanive et al., 2018). Interestingly, W0336B appears to lie at or below the deuterium burning limit of $13\,M_{\rm Jup}$, sometimes used as a boundary between brown dwarfs and planets (Spiegel et al., 2011). If the system is 2 Gyr old or younger, both components lie below this limit. In any case, the companion joins a growing list of cold brown dwarfs and isolated young brown dwarfs which may serve as a constraint on the minimum mass for opacity limited fragmentation.

Table 3.6: Properties of the W0336 binary system

| Band | F150W | F480M |
|---|---|---|
| Separation [mas] | $89.8^{+3.8}_{-4.1}$ | $83.7^{+4.9}_{-8.2}$ |
| Position angle [deg E of N] | $299.1 \pm 3.4$ | $295.4^{+2.3}_{-2.6}$ |
| Contrast [mag] | $2.82^{+0.19}_{-0.11}$ | $1.81^{+0.14}_{-0.31}$ |
| W0336 AB | $21.97 \pm 0.01$ | $14.52 \pm 0.01$ |
| W0336 A | $22.05 \pm 0.01$ | $14.71^{+0.02}_{-0.05}$ |
| W0336 B | $24.87^{+0.18}_{-0.10}$ | $16.51^{+0.12}_{-0.26}$ |
| Component | Primary | Secondary |
| $T_{\rm eff}$ [K] | $415 \pm 20$ | $325^{+15}_{-10}$ |
| $M$ [$M_{\rm Jup}$] (1 Gyr) | $8.5 \pm 1$ | $5 \pm 1$ |
| $M$ [$M_{\rm Jup}$] (5 Gyr) | $18 \pm 2$ | $11.5 \pm 1$ |
| Physical separation [au] | $0.97^{+0.05}_{-0.09}$ | |
| Orbital period [years] | $7 \pm 2$ | |
| Mass fraction $q = M_{\rm B}/M_{\rm A}$ | $0.61 \pm 0.05$ | |

Applying the conversion factor of 1.16 between projected and physical orbits from Dupuy and Liu (2011) for isotropic randomly distributed inclinations with the measured distance, we find the W0336 binary to be separated by $0.97^{+0.05}_{-0.09}$ au. Combining this with the mass-range from the evolutionary models, a tentative orbital period can be estimated for the system of 5-6 years in the higher system mass scenario, and 7-9 years in the lower system mass case. A dynamical mass from orbital monitoring could thus be obtained in a relative short time span for the system. The system is far too faint for Gaia to observe any astrometric acceleration that could otherwise aid to place dynamical mass constraints.

Among the few brown dwarf binaries where the primary has spectral type of T8 or later, few have been reported to be low $q$ systems: WISEPC J121756.91+162640.2 (T9+Y0, 12+8 $M_{\rm Jup}$) and WISEPA J171104.60+350036.8 (T8+T9.5, 20+9 $M_{\rm Jup}$ Liu et al., 2012). However, both these systems have much larger separations of $\sim$ 8-15 au and break from the expected orbital distribution trend otherwise observed. Dupuy et al. (2015) reported on the T+Y dwarf binary WISE J014656.66+423410.0, with a similar projected separation as W0336 of $0.93^{+0.16}_{-0.12}$ au, albeit with a higher mass ratio $q \geq 0.9$. That W0336 in contrast is a tightly bound system with low mass-ratio is an intriguing discovery. With the low number statistics for these extreme systems it is unclear whether they represent the true binary population of ultracool dwarfs or can be considered as peculiar systems. It is also possible that many systems go undetected where the separation is too

tight for them to be retrieved. Indeed, W0336 confirms that late-type and low-mass brown dwarf binaries exist and survive in tight configurations, and surveys approaching sub-au separations are needed to discover them. Such endeavors could be taken using for example Kernel Phase Interferometry (Ceau et al., 2019).

Follow-up spectroscopic and photometric observations over a wide wavelength range are needed to further constrain the properties of both the primary and its companion. Sub-stellar binaries on small separations such as these can be resolved with integral field units to obtain valuable spectral information (e.g. Calissendorff et al., 2019). Such multiple pairs, assuming a common formation age and composition, represent critical constraints on atmospheric physics as well as the theory of formation and evolution of sub-stellar companions.

We thank the reviewer for the constructive comments. This work is based on observations made with the NASA/ESA/CSA James Webb Space Telescope. The data were obtained from the Mikulski Archive for Space Telescopes at the Space Telescope Science Institute, which is operated by the Association of Universities for Research in Astronomy, Inc., under NASA contract NAS 5-03127 for JWST. These observations are associated with program #2473 and can be accessed via 10.17909/9zgc-m183. Support for program #2743 was provided by NASA through a grant from the Space Telescope Science Institute, which is operated by the Association of Universities for Research in Astronomy, Inc., under NASA contract NAS 5-03127. L.A. acknowledges support of the Canadian Space Agency through contract 22JWGO1-11. T.L.R. would like to acknowledge the support of the NASA Science Mission Directorate under WBS 411672.07.05.05.03.01. This work was authored by employees of Caltech/IPAC under Contract No. 80GSFC21R0032 with the National Aeronautics and Space Administration.

# CHAPTER 4

# Multiplicity in the Galactic Field: Probing Intermediate Mass A-type Primary Stars

The work presented in this chapter was originally published in the Astrophysical Journal in De Furio et al. (2022c) with a second paper in preparation and planned for submission in fall of 2023. I led the proposal writing through NSF's NOIRLab community access program (PropID: 2020B-0290; PI: M. De Furio) and later through the CHARA consortium. I also led the observing, data analysis, statistical interpretations, and the manuscript writing. I would like to give special thanks to Tyler Gardner and Gail Schaefer for helping with and carrying out a portion of the observations. Also, I would like to give special thanks to Tyler Gardner and John Monnier for their outsized role in data reduction and analysis. I would also like to thank all my co-authors.

## 4.1 Abstract

We present results from our long-baseline interferometry (LBI) survey to constrain the multiplicity properties of intermediate-mass A-type stars within 80pc. Previous multiplicity studies of nearby stars exhibit orbital separation distributions well-fitted with a log-normal with peaks >15 au, increasing with primary mass. The A-star multiplicity survey of De Rosa et al. (2014), sensitive beyond 30 au but incomplete below 100 au, found a log-normal peak around 390 au. Radial velocity surveys of Am stars (chemically peculiar and slowly rotating intermediate mass stars) identified a significant number of very close companions with periods $\leq$ 5 days, $\sim$ 0.1 au, a result similar to surveys of O- and B-type primaries. With the improved performance of LBI techniques, we can probe these close separations for normal A-type stars where other surveys are incomplete. Our sample consists of 54 A-type primaries with estimated masses between 1.44 - 2.93 $M_{\odot}$ and ages 10 - 790 Myr, which we observed with the MIRC-X instrument at the CHARA Array. We use the open source software CANDID to detect 7 companions, and perform a Bayesian demographic analysis to characterize the companion population. We find a separation distribution consistent with

a flat distribution, and estimate a power-law fit to the mass ratio distribution with index $-0.22^{+0.94}_{-0.88}$ and a companion frequency of $0.25^{+0.16}_{-0.11}$ over mass ratios 0.1-1.0 and projected separations 0.01 - 27.54 au. We find a posterior probability of 0.53, 0.007, and 0.04 that our results are consistent with extrapolations based on previous models of the solar-type, A-type, and B-type companion population, respectively. Our results suggest that the models for A-type stars at close separations must be improved, that the close companion population to A-type stars is comparable to that of solar-types, and that close companions to B-type stars are likely more frequent which is potentially indicative of increased disk fragmentation for stars $\gtrsim 2.5$ $M_{\odot}$.

## 4.2 Introduction

Multiplicity is a common outcome of the star formation process, the properties of which, e.g. orbital separation and mass ratio, seemingly depend on the primary mass of the system (Duchêne and Kraus, 2013; Moe and Di Stefano, 2017). Multiple systems tend to form through two common processes: disk fragmentation (Adams et al., 1989; Bonnell and Bate, 1994; Kratter et al., 2008) and turbulent fragmentation (Goodwin et al., 2004a; Offner et al., 2010). Disk fragmentation is thought to account for the origin of companions at separations on the order of the size of the disk (10-100s au), while turbulent fragmentation is thought to account for the origin of companions at wider separations (100s-1000s au). Close companions (0.1 - 10 au) are found around various types of stars regardless of mass (e.g. Reid et al., 2006; Raghavan et al., 2010; Sana et al., 2012), but additional processes are needed to explain their separations. Orbits can shrink, even for initially wide binaries, through interactions between the companion and infalling gas from the natal cloud, direct interactions with a circumstellar disk, and dynamical interactions of unstable multiple systems (Bate et al., 2002, 2003; Offner et al., 2010; Bate, 2012). These small separation companions have significant impacts on our fundamental understanding of planet formation and stellar evolution, as well as star formation.

Many volume-limited surveys have characterized the stellar multiple population based on primary star mass, mass ratio, and orbital separation. They find that the companion orbital separation distribution can be fitted as a log-normal distribution with a peak > 15 au that increases with primary mass. Low-mass M-type primaries have a companion separation peak around 20 au (Janson et al., 2012; Winters et al., 2019), solar-type primaries have a peak at 50 au (Raghavan et al., 2010), and A-type primaries have a peak around 390 au (De Rosa et al., 2014). However, the A-type multiplicity survey of De Rosa et al. (2014) is incomplete for separations < 100 au, leaving open the possibility for a significant population of close separation companions to A-type primaries.

Radial velocity surveys of chemically peculiar Am stars with small rotational velocities identified a significant number of very close companions with a characteristic period of 5 days, $\sim$ 0.1 au

(Abt and Levy, 1985; Carquillat and Prieur, 2007). Close companions could drive the decreased rotational velocity and thus the peculiar chemical composition of Am stars. But, a similar peak has been identified for O-type primaries (Sana et al., 2012). Interferometric studies of OB primaries in the Orion Nebula Cluster found a bi-modal distribution with peaks at $\sim$ 1 au and 400-600 au (Gravity Collaboration et al., 2018). A similar population of close companions to normal A-stars would be vitally important to understanding possible planetary architectures around intermediate-mass stars and the formation mechanisms required to form small separation binaries as a function of primary mass.

If small separation companions to intermediate mass stars are common, they could represent a likely formation mechanism of Type Ia supernova progenitors, i.e. white dwarfs with masses $\geq$ 0.7 $M_{\odot}$ evolved from intermediate mass stars (Cummings et al., 2018). One such binary with a high mass ratio could result in the double-degenerate scenario where two white dwarfs with masses $\sim$ 0.7-0.8 $M_{\odot}$ form and eventually merge, producing a Type Ia Supernova as its combined mass exceeds the Chandrashekhar mass limit (Webbink, 1984). These types of multiples could also produce the single-degenerate scenario where a white dwarf accretes hydrogen from a close companion star and eventually detonates when surpassing the Chandrashekhar mass limit (Whelan and Iben, 1973).

Identifying close companions to A-stars with the radial velocity method can be more difficult than to solar-type stars as their spectral lines are quite broad due to their fast rotation (Borgniet et al., 2019). Radial velocity surveys also require frequent observations over multiple years to detect companions at several au in separation for a typical A-type star. Extreme adaptive optics (AO) systems can achieve angular resolutions down to $\sim$ 20 milli-arcseconds (mas), but cannot resolve the region in which Am stars have close companions ($\sim$ 0.1 au) at distances > 5 pc. Therefore, we used the Michigan Infra-Red Combiner-eXeter (MIRC-X) instrument (Anugu et al., 2020) on the long-baseline interferometric array at the Center for High Angular Resolution Astronomy (CHARA, ten Brummelaar et al., 2005) to observe a sample of A-type stars within 80 pc and search for close companions down to separations of 0.5 mas.

In Section 4.3, we describe the data and the methods to identify companions. In Section 4.4, we present the companion detections, describe our detection limits, and characterize the close companion population of A-type primary stars. In Section 4.5, we compare our results to various multiplicity surveys and discuss the implications. In Section 4.6, we summarize our conclusions.

## 4.3 Methods

### 4.3.1 Observations

We observed 57 A-type stars over the course of six nights (UT December 20-21, 2020, May 6-8 and July 30, 2022) at the CHARA Array with the MIRC-X instrument in the near-infrared H photometric band ($\sim$ 1.6 microns), listed in Table 4.1. The CHARA Array is an interferometer made up of six 1-meter telescopes which operate in the optical and near infrared with baselines ranging from 34-331 meters. MIRC-X is a beam combiner instrument (Monnier et al., 2006; Anugu et al., 2020) that operates in the near infrared, using all CHARA telescopes. All of our observations were taken in the grism mode with R $\sim$ 190. This spectral mode allows us to search out to wide angular scales ($\sim$ 0.3") as the increased spectral dispersion increases the interferometric field of view (Anugu et al., 2020). At the same time, the spectral resolution is not so high that flux is spread out across many spectral channels, reducing the signal-to-noise (S/N) and thus reducing the achievable contrast. The R190 grism is ideal for observing our relatively bright targets (typically H = 4-5.5 mag) and searching for companions on wide angular scales. One other target (HD 31647) was observed on UT October 21, 2021 with a 5 telescope setup (missing telescope W2) using both MIRC-X (R190) and MYSTIC (prism, R50) (Monnier et al., 2018), a beam combiner in the same vein as MIRC-X which operates in the K-band ($\sim$ 2.2 microns), making our sample size a total of 58. The ten stars observed on July 30, 2022 were also observed simultaneously with MIRC-X (R190) and MYSTIC (R50), identified in Table 4.1.

For each target, we had the same observing sequence: 10 min source integration, the standard shutters sequence (Anugu et al., 2020), and repeated 10 min source integration. For HD 56537, we performed 5 min source integrations instead due to the high flux of the primary to achieve equivalent S/N to all other targets. Throughout our 2020 run, we observed calibrator stars for every few targets using an observing sequence of 5-10 min integrations, shutters, followed by 5-10 min integrations. Two of our calibrators (HD 15734 and HD 78234) are resolved binaries, and instead we opted to use science targets well fit by a single star model to calibrate other targets observed in proximity, see Table 4.3. We opted to observe more science targets instead of more frequent calibrators because our search for companions relies on closure phases and does not need highly calibrated visibilities, see Sec. 4.3.3. For our 2022 run, we observed no calibrators and all science targets as the majority of targets in our previous run were identified as singles.

### 4.3.2 Data Reduction

We used the standard MIRC-X data pipeline (version 1.3.3) to produce OIFITS files for each night, described in Anugu et al. (2020). The MIRC-X pipeline and its documentation is maintained

Table 4.1: Table of sources in our sample with Modified Julian Date (MJD) of observation. Listed spectral types, ages, and masses for each star were taken from De Rosa et al. (2014) who describe their method of estimating age and mass in their Appendix. Distances and their errors (16% and 84% confidence level) were extracted from the Gaia DR3 archive (Gaia Collaboration et al., 2016, 2022; Babusiaux et al., 2022), except where noted. *Observed with both MIRC-X and MYSTIC at CHARA Array. a) Distance from De Rosa et al. (2014) using the Hipparcos catalog (Hip, 1997).

| Target Name | SpType | Distance (pc) | Age (Myr) | Mass ($M_\odot$) | MJD |
|---|---|---|---|---|---|
| HD 1404* | A2V | $43.00^{+0.34}_{-0.33}$ | 200 | 2.26 | 59790.43 |
| HD 4058* | A5V | $54.77^{+3.39}_{-0.65}$ | 250 | 1.9 | 59790.45 |
| HD 5448 | A5V | $42.37^{+0.11}_{-0.19}$ | 450 | 2.39 | 59203.08 |
| HD 11636[a] | A5V | $18.27^{+0.25}_{-0.25}$ | 630 | 2.01 | 59204.08 |
| HD 14055* | A1Vnn | $35.74^{+0.60}_{-0.58}$ | 100 | 2.57 | 59790.48 |
| HD 15550 | A9V | $71.77^{+1.84}_{-0.56}$ | 790 | 1.84 | 59204.14 |
| HD 20677 | A3V | $48.11^{+0.30}_{-0.25}$ | 250 | 2.11 | 59203.18 |
| HD 21912 | A3V | $56.29^{+0.16}_{-0.15}$ | 40 | 1.77 | 59203.16 |
| HD 24809 | A8V | $63.76^{+0.12}_{-0.11}$ | 100 | 1.70 | 59203.22 |
| HD 28910 | A8V | $46.97^{+0.38}_{-0.37}$ | 630 | 2.21 | 59204.22 |
| HD 29388[a] | A6V | $47.1^{+1.2}_{-1.2}$ | 630 | 2.17 | 59204.19 |
| HD 31647* | A1V | $49.91^{+0.29}_{-0.29}$ | 30 | 2.39 | 59508.56 |
| HD 32301 | A7V | $57.55^{+4.80}_{-1.87}$ | 630 | 2.22 | 59204.25 |
| HD 46089[a] | A3V | $63.7^{+1.5}_{-1.5}$ | 560 | 2.20 | 59203.29 |
| HD 48097[a] | A2V | $43.6^{+1.3}_{-1.3}$ | 30 | 1.94 | 59203.32 |
| HD 56537[a] | A3V | $30.9^{+0.2}_{-0.2}$ | 320 | 2.39 | 59204.28 |
| HD 59037 | A4V | $55.91^{+3.84}_{-1.44}$ | 500 | 2.16 | 59203.35 |
| HD 66664 | A1V | $65.89^{+0.70}_{-0.58}$ | 320 | 2.42 | 59204.33 |
| HD 74198[a] | A1IV | $55.6^{+0.6}_{-0.6}$ | 320 | 2.49 | 59204.39 |
| HD 74873 | A1V | $54.82^{+0.15}_{-0.14}$ | 50 | 1.88 | 59204.36 |
| HD 77660 | A8V | $78.28^{+0.20}_{-0.19}$ | 710 | 1.81 | 59203.43 |
| HD 84107 | A2IV | $51.24^{+2.38}_{-0.98}$ | 10 | 1.44 | 59203.45 |
| HD 92941[a] | A5V | $66.9^{+1.4}_{-1.4}$ | 450 | 1.84 | 59204.48 |
| HD 97244 | A5V | $62.19^{+0.18}_{-0.15}$ | 60 | 1.72 | 59204.45 |
| HD 99787 | A2V | $69.64^{+0.68}_{-0.89}$ | 280 | 2.32 | 59203.48 |
| HD 106591 | A3V | $24.86^{+0.58}_{-2.58}$ | 320 | 2.31 | 59706.22 |
| HD 106661 | A3V | $66.01^{+0.09}_{-0.21}$ | 400 | 2.29 | 59204.51 |
| HD 112734 | A5 | $73.73^{+0.44}_{-0.30}$ | 40 | 1.69 | 59203.53 |
| HD 115271[a] | A7V | $74.1^{+2.4}_{-2.4}$ | 560 | 2.10 | 59203.59 |
| HD 118232 | A5V | $56.83^{+0.36}_{-0.35}$ | 500 | 2.38 | 59706.27 |
| HD 120047 | A5V | $52.84^{+0.79}_{-0.39}$ | 500 | 1.78 | 59204.60 |
| HD 121164 | A7V | $73.60^{+0.58}_{-0.44}$ | 500 | 1.97 | 59204.57 |
| HD 124675 | A8IV | $49.62^{+0.27}_{-0.27}$ | 500 | 2.38 | 59706.31 |
| HD 125161 | A7V | $29.86^{+0.97}_{-0.35}$ | 50 | 1.81 | 59706.33 |
| HD 130109 | A0V | $43.46^{+0.45}_{-0.42}$ | 320 | 2.71 | 59705.32 |
| HD 141378 | A5IV | $53.77^{+0.20}_{-0.19}$ | 250 | 2 | 59705.35 |
| HD 147547 | A9III | $61.84^{+0.51}_{-0.56}$ | 500 | 2.5 | 59707.37 |
| HD 152107 | A2Vspe... | $53.31^{+0.27}_{-0.27}$ | 400 | 2.31 | 59706.37 |
| HD 154494 | A4IV | $42.22^{+0.20}_{-0.02}$ | 280 | 2.02 | 59707.41 |
| HD 156729* | A2V | $52.08^{+0.07}_{-0.06}$ | 350 | 2.4 | 59790.18 |
| HD 158352 | A7V | $64.03^{+0.05}_{-0.07}$ | 630 | 2.1 | 59705.42 |
| HD 165777 | A4IVs | $27.72^{+4.18}_{-0.60}$ | 400 | 2.08 | 59705.45 |
| HD 173582 | A3 | $48.32^{+0.96}_{-0.92}$ | 400 | 2.13 | 59706.41 |
| HD 173607 | A5 | $49.17^{+0.25}_{-0.25}$ | 350 | 1.99 | 59706.45 |
| HD 173880 | A5III | $27.95^{+0.04}_{-0.03}$ | 110 | 1.94 | 59705.48 |
| HD 174602* | A3V | $74.20^{+1.55}_{-1.10}$ | 500 | 2.32 | 59790.22 |

Table 4.2: Continuation of Table 4.1

| Target Name | SpType | Distance (pc) | Age (Myr) | Mass ($M_\odot$) | MJD |
|---|---|---|---|---|---|
| HD 177724 | A0Vn | $26.16^{+0.24}_{-0.24}$ | 130 | 2.93 | 59705.51 |
| HD 184006 | A5V | $37.54^{+0.24}_{-0.24}$ | 450 | 2.34 | 59706.49 |
| HD 192640* | A2V | $40.74^{+0.15}_{-0.15}$ | 40 | 2.71 | 59790.26 |
| HD 199254 | A4V | $61.29^{+1.31}_{-0.52}$ | 450 | 2.06 | 59705.53 |
| HD 204414* | A1V | $60.25^{+0.39}_{-0.32}$ | 200 | 2.19 | 59790.3 |
| HD 205835* | A5V | $67.33^{+4.37}_{-3.14}$ | 630 | 2.2 | 59790.33 |
| HD 210715* | A5V | $55.61^{+0.65}_{-0.80}$ | 500 | 2.04 | 59790.37 |
| HD 213558* | A1V | $31.75^{+0.20}_{-0.20}$ | 130 | 2.45 | 59790.39 |

Table 4.3: Table of calibrators. *) Observed with both MIRC-X and MYSTIC at CHARA Array. 1) Swihart et al. (2017), 2) Bourges et al. (2017)

| Calibrator Name | UD diameter (mas) | Night UT | UD Reference |
|---|---|---|---|
| HD 99787 | 0.303 ± 0.024 | 20 Dec. 2020 | 1 |
| HD 44851 | 0.58 ± 0.014 | 20 Dec. 2020 | 2 |
| HD 21912 | 0.276 ± 0.007 | 20 Dec. 2020 | 2 |
| HD 120047 | 0.308 ± 0.008 | 21 Dec. 2020 | 2 |
| HD 32301 | 0.479 ± 0.033 | 21 Dec. 2020 | 2 |
| HD 74198 | 0.362 ± 0.024 | 21 Dec. 2020 | 2 |
| HD 19066* | 0.85 ± 0.06 | 21 Oct. 2021 | 2 |
| HD 141378 | 0.314 ± 0.009 | 6 May 2022 | 2 |
| HD 158352 | 0.41 ± 0.01 | 6 May 2022 | 2 |
| HD 173880 | 0.47 ± 0.05 | 6 May 2022 | 2 |
| HD 124675 | 0.55 ± 0.06 | 7 May 2022 | 2 |
| HD 152107 | 0.39 ± 0.03 | 7 May 2022 | 2 |
| HD 184006 | 0.59 ± 0.04 | 7 May 2022 | searchcal |
| HD 161868 | 0.57 ± 0.04 | 8 May 2022 | JMMC |
| HD 174602* | 0.36 ± 0.01 | 30 July 2022 | 2 |
| HD 204414* | 0.282 ± 0.009 | 30 July 2022 | 2 |
| HD 14055* | 0.47 ± 0.033 | 30 July 2022 | searchcal |

on Gitlab [1]. This pipeline measures the visibilities, closure phases, and differential phases from each baseline pair in the raw interferometric data. We reduced our data with most of the default reduction parameters, setting the number of coherent integration frames (ncoh) to 10. We used an oifits maximum integration time of 60 seconds, which is lower than the default value of 150 seconds. This allows us to search for wider binaries, which create signals in visibility and phase that vary on faster timescales.

To calibrate the data and produce our final OIFITS files we used a modified version of the MIRC-X pipeline, which uses similar routines in IDL as the pipeline for the previous Michigan InfraRed Combiner (MIRC, Monnier et al. 2007; Zhao et al. 2009; Che et al. 2011; Monnier et al. 2012). This routine is well-tested with previous MIRC data to properly flag and remove bad data, which can otherwise corrupt binary fits and lead to worse non-detection maps.

### 4.3.3 Data Analysis

In order to identify companions to the targets in our sample of A-type stars, we applied the open source python code CANDID (Companion Analysis and Non-Detection in Interferometric Data, Gallenne et al., 2015) to the OIFITS data of each observation. This code is designed to identify companions through a grid search of three dimensional space (position and flux ratio). It can use information from the visibilities, bi-spectrum amplitudes, and/or closure phases to perform binary model fitting for a given dataset. Closure phase is an interferometric quantity derived from the fringe phases of each pair of apertures within a closed triangle of three baselines (e.g. three telescopes), utilized to remove phase errors (Jennison, 1958; Rogers et al., 1974; Monnier, 2000; Monnier et al., 2004). For our purposes, we only used the closure phase information to find companions.

A symmetric brightness distribution will have measured closure phases of 0 or 180 degrees within the errors of the measurements for each combination of three telescopes. Any scene deviating from a point-symmetric object (e.g. a binary) will produce non-zero closure phases with amplitudes on the order of the amount of deviation (e.g. flux ratio). In this case, the grid search of CANDID will find the best-fit binary model that best replicates the observed closure phases including those deviating from zero.

CANDID provides a figure of merit in terms of n$\sigma$ calculated from $\chi^2$ statistics, defined in Gallenne et al. (2015), to differentiate between a single source (uniform disk) and a binary model from the searched grid space. First, we used the closure phase and visibility information to best estimate the diameter of the primary star with CANDID, which we then used as the diameter of the uniform disk model. We then searched for companions within the closure phase data out to

[1] https://gitlab.chara.gsu.edu/lebouquj/mircx_pipeline, remember to include the underscore in copied link

Table 4.4: Detected binaries with resolved flux and flux ratio in percent relative to the primary, projected separations in arcseconds, position angles in degrees, uniform disk diameter of the primary and secondary in milli-arcseconds, and the reduced chi squared test statistic of a single star model and binary star model. All parameters were derived using CANDID fitting to the closure phase and visibility data. All detections achieved the maximum significance threshold on CANDID, $8\sigma$.

| Target Name | Resolved Flux (% Primary) | Flux Ratio (% Primary) | Projected Sep. (mas) | PA (deg) (E of N) | $UD_1$ (mas) | $UD_2$ (mas) | $\chi^2_{\nu,1}$ | $\chi^2_{\nu,2}$ |
|---|---|---|---|---|---|---|---|---|
| HD 5448 | $-3.61^{+0.64}_{-0.70}$ | $1.573^{+0.039}_{-0.042}$ | 65.132 ± 0.007 | 144.324 ± 0.007 | 0.695 ± 0.002 | - | 1.75 | 1.22 |
| HD 11636 | $1.97^{+0.34}_{-0.38}$ | $13.546^{+0.11}_{-0.089}$ | 63.632 ± 0.002 | 102.271 ± 0.002 | 1.0819 ± 0.0008 | 0.549 ± 0.007 | 159.5 | 3.18 |
| HD 28910 | $4.09^{+0.72}_{-0.87}$ | $80.146^{+0.064}_{-0.067}$ | 6.135 ± 0.0013 | 304.81 ± 0.012 | $0.377^{+0.007}_{-0.006}$ | $0.341^{+0.008}_{-0.007}$ | 1332 | 1.17 |
| HD 29388 | $1.535^{+0.29}_{-0.32}$ | $2.488^{+0.024}_{-0.023}$ | 10.180 ± 0.002 | 23.59 ± 0.02 | 0.553 ± 0.005 | - | 4.39 | 1.14 |
| HD 48097 | $7.25^{+0.69}_{-0.66}$ | $2.84^{+0.119}_{-0.11}$ | 28.296 ± 0.007 | 14.16 ± 0.02 | 0.288 ± 0.015 | - | 2.26 | 1.51 |
| HD 205835 | - | 31.26±0.06 | 16.720 ± 0.001 | 181.55 ± 0.006 | 0.5 | - | 158.13 | 1.75 |
| HD 213558 | - | 3.42±0.03 | 158.138 ± 0.006 | 119.07 ± 0.012 | 0.5 | - | 2.37 | 1.48 |

Table 4.5: Physical separation in au, masses ($M_\odot$), and mass ratios (q). Companion masses are estimated using the MIST evolutionary models and the assumed primary mass and age from De Rosa et al. (2014), see Table 4.1. *) Mass may be overestimated due to high mass ratio and prior method of estimation. Mass ratios are still reliable. Cf. other A8V stars in sample.

| Target Name | Physical Sep. (au) | $M_{prim}$ ($M_\odot$) | $M_{sec}$ ($M_\odot$) | q |
|---|---|---|---|---|
| HD 5448 | 2.760 ± 0.013 | 2.39 | 0.60 | 0.25 |
| HD 11636 | 1.145 ± 0.013 | 2.01 | 1.05 | 0.52 |
| HD 28910* | 0.288 ± 0.002 | 2.21 | 2.12 | 0.96 |
| HD 29388 | 0.480 ± 0.012 | 2.17 | 0.67 | 0.31 |
| HD 48097 | 1.23 ± 0.04 | 1.94 | 0.40 | 0.21 |
| HD 205835 | 1.105 ± 0.002 | 2.20 | 1.57 | 0.71 |
| HD 210715 | 8.86 ± 0.004 | 2.04 | 0.70 | 0.34 |

separations of 0.3", the extent of the interferometric field of view in grism mode. We define $5\sigma$ as the cutoff for companion detection as suggested by the CANDID authors.

Upon detection of a companion, we re-run CANDID using all available variables to derive the best fit binary model to the closure phase and visibility data. CANDID allows for the fitting of the diameter of both components of the binary as well as fitting the "resolved flux" value which represents the visibility at a baseline of zero, typically accounting for any errors in calibration. For binaries where we can resolve both components, our final binary model has six parameters: separation and position angle of the companion relative to the primary, the diameters of each components, the flux ratio between components, and the resolved flux of the visibility data. For binaries with only a resolvable primary, we assume a diameter of 0.01 mas for the companion and use a five parameter binary model. See Table 4.4 showing the values of each of these parameters for our detections. For two detections, HD 205835 and HD 213558, the squared visibilities were noisy, and it was difficult to estimate the diameters and resolved flux. Therefore, we only used the closure phases to identify companions and estimate fluxes. There was no obvious impact of a resolved primary on the derived companion parameters, and thus our exclusive use of the closure phases for these two sources is appropriate.

## 4.4 Results

### 4.4.1 Detections

We detected 7 companions out of the 58 A-type stars in our sample. All detections had a significance of $8\sigma$, the maximum permitted value in CANDID, indicative of strong detections. These companions were detected at projected separations = 6 - 158 mas (physical separation = 0.288 - 8.86 au) with flux ratios = 1.5 - 80%, see Fig. 4.1 and Table 4.4. Two of these detections, HD 11636 and HD 28910, were previously reported as spectroscopic binaries (Abt, 1965; Pourbaix, 2000) with only HD 11636 having reliable orbital parameters. Based on the inclination, eccentricity, and semi-major axis estimates of Pourbaix (2000), we estimate the range of possible projected separations for HD 11636 to be from 4-68 mas, consistent with our detection at 64 mas near apocenter. All seven targets to which we detected a companion (except HD 11636, too bright for reliable Gaia information) were reported as having a proper motion anomaly using Hipparcos and Gaia catalogs that could be indicative of a companion (Kervella et al., 2019). However, only two of the seven detections we made (HD 28910 and HD 205835) were identified in Gaia Data Release 3 (DR3) as a non-single star (Gaia Collaboration et al., 2022). Gaia DR3 reports a period of 58.94 ± 0.09 days and an eccentricity of 0.31 ± 0.16 for HD 28910. Given our mass estimate of this system, see Table 4.5, and the period from Gaia, we estimate a semi-major axis of 0.48

au and a minimum and maximum distance from the primary as 0.33 and 0.63 au assuming the eccentricity from Gaia. Our estimate of 0.288 au is within the errors of the current Gaia estimate, indicative of a larger eccentricity than the median Gaia value. For HD 205835, Gaia DR3 reports a period of 596 days and an eccentricity of 0.51. We estimate a semi-major axis of 2.16 au and a minimum and maximum distance from the primary as 1.06 and 3.26 au assuming the eccentricity from Gaia which is within the range of our estimate, 1.105 au. Only two other sources in our sample were identified in Gaia DR3 as being non-single stars, HD 21912 and HD 106591. HD 21912 has a spectroscopically identified companion with a period of 0.92 days (Gaia Collaboration et al., 2022), likely at a separation smaller than our sensitivity. HD 106591 has an astrometrically identified companion with a period of 53 days and eccentricity of 0.45. Given its distance, the companion should have a distance of $\sim$ 0.2-0.5 au (3 - 8 mas) from the primary, but without a companion mass estimate we are unable to determine whether such a source should be detectable in the interferometric data. All other sources within our sample had no companion detections in either our analysis or Gaia DR3.

Because the estimated ages of our targets range from 10-790 Myr, see Table 4.1, we estimated the masses of each companion using the MIST evolutionary models (Paxton et al., 2011, 2013, 2015, 2018; Choi et al., 2016; Dotter, 2016). We assumed the primary mass and age estimates from De Rosa et al. (2014). They estimated ages based on the source position on the color-magnitude diagram relative to theoretical isochrones, and estimated masses based on their 2MASS K-band magnitude and estimated ages. We adopt these values for the primary stars and use the MIST isochrones to determine companion masses from the magnitude differences derived in CANDID. The mass ratios (q) of the detected multiple systems range from 0.21 - 0.96. The detections and the derived quantities of each system are listed in Table 4.5.

### 4.4.2 Detection Limits

CANDID offers a feature that derives the detection limit to any particular target. This is accomplished by injecting artificial companions at particular positions with specific flux ratios and evaluating the significance of a binary fit with those given values. The code then identifies the flux ratio at each step in separation where the detection significance level relative to the single star model is equal to $5\sigma$, see Gallenne et al. (2015). Because it searches the entire field of view, any given separation would have many injected companions at many position angles. To determine the detection limit at any given separation without position angle bias, we take the 99th percentile flux ratio that returns the $5\sigma$ result. In this case, there could be fainter companions at other position angles that correspond to the $5\sigma$ limit. This process results in a flux ratio at all steps in separation in which we can recover companions. For targets with detected companions, CANDID also offers

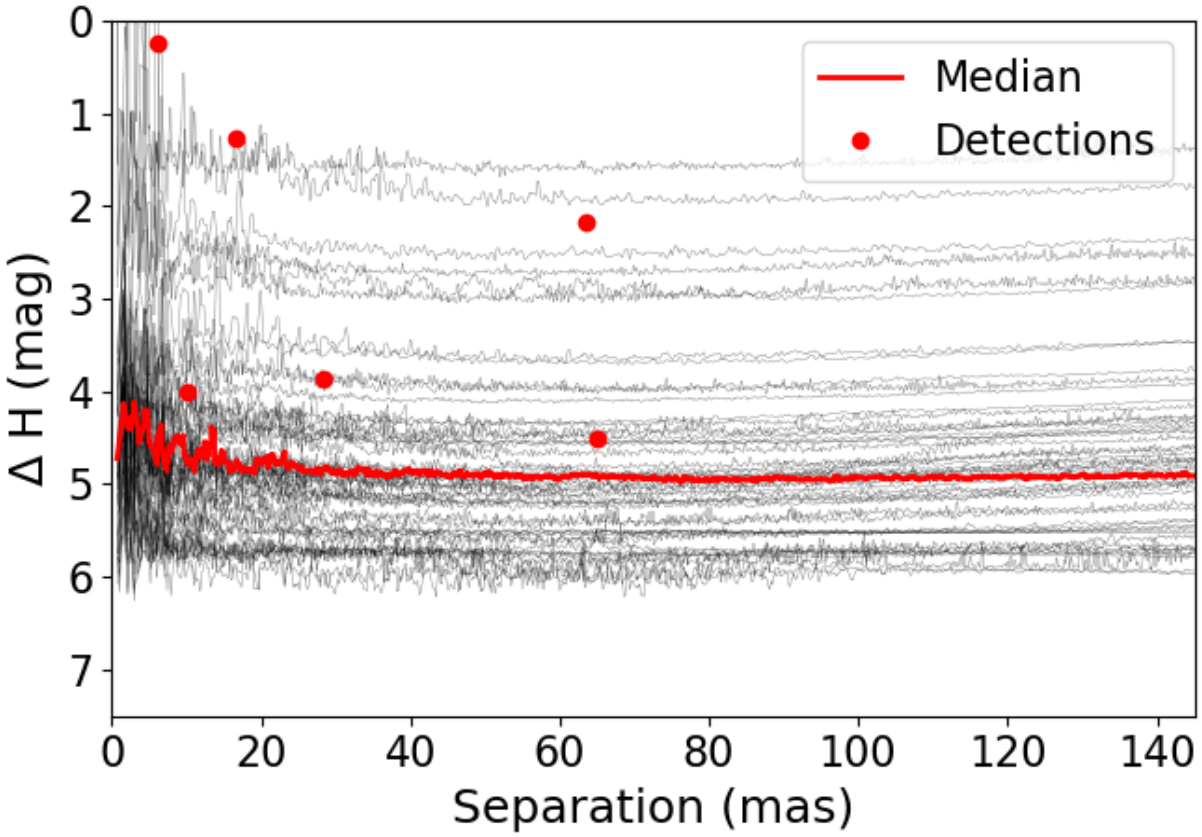


Figure 4.1: Detection limits derived from CANDID for each source are plotted in black with the median value at each separation displayed in red. Detection limits correspond to the 99th percentile companion flux at a given separation that results in a $5\sigma$ detection. Red circles represent the detections made in our survey at their given separation and contrast.

the ability to remove the signal of the detection and then carry out the detection limit procedure on the edited data. For sources with detected companions, we defined companion parameters by fitting the closure phase and visibility data for all free parameters, removed the signal, and then performed the detection limits procedure on the residual closure phase data.

Importantly, CANDID assume that errors in the interferometric observables are uncorrelated. However, interferometric observables are known to have correlated errors. Kammerer et al. (2020) estimated that the attainable contrast increases by a factor of 2 when estimating correlations as opposed to assuming uncorrelated errors. While assuming uncorrelated errors is a common approach to analyzing interferometric data (e.g. Gallenne et al., 2015; Lanthermann et al., 2023), it must be stated that this will only provide a conservative estimate to our limits, and does not achieve the absolute attainable contrast limit. No open-source software is available for the CHARA array that estimates correlations within the interferometric observables, and so we proceed with

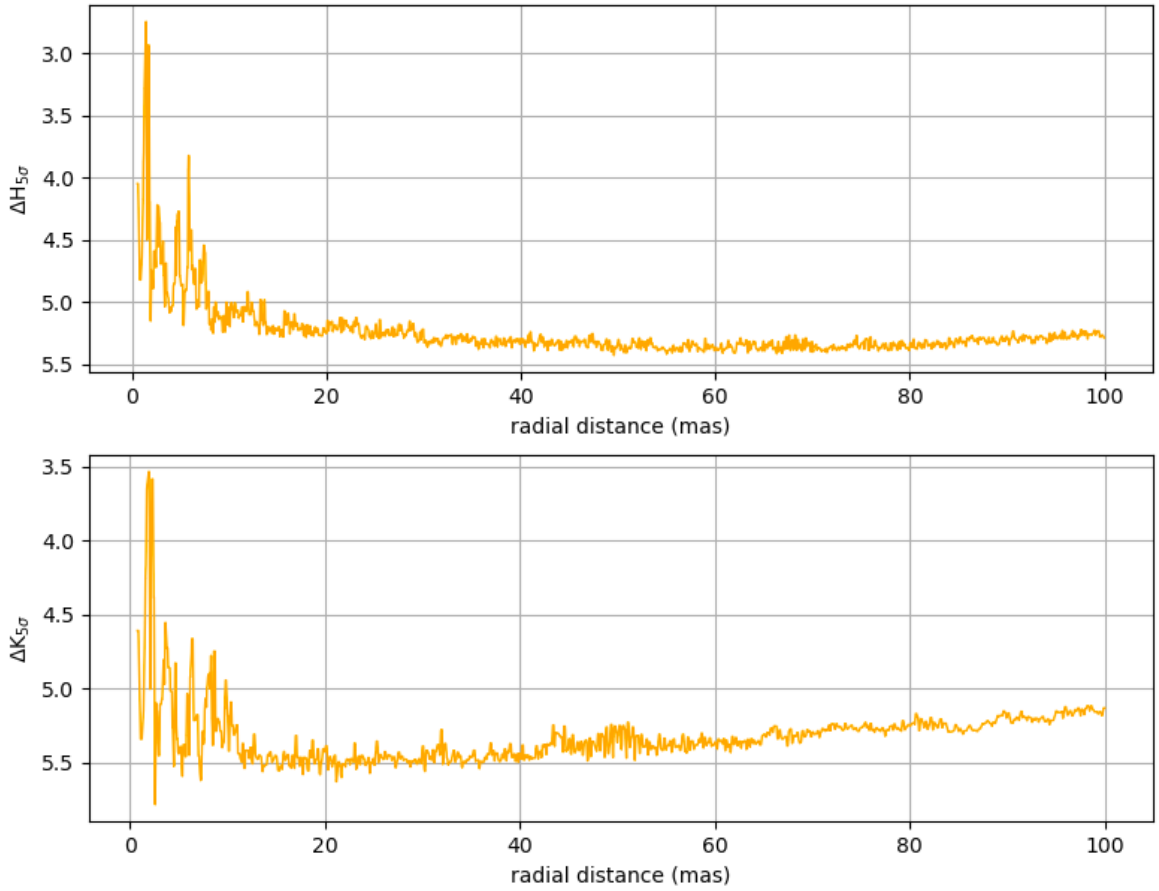


Figure 4.2: Derived detection limit for HD 31647 as a function of radius from the central star on both the MIRC-X and MYSTIC instrument. These data were collected simultaneously with 15 min integrations.

our analysis acknowledging that detection limits are conservative estimates.

Achievable contrasts typically range from $\Delta$H = 4.0-5.5 mag beyond $\sim$ 10 mas. The H-band mag of our targets range from 2.43 - 6.39 mag. For targets with H $\lesssim$ 5.8 mag, we can achieve typical contrasts under good conditions. For target with H $\gtrsim$ 5.8 mag, the achievable contrast is $<$ 4 mag at 10 mas, especially with worse weather conditions. In Fig. 4.1, we show the detection limits for each source in our sample with the median value at each separation highlighted in red and the values of the detections represented by red circles.

Using the achievable contrast at a given separation, we can calculate the lowest mass of a detectable companion for each target as a function of separation. Given the age (ranging from 10-790 Myr) and mass of the primary from De Rosa et al. (2014), we use the MIST evolutionary models to estimate the lowest mass of a detectable companion, and the lowest mass ratio of a detectable multiple system, at each separation.

Six targets stand out as having poor sensitivity (higher mass ratio limits) relative to the rest of

the sample. All were observed during poorer observing conditions. Three of these are the faintest sources in our sample and have H-band ≥ 5.9 mag (HD 77660, HD 24809, and HD 112734).

As an example of the detection limits with both MIRC-X and MYSTIC, we display the results for one target (HD 31647) which was observed simultaneously using 5 telescopes (instead of all 6) with 15 min total integration time. HD 31647 has H = 4.98 mag, a typical brightness for our sample, and we are able to detect companions at the $5\sigma$ level down to contrast of 5 mag beyond 10 mas with both MIRC-X and MYSTIC. The achievable contrast was similar between both instruments as shown in Fig. 4.2, but slightly better for MYSTIC.

### 4.4.3 Companion Population Analysis

Out of 58 A-type stars observed at CHARA, we detected seven companions. Four of these primaries had data that were very noisy and were not included in our final demographic analysis, which includes 54 A-type primaries. We must take into account our sensitivity to companions for each source in terms of flux ratio and separation in order to adequately characterize this stellar population.

As in Sec. 2.7.1.3, we can use the derived detection limits to each source and the estimated companion parameters of our detections to place constraints on the companion population. Detection limits in terms of mass ratio and projected separation were defined as described in Sec. 4.4.2, using the age and mass estimates of De Rosa et al. (2014), the MIST evolutionary models, and distance estimates from Gaia DR3. We then constructed a detection probability map to determine the sensitivity of the whole survey, see Fig. 4.3. Due to the different distances to our sources, the inner and outer working angle is not the same in terms of physical separation for each source and therefore there is a gradient of sensitivity up to the region of common sensitivity of all sources.

We model the companion population just as in Sec. 2.7.1.3 with two models. The two-parameter model assumes a power-law fit to the mass ratio distribution and a flat separation distribution. The four-parameter model assumes a power-law fit to the mass ratio distribution and a log-normal fit to the separation distribution. We generate companions over 0.01-27.54 au and q=0.1-1.0, the range of sensitivity of our survey. Additionally, we define flat priors with -5.0 < $\beta$ < 5.0, 0.001 < $\overline{a}$ < 20.0 au, 0.1 < $\sigma_{loga}$ < 3.0, and 0.0 < $CF$ < 1.0. Then, the Bayesian analysis is performed just as in Sec. 2.7.1.3.

From our sample of 54 A-type primaries, we estimated the following four parameters over mass ratios = 0.1-1.0 and projected separation 0.01-27.54 au with $1\sigma$ errors (68% confidence interval): $\beta = -0.21^{+0.83}_{-0.85}$, $CF = 0.23^{+0.15}_{-0.1}$, $\overline{a} = 7.41^{+8.3}_{-5.5}$ au, and $\sigma_{loga} = 1.62^{+1.02}_{-0.83}$. As shown in Fig. 4.4, the parameters of the projected orbital separation distribution are unconstrained, likely due to the low number of detections in our sample. For the two parameter model, we find: $\beta = -0.22^{+0.94}_{-0.88}$, $CF$ =

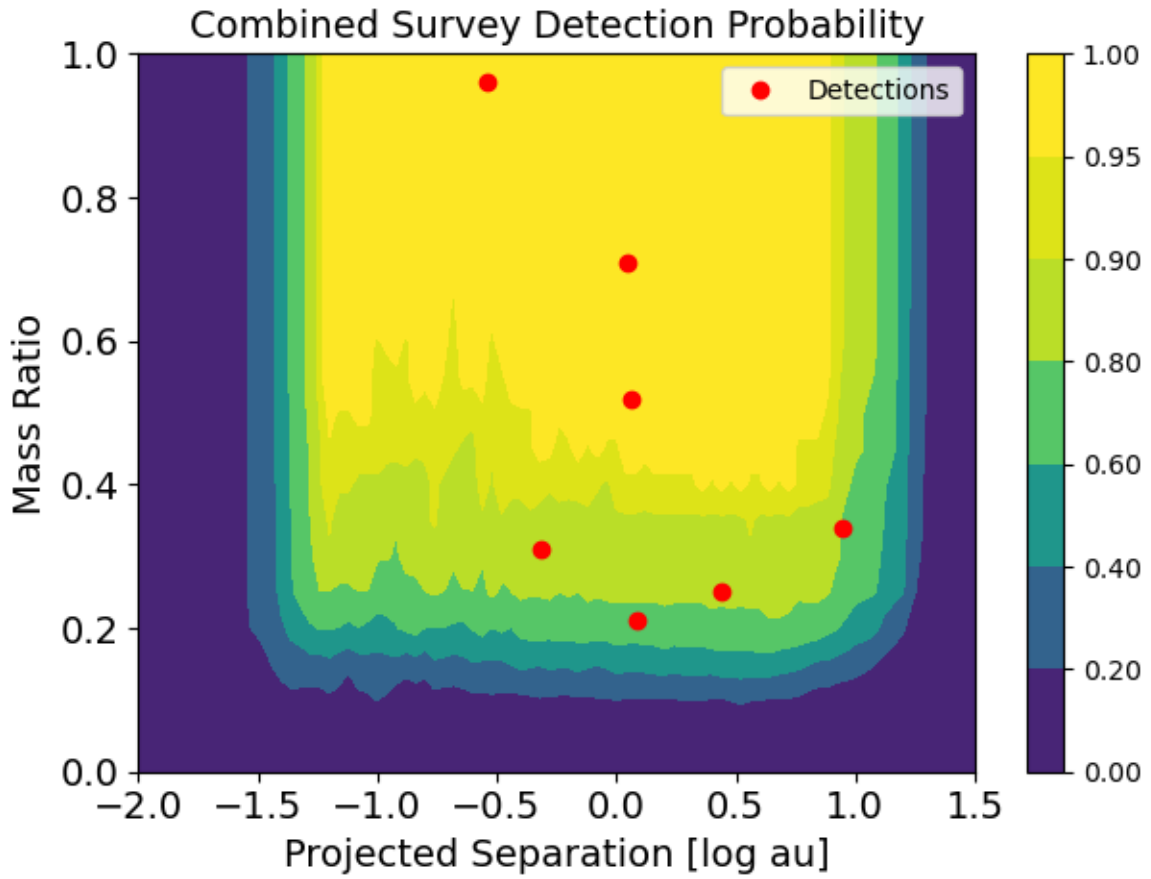


Figure 4.3: Summed detection probabilities for all the 54 sources in our survey. Red circles show the projected separation and estimated mass ratios for all detected companions. We use this map in Sec. 4.4.3 to model the separation and mass ratio distribution of the companion population to A-type primaries within 80 pc.

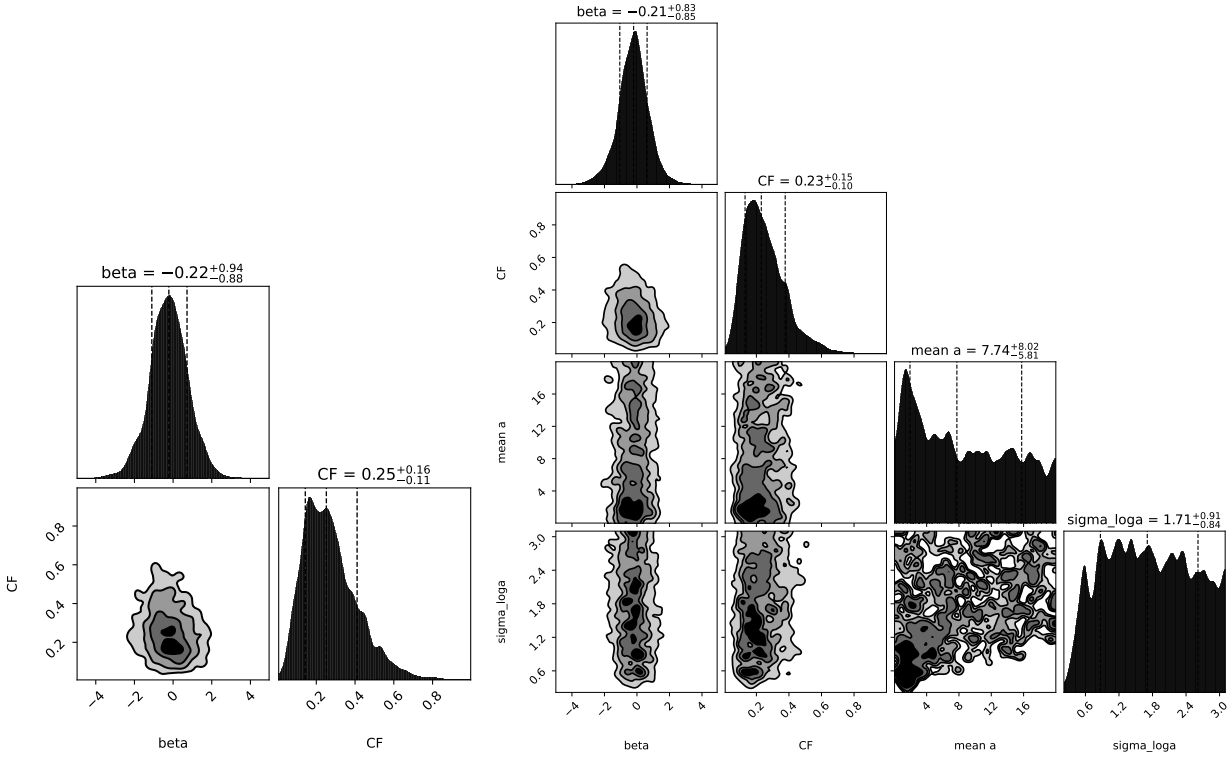


Figure 4.4: Corner plots representing the posterior distributions of the companion population model used in our fit. Beta is the exponent to the power law model of the mass ratio distribution, CF is the companion frequency over q=0.1-1 and a=0.01-27.54 au, mean a is the mean separation of the log-normal separation distribution in units of au, and sigma_log(a) is the standard deviation of the log-normal separation distribution. The separation distribution is unconstrained with a log-normal, likely due to the low number of detections in our survey.

$0.25^{+0.16}_{-0.11}$. Between these two models, the difference in the Bayesian evidence is 0.2. Therefore, the comparison is inconclusive and we draw no distinction between the two models. This allows us to conclude that the observed companion population is not better modeled by a log-normal distribution fit compared to a flat separation distribution, and we will use the two-parameter model for further analysis.

## 4.5 Discussion

Our source list was derived from the De Rosa et al. (2014) VAST sample. We excluded sources with known Ap or Am spectral types, but did not make sample selections based on previously detected companions. Sources were then randomly selected based on the nights allocated. Of the seven binary detections we made over separations of 0.288-8.86 au, five of the sources were targeted for companion search through adaptive optics imaging and common proper motion analysis. Only one

was found to have a companion over separations sampled, HD 205835, at a separation of 454 au and mass ratio of 0.05. Therefore, this is a triple system. HD 5448 was observed from 32 - 794 au and 3980 - 45000 au. HD 11636 was observed from 32 - 158 au and 3980 - 45000 au. HD 48097 was observed from 70 - 354 au and 1780 - 45000 au. HD 205835 was observed from 32 - 794 au and 3980 - 45000 au. HD 210715 was observed from 32 - 794 au.

### 4.5.1 Comparing the Companion Population to Models

#### 4.5.1.1 Comparing the Mass Ratio Distribution

We derived a best fit power-law index of $-0.22^{+0.94}_{-0.88}$ to the mass ratio distribution for the close companions to A-stars. Interestingly, Moe and Di Stefano (2017) and El-Badry et al. (2019) both describe a model of the companion population to A-stars as weighted towards smaller mass ratios with an excess twin binary component by analyzing results for wider companions from De Rosa et al. (2014). Although we only have seven detections, five of those seven are smaller mass ratios between q=0.21-0.52 where one (q=0.96) is considered a twin ($q \geq 0.95$).

The De Rosa et al. (2014) multiplicity survey of A-type stars is sensitive to companions beyond $\sim$ 30 au and mass ratios $\geq$ 0.15 for a majority of their sample. For companions between 30-125 au and 125 - 800 au, they describe the mass ratio distribution as a power law with a best-fit index $\beta$ = $-0.5^{+1.2}_{-1.0}$ and $-2.3^{+1.0}_{-0.9}$ respectively. Our results are consistent with both of these power-law fits given the relatively large errors in both our estimate and that of De Rosa et al. (2014). A future expansion of this survey would allow for a larger sample of detected companions which would greatly reduce errors on the power-law index to the mass ratio distribution.

#### 4.5.1.2 Comparing the Companion Frequency

Previous surveys have estimated the companion frequency to A-type stars with methods other than long-baseline interferometry. Murphy et al. (2018) used a phase modulation technique on Kepler light curves (see Murphy et al., 2014) to identify companions to $\delta$ Scuti variable stars (type A/F stars). With these data, they are sensitive to companions with periods $\gtrsim$ 100 days where incompleteness becomes large, and < 1500 days, or a $\sim$ 0.6 - 3.6 au. They found a companion frequency of 0.139 $\pm$ 0.021 after accounting for white dwarf companions (evolved higher mass stars that would have served as the primary before evolution). Roughly two-thirds of their companions have q > 0.25 after accounting for incompleteness, for a companion frequency of $\sim$ 0.095 $\pm$ 0.021. For our sample over a = 0.6 - 3.6 au (the sensitivity of Murphy et al., 2018) and $q \geq 0.25$, we detected three companions out of the 54 sources in our sample for a rough companion frequency estimate of $0.06^{+0.05}_{-0.02}$, consistent with their results.

Table 4.6: Companion population parameters and sensitivities of each tested model with the resulting statistics, integrated over 0.01-27.54 au and mass ratios 0.1-1.0. 1) Raghavan et al. (2010), 2) De Rosa et al. (2014), 3) Rizzuto et al. (2013)

| Primary Spectral Type | $\beta$ | log($a_o$) | $\sigma_{loga}$ | CF | log(a) range | q range | Expected CF | Posterior Probability |
|---|---|---|---|---|---|---|---|---|
| FGK-type[1] | 0 | 1.7 | 1.68 | 0.61 ± 0.02 | -2 ≤ log(a) ≤ 4 | q ≥ 0.1 | 0.29 ± 0.01 | 0.53 |
| A-type[2] | $-0.5^{+1.2}_{-1.0}$ | 2.59 ± 0.13 | 0.79 ± 0.12 | 0.219 ± 0.026 | 1.5 ≤ log(a) ≤ 2.9 | q ≥ 0.1 | $0.028^{+0.018}_{-0.014}$ | 0.007 |
| B-type[3] | -0.46 ± 0.14 | 1.05 ± 0.2 | 1.35 ± 0.2 | 1.35 ± 0.20 | -2 ≤ log(a) ≤ 4 | q ≥ 0.1 | $0.70^{+0.14}_{-0.13}$ | 0.04 |

Abt (1965) searched for companions to A-type stars using radial velocity measurements from many different publications. It is difficult to constrain the sensitivity of this program (i.e. mass ratio limits) due to undefined errors in some of the measured velocities from past observations. However, they give a measurement error of $\sim$ 2 km/s for their own measurements, meaning they should be sensitive to stellar companions to intermediate mass stars from periods of roughly 100-1500 days, the sensitivity of Murphy et al. (2018). Nine of their detections have measured periods between 100-1500 days for a companion frequency of $0.16^{+0.06}_{-0.04}$ or $0.13^{+0.06}_{-0.04}$ after accounting for expected white dwarf companions (21% of expected companions). These results are consistent with both the Murphy et al. (2018) results and our own.

Additionally, our survey is sensitive over a defined range of orbital separations and mass ratios that may not correspond to the same sensitivity of previous surveys. However, many large surveys have modeled the distribution of orbital separations and mass ratios of their companion population using functional forms. We can take those functions, and integrate them over the sensitivity of our survey to derive an expected companion frequency (CF) of the model over our sensitivity. Then, we can derive a probability that our observations can be described by this model, and determine whether the model is representative of our results. We use the models for the companion population to solar-type primaries (Raghavan et al., 2010), A-type primaries (De Rosa et al., 2014), and B-type primaries (Rizzuto et al., 2013) to determine if any may be consistent with our results.

For these other surveys, the mass ratio distribution is well-fit with a power law and the orbital separation distribution is well-fit with a log-normal distribution with a peak (log($a_o$)) and a width ($\sigma_{loga}$), see eqs. 2.9 and 2.10. Integrating the mass ratio distribution of eq. 2.9 and the orbital separation distribution of eq. 2.10, we can calculate the expected CF over specified separations and mass ratios assuming they are independent:

$$CF = C_n \times \int_{q_1}^{q_2} \frac{dN_1}{dq} \int_{a_1}^{a_2} \frac{dN_2}{da} \tag{4.1}$$

First, we solve for $C_n$ by sampling from the companion distribution parameter values of each survey (see Table 4.6) $10^5$ times, assuming Gaussian errors and integrating over the stated sen-

sitivities. Then, we used the value of the constant to calculate the expected CF assuming those companion parameters over the sensitivity of our sample, q=0.1-1.0 and a=0.01-27.54 au. We integrate the posterior distribution of the companion frequency from our two parameter model, see Fig. 4.4, from 0 to the CF of each sampling stated above for the A-type model and from the CF of each sampling to infinity for the FGK- and B-type models. This ensures that the correct tail of the posterior distribution is evaluated to determine the posterior probability that the model can describe our observations of A-stars.

The expected companion frequencies are summarized in Fig. 4.5 where they are presented according to the individual survey. As shown in Table 4.6, the estimated posterior probabilities for the companion population models to solar-type, A-type, and B-type primaries are 0.53, 0.007, and 0.04 respectively. These results allow us to conclude that: a) there is a significant population of close companions to A-type stars that previous models from De Rosa et al. (2014) do not describe which must be modeled to have a complete picture of the companion population to intermediate mass stars, b) we find no evidence for a difference between the multiple population of our A-type sample and that of solar-type stars, and c) the companion frequency to B-type primaries is potentially larger than A-type primaries over mass ratios and separations sampled.

Additionally, it is important to note that Moe and Di Stefano (2017) refute the decrease of the separation distribution of De Rosa et al. (2014) for A-type primaries for a $< 100$ au. They argue that this decrease is due to incompleteness for $q < 0.2$, and calculate a consistent companion frequency per decadal bin in the log of the orbital period across roughly a=20-50 au and a=50-450 au, consistent with flat in log-period space. De Rosa et al. (2014) themselves argue that their model of the orbital separation distribution is inconsistent with the detected companions through radial velocity measurements of Abt (1965), and state that further observations are required to define the close companion population.

It is noteworthy that we excluded Am (chemically peculiar and weakly magnetic) and Ap (chemically peculiar and strongly magnetic) stars from our observed sample. Am stars have large companion frequencies at close separations (lower limit of 0.64, Carquillat and Prieur, 2007), while Ap stars are expected to have similar companion frequencies to their normal A-type counterparts. Abt and Levy (1985) hypothesize that the Am star (chemically peculiar and slowly rotating) phenomena are the result of a close companion causing tidal braking which slows the rotation of normal A stars. Once the rotation decreases below $\sim$ 100 km/s, diffusion within the star is allowed to bring metals to the surface which produces the metallic lines seen in Am stars (Michaud, 1980; Michaud et al., 1983). However, not all Am stars appear to have close companions, and the presence of metallic lines may need to be explained without tidal braking. One hypothesis is that as the star evolves off the main sequence, its expansion will slow down the rotation rate (Abt and Levy, 1985) below 100 km/s, allowing diffusion to proceed, producing the metallic lines seen in the Am spectra.

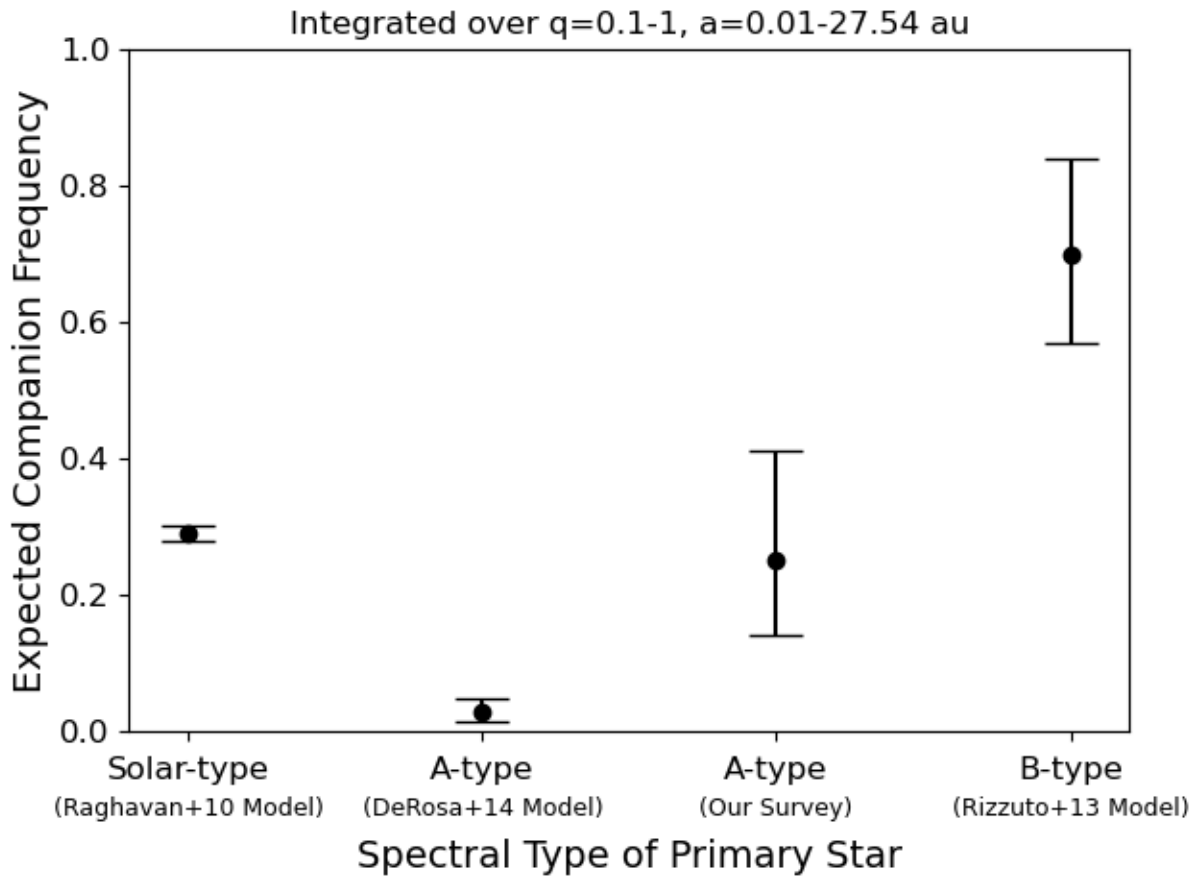


Figure 4.5: Companion frequencies based on spectral type of the primary star from the various models listed in Sec. 4.5.1.2. All frequencies are calculated over mass ratios = 0.1 - 1.0 and separations (a) = 0.01 - 27.54 au. The companion frequency for Solar-type primaries is derived from the model of Raghavan et al. (2010), A-type primaries from the model of De Rosa et al. (2014) and this survey, and B-type primaries from the model of Rizzuto et al. (2013).

Estimates for the occurrence of Am stars among all A-type stars range based on effective temperature. Abt (1981) and Gray et al. (2016) find an Am star incidence of ~ 30-35% among spectral types of A4-F1, but only a ~ 5% incidence for A0-A3. We can estimate the anticipated companion frequency of our survey if we selected a similar fraction of Am stars as is observed in the field. Thirty stars in our sample have spectral types between A4-A9, and 24 have A0-A3. If those 30 A4-A9 stars had the ~30% Am stars included in the sample, we would have observed 9 Am stars. Lower limits to the companion frequency of 0.64 mean we would expect to detect 6 companions to these hypothesized Am stars assuming we can detect all the companions, while the remaining 45 stars would have ~ 6 companions if they had the same occurrence rate of the real sample. This would result in a roughly 9% higher companion frequency than observed, still within the errors of our estimate. A volume-complete survey of all stars with masses ~ 1.5-2.5 $M_{\odot}$ would allow us to definitively characterize the companion population for these intermediate mass stars.

### 4.5.2 Implications

Our analysis of 54 A-type stars within 80 pc observed with long-baseline interferometry reveals a companion frequency of $0.25^{+0.16}_{-0.11}$ over mass ratios 0.1-1.0 and projected separations 0.01-27.54 au. In comparison to other multiplicity studies of stellar populations, we find that an extrapolation of the fitted companion properties to A-type primaries of De Rosa et al. (2014) cannot reproduce the observed companion frequency of our A-star survey over our sensitivity. However, they state that their model is inconsistent with previous detections at close separations and further investigations are required to define the companion population at small separations. We could not rule out their best-fit mass ratio distribution for either outer ($\beta$ = -2.3) or inner ($\beta$ = -0.5) binaries based on our results. We do not find any strong statistical difference between the companion frequency of solar-type stars in the field (Raghavan et al., 2010) and our sample of A-type stars, over common mass ratios and separations sampled. However, we calculate a probability of 0.04 that the companion frequency to B-type stars can describe the observations to our sample of A-type stars. These companion frequencies are summarized in Table 4.6 and Fig. 4.5 where they are presented according to the individual survey.

It is important to note that six of the seven companions were found at separations between 0.288-2.760 au. For many sources in our sample, our survey was sensitive to companions at separations greater than 2.760 au due to their distance (up to 78 pc) and our ability to detect companions out to 0.3", yet only one was found. It is a potentially curious observation, and a larger survey would allow us to probe whether this defecit of companions beyond 2.760 au is statistically significant.

Companions formed through turbulent fragmentation (Goodwin et al., 2004a; Offner et al., 2010) are thought to originate at separations of 100s-1000s au, while companions formed through

disk fragmentation (Adams et al., 1989; Bonnell and Bate, 1994; Kratter et al., 2008) are thought to originate at separations on the order of the size of the disk, 10-100s au. Various processes can reduce the separation of the companion below 10 au (Bate et al., 2003; Bate, 2012). These processes include accretion from the natal cloud, interactions with the circumbinary disk and gas in the natal cloud, dynamical effects within an unstable triple, the Kozai-Lidov mechanism, and more (Offner et al., 2010; Kratter, 2011; Moe and Kratter, 2018; Lee et al., 2019; Tokovinin and Moe, 2020). We cannot specifically determine which processes affected the binaries observed in our sample. However, we can conclude that these processes are important to a significant portion of the A-star population and are required to replicate our observations. Our results begin to place constraints on the companion population to intermediate mass A-type stars, and they indicate that such a population is significant and must be precisely characterized for a global understanding of star formation processes to intermediate mass stars. Our results also indicate a possible difference in companion frequency for A-type and FGK-type primaries relative to B-type primaries. If proven true, this may support the idea of an increased occurrence of disk fragmentation around stars more massive than $\sim$ 2.5 $M_\odot$ which could produce the large frequency of companions at such close separations. With a larger sample of A-type stars, we will be able to: a) place strong constraints on the companion frequency to A-type stars at close separations and look for differences as a function of primary mass, b) fit various mass ratio distributions to a larger set of companions to differentiate between potential formation mechanisms, and c) probe the functional form of the close companion orbital separation distribution which was unconstrained in this work.

## 4.6 Conclusion

We have conducted a survey of 54 nearby A-type stars within 80 pc using long baseline interferometry at the CHARA Array with the MIRC-X and MYSTIC instruments to search for close companions. To summarize the results of our survey:

1) We have shown that 20 min integrations with the Grism190 mode on targets with H $\leq$ 5.8 mag MIRC-X can achieve contrasts of 4-5.5 mag beyond $\sim$ 10 mas and 3-4.5 mag beyond 2 mas. We have also shown that MYSTIC has comparable, if not slightly better, sensitivity to faint companions compared to MIRC-X.

2) We detected 7 companions with projected separations 6-158 mas (0.288-8.86 au) and mass ratios = 0.21-0.96. For our sample of A-type stars with masses of 1.44-2.93 $M_\odot$, we observed a companion frequency of $0.25^{+0.16}_{-0.11}$ over mass ratios 0.1-1.0 and projected separations 0.01-27.54 au. This measurement is consistent with that of the spectroscopic survey of Abt (1965) and the pulsation timing analysis of Murphy et al. (2018) for AF-type primaries over separations and mass ratios sampled.

3) Our estimate of the companion frequency is larger than the calculated companion frequency after extrapolating the model fits of De Rosa et al. (2014) to the sensitivity of our survey with a probability of 0.007 that they can describe our observations. Although, they stated that further investigations are required to completely characterize the companion population down to small separations that are not included in their analysis.

4) Our estimate of the companion frequency is consistent with that of FGK-type stars, but we find a probability of 0.04 that the B-type companion population model can replicate our observed companion frequency to A-type primaries. This may be indicative of an increased occurrence of companions to B-type stars ($\gtrsim 2.5\ M_{\odot}$), potentially due to a higher incidence of disk fragmentation.

5) Our detections are consistent with being drawn from both a flat and negatively weighted mass ratio distribution. A larger sample size is crucial to characterizing the mass ratio distribution of close companions to A-type stars, and hence constraining potential formation mechanisms.

This work is based upon observations obtained with the Georgia State University Center for High Angular Resolution Astronomy Array at Mount Wilson Observatory. The CHARA Array is supported by the National Science Foundation under Grant No. AST-1636624 and AST-2034336. Institutional support has been provided from the GSU College of Arts and Sciences and the GSU Office of the Vice President for Research and Economic Development. Time at the CHARA Array was granted through the NOIRLab community access program (NOIRLab PropID: 2020B-0290; PI: M. De Furio). MIRC-X received funding from the European Research Council (ERC) under the European Union's Horizon 2020 research and innovation programme (Grant No. 639889). JDM acknowledges funding for the development of MIRC-X (NASA-XRP NNX16AD43G, NSF-AST 1909165) and MYSTIC (NSF-ATI 1506540, NSF-AST 1909165). We would like to thank the Jean-Marie Mariotti Center for providing the tools ASPRO2 and SearchCal, used to plan observations, available at http://www.jmmc.fr/aspro. S.K. acknowledges support from ERC Starting Grant and Consolidator Grant (Grant Agreement Nos. 639889 and 101003096). This work has made use of data from the European Space Agency (ESA) mission *Gaia* (https://www.cosmos.esa.int/gaia), processed by the *Gaia* Data Processing and Analysis Consortium (DPAC, https://www.cosmos.esa.int/web/gaia/dpac/consortium). Funding for the DPAC has been provided by national institutions, in particular the institutions participating in the *Gaia* Multilateral Agreement.

# CHAPTER 5

# Discussion

Multiplicity plays an important role in the formation of stellar populations across the mass spectrum. We must have a thorough understanding of the formation process of companions in order to obtain a comprehensive, predictive theory of star formation and understand how most stars form. The features of multiplicity are also key inputs to many other astrophysical phenomena from circumstellar disks and planets to Type Ia supernovae and gravitational waves sources. In this chapter, I discuss how my analyses impact our understanding of star formation as a function of primary mass and the effects of stellar environment. I also lay out open questions and speculate on their potential solutions that can be thoroughly explored with many of the same approaches described in this thesis.

## 5.1 Impact of Star-forming Environment on Companion Populations

In this section, we place observations of Class 0 protostars (young protostars where the majority of the final stellar mass is within the envelope yet to be accreted) in context of our observations of the companion population in the ONC and the impact of dynamics on the companion population. We also place our brown dwarf binary observations in the ONC in context of the theoretical framework of possible formation channels. Lastly, we discuss future programs designed to thoroughly explore companion populations in many varied star-forming environments and how these observations can answer the open questions of the origin of the Galactic field population, the precursor to OB associations, and impact of dynamics within regions of various stellar densities on companion populations.

### 5.1.1 Stellar Primaries

Observations of young protostars, as young as Class 0, in the Orion A, Orion B, and Perseus molecular clouds with the Atacama Large Millimeter Array (ALMA) show a prominent excess in observed companion frequencies compared to the field at separations 1,000 - 10,000 au after accounting for line-of-sight projections (Tobin et al., 2022). Unfortunately, these radio surveys of protostellar systems cannot estimate masses. Therefore, it is unclear how low in mass ratio these surveys reach and thus the measured companion frequency serves only as a lower limit. They speculate that turbulent fragmentation and disk fragmentation are both at play in order to replicate the observed companion frequencies, and that migration must occur at some level to reduce the amount of very wide companions and move them to closer separations. However, they are incomplete below 20 au and cannot constrain the quantity required to migrate in order to replicate the field population. They claim an increase in companion frequency within regions of surface density $> 30$ pc$^{-2}$ compared to those in lower surface density regions, attributing this to fragmented cores closer in proximity to one another in higher density regions which provides more sources to become bound, a result tentatively supported in Kounkel et al. (2016). However, the regions they explored are relatively low density compared to the stellar density of regions like the ONC. While these wide protostellar companions may form during the early Class 0 phase, in high density regions like the ONC, dynamical disruptions of multiple systems are likely to reduce the companion frequency at wide separations within $< 1$ Myr. Initial protostellar cores may frequently result in wide companions between 1,000-10,000 au, but dynamical interactions determined by the stellar density of the environment will shape the final configuration of the companion population.

Previous studies within the Taurus molecular cloud by Kraus et al. (2011) identify a significant excess of companions to stellar primaries over 3-5,000 au. My work in the Orion Nebula Cluster found that the companion frequency to low-mass primaries (0.1-0.7$M_\odot$) over 10-200 au was consistent with the Galactic field, but that Taurus was in excess of both the ONC and the field over those same separations. The differing companion frequencies between Taurus and the ONC can potentially be explained through the ALMA protostellar observations. Many companions form through turbulent fragmentation at wide separations, e.g. 100 - 10,000 au. For those at the widest separations (1,000 - 10,000 au), dynamical interactions at early times can disrupt a significant portion of the protostellar multiples. In the ONC, dynamical interactions have a larger impact on the frequency of companions at initially wide separations, preventing their future migration. This is especially important when dense environments experience a cool collapse phase that temporarily increases the stellar density by roughly an order of magnitude (Allison et al., 2009, 2010). In less dense environments, e.g. Taurus, dynamical interactions are much less likely to occur. With a longer amount of time to evolve without disruption, wide companions are able to migrate to closer separations due to dynamical friction from the gaseous envelope of both protostars, and can

eventually migrate within the disk of the primary as well (Bate et al., 2002, 2003). The inward migration increases the binding energy of the system, making it even more difficult to disrupt them.

Importantly, our analyses in Chapter 2 found that the power-law index of the fit to the mass ratio distribution was consistent between the field, the ONC, and Taurus for low-mass primaries over intermediate separations 10-200 au. The conserved shape of the mass ratio distribution may be crucial evidence for formation of low-mass stellar multiple systems invariant with respect to stellar density, and unaffected by local high-mass stars which impart a large amount of high energy photons into the gas. Parker and Reggiani (2013) performed an N-body simulation tracking the state of binary systems within a clustered environment. They concluded that the mass ratio distribution remains mostly unaffected by dynamical interactions because the perturbers that disrupt binary systems typically impart much larger energies than the binding energy ($E_{bind} = GM_1M_2/a \propto M_1^2 q/a$) of the system itself. Therefore, disruptions are less sensitive to the mass ratio of the system, which usually modifies the binding energy by up to a factor of 10 (90% of companions exist in systems with q=0.1-1.0 for a flat mass-ratio distribution), but are more sensitive to wide separations, which can range over many orders of magnitude out to 10,000 au. The significantly lower binding energy of wide companions would then mean that there are many more potential cluster members that could impart energies high enough to perturb those systems. In this scenario, companions form through both disk and turbulent fragmentation, migrating and accreting within the natal cloud and disk. Wide companion cores are disrupted in high density regions but remain intact in low density regions, allowed to continue their evolution. For cores that achieve intermediate separations, their mass ratios are determined by the initial core mass and the preferential accretion from the disk which would attain the same characteristic mass ratio distribution regardless of stellar density. The only tracer of this difference would be the companion frequency from intermediate to wide separations.

Using the formalism of Weinberg et al. (1987), we can estimate the characteristic lifetime of a binary system where catastrophic gravitational events disrupt the system, $t_{char} \propto \frac{M}{a} \times \frac{1}{n} \propto \frac{M_1(1+q)}{a} \times \frac{1}{n}$, where a is the separation of the binary, M is the total mass of the system, $M_1$ is the mass of the primary, q is mass ratio, and n is number density. Mass ratio (by definition between 0-1), can only impact this lifetime by a factor of two but the separation spans many orders of magnitude and has drastic effects. Within a high density environment, e.g. n = 1000 $pc^{-3}$, a binary with a 100 au separation, primary mass of 0.2 $M_\odot$ and mass ratio = 0.1 has a characteristic lifetime of $\sim$ 40 Myr. For separations of 1,000 and 10,000 au, the same binary has a characteristic lifetime of $\sim$ 4 Myr and 0.4 Myr respectively. Unbound star-forming regions will not remain at high densities for 10s of Myr, and therefore binaries at 100 au are expected to remain stable. However, wider systems at 1,000-10,000 au can be easily broken up within $\lesssim$ 1-10 Myr. Therefore, companions between 1,000-10,000 au where the excess was observed among Class 0 protostars can be disrupted

in high density regions, while the same binary in a low density region cannot be broken up within the time it takes the region to dissociate (e.g. Taurus with n∼1-10 $pc^{-3}$). Potentially, this allows wide companions in low stellar density regions to migrate inward and would result in an excess of companions compared to high density regions. The effect of dynamics is clearly important in shaping the companion populations within star-forming regions, and the outcome is a useful tracer of the environment in which multiple systems are born. Potentially, these low density regions do not contribute a significant fraction of the Galactic field population. However, it is also possible that low density regions contribute more intermediate separation multiples than ONC-like regions, but even higher density regions (e.g. Westerlund 1) contribute much less intermediate separation multiple systems than ONC-like regions (Patience et al., 2002). In this case, the Galactic field population has significant contributions from all regions, but ONC-like regions serve as an average companion population. Future observations in more varied environments are required to pursue this hypothesis.

### 5.1.2 Sub-stellar Primaries

Within the Galactic field, multiplicity surveys targeting sub-stellar primaries find very few companions beyond 20 au. These surveys are often small to moderate in size, between about 50-90 targets, but find a companion frequency of ∼ 0.01 for companions > 20 au. Wide companions to brown dwarfs have been detected in the Galactic field (e.g. Softich et al., 2022), but are more frequently discovered in young star-forming regions (e.g. Luhman, 2004). In the ONC, we find a companion frequency of 0.12 to brown dwarf primaries, in excess of that observed in the Galactic field over 20-200 au and q=0.5-1.0. However, the sub-stellar multiplicity surveys we compiled in nearby star-forming regions typically only have up to a few dozen targets. This makes statistical comparisons of companion populations more difficult due to large error bars. Relative to the Pleiades, we calculate a probability of 0.02 that its companion frequency to brown dwarfs is the same as that observed in the ONC. As the Pleiades is bound and a potential outcome of an ONC-like region (Kroupa et al., 2001a), it follows that dynamical interactions of wide sub-stellar binaries over 100 Myr could reduce the observed companion population of the ONC to resemble that of the Pleiades and also the field. We estimate that the observed sub-stellar binaries with the lowest binding energy can be broken up within 5 Myr and those with higher binding energies may take 10s of Myr. However, if the ONC remains bound as expected, a sizable number of these sub-stellar binaries will be disrupted.

Interestingly, Kraus and Hillenbrand (2012) estimated the power-law index to the mass ratio distribution for very low-mass/sub-stellar primaries (0.07-0.15 $M_{\odot}$) in Taurus and found an index = $4.0^{+1.9}_{-1.6}$ for companions at < 25 au and an index = - $0.3^{+0.7}_{-0.5}$ for companions at > 25 au. In our

estimates in the ONC over 20-200 au, we find that the mass ratios of our detected companions result in a p-value of 0.02 for a KS-test comparison to the Reid et al. (2006) mass ratio distribution ($\gamma$ = 3.6± 1.0) but 0.42 relative to a flat mass ratio distribution. While the Kraus and Hillenbrand (2012) sample was preferentially higher mass to our own and only had twelve detections, if these trends hold, it is possible that wide companions to brown dwarfs are disrupted in higher density regions (therefore not frequently seen in the field) while the closer companions were able to migrate inward at early times and competitively accrete within the disk of the primary building the mass ratio closer to one and thus a power law index highly biased to higher mass ratios (e.g. $\gamma$ = 3.6 for L-dwarf field sample, 6.1 for T-dwarf field sample, Reid et al., 2006; Fontanive et al., 2018). For example, if we assume that companions to brown dwarfs are drawn from the IMF through turbulent fragmentation and that the IMF can be modeled as a log-normal down to very low masses (Chabrier et al., 2000), then the resulting mass ratio distribution would be effectively linear where $\gamma \sim 1.0$ for the $\sim 0.07$ $M_\odot$ primaries in the Reid et al. (2006) sample (and more steeply peaked for lower mass primaries). While biased to higher mass ratios, the estimated power-law fit to the field data is even steeper, likely requiring preferential accretion within the disk to increase the mass ratio distribution to resemble that observed in the Galactic field population. As most companions to brown dwarfs in the field are within 10 au of the primary and would interact with the disk, this is a plausible mechanism to produce the observed field brown dwarf binaries (high q and a $\lesssim$ 10 au). The remaining wide systems in low density regions will then be the likely origin of the rare wide brown dwarf binaries found in the field (e.g. Softich et al., 2022).

### 5.1.3 Future Work

With the work carried out in this thesis, it is evident that environment plays a significant role in shaping the companion population of low-mass stellar and sub-stellar primaries. The primordial population is likely independent of stellar density, but then sculpted by migration and dynamical interactions. Over time, associations dissolve into the Galactic field population and even bound clusters expel a majority of their members into the Galactic field. Importantly, neither Taurus nor the ONC are likely dominant contributors to the Galactic field population. Taurus is a low mass, low density T-association that is likely a less common location for star formation compared to its higher density, similar mass counterparts. The ONC is a high density yet bound cluster, and remaining bound is an infrequent outcome for star-forming regions ($\sim$ 10% of stellar mass remains bound in long-lived clusters, e.g. the Pleiades, Johnson et al., 2016; Krumholz et al., 2019). The embedded cluster mass function predicts that equally spaced logarithmic bins in cluster mass creates a similar number of stars assuming the same IMF across 50-1000 $M_\odot$ (Lada and Lada, 2003), but this does not include stellar density as an input. Therefore, we must explore the companion populations of

more varied environments that span the possible range of stellar density and stellar mass in order to identify the major contributors to the Galactic field population and determine the extent to which dynamical interactions impact the companion populations across a broad range of primary masses and orbital separations.

Embedded clusters are intermediate density regions ($\sim$ 100-1000 $M_{\odot}pc^{-3}$, see Fig. 5.1) between Taurus and the ONC, have hundreds to thousands of members (spanning the embedded cluster mass function range), and account for up to 90% of all stars formed in giant molecular clouds (Lada and Lada, 2003), perhaps representing the most likely mode of star formation. These regions are also likely to become unbound after the gas is expelled from the region in contrast to regions like the ONC that are bound. Many embedded clusters exist within the Orion molecular clouds as well as others at comparable distances. An HST Cycle 30 program (ID 17141, PI: De Furio) is designed to observe NGC 1333, a more moderate density cluster, and perform a similar analysis to that presented in Chapter 2 across 0.01 - 1.0 $M_{\odot}$. Based on distance estimates to NGC 1333, projected separations down to 7.5 au are attainable. Other embedded clusters like IC 348 and NGC 2024 have JWST GTO programs dedicated to directly imaging these regions with NIRCam as a probe of the low mass end of the IMF (e.g. GO-1190, PI: Meyer). With an improved characterization of the bottom of the IMF, we will have strong predictions on the mass ratio distribution through turbulent fragmentation, particularly important for brown dwarf primaries . With these observations, multiplicity analyses can also be performed in a similar manner to Chapter 2 and 3.

Future JWST programs with NIRCam (some already planned through the GTO consortium, ID: 1190, 1202, 1228, 1229, and 1256) at 3-5 microns can efficiently target many embedded regions that would allow for the probe of the youngest regions closest to the primordial population attainable. This would then allow us to explore the sequential effects of dynamics, observing regions $\lesssim$ 1Myr to those between 1-10 Myr given similar densities. This would also allow for observing through highly extincted populations (e.g. NGC 2024), down to very low mass primaries (i.e. the opacity limit of fragmentation, due to JWST's unparalleled sensitivity), and image many cluster members simultaneously with the large NIRCam field of view while requiring only a few fields per region. Observing more regions also reduces the likelihood of companion population statistics from being stochastic which Parker and Goodwin (2012) warn can occur for individual regions.

In addition to embedded clusters, OB associations are another type of star-forming region that is likely a common location for stars to form. These regions are present-day low density environments with hundreds to thousands of stars as well as high mass stars. They are observationally unique from a region like Taurus due to the presence of high mass stars and the sheer amount of stars formed within them, but are not physically unique from lower mass T associations other than size. However, their origin is still debated. They could emerge from the expansion of an embedded cluster after the removal of its gas, and simply be an older phase of this star-forming region (Hills,

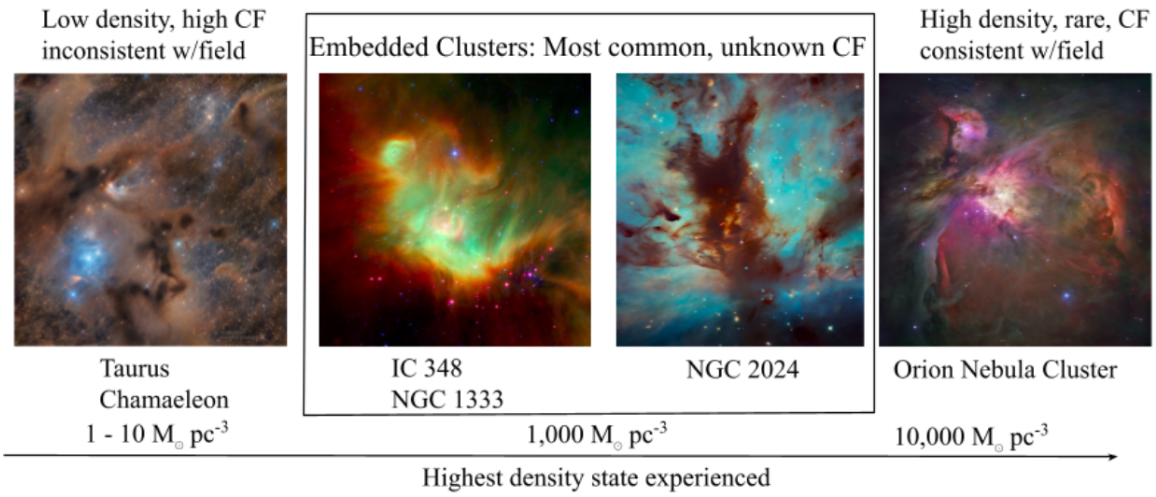


Figure 5.1: Example star-forming regions as a function of highest stellar density experienced throughout its lifetime, with estimates from Parker (2014). As differences in companion populations are seen between low density and high density regions, we must explore more moderate density regions to determine whether the companion population has a strong dependence on stellar density. Image credit left to right. Chamaeleon I: S. Volskiy (Chilescope.com), R. Eder, IC 348: NASA, ESA, J. Muzerolle, E. Furlan, K. Flaherty, Z. Balog, and R. Gutermuth, NGC 2024: NASA, ESA, N. Da Rio, G. Kober, ONC: F. Summers, M. Robberto.

1980; Kroupa, 2001; Goodwin and Bastian, 2006). However, recent observations of sub-structure within these regions indicates that they could form in situ having only ever experienced this low density environment, as sub-structures should be erased by the other cluster members in higher density regions (Könyves et al., 2010, 2020; Wright et al., 2022). If they emerge from embedded clusters, their primordial populations would have experienced significantly higher densities than presently observed which would sculpt their companion populations. If they formed in situ, multiple systems are likely unaffected by dynamical interactions due to the low density (Parker and Meyer, 2014). Therefore, their origin and their prevalence as a major contributor to the Galactic field population can be probed through their companion populations. It is difficult to perform high angular resolution surveys on OB associations as sources must be observed individually over large fields. However, with the launch of the Nancy Grace Roman Space Telescope planned in 2026, large regions can be observed with the Wide Field Instrument in the near infrared with diffraction limited imaging down to $\sim 0.1$" and nearly 100x the field of view of HST WFC3/IR. Other approaches to characterizing the multiplicity of OB associations are currently ongoing. One approach is to use the Gaia observatory to search for potential binary signatures within the archival data. The renormalised unit weight error (RUWE) is a measure of how well a single PSF fits the data, and poor fits are likely an indication that a companion exists. Gaia cannot resolve these companions or detect them astrometrically, but Wood et al. (2021) mapped out the region of angular separation

and contrast space where high RUWE values correspond to known binary parameters, sensitive over 0.03-1.0" and $\Delta$G = 0-5mag. With this metric, one can identify the sub-set of a region with companions over 0.03-1.0" from Gaia RUWE values, and observe only these systems to obtain accurate companion parameters. Then, the entire region can be characterized over this parameter space while only observing the sub-set of binary candidates. One such program is underway in Orion OB1a and OB1b (Briceño et al., 2019) using Keck/NIRC2-LGSAO (PID 121/2023B_N238, PI: De Furio) and Gemini speckle interferometry (GN-2023B-Q-226, GS-2023B-Q-218, PI: De Furio) where $\sim$ 20% of the region must be followed up from the ground to characterize their companion populations over 12-400 au.

Another important factor in the formation of multiple systems is the metallicity of the star-forming region in which these systems form. Previous analyses identified an increase in the frequency of multiples at close separations for solar-type stars with low metallicity, and a significant decrease for regions with high metallicity, from [Fe/H] = -1.0 to +0.5 (Moe et al., 2019). This was attributed to the gas of a circumstellar disk being coupled to the dust which radiates more efficiently as metallicity decreases and the opacity of the dust decreases. This more efficient cooling therefore makes the disk more susceptible to fragmentation. This was not observed for very low metallicity solar-type stars ([Fe/H] < -1.0) or for higher mass stars as they are already very susceptible to disk fragmentation. El-Badry and Rix (2019) saw a similar effect for stars with masses 0.45 - 1.5 $M_{\odot}$ with suspected unresolved companions between 50-200 au from the Gaia archive. However, this has never been observed for low-mass stars. Offner et al. (2010) concluded from simulations that low-mass stars are stable to disk fragmentation, but perhaps at low metallicities their disks will cool enough to fragment. We can explore this in more distant young star-forming environments that are currently too far away to probe 10-200 au separations. This is a particularly interesting question to answer for sub-stellar primaries as they become very faint with age and are difficult to observe within the Galactic field. Future thirty meter class telescopes with adaptive optics will provide diffraction limited imaging in the near infrared. The Extremely Large Telescope (ELT) will have a 39.3m diameter, and will be able to achieve 5 milli-arcsecond (mas) resolution, equivalent to 20 au at a distance of 4 kpc. The MICADO instrument on the ELT is a wide-field imager that will operate with the multi-conjugate adaptive optics module to achieve 5 mas resolution (with 4 mas pixels) within a 50.5" x 50.5" field of view. Although this is $\sim$ 6x smaller than HST WFC3/IR, the attainable resolution is 20x larger without having severely undersampled pixels. With this instrument, we will be able to explore star-forming regions with high angular resolution at distances never before studied. Sh2-284, the lowest known metallicity star-forming region in the Galaxy, is at a distance of 4.5 kpc making the diffraction limit at 1 micron comparable to $\sim$ 23 au. These types of observations will allow us to directly probe the effects of metallicity in the formation of companions at very early times, particularly at separations < 200 au and down to sub-stellar primaries.

Star-forming regions span orders of magnitude in size, density, and number of stars. These environments eventually populate the Galactic field population and can produce differing companion populations. With the onset of the largest space- and ground-based telescopes to date, the impact of dynamics on companion populations within young star-forming regions can be thoroughly described. These telescopes also allow us to probe the lowest masses that can be produced through the star formation process and thus test the many theoretical processes that produce stars, brown dwarfs, and multiple systems.

## 5.2 Formation of Stellar and Sub-stellar Multiples as a Function of Primary Mass

As described in Section 1.4, companion properties in the Galactic field population appear to heavily depend on primary mass. The peak in the separation distribution appears to decrease with primary mass from solar-type primaries to brown dwarf primaries (Duchêne and Kraus, 2013), where higher mass A- through O-stars appear to have a flat separation distribution across a broad range of separations (Moe and Di Stefano, 2017). Additionally, the power-law index of the fit to the mass ratio distribution increases as primary mass decreases, e.g. from -1.4 ± 0.4 to 4.8 ± 2.2 for O-type primaries to brown dwarf primaries over 1-100 au (Offner et al., 2023). These observed populations must be a direct result of turbulent and disk fragmentation, additional migration and accretion, and dynamical interactions both within the star-forming region and within the Galactic field. Some features of the field companion population have been thoroughly described and well explained, e.g. for higher mass O and B stars as well as FGK stars for $q > 0.1$ (Raghavan et al., 2010; Rizzuto et al., 2013; Sana et al., 2014). However, other features within the field population remain either unconstrained or incomplete.

There is also a reported trend that the companion frequency continues to decrease as a function of primary mass through low-mass brown dwarf primaries (Fontanive et al., 2018). However, some comparisons between M-type, FGK-type, and A-type primaries in the Galactic field over 0-10,000 au and $q \geq 0.6$ finds that the companion frequencies are more similar than appreciated (Susemiehl and Meyer, 2022). This analysis was performed by assuming functional forms (e.g. log-normal and power law), calibrating each survey to the observed companion frequency over its region of sensitivity, and integrating over the defined parameter space. While this result would seem to contradict reported companion frequency trends, it is important that these field surveys frequently suffer from incompleteness for which they do not correct and likely bias these results. In the same vein, analyses of the mass ratio distribution for low-mass stellar and sub-stellar primaries appear to show the power-law index increasing as primary mass decreases, but these estimates have large

error bars for brown dwarf primaries, making it difficult to truly identify significant differences with respect to their stellar counterparts.

Open questions still remain in the demographics of companions for particular primary masses and over specific separations in the Galactic field. In this section, I describe how results from this thesis inform our understanding of multiplicity in the Galactic field, and discuss potential programs that would greatly improve our characterization of companion populations for A-type stellar, M-type stellar, and brown dwarf primaries.

### 5.2.1 Intermediate Mass Stars

Previous spectroscopic surveys in the Galactic field observed chemically peculiar A-type stars that make up $\sim$ 15% of all A-stars (30-35% of A4-F1 stars), yet the vast majority of typical A-type stars were ignored (Abt, 1961; Carquillat and Prieur, 2007). A survey of $\delta$ Scuti variable stars (Murphy et al., 2018) characterized the companion population between 0.6-3.6 au for A and F stars in the field. A direct imaging survey by De Rosa et al. (2014) observed A-type primaries in the field, and were sensitive beyod 30 au but incomplete below $\sim$ 100 au. In this thesis, we observed 54 A-type field stars with the MIRC-X and MYSTIC instruments on the CHARA array and found a significant population of close companions over 0.01 - 27.54 au and q=0.1-1.0, with a companion frequency of $0.25^{+0.16}_{-0.11}$, and constrained the power law index of the mass ratio distribution, $\gamma$ = $-0.22^{+0.94}_{-0.88}$. This power-law index is consistent with a flat distribution, potentially resulting from disk fragmentation and turbulent fragmentation plus migration and preferential accretion. On the other hand, the companion frequency appears consistent with the FGK-type population, but lower than that of B-type stars. If true, then enhancement in the occurrence of disk fragmentation may begin at masses > 2.5 $M_\odot$. However, we only detected seven systems in our survey which leaves large error bars on the companion parameters. Therefore, a volume-complete sample of all primaries with intermediate masses 1.5-2.5 $M_\odot$ at distances $\lesssim$ 50 pc ($\sim$ 230 sources) using long-baseline interferometry would serve as the definitive statistical analysis of such a close companion population.

If the companion frequency increases continuously from FGK-stars (Raghavan et al., 2010) to B-type (Rizzuto et al., 2013) stars at close separations, with signs of competitive accretion in the mass ratio distribution, that would be evidence for enhancement of companions by disk fragmentation. Our results do not distinguish between the companions to A-type stars and FGK stars, but do show potential differences relative to B-type stars. In Fig. 1.3, analyses of field multiplicity surveys show a trend in the mass ratio distribution as a function of separation from FGK stars to O and B stars. However, the A-type population is not well characterized. With a large volume-complete survey extending from the current sample, we can characterize the companion population of A-type stars, and reduce the measured errors on the companion properties from the 54 star sample. The

trend in companion frequency across ~ 1-3 $M_\odot$ will determine whether disk fragmentation occurs continuously from ~ 1 $M_\odot$ or sharply near 2.5 $M_\odot$.

### 5.2.2 Low-Mass Stars and Brown Dwarfs

Most M-star surveys do not have a large sample of primaries between 0.1-0.3 $M_\odot$ (e.g. Ward-Duong et al., 2015). Large changes in the companion frequency are reported between M-type stars (~ 0.30-0.40) and brown dwarfs (~ 0.10-0.25). Also, brown dwarf surveys typically have small sample sizes which result in large 1-sigma error bars on the companion frequency of order 0.05-0.1. Due to the incompleteness in low-mass stellar primaries and uncertainties in brown dwarf companion statistics, it is unclear how companion properties change as a function of primary mass at the low mass end of the mass spectrum. Because of the apparent change in the mass ratio distribution and companion frequency between early M and TY-dwarfs, we must explore the companion populations for mid-/late-M and L-dwarfs to identify either a smooth transition or a steep break in companion properties.

The early M-star (0.3-0.6 $M_\odot$) population characterization would benefit greatly from a Bayesian demographic analysis. However, most surveys report statistics relative to some average contrast curve or correct for incompleteness after assuming a given model of the mass ratio or separation distribution. They also suffer from incompleteness at low mass ratios or small separations, that can leave surveys susceptible to biases not accounted for within their errors. There are two straightforward ways to improve our understand of this companion population. One way is to gather reported contrast curves on a source by source basis and companion detections across a broad range of surveys and perform a Bayesian demographic analysis similar to Sec. 2.7.1.3. This approach is complicated as most surveys do not present or report contrast curves in an easily digestible way, and it may suffer from Malmquist bias of the parent sample. Another possible approach is to perform a new volume complete survey within 10-20 pc using 4m class telescopes to resolve companions down to 0.1". With the sensitivity to 1-2 au and the derived contrast curves, a Bayesian analysis can be easily performed to determine the companion frequency and to characterize the mass ratio distribution and separation distribution. For the lower mass stellar portion (0.08-0.3 $M_\odot$), a similar analysis needs to be performed that will allow for the distinction between the higher mass M-stars and brown dwarfs, if one exists. Both samples must have hundreds of stars in order to produce small error bars. For a sample of 500 stars assuming a companion frequency of 0.30, we derive binomial errors to the companion frequency of 0.02, significant improvement over previous work. With the HRCAM at the 4.1m Southern Astrophysical Research Telescope, the typical limiting magnitude is I=12 mag (~ a 0.1$M_\odot$ star from 1-10 Gyr) and one can observe ~ 100 stars per night and detect companions through speckle interferometry down to 0.1" (Tokovinin et al., 2022). In 10 nights,

1000 stars spanning 0.1-0.6 $M_\odot$ can be observed to definitively constrain the companion population demographics down to small separations and high contrasts. On top of these analyses, the Gaia mission is expected to detect the astrometric signal from the presence of companions to sources with G mag $\gtrsim$ 21 mag. As the mission runs for five years, a 0.4 $M_\odot$ star with a 0.2 $M_\odot$ companion at 2.5 au in separation will complete one orbit within that time. Therefore, companions can be detected astrometrically with Gaia up to a few au in separation for primaries near the sub-stellar limit within $\sim$ 20 pc. Further away and lower mass primaries will not be strongly detected due to their low flux in the G band. The combination of Gaia and speckle imaging would provide strongly constrained estimates to the companion frequency and the parameters of the separation and mass ratio distributions to which we can compare to other surveys as a function of primary mass with sensitivity across a broad range of separations.

For the even lower end of the primary mass range, brown dwarf surveys in the Galactic field typically have small sample sizes, and resolution near the expected peak in the brown dwarf companion separation distribution. To combat the problems with large error bars across the sub-stellar mass range, a large multiplicity survey of brown dwarfs with sensitivity down to $\sim$ 1 au is needed. These programs are expensive and require large ground-based telescopes with laser AO or space-based imaging of sources individually. Luckily, many brown dwarfs have been previously observed in separate HST programs with various science goals. Through a review of the HST archive, up to 370 brown dwarfs can be explored for multiplicity using the same techniques as those described in Chapter 2 which would result in the largest brown dwarf multiplicity survey to date. Assuming a 0.15 companion frequency, we achieve 0.02 error bars for the full sample and 0.03 error bars if we split the sample in half for a high mass and low mass portion. A smaller number of detections and sample size in our stellar multiplicity ONC survey achieved power-law index errors of 1, whereas current errors for the low-mass brown dwarfs of Fontanive et al. (2018) are +4/-3. We would be able to see where and how the companion frequency, the peak of the separation distribution, and the power-law index to the mass ratio distribution change as a function of primary mass with a much greater degree of certainty compared to current studies. Current work with JWST (e.g. GO-2473, PI: M. Meyer, L. Albert) is targeting the coldest (i.e. oldest or lowest mass) primaries (Y-dwarfs) in a search for close companions, described in Chapter 3. This analysis will probe mass ratios down to $\sim$ 0.05-0.1 and separations down to 0.5 au. With well defined limits and a larger sample of brown dwarfs at the lowest mass ends, these analyses can be incorporated into a larger sample, like described above, to determine whether trends in the companion properties continue to decrease throughout the sub-stellar mass range. As these objects are the lowest mass free-floating field objects found to date, this analysis will serve as the best characterization of the companion population approaching the fundamental limit of turbulent fragmentation. With the detection of the first Y-Y dwarf binary system at 1 au in separation, this

program is already producing results that allow us to constrain the population of companions to the lowest primary masses explored. Companions may exist at closer separations < 1 au which can be explored with the onset of ELTs and with JWST spectroscopy searching for radial velocity signals.

We can also use the Very Large Telescope Interferometer (VLTI) and GRAVITY instrument to explore separations down to 1 mas for very low mass primaries. The dual-field wide mode of VLTI/GRAVITY allows for fringe tracking on references stars with K ≤ 10.5 mag with the science channel simultaneously focused on targets with K ≤ 17.5 mag as long as the reference is within 30" of the science target. For 10 $M_J$ objects with ages of 5 Myr and within a distance of 300 pc, VLTI/GRAVITY has the ability to resolve companions down to 1 mas as long as there is a brighter reference within 30". While appropriate references for fringe tracking may not exist for many field brown dwarfs, we can identify references within star-forming regions for sources with masses approaching the limit of fragmentation. We can define the primordial companion population to very low mass brown dwarfs within star-forming regions at separations down to 0.1 au for objects with distances of 100 pc. These observations achieve separations so far unattainable with any other observing technique for field brown dwarfs and would also allow for a comparison of the previously observed field companion population to that at very young ages beyond ∼ 1 au.

These observations of low-mass stars and brown dwarfs are complementary to the work performed in star-forming regions. The targeted star-forming regions discussed in Sec. 5.1.3 are too distant to resolve companions down to 1 au, but can detect Jupiter mass primaries while testing the impact of dynamics. These observations in the Galactic field will both define the final state of multiple systems at close separations as well as probe star formation processes down to ∼ 1 au. Mass ratio differences in the Galactic field as a function of separation have never before been shown for M-type stars or brown dwarf primaries. We identified a potential signal in our brown dwarf survey in the ONC, but cannot resolve companions down to the closest separations. With a thorough characterization of the companion population to primaries of ∼ 0.01-0.6 $M_\odot$ in the Galactic field, we can search for differences as a function of separation and primary mass. Then, we can compare the observations to purely being drawn from the IMF, or if further accretion after fragmentation was required to produce higher mass ratio systems. As low-mass stars are likely stable to disk fragmentation (at least for solar metallicity Offner et al., 2010), we can test the two hypotheses of either being drawn directly from the IMF with no further processes modifying the companion or requiring additional accretion to modify the companion properties.

While much is known about the companion population to stars in the Galactic field, there are still many open questions which must be explored through future analyses. These surveys have substantial consequences for our understanding of specific star formation processes that occur across the mass spectrum and across a broad range of orbital separations. With the success of the JWST and expectations of Roman and the ELT, there are many aspects of multiplicity formation

and evolution that will be answered in the years to come.

# CHAPTER 6

# Summary and Conclusion

In my thesis, we explored the formation of multiple systems both as a function of environmental properties and primary mass. This work utilized novel approaches to high angular resolution imaging as well as long-baseline interferometry to detect companions in a variety of astrophysical situations. While much is known about the formation of multiple systems, many questions still remain about the dominant formation mechanisms as a function of primary mass, mass ratio, and orbital separation. With better knowledge of companion populations as a function of primary mass, orbital separation, metallicity and environmental stellar density, we can construct a predictive theory of star formation that generates observed stellar populations in star-forming galaxies.

First, we used wide-field, diffraction limited imaging on the Hubble Space Telescope to explore the companion population of brown dwarf and low-mass stellar primaries within the Orion Nebula Cluster (ONC) down to 0.025" (10 au at 400 pc). We implemented a double point-spread function (PSF) fitting algorithm using empirically derived PSFs in order to detect companions within the wide field imaging data on the Advanced Camera for Surveys (ACS). We demonstrated the ability of this technique to recover companions down to 0.025" (0.5 ACS pixels, $\sim 0.5\lambda$/D). Then, we applied this technique to a sample of known brown dwarf and low-mass stellar members. We detected seven companions to 75 very low-mass stars and brown dwarfs ($\sim$ 0.012-0.1$M_{\odot}$), five of which are new detections. We also detected 44 companions to 276 low-mass stellar members (0.08-0.7 $M_{\odot}$), 19 of which (mostly at close separations) are new.

With these detections and defined detection limits to all sources (M=0.1-0.7$M_{\odot}$) in the sample, we performed a Bayesian analysis of the companion population to the stellar primaries. We estimate a companion frequency of $0.13^{+0.05}_{-0.03}$ and the index of the power law fit to the mass ratio distribution as $2.08^{+1.03}_{-0.85}$ over projected separations of 10 - 200 au and all mass ratios. The mass ratio distribution is consistent with both the Galactic field population and the companion population in Taurus and Upper Sco, indicating a possible sign of a formation mechanism independent of stellar density. We find that the companion frequency to low-mass stars in the ONC is consistent with the Galactic field, but that there is a probability of 0.002 that it can describe the observed companion population in Taurus, thus likely differing populations.

In our analysis of the companion population to very low mass stars and brown dwarfs, we find a companion frequency of $0.12^{+0.06}_{-.032}$ over physical separations of 23-230 au and mass ratios 0.5-1.0. In comparison to the Galactic field population, there is a probability of $10^{-6}$ that our results in the ONC can be modeled by the observations of field L-dwarfs, see Reid et al. (2006). Additionally, we see no evidence for a difference between this companion population and that of Chamaeleon I, Upper Sco, and Taurus for very low mass star and brown dwarf primaries. However, we estimate a probability of 0.02 that these results can be replicated by the observations within the Pleiades, potentially indicative of the impact of dynamics within bound clusters over 100 Myr. Further analysis predicts that many of these detected wide companions to brown dwarf primaries will be broken up by dynamical interactions within 5-10 Myr, while the stellar population will remain mostly stable due to larger binding energies. This effect will likely reduce the companion frequency to resemble that of the Galactic field and the Pleiades.

Our observations of the ONC suggest that dynamical processing of multiple systems during early periods of the life of a dense star cluster is important in shaping the companion population, particularly at wide separations. These results point to the possibility that the ONC may serve as a more representative star-forming region that will contribute to the Galactic field than low-density regions like Taurus-Auriga. However, neither of these types of regions (bound high density and unbound very low density) are thought to be common environment in which stars form. Future observations of OB associations, low density yet very large regions, and embedded clusters, high density yet eventually unbound regions, will provide significant evidence to probe the impact of stellar density on the formation and evolution of multiple systems. These environments represent perhaps two stages of evolution of the same type of region, i.e. embedded cluster expanding into an OB association, or have different initial environmental properties. Current programs in Orion OB1a and Orion OB1b are in preparation with both the Gemini (GN-2023B-Q-226, GS-2023B-Q-218, PI: De Furio) and Keck Observatories (PID 121/2023B_N238, PI: De Furio) to probe companion populations down to $\sim$ 10 au. Other programs with HST in NGC 1333 (ID: 17141, PI: De Furio) and JWST (ID: 1190, PI: Meyer) in NGC 2024 will explore the companion population to low-mass stars and brown dwarfs within these embedded clusters with intermediate stellar densities and compare to that of Taurus and the ONC. This work will produce a large exploration of companion populations down to $\sim$ 10 au within various environments to determine the impact of stellar density on the formation of multiple systems.

In addition to this work in the ONC, I explored multiplicity within the Galactic field over specific regimes of primary mass where multiplicity properties are underexplored. An in depth exploration has significant ramifications on our understanding of when and how specific formation processes occur. We used the JWST to explore the companion population to the coldest free floating objects in the Galactic field, Y-dwarfs. This work utilized imaging data from NIRCam and NIRISS as a

part of two separate programs, a GTO program (ID:1189) and a Cycle 1 GO program (ID:2473).

Within the GTO program, we obtained photometry of WISE1828+2650 with seven separate filters which were difficult to reproduce with our current state-of-the-art atmospheric models of planetary mass objects. Due to this discrepancy, this source was predicted to have a close companion which may better reproduce the observed data. With the NIRCam imaging data in the F360M filter, we explored the possibility of the presence of a close companion. We implemented a double-PSF fitting routine that incorporates an empirical PSF model which we derived from other sources within the field of view. Artificial binary tests show the ability to recover companions down to 0.05" in the long-wave channel, $\sim 0.5\lambda$/D, with this technique. We were unable to detect the presence of a companion down to 0.05", 0.5 au at 10 pc, and find that the single PSF model fits the data equally well as a double PSF model. Without the detection of a companion, either one exists at even closer separations or more advanced atmospheric modeling is required to explain the peculiar observations. Current programs are underway that obtained NIRSpec and MIRI spectroscopy of WISE1828+2650 which will further investigate its atmospheric properties.

The larger Cycle 1 GO program is designed to explore multiplicity to all known field Y-dwarfs unobserved within the GTO consortium, a sample of 20 sources. This program obtains long exposures in the F480M and F150W filters, intended to detect companions down to 1 $M_J$ beyond 1 au. While observations are still ongoing, we report the detection of the first Y-Y dwarf binary system, W0336-0143, using the same double-PSF fitting technique as before. The companion is detected in both the F150W and F480M filters at a separation of $\sim$ 84 mas (0.97 au) and a $\Delta$mag of 2.82 and 1.81, respectively. We estimate effective temperatures of 415 and 325 K for each component of the system, and masses of 8.5-18 and 5-11.5 $M_J$ (1 and 5 Gyr estimates), respectively, for a mass ratio of 0.61. This system is the first of its kind, and with an estimated orbital period of seven years, ideal for follow-up observations to obtain dynamical masses and study the spectral energy distribution of each component of the system. With the completion of the observations and the search for companions, a demographic analysis will also be implemented with the tools outlined above to place constraints on the companion population for the lowest mass primaries ever explored. Following the demographic analysis, we will be able to understand the possible formation mechanisms that would produce a companion to such a low mass system as W0336.

The last portion of my thesis explored another area of multiplicity that was underexplored, the close separation companion population ($\lesssim$ 30 au) to intermediate mass A-type stars. Previous spectroscopic studies of Am stars, chemically peculiar and slowly rotating, find a large companion frequency with a lower limit of 0.64 Carquillat and Prieur (2007). We set out to observe chemically normal A-type stars within 80 pc to characterize their multiplicity within the same separation regime as the spectroscopically identified companions. Using long-baseline interferometry, we observed 58 sources with the MIRC-X instrument (11 with MYSTIC) at the CHARA Array, 54 of which

had usable data for our analysis. We identified seven companions with the CANDID open-source software that have projected separations between 0.288-8.86 au and mass ratios 0.21-0.96. We defined detection limits to each source with the commonly used technique offered within CANDID, see Gallenne et al. (2015). Then, we performed a Bayesian demographic analysis, and estimate a companion frequency of $0.25^{+0.16}_{-0.11}$ and a power law index for the mass ratio distribution of $-0.22^{+0.94}_{-0.88}$ over mass ratios 0.1-1.0 and projected separations 0.01-27.54 au. We also determined that a flat separation distribution models the data just as well as a log-normal distribution. From these estimates, we can conclude that the De Rosa et al. (2014) model cannot replicate the observations of close companions to A-type stars, a result they speculated about in their own analysis. We also find no evidence for a difference between the companion frequency to solar-type field stars and that of A-stars over mass ratios and separations sampled, while we do find a probability of 0.04 that the B-type companion model can reproduce our results. This analysis leads us to conclude that a larger, volume-complete survey of A-type stars will allow us to constrain the companion population parameters to high precision while potentially answering whether the occurrence of companions has a strong dependence on primary mass with either a continuous or sudden increase over $\sim$ 1-3$M_{\odot}$.

With these observations of field brown dwarfs and A-type stars, we have improved the characterization of their companion populations and extended the companion exploration to primaries in the planetary mass regime. While this work provides important constraints, many questions still remain. Future planned work will attempt to extend the sample of A-type stars to a volume-complete sample with hundreds of primaries to obtain high precision estimates of the companion population properties. In addition, proposed work with the Hubble Space Telescope is planned to perform a multiplicity survey of $\sim$ 370 field brown dwarf primaries, the largest sample to date, which would greatly improve the statistical description of the companion population down to planetary mass primaries. These analyses will allow us to compare the observations to various formation models, e.g. turbulent fragmentation or disk fragmentation with preferential accretion, placing strong constraints on the origin of observed companion populations. Many theoretical questions still remain about the formation of multiple systems, and with the implementation of modern telescopes and detection techniques we may yet have the capacity to generate a complete, predictive theory of star formation.

# APPENDIX A

# Wavefront Error Recovery and Companion Identification with the James Webb Space Telescope

The work presented in this appendix has been submitted for publication in the Astronomical Journal, and we are currently working on revisions for re-submission based on the reviewer report. This work was done in collaboration with NASA Jet Propulsion Laboratory through a Strategic University Research Partnership grant with the University of Michigan. I led and performed the data simulations, data analysis, statistical comparisons, and manuscript writing. I want to give special thanks to Alexandra Greenbaum for leading the simulation code (ami_sim) which we use in this appendix, and to Steph Sallum for performing the interferometric analysis on these same data for direct comparison to our technique. I want to also thank Marie Ygouf and Graça Rocha for their mentorship and support throughout this project as well as all other collaborators for their contribution to this project.

## A.1 Abstract

The James Webb Space Telescope is orders of magnitude more sensitive than any other facility across the near to mid-infrared wavelengths. Many approved programs take advantage of its highly stable point spread function (PSF) to directly detect faint companions using diverse high-contrast imaging (HCI) techniques. However, periodic re-phasing of the Optical Telescope Element (OTE) is required due to slow thermal drifts distorting to the primary mirror backplane along with stochastic tilt events on individual mirror segments. Many programs utilize observations of a reference star to remove the stellar contribution within an image which can cost a significant portion of the total allocated time. We present a high-contrast imaging technique for the NIRISS instrument that uses the measured wavefront error (WFE) from a phase calibration observation (performed roughly every 48 hours) as prior information in a Bayesian analysis with nested sampling. This technique estimates the WFE of a given observation and simultaneously searches for faint companions, without

using a reference star. We estimate the wavefront error for both full aperture and aperture masking interferometry (AMI) imaging modes using three low order Zernike coefficients per mirror segment to generate synthetic PSFs and compare to simulations. We compare our technique to traditional interferometric analysis in realistic NIRISS F430M simulations both relative to the photon noise limit, and through recovering an injected companion with contrast of 8 mag at 0.2". Our use of wavefront error measurements in place of a calibrator will save significant amounts of observing time in most HCI observing modes.

## A.2 Introduction

Thousands of exoplanets have been discovered over the last twenty years, revealing a large diversity of properties (Gaudi et al., 2021). These planets span orders of magnitude in mass, radius and semi-major axis, and exhibit varied atmospheres. Exoplanets are most commonly detected using the radial velocity method (Mayor and Queloz, 1995) and the transit method (Charbonneau et al., 2000). However, these methods are indirect and typically sensitive at separations < 10 au. Direct imaging is another observing technique that can detect exoplanets, and is most sensitive at wide separations where high contrast is achievable (Bowler, 2016). Through the direct detection of exoplanets, we can test the accuracy of theoretical models, obtain spectra to characterize atmospheres, and constrain fundamental models of planet formation. With the launch of the *James Webb Space Telescope* (JWST, Gardner et al., 2006), many programs will utilize high contrast imaging techniques over 0.6 - 28 microns to explore wide separations, sensitive to planetary masses previously unattainable from the ground.

Many observing and post-processing techniques have been developed to increase sensitivity to planets by removing the stellar contributions present within the image. Reference differential imaging (RDI) involves observations of an assumed single star close in time to the target of similar spectral type, followed by subtraction of the two to identify a faint companion in the residuals (Lafrenière et al., 2009). Ground-based applications of this technique are sensitive to changes in the atmosphere and works best in scenarios with stable telescope optics and point-spread function (PSF). Another approach to high-contrast imaging (angular differential imaging, ADI) takes advantage of angular diversity. From the ground, ADI involves many integrations of a target over an extended period of time with the telescope rotator turned off to allow for motion of the field of view due to the Earth's rotation (Marois et al., 2006). This causes a potential companion to rotate in the image while keeping quasi-static speckles of the star at the same position. ADI is also applied to space-based imaging where the target is observed at multiple angles after the roll of the telescope, also referred to as roll subtraction. Principal component analysis (PCA) is a post-processing technique applied to various high-contrast imaging data sets which attempts to

reconstruct the PSF of an observation fitting an orthogonal basis set to the images determined by variation in the data and estimating the component coefficients within each integration (Jee et al., 2007; Amara and Quanz, 2012; Soummer et al., 2012). However, these post-processing techniques are difficult to perform on small angular scales (< 1") due to either the physical size of a coronagraphic mask, the dominance of residual starlight, or the evolution of speckles in ground-based imaging on a faster scale than the time required for the rotation to translate to motion of one full width at half maximum (Marois et al., 2006).

Aperture masking interferometry (AMI, Haniff et al., 1987; Tuthill et al., 2000) is an observing mode that utilizes a pupil mask to convert the telescope into a non-redundant interferometric array where the interference of the light from each sub-aperture produces an interferogram from which interferometric observables can be extracted. Analyses are then applied to the interferometric observables (e.g. closure phases, squared visibilities) after calibration from reference star observations. Kernel-phase interferometry (KPI, Martinache, 2010) is a similar interferometric analysis but applied to full aperture direct images. With knowledge of the telescope pupil, models in the interferometric observables are explored to find a signal from the planet that deviates from the expectations of a point source (e.g. closure phases equal to zero, squared visibilities equal to one). These techniques are most sensitive to companions at close separations.

Space-based imaging offers significant advantages over ground-based imaging. The PSF is stable due to the location of the telescope above the atmosphere. JWST provides an excellent opportunity for directly imaging exoplanets as it has a significantly larger diameter than previous infrared telescopes (e.g. 0.85m diameter of Spitzer) and there is low background emission in the thermal infrared. JWST is unique compared to other space-based telescopes in that it has 18 hexagonal mirror segments that define the primary mirror. Within the pupil and filter wheels of the NIRCam short-wave channel, four weak lenses are used to inject a specified amount of defocus roughly every two days for wavefront sensing and control (WFSC) operations to measure the integrity of the PSF (Perrin et al., 2016). The optical path difference (OPD) is extracted from these observations, and then evaluated to determine any required fine-phasing due to changes in the OPD over time, correcting for large rms residuals when appropriate using actuators on each mirror segment. Small wavefront drifts occur gradually due to minor changes in the equilibrium temperature (Perrin et al., 2018; McElwain et al., 2023) which will be realized over the two days of observing between WFSC operations (e.g. 8-50 nm Rigby et al., 2022).

Many high-contrast imaging programs observe a reference star directly before or after the target star in order to perform RDI and minimize the amount of residual WFE between observations (e.g. Hinkley et al., 2022b). Reference stars are chosen based on their proximity to the target and with similar color and brightness as the target in order to ensure a similar PSF, requiring roughly the same amount of time as that on target. Instead, it is possible to use synthetic reference PSFs as

models in post-processing techniques due to the optical stability of JWST, its slowly varying PSF, and frequent OPD measurements (Greenbaum et al., 2023). Additionally, synthetic PSF models constructed from the measured OPD can be used as prior information to inform a fitting routine that accounts for WFE drifts through modeling the instrumental OPD to estimate both the signal and the wavefront simultaneously (Ygouf et al., 2013, 2016; Cantalloube et al., 2018; Ygouf et al., 2020).

In this paper, we investigate the WFE estimation technique with JWST imaging simulation tools where we construct synthetic PSFs from an instrument model (informed by simulated WFS OPDs) and compare to simulated data in order to estimate the real OPD used in constructing the simulation. We simultaneously search for faint companions within the simulated data and evaluate our ability to detect them relative to other post-processing techniques. Our method uses publicly available OPD maps and does not require the use of a reference star, significantly reducing the total charged time for a high contrast imaging program.

In Section 2, we describe the process of constructing simulated data and our estimation routine. In Section 3, we present the achievable contrast of this technique for both full pupil and AMI imaging modes, compare them to other post-processing techniques, and demonstrate the ability to recover an injected faint companion. In Section 4, we discuss the utility of this method and its practical application, as well as potential future development. In Section 5, we summarize our conclusions.

## A.3 Methods

Our method requires the knowledge of JWST's optics and the wavefront error associated with the optical telescope element (OTE) measured during WFSC operations. Because the OTE does not experience major changes in wavefront error, we can use this information as priors to perform a Bayesian analysis with nested sampling to estimate the wavefront error during the observation while simultaneously searching for a companion and estimating its position and flux.

### A.3.1 Simulations

First, we describe the simulation tools used to produce NIRISS images, the components of the WFE that define the specific structure of a simulated PSF, and our approach to simulating a real JWST observing program.

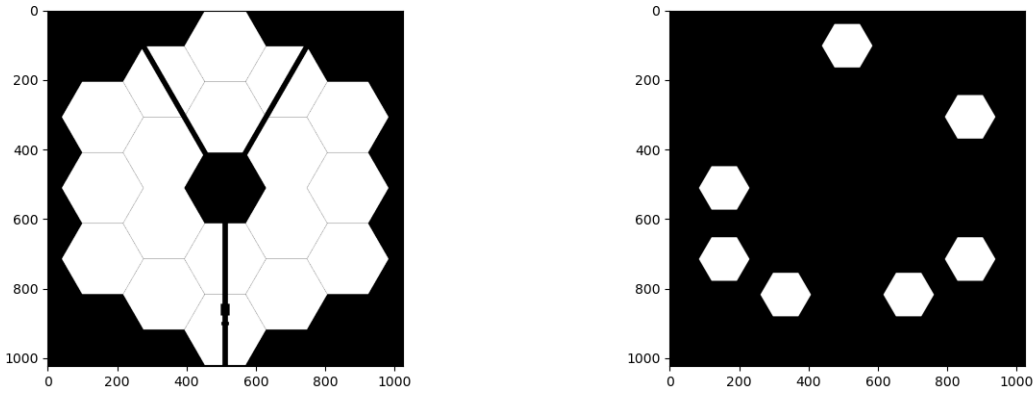


Figure A.1: Input transmission to POPPY for the full pupil (left) and AMI (right) observing modes. X and y units are pixels.

#### A.3.1.1 Tools

POPPY (Physical Optics Propagation in PYthon, Perrin et al., 2012) is a python package that can be used to simulate PSFs of a given optical system. It requires user defined inputs that characterize the pupil geometry, the primary mirror diameter, the wavefront error for the observation, detector characteristics, and the desired field of view and sampling of the constructed image. It is used within WebbPSF (Perrin et al., 2014) to simulate realistic expectations of JWST images.

We use POPPY to produce a noiseless PSF for both the full pupil and AMI observing modes for NIRISS. Using POPPY, as opposed to WebbPSF, is crucial to directly compare estimated OPD maps to those that are used to produce the simulated images. We define the OPD as a combination of the prelaunch predicted OTE OPD with an added correction, specified by a Zernike polynomial expansion to describe the OPD at a field point in NIRISS, both of which are available through WebbPSF. Zernike polynomials are a set of complete orthogonal basis functions on the two-dimensional unit disk. Each Zernike polynomial describes a specific type of optical phase aberration that can contribute to the WFE (e.g. tip/tilt, astigmatism, defocus, coma). Each type of aberration can be more or less prominent depending on the position of the science instrument (SI) along the optical axis and the location on the detector where a target is observed. POPPY contains a function that converts Zernike coefficients into an OPD map, which we use before combining the SI and OTE contributions of WFE. Then, we import the transmission corresponding to each observing mode, i.e. JWST pupil or aperture mask, see Fig. A.1. Lastly, we define the details of the detector and the image we require for our program: plate scale of NIRISS (0.065”/pixel), field of view (4” x 4”), sampling factor (5x), and wavelength (4.2784 $\mu$m, the effective wavelength in the F430M filter). With this information, we can then produce a noiseless PSF model for NIRISS.

We import this oversampled PSF model into `ami_sim` [1], a python package intended to simulate realistic data from NIRISS with detector level noise effects (Thatte et al., private communication). `ami_sim` injects typical appropriate noise sources including photon noise, dark current, read noise, and background. It also simulates the flat field error, as well as incorporating pointing error through sub-pixel shifts between integrations and Gaussian smoothing to represent small motion during the integration. These pointing errors are set to 1 milli-arcsecond (mas) as is the measured value on JWST from commissioning (Rigby et al., 2022). Expected noise effects not included are 1/f noise, inter-pixel capacitance, charge migration from saturated pixels, and the brighter/fatter effect.

We then define the number of groups per integration, number of integrations used in the simulation, and the electron count rate in order to simulate the desired observing program. The count rate is derived from the JWST Exposure Time Calculator (ETC) using the same observing setup as `ami_sim` and scaled to the desired magnitude and spectrum of the target. `ami_sim` convolves the input oversampled PSF with a user-defined scene to produce the detector-sampled image, e.g. single star, star with faint companion, etc. `ami_sim` then produces a data cube of the astrophysical scene with the number of frames equal to the number of integrations.

#### A.3.1.2 Components of Wavefront Error

The final observed PSF is a function of the wavefront error of the entire optical system (OTE + SI), geometric distortion, and detector-level effects such as plate scale and pixel response, all of which depend on field position to varying degrees. The primary mirror of JWST is made of 18 hexagonal mirror segments which are all aligned and co-phased to produce a single PSF (Dean et al., 2006). Each segment has mechanical supports with actuators which can be controlled to ensure the fidelity of the PSF. Below, we summarize all components of the total OPD used to construct a simulated PSF which are more thoroughly described in Perrin et al. (2018) and Rigby et al. (2022). As our technique depends on the estimation of the WFE, it is important to understand the various contributions and how those can be taken into account when producing synthetic PSFs.

Some components of the overall WFE are time-invariant. The OTE has static features caused by its physical characteristics, e.g. small imperfections due to mirror polishing, that are seen as high frequency errors. In Fig. A.2, we show the static wavefront error of the OTE, measured at the X-ray and Cryogenic Facility at NASA's Marshall Space Flight Center (McElwain et al., 2023).

There are also low frequency errors from internal SI WFE that vary across the focal plane. These can be modeled by a set of Zernike polynomial coefficients, some examples of which are publicly available through WebbPSF for multiple field points across an instrument's focal plane. However, these effects can be measured and are expected to be time invariant, allowing for their detailed

[1] https://github.com/agreenbaum/ami_sim

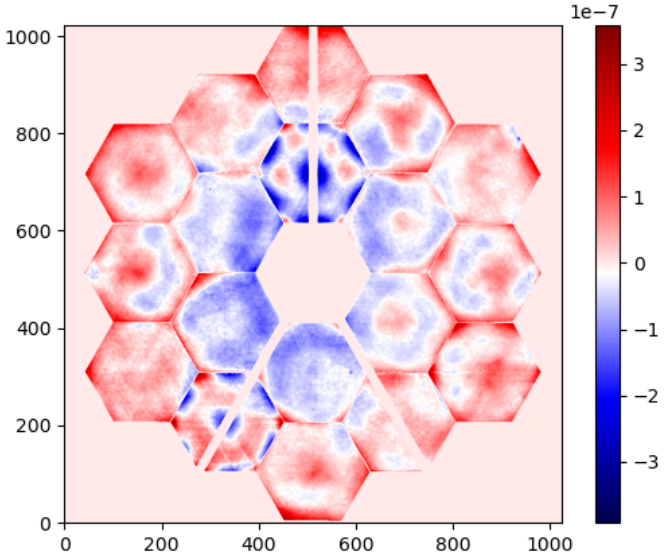


Figure A.2: The static wavefront error of the JWST OTE measured in lab. Units are meters. X and y units are pixels.

modeling on sky given the position of a target (e.g. Nardiello et al., 2022). These static WFE variations arise from differences in how different portions of the internal optics are illuminated depending on the position of a star in the field. Ground cryovac testing campaigns have shown the SI WFE variations to be stable (Sullivan et al., 2016). Shown in Fig. A.3 is the internal WFE for the NIRISS instrument at various positions along the field of view. There are also small OTE field-dependent WFEs, but they similarly introduce low frequency errors and their inclusion is not required to test our ability to recover the WFE of an observation thus not included in our model (see Sec. A.3.2).

Lastly, micro-meteorite impacts can effectively change the time-invariant WFE of the OTE instantaneously by introducing new imperfections to the mirror segments (McElwain et al., 2023). These impacts will remain unaltered unless another micro-meteorite type event occurs in the same location. Therefore, any micro-meteorite impacts must be included in any model of the WFE to accurately reproduce the real PSF of a given observation. These are characterized during on-sky WFSC operations and can then be included in the OPD model.

In addition to static WFE features, there are dynamic contributions which alter the total wavefront error, which in turn affects the observed PSF. Two effects are due to changes to the angle of the sunshield relative to the incident solar radiation causing differential thermal changes across the primary mirror backplane. One effect is that the backplane will expand or contract. Another effect is the thermal expansion of the frill which is connected to the primary mirror, generating motion

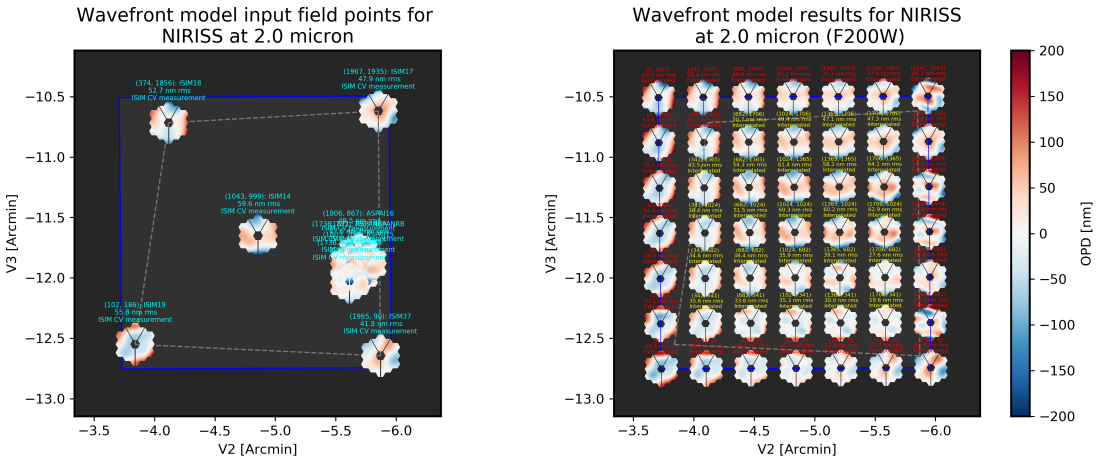


Figure A.3: Internal WFE measurements in NIRISS from ISIM CV3 testing (Aronstein et al., 2016). The left image gives WFE measurements at each input field point, and the right image gives the WFE model across the entire detector. Image credit: WebbPSF Documentation https://webbpsf.readthedocs.io/en/latest/ (Perrin et al., 2014)

of the segment supports and introducing segment specific wavefront drift. A small component of the dynamic wavefront drift is due to oscillations from heater switching on the Integrated Science Instrument Module Electronics Compartment (IEC). The last potential dynamic contribution to the wavefront error is a "tilt event". These are large motions of individual mirror segments that typically occur only one segment at a time, seemingly due to changes of stress on the backplane, which can cause large changes in the wavefront error very quickly (adding ~ 20-40 nm rms WFE, McElwain et al., 2023). In the case of tilt events, they are discovered during WFS measurements and then corrected, where that WFS OPD can also be used to build an accurate model of the observed PSF. All of these components combined will change the total wavefront error between WFSC operations and the observation in question, resulting in a modified PSF.

These dynamic contributions will cause the WFE to drift over time, and therefore these factors must be included in modeling an example WFE for a given observation. Leisenring et al. (in prep.) developed simulation tools (pyNRC) for various observing modes on NIRCam [2]. Within pyNRC, they simulate the processes listed above that can cause the OPD of the OTE to change over time. These processes follow specific functional forms which will drift the OPD by an expected amount and with an expected pattern. Given an input amount of time and pitch angle relative to the Sun, the effects from changes in the equilibrium temperature can be calculated and the difference in the WFE estimated. As shown in Fig. A.4, the wavefront drift is confined to individual segments and the wings of the primary mirror. It follows a low frequency pattern across individual segments. In order to simulate the appropriate data for our technique, we first construct the OPD map (containing

[2] https://pynrc.readthedocs.io/en/latest/index.html

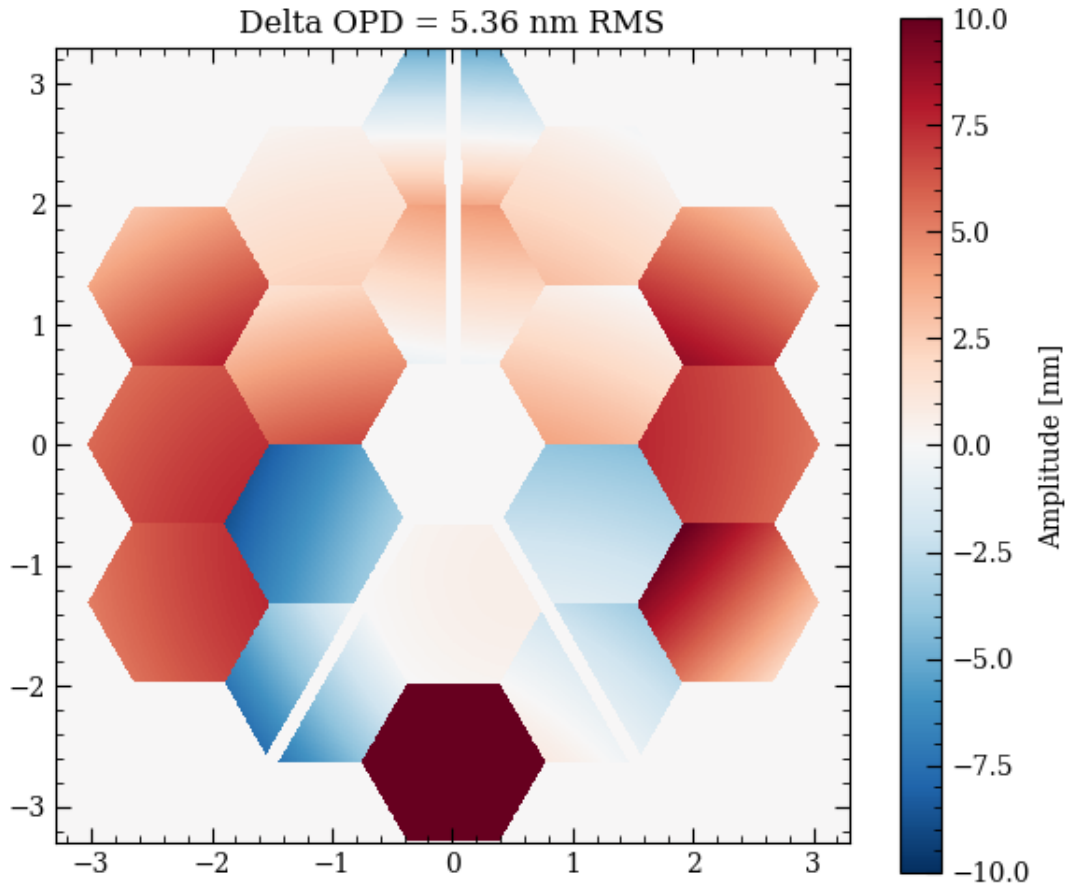


Figure A.4: The difference in the OTE OPD after simulating some input amount of drift equivalent to rms residual WFE ~ 5 nm. Differences in the WFE are both specific to individual segments and affect the segments connected to each wing (leftmost and rightmost three segments).

contributions from the OTE and SI) to serve as the WFSC measured OPD. Then, we drift this OPD using pyNRC to represent a large motion of 45 degrees relative to the pitch angle of the Sun over the course of 24 hours, the expected longest time between WFSC observations. That drifted OPD is used to generate a PSF with POPPY which is then imported into ami_sim to include detector-level noise sources and generate a data cube of the target observation.

#### A.3.1.3 Simulating a Real Observing Program

For our purposes, we chose to simulate a planned observing program using NIRISS AMI for high-contrast imaging. GO-1843 (PI: Kammerer) will observe HD 206893 in order to directly image HD 206893 B in the F380M, F430M, and F480M filters. HD 206893 B (first discovered by Milli et al., 2017) has a dynamical mass estimate of $27.4\ ^{+2.3}_{-2.3}\ M_{Jup}$ (Hinkley et al., 2022a) with a semi-major axis of $9.7^{+0.4}_{-0.3}$ au from the star at 40.707 ± 0.067 pc (Gaia Collaboration et al., 2018) and a very red color with a contrast of 7.91 mag in L' (3.8 $\mu$m) on VLT/NACO. To generate a simulation of this target observation in AMI and FP modes, we extract the electron count rate (here 2.15 * $10^6$ $e^-$/s in the AMI case and 1.138 * $10^7$ $e^-$/s in the FP case) as input to `ami_sim` from the JWST ETC using the planned observing setup in the F430M filter and scaling the flux to 2MASS $K_s$ = 5.593 mag with a spectrum of a blackbody with $T_{eff}$ = 6500 K for this F5V star.

The exposure configuration for GO 1843 consists of observations with the F430M filter using 2177 integrations of 8 groups for a total exposure time of ~ 1523s. `ami_sim` produces the same number of frames in the data cube as integrations. In order to avoid making a computationally prohibitive algorithm fitting to 2177 frames, we instead produce 14 frames to which we can compare our model. The total exposure time is ~ 25 min with each frame representing a co-added image over ~ 1.8 min. These 14 frames serve as co-added slices of the observation as the wavefront is not expected to change in any meaningful way during the course of this relatively short observation. We conserve the number of total groups for the planned observation to correctly simulate the noise and the expected signal-to-noise. Instead of 2177 integrations of 8 groups each, we produce a data cube of 14 integrations of 1244 groups in `ami_sim` which does not include saturation effects. We simulate the two observing modes for a target without a companion to define sensitivity limits (see Sec. A.4.1) and with a companion that has the expected features of HD 206893 B at the time of observation to determine our ability to recover and estimate the parameters of a known injected companion (see Sec. A.4.3). The target observation both with and without a companion was simulated using the drifted OPD to represent the expected rms residual WFE between the WFSC operations and the real observation, as stated in Sec. A.3.1.2.

### A.3.2 Estimation

#### A.3.2.1 Modeling the Wavefront Error

Our synthetic PSF model is generated from OPD maps using POPPY in the same manner as the simulations. High frequency errors are static, and the portion of the WFE that is dynamic is either confined to the wings or to individual mirror segments, see Fig. A.4. Therefore, we chose the hexagonal mirror segment specific Zernike coefficients (Hexikes) to serve as the basis with which we construct an OPD map. We use three Hexike terms per segment (piston, tip, and tilt) to realistically model the WFE without being computationally prohibitive as the WFE drift is limited to the piston, tip, and tilt coefficients (see Fig. A.4). Our model to reproduce full pupil images contains 54 Hexike parameters (3 for each of the 18 segments), and that for AMI images contains 21 Hexike parameters (3 for each of the 7 segments).

While Hexike coefficients are appropriate to model low frequency errors across individual mirror segments, high frequency errors cannot be well modeled with a reasonable number of Hexike coefficients. Importantly, the high frequency errors are a direct result of mirror imperfections that are well measured on the ground and are continuously monitored through WFS observations. We can use the known high frequency errors to inform our model of the remaining segment specific low frequency WFE drift. Our model of the total WFE of a given observation is a combination of the static WFE (shown in Fig. A.2) and the estimated low frequency error on a segment by segment basis where the Hexikes are free parameters.

#### A.3.2.2 WFE Optimization and Companion Detection

We perform a Bayesian analysis using the Nested Sampling Monte Carlo routine to derive the best fit PSF model to our simulations with the python module PyMultiNest, a fast sampling technique that derives the Bayesian evidence of the input model (Feroz et al., 2009b; Buchner et al., 2014b; Golomb et al., 2021). PyMultiNest generates a user defined number of live points that sample the prior distribution and evaluates the likelihood of the sampled model solution. It then lists these likelihood values in order from highest to lowest likelihood, and re-samples the prior distribution. Samples with likelihoods higher than the previous list of likelihoods are then saved to that list with the rest rejected, ensuring a maximization of the likelihood of the model. PyMultiNest continues this process of sampling and rejecting model solutions until the difference in the likelihood of new samples is negligible. The evidence is the integral of the likelihood times the prior over all parameters which allows us to test different models and determine which model is preferred given the data, e.g. if a star with a companion is preferred over just a star.

Our free parameters are the three Hexike coefficients to each mirror segment (which combined with the static WFE produces a total WFE), three parameters describing the primary star (x and

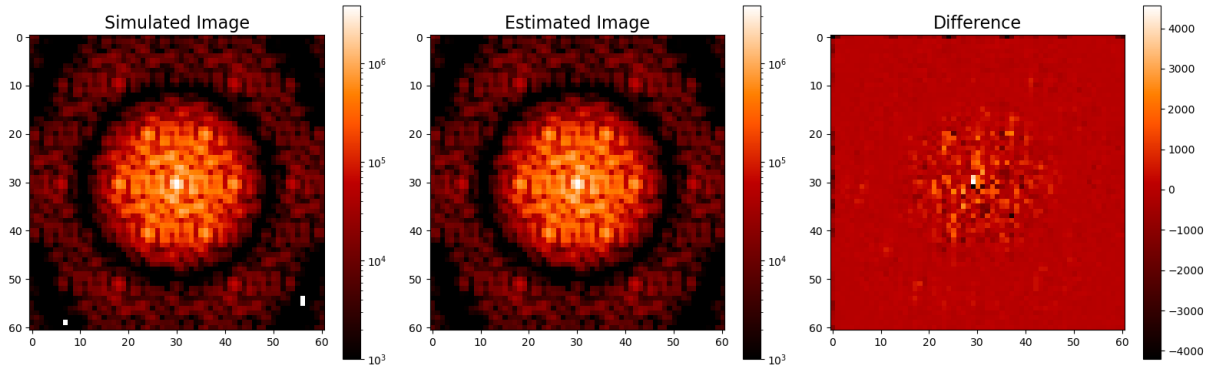


Figure A.5: Left: First simulated frame from data cube produced by ami_sim in the AMI observing mode for NIRISS. Center: Image produced with the maximum likelihood estimate of the WFE for the simulated image. Right: Residuals of first simulated frame minus our maximum likelihood estimated image. Note: Colorbar scales are the same for the left and center image, but different for the right image. Units are ADU.

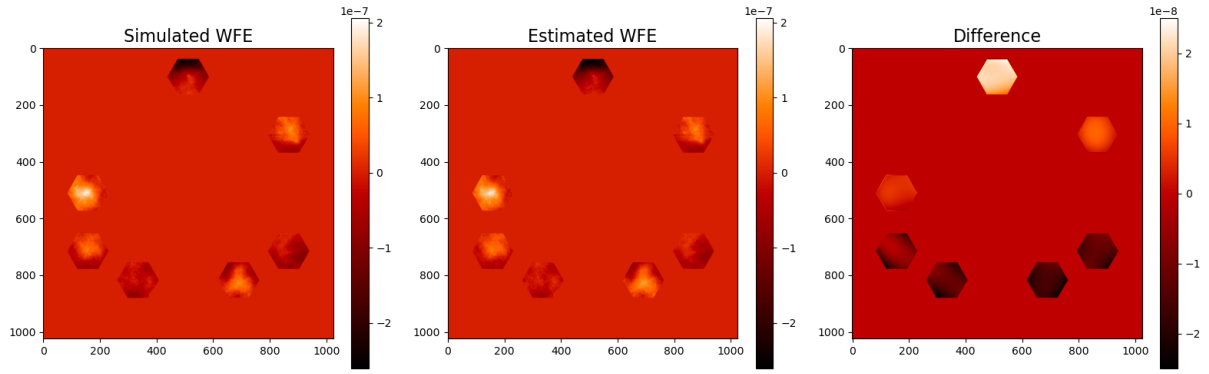


Figure A.6: Left: Simulated WFE of target for AMI observation. Center: Maximum likelihood estimate of the WFE. Right: Residuals of simulation minus estimate. Note: Colorbar scales are the same for the left and center image, but different for the right image. Units are meters.

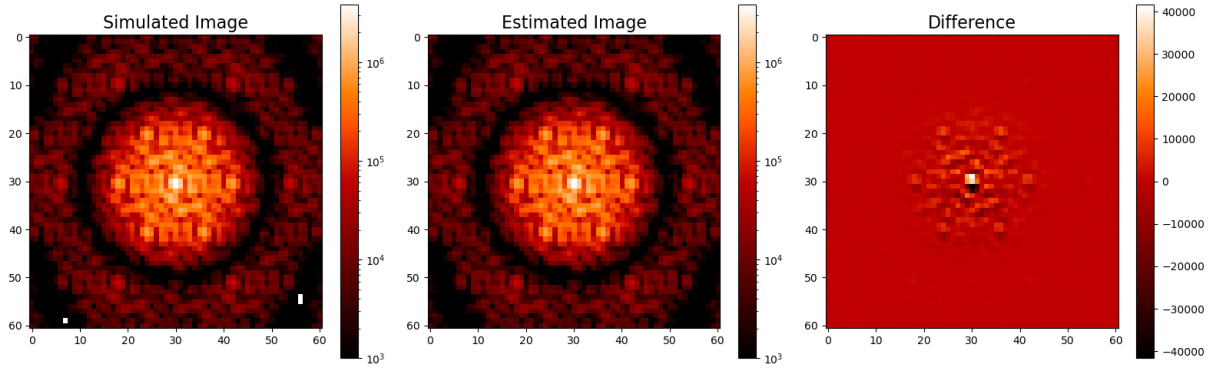


Figure A.7: Left: First simulated frame from data cube produced by ami_sim in the AMI observing mode for NIRISS. Center: Image produced from the WFSC OPD that was used to define the priors in our technique. Right: Residuals of first simulated frame minus image produced from WFSC OPD. Note: Colorbar scales are the same for the left and center image, but different for the right image. Units are ADU. Residuals from just subtracting the WFSC OPD (i.e. not fitting for the WFE) are higher compared to Fig. A.5 where we show the results after fitting for the WFE.

y position of the center of the PSF and flux), and three additional parameters for each additional source in the field (separation between center of primary star and center of companion, position angle of companion, and difference in magnitude between primary and companion). The total WFE is used to generate a PSF model from poppy, and the astrophysical scene is constructed using that PSF and the positions of all sources included in the model. We then evaluate the log-likelihood of the model by comparing the constructed astrophysical scene to all the frames of the simulation from `ami_sim`. The log-likelihood is defined by a chi squared where n is the total number of pixels in all simulated data frames and $\sigma_{\gamma,i}$ is the photon noise in each pixel ($\sqrt{(data_i)}$):

$$\mathcal{L} = \sum_{i=1}^{n} -0.5 \times (\frac{\text{model}_i - \text{data}_i}{\sigma_{\gamma,i}})^2 \tag{A.1}$$

For a scene with a single star, we center the data in the brightest pixel and set the priors as flat for the central position of the star: -0.13" $\leq x_{cen} \leq$ 0.13" and -0.13" $\leq y_{cen} \leq$ 0.13". The flux of the star is defined as a normalization constant to the PSF model from POPPY where we define a flat prior between $10^5$-$10^{12}$. For a scene with a star and a companion, we define the stellar priors the same as above, and define the companion priors as flat: 0.5 pixels $\leq$ separation $\leq$ 10.0 pixels from the center, 0 degrees $\leq$ position angle $<$ 360 degrees, and 3.0 mag $\leq \Delta$mag $\leq$ 10.0 mag.

Importantly, we must also set the priors to each Hexike coefficient that will define the estimated WFE of the target observation. As stated in Sec. A.3.1.2, a realistic observation for our high-contrast imaging program includes a realization of an OPD map intended as a stand-in for the measured OPD during WFSC operations that is then drifted to produce the target observation. To

set the priors for the Hexike coefficients in estimating the WFE of the target observation, we take this WFSC OPD map, subtract the static WFE, and deconstruct the residual into its constituent Hexike coefficients for each mirror segment using the decompose_opd function in POPPY and a mask for each segment. We also perform the same task for the drifted OPD used to represent the WFE at the time of observation to determine the amount any individual Hexike is expected to drift. The maximum difference in any Hexike between the WFSC OPD and the drifted OPD then serves as the amplitude for the priors of each Hexike, centered around the Hexike value of the deconstructed WFSC OPD. We found that at most, a given Hexike term will drift 20 nm, and therefore our priors are the deconstructed WFSC OPD Hexike terms ± 25 nm.

## A.4 Results

We applied our companion detection and WFE estimation technique on the simulations of the observing program GO 1843 to determine how well we expect to recover companions. We performed this analysis on both AMI and FP simulations of single stars and a star with an injected companion. Then, we compared our expected performance to other post-processing techniques that utilize the observation of a reference star.

### A.4.1 Sensitivity Limits of Technique

To derive sensitivity limits, we applied our WFE estimation technique to a simulation of an observation of a single star, defined in Sec. A.3.1.3.

In the AMI case, we show the image produced from the maximum likelihood estimate of our 24 parameter model (3 Hexikes for each of the 7 mirror segments, 3 parameters for the position and flux of the star) relative to the first frame within the simulated data cube in Fig. A.5. In Fig. A.6, we show our ability to recover the WFE of the simulated data. The pattern of the residual WFE corresponds to higher order Zernike polynomials, which were not included in our model. Higher order terms contribute a small amount to the overall WFE, but their inclusion in the model introduces degeneracies that prevent accurate estimates of the piston, tip, and tilt terms of each mirror segment within a reasonable run-time of the algorithm. In this case, the code often over-fits the data and the dominant first three coefficients are less well constrained, hence our use of 3 Hexikes per mirror segment. In Fig. A.7, we also show the image produced from subtracting the PSF generated from WFSC OPD from the simulated images. In comparing the residuals in Figs. A.5 and A.7, the WFE drift introduces features in the fringes of the AMI PSF, both in the center and where the sub-apertures constructively interfere to create additional peaks in the image further from the center. Our WFE estimation technique models the change in OPD that creates these features

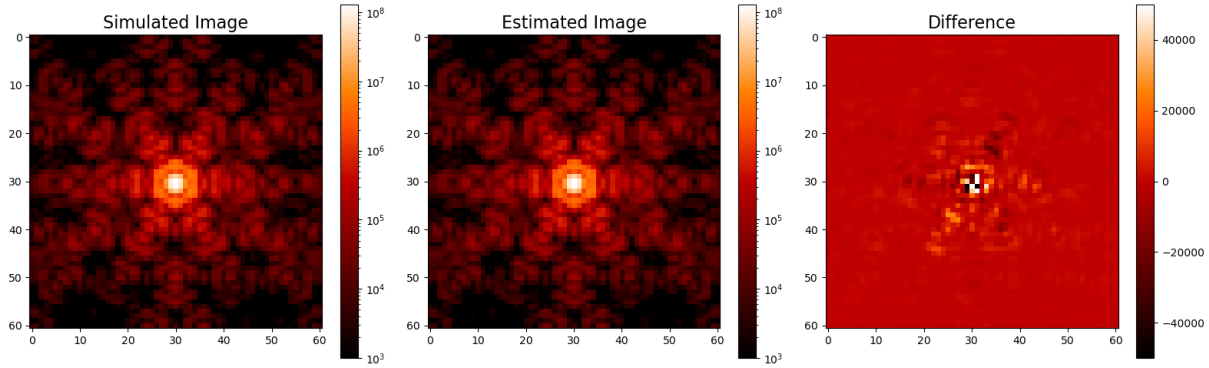


Figure A.8: Left: First simulated frame from data cube produced by ami_sim in the full pupil observing mode for NIRISS. Center: Image produced with the maximum likelihood estimate of the WFE for the simulated image. Right: Residuals of first simulated frame minus our maximum likelihood estimated image. Note: Colorbar scales are the same for the left and center image, but different for the right image.

allowing for a deeper search for companions.

We also applied our technique to simulations of the full pupil observing mode. For this mode, we show the image constructed from the maximum likelihood estimate of our model compared to the simulated data in Fig. A.8. In Fig. A.9, we show the recovered WFE relative to the WFE used to simulate the target observation. As with the AMI case, the residual WFE appears to follow the pattern associated with higher order Zernike polynomials. The estimate of the wavefront with 54 parameters already requires long computation time, and any increase in number of coefficients per segment would both increase degeneracy and make computation times prohibitively long. In Fig. A.10, we also show the image produced from subtracting the PSF generated from WFSC OPD from the simulated images. In comparing the residuals in Figs. A.8 and A.10, the WFE drift introduces large features in the PSF at separations close to the star. Our WFE estimation technique models the change in OPD that creates these features allowing for an improved search for companions at close separations.

In Figs. A.11, we show the contrast curves derived from our maximum likelihood estimate of the WFE of the target observation for both the AMI and FP observing modes, respectively. We measure our ability to recover companions by taking the difference between each frame of the simulated observation and the image produced from the maximum likelihood estimate model. Then, we define successive annuli, centered on the star, with a 0.14" width equivalent to the full width at half maximum (FWHM) in the F430M filter ($\sim$ 2 pixels). Within each annulus, we construct adjacent circular sub-apertures with diameters equivalent to the FWHM and calculate the flux within each sub-aperture over all frames. We then evaluate the t-test distribution for a $5\sigma$ detection given the calculated standard deviation and number of sub-apertures within the annuli. We use the approach

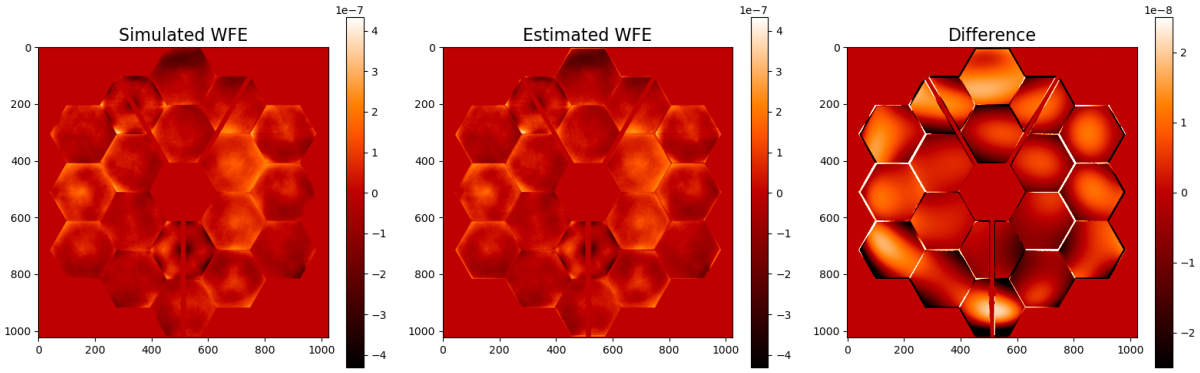


Figure A.9: Left: Simulated WFE of target for full pupil observation. Center: Maximum likelihood estimate of the WFE. Right: Residuals of simulation minus estimate. Note: Colorbar scales are the same for the left and center image, but different for the right image.

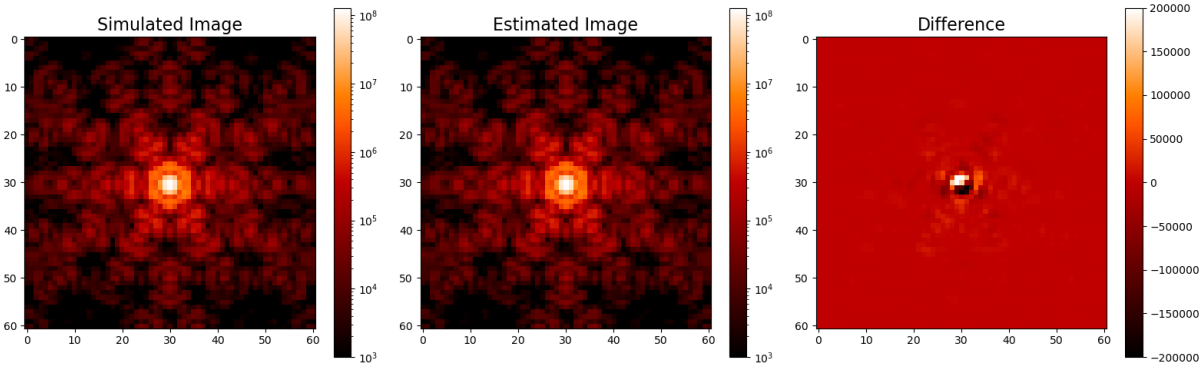


Figure A.10: Left: First simulated frame from data cube produced by ami_sim in the full pupil observing mode for NIRISS. Center: Image produced from the WFSC OPD that was used to define the priors in our technique. Right: Residuals of first simulated frame minus image produced from WFSC OPD. Note: Colorbar scales are the same for the left and center image, but different for the right image. Residuals are higher compared to Fig. A.8.

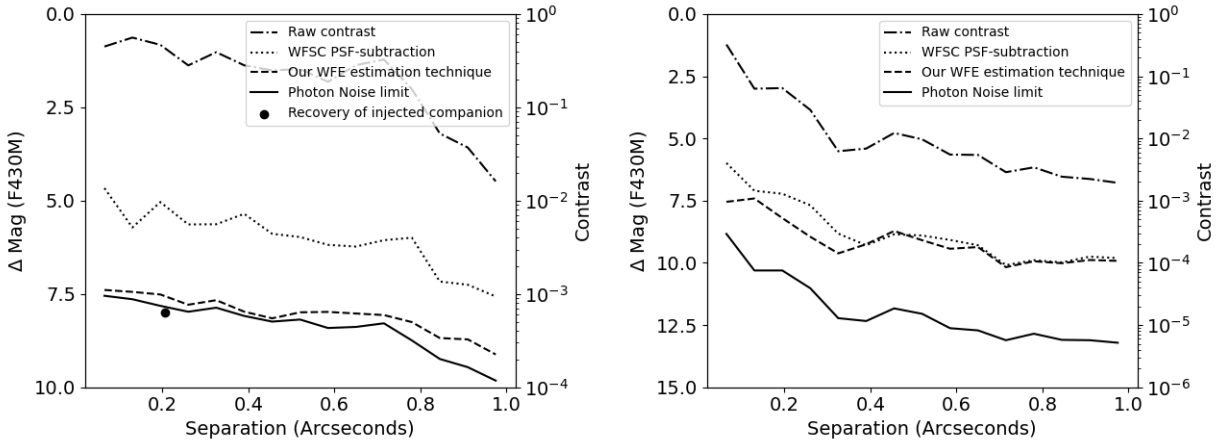


Figure A.11: Left: $5\sigma$ contrast curve for the AMI case. Right: $5\sigma$ contrast curve for the full aperture case. The dot-dashed line corresponds to the raw contrast, the dotted line corresponds to the contrast curve when using the WFSC OPD to reconstruct a single star, the dashed line corresponds to the contrast curve derived after the application of our WFE estimation method, and the solid line corresponds to the photon noise limit. The black dot represents the values of the source injected and recovered in Sec. A.4.3. Our Bayesian wavefront estimation improves on current PSF subtraction methods that utilize the temporally closest WFSC measurements of the OPD across all separations in the AMI case and for separations < 0.4" in the FP case.

of Mawet et al. (2014) (in their Sec. 3.4) to correct for small sample sizes (i.e. at small angles due to a low number of sub-apertures) to arrive at the flux that corresponds to the $5\sigma$ value above the residuals within each annulus. We calculate the flux of the primary star by summing the pixels within an aperture with diameter equivalent to the FWHM centered on the primary. With this measurement, we can compare the detectable flux to that of the primary for an achievable relative contrast measurement in flux ratio or $\Delta$mag. We also perform this calculation for the raw contrast of the simulated images, the contrast after subtracting the PSF generated from the WFSC OPD, and the contrast after subtracting the simulated images with no noise from those with only photon noise to define the photon noise limit. The difference between the WFSC OPD results and that of our method demonstrate the improvement our technique generates after WFE drift of the telescope.

### A.4.2 Traditional Interferometric Analysis with Calibrator

Interferometric analysis is commonly performed on AMI imaging data in order to search for faint, close companions. Interferometric analysis techniques on AMI data take advantage of a non-redundant aperture mask, such as that utilized on NIRISS (Greenbaum et al., 2015; Sivaramakrishnan et al., 2022) where the squared visibilities and closure phases are calculated from the data. Closure phases are an interferometric quantity derived from the fringes of each pair of

apertures within a closed triangle of three baselines (e.g. three sub-apertures), utilized to remove phase errors (Jennison, 1958; Rogers et al., 1974; Monnier, 2000; Monnier et al., 2004). Any scene deviating from a point-symmetric object (e.g. a binary or an extended structure) will produce non-zero closure phases with amplitudes on the order of the amount of deviation (e.g. flux ratio). This technique relies on the observation of a reference star in order to account for any bias in the closure phases as a result of differences in detector levels effects (e.g. charge migration) and to second order wavefront drift, thus increasing total program observing time.

Sallum and Skemer (2019) applied this technique to simulations of JWST data. We apply their same algorithm to the simulation produced in our paper to determine the sensitivity limits of this technique. We use a single star as a reference that was produced from an OPD with rms residual WFE of 5 nm relative to the simulated target observation (roughly the expected WFE drift through the course of a full JWST reference-target observation). This serves as the calibrator source to remove bias, after which the derived closure phases and squared visibilities are used to estimate sensitivity.

Because these observables are in the Fourier plane and not the image plane, the definition of the sensitivity to companions cannot be the same as done in Sec. A.4.1. In this case, the closure phases and squared visibilities of the simulated single star were extracted and then fitted with a grid of single companion models with varying separation, position angle, and contrast. For each grid point, the difference in $\chi^2$ is calculated between that binary model and the null (no companion) model. These values are averaged over position angle, and for each value in separation a $\Delta\chi^2$ interval is then used to determine the single companion contrast that would be distinguishable from the no companion model with $5\sigma$ significance. This detection limit is defined as $\chi^2$ - $\chi^2_{single}$ = 25. We also estimate the theoretical photon noise limit for these data with the interferometric observables using the method of Ireland (2013). These limits are shown in Fig. A.12.

Although we cannot use the same statistical method to compare techniques, we can compare the ability of each technique relative to its calculated theoretical detection limit, the photon noise limit. These limits are arrived at in differing ways, but give an indication as to how these methods compare. Shown in Fig. A.13 is the ratio of the $5\sigma$ recovery limit to the photon noise limit for each method. The traditional interferometric analysis sensitivity is estimated in the interferometric observables, while the sensitivity estimate of our technique is carried out in the image plane. The traditional interferometric analysis is sensitive at roughly twice the photon noise limit (due to the 5 nm rms residual WFE from the reference star to the target), while our technique is sensitive between roughly 1.1-2.0x the photon noise limit across 1". The absolute attainable contrast with the traditional interferometric analysis is roughly 9 mag beyond 0.1", while ours is roughly 7.5 mag, but both approach the photon noise limit as these numbers are derived in different ways.

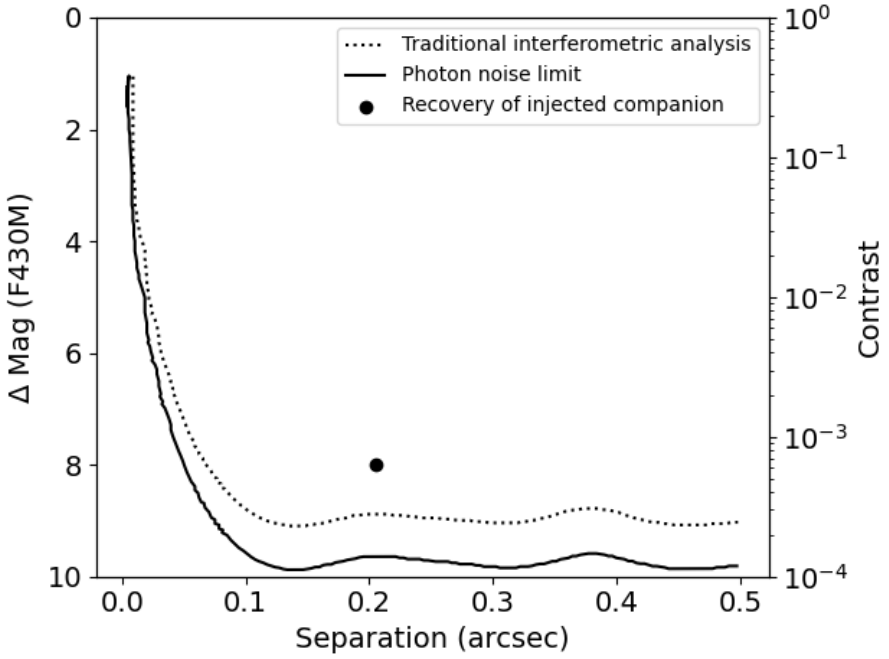


Figure A.12: Contrast curve for the AMI case using traditional interferometric post-processing analysis (Sallum and Skemer, 2019) on the observables. The dotted line is the sensitivity limit that corresponds to a $\chi^2$ - $\chi^2_{single}$ = 25, where $\chi^2$ is the value associated with a single companion model. The solid line is the theoretical photon noise limit for these data derived with the technique of Ireland (2013). This contrast curve is extended to small, sub-pixel separations as the sensitivity is defined based on the $\Delta\chi^2$ calculation from closure phases.

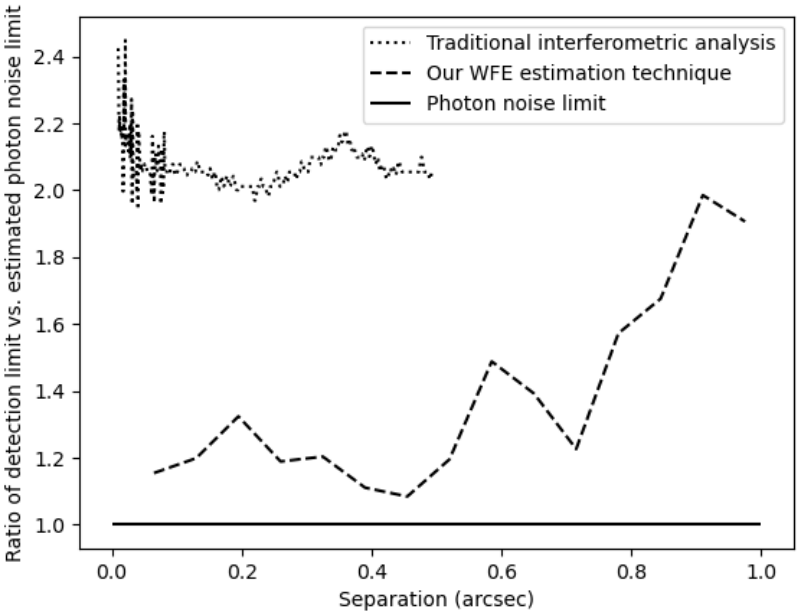


Figure A.13: Comparison of the sensitivity limit of each technique in the AMI case to its estimated photon noise limit. The two techniques must be evaluated in different ways, and this comparison shows the ability relative to its theoretical limit estimates. Both techniques approach their theoretically derived photon noise limits.

### A.4.3 Companion Recovery

Both our WFE estimation technique and the technique of Sallum and Skemer (2019) are designed to detect and characterize faint companions. As a more direct test of the ability of each technique, we created a simulation of a faint companion and attempted to recover the signal with both methods. We simulated the expected scene for GO 1843 with a companion at 0.2055" in separation from the central star ($\sim 1.5\ \lambda/D$), $\Delta$mag = 8 mag in the F430M filter, and a position angle of -71.57°.

We applied our WFE estimation and companion search method on these data. Shown in Fig. A.14 are the posteriors of the companion parameters that were estimated with our technique. The maximum likelihood estimate gives the following parameters: separation of the companion = 0.195" , position angle = -70.7°, and contrast = 7.85 mag. The median and the enclosed 68% of the marginalized posterior are given in Table A.1 These estimated companion parameters are within the 68% confidence interval encompassing the known companion parameters. In addition, we applied our WFE estimation routine to this data fitting only a single star and no companion. After evaluating the Bayesian evidence of the fit with and without a companion, we find a difference of 1300 in favor of the fit with a companion, evidence for a strong detection (Trotta, 2008a). See Fig. A.17 for the posteriors of both the companion parameters and the Hexike coefficients of each mirror segment that define the WFE estimate.

We then applied the Sallum and Skemer (2019) technique to the same data and show the posteriors of the companion estimate in Fig. A.15. We also show the measured closure phases of the simulated data and the fitted closure phases of the binary model in Fig. A.16 that are indicative of a binary detection. The real companion signal is being detected with this technique as well. The estimated companion parameters, displayed in Table A.1, are: PA(∘) = $-72.53^{+1.31}_{-1.20}$, separation ($\rho$)= $0.210^{+0.006}_{-0.008}$, and contrast = $8.19^{+0.18}_{-0.15}$ mag. The companion is detected within roughly the 68% confidence interval for each parameter, and underestimates the contrast likely due to an underestimate of the closure phase errors. The error bars for the fitted companion parameters are comparable to those of our technique. It appears that in detecting such a faint companion, the ability to estimate accurate parameters are comparable between techniques.

Importantly, the injected companion has parameters that are below the $5\sigma$ limit of our technique shown in Fig. A.11. Our estimate of the sensitivity limit is based on aperture photometry. However, the PSF of an AMI image has significant azimuthal structure and is well spread out, making our image plane WFE estimation technique more sensitive to faint companions than a $5\sigma$ aperture photometry limit can illustrate. Therefore, this injection/recovery approach displays the power and similar performance of both the traditional interferometric technique and our WFE estimation technique. To attain more precise limits and comparisons, future work may depend on rigorous injection/recovery and false positive analysis.

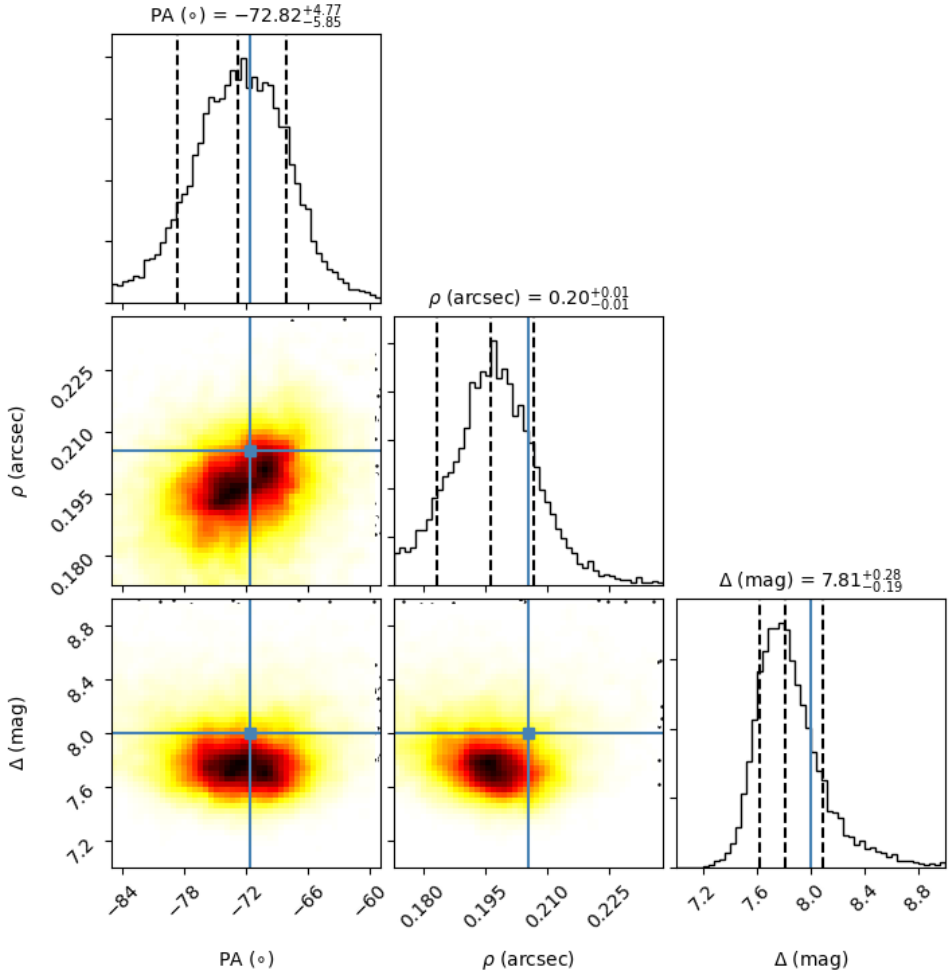


Figure A.14: Posterior distributions for the companion parameters derived for HD 206893 B using our novel technique. Blue lines are the simulated values, and left/right black dashed lines enclose 68% of the marginalized posterior around the median (central black dashed line). Displayed values are the median with the enclosed 68% of the marginalized posterior.

Table A.1: True parameters of the injected companion, estimate of the companion values with traditional interferometric analysis, and estimate of the companion values with our WFE estimation technique (median with 68% marginalized posterior enclosed).

| | Separation (arcsec) | Position angle (degrees) | Δmag (F430M) |
|---|---|---|---|
| Truth | 0.2055 | -71.57 | 8.0 |
| Traditional Interferometric Analysis | $0.210^{+0.006}_{-0.008}$ | $-72.53^{+1.31}_{-1.20}$ | $8.19^{+0.18}_{-0.15}$ |
| Our WFE Estimation Technique | 0.20±0.01 | $-72.82^{+4.77}_{-5.85}$ | $7.81^{+0.28}_{-0.19}$ |

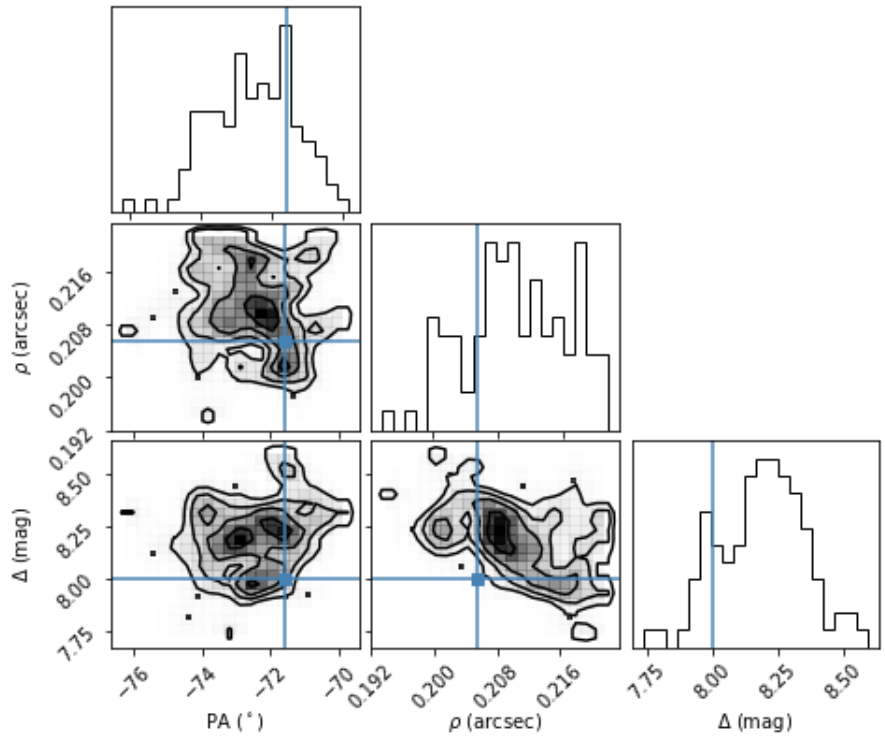


Figure A.15: Posterior distributions for the companion parameters derived for HD 206893 B using traditional interferometric analysis techniques in the interferometric observables. Blue lines are the true simulated values.

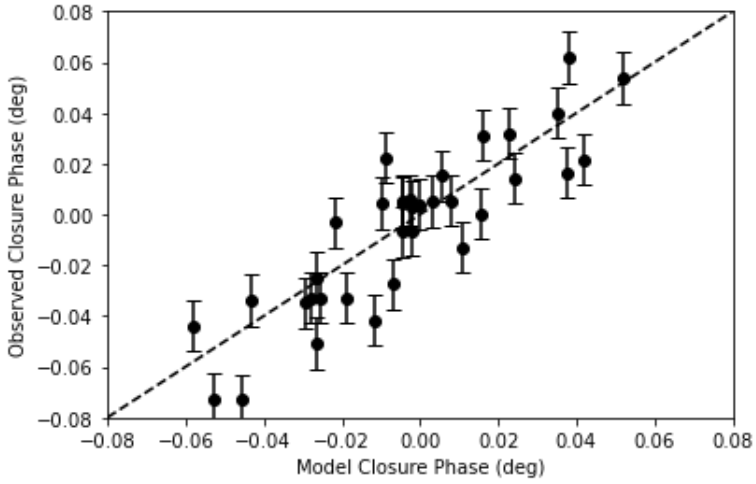


Figure A.16: Closure phases of the model with a companion compared to the measured closure phases. This is indicative of a companion detection.

## A.5 Discussion

### A.5.1 Utility of method

Our technique utilizes WFSC information (scheduled to be taken every 48 hours) to inform a WFE estimation routine that models the OTE OPD for a given data set. This technique is paired with a companion search that allows for the simultaneous fitting of the WFE, primary star parameters, and companion parameters. With the success of this routine, we have proven the effectiveness of using synthetic PSF models to estimate the WFE of the target observation and perform high contrast imaging post-processing for full pupil and AMI data on the NIRISS instrument. The use of synthetic PSFs and WFSC information as priors to estimate the WFE reduces observing time by nearly 50%, providing significant efficiency for highly coveted JWST time.

As shown in Figs. A.7 and A.10, the WFE drift accumulated from changes in equilibrium temperature of the telescope will introduce significant differences in the PSF, especially at close separations. The application of our technique provides a marked improvement on the modeling of the PSF, allowing for the search for companions at close separations, see Figs. A.5 and A.8. For the AMI case, the constructive interference of the light through the seven sub-apertures creates bright fringes far from the core of the PSF, distinct from the full pupil case. This PSF is more sensitive to small changes in an individual Hexike coefficient. Combined with the small number of Hexike coefficients required to model the WFE, this results in a reduction in degeneracy between Hexike terms and allows for the improved modeling of the WFE and better achievable contrast, see Fig. A.11. In the FP case, the improvement from our WFE modeling is concentrated in the core of the PSF where we gain sensitivity over the WFSC model at separations $< 7$ pixels (0.455").

We also set out to determine if we could recover companions expected from scheduled JWST programs. We simulated a companion at 0.2055" in separation and 8 magnitudes in contrast in the F430M filter, as expected for JWST observations of HD 206893 (GO-1843). We are able to recover the companion while simultaneously estimating the WFE, see Fig. A.14. As shown in Fig. A.15, the companion parameter estimates from our novel technique in the AMI observing mode are comparable to that of Sallum and Skemer (2019) applied to the same simulated data. Although the estimated sensitivity limits differ between techniques, the approach to derive these limits are in two different planes. Therefore, the injection and recovery of a faint companion at a close separation shows the direct ability of both techniques, the traditional interferometric technique with a reference star and our WFE estimation technique without a reference star.

### A.5.2 Future Development and Applications

There are several ways to improve on this technique and topics to explore using synthetic PSFs. In Figs. A.11, we show the contrast curves for this technique in AMI and FP modes, respectively. Full pupil PSF modeling is difficult due to the many degeneracies among the mirror segments and Hexike values. However, we can improve on WFE modeling if we simultaneously fit FP and AMI images (Greenbaum and Sivaramakrishnan, 2016). Our fitting routine converges on the Hexike values of each segment for AMI quickly, but it is a much slower process with just FP data. If we fit both simultaneously, then the Hexikes for 7 of the 18 segments used in AMI observing will converge quickly, and that information will be able to break many degeneracies with the 11 other segments. As AMI imaging blocks $\sim 80\%$ of the light from the target, one would only need $\sim 20\%$ increased observing time to have comparable flux in both observing modes.

In this paper, we applied our novel technique to a single source, like will be performed in most high-contrast imaging programs. However, it should be noted that this type of technique can be applicable to wide-field images as well. The position along a detector will introduce low frequency WFE, as described in Sec. A.3.1.2, due to internal optics and the position along the focal plane. This effect can be extensively modeled with efforts currently ongoing (e.g. Nardiello et al., 2022). However, the WFE contribution from the OTE will be constant across the field of view. With an estimate of low frequency errors based on position, we can also model the WFE from the OTE using all sources in the field of view as inputs. This type of analysis can also be useful when applied to future space missions like the Nancy Grace Roman Space Telescope (Roman) with the Wide-Field Instrument, a 0.28 square degrees field of view, where thousands of sources can be simultaneously observed to inform the WFE model.

Importantly, we showed that the residual WFE unaccounted for with our technique appears to be constructed of higher order Hexike coefficients. Because the drift is known to be confined to the first three Zernike coefficients of each mirror segment, the residual WFE from higher order coefficients is a result of not knowing the WFE associated with a given detector position. With the measured description of the low order WFE based on detector position, we can also improve upon our high contrast imaging approach as we model the three coefficients per segment that contain the drift.

Reference PSF modeling can also be useful for traditional interferometric post-processing techniques. The extracted interferometric observables are fit with models that describe the expected scene (e.g. one point source vs. two point sources). Importantly, biases exist in these observables that must be precisely calibrated, hence the observation of a reference star directly before or after the target. However, it is possible to instead use the WFSC information to produce PSF models and calibrate the bias in the interferometric observables. This procedure would also increase the efficiency of any observing plan by removing the observation of the reference star, like with our

technique.

This technique is planned to be applied as part of the Cycle 1 program, GO-2627 (PI: M. Ygouf). In this program, JWST WFSC operations will be performed to derive the OTE OPD. Then, successive observations with NIRCam full pupil imaging and coronagraphic imaging are performed on a target, followed by another set of WFSC observations to again evaluate the OTE OPD which may have changed due to WFE drift from slewing. To determine the ability to estimate the WFE of a given observation, a technique similar to what we presented here will be applied to the full pupil and coronagraphic imaging. These estimates will be compared to the measured OTE OPD to determine how well this type of analysis performs on these different observing modes.

Other future space missions, like Roman, will also focus heavily on coronagraphic imaging with the goal of achieving contrasts of $10^{-9}$. One feature of Roman is its active wavefront control which is intended to maintain a highly stable PSF during the course of observations (Kasdin et al., 2020). The low order wavefront sensing and control is viable for V $<$ 5 mag and operates continuously. Higher order wavefront errors can be estimated during reference star observations, and corrected for during target observations. Additional higher order wavefront sensing measurements are taken once per day and evaluated from the ground that can inform post-processing analyses. A residual WFE will still remain due to WFE drift which can be modeled by a technique like our own. Also, removing the reference star will significantly reduce observing time if post-processing techniques like ours can be informed by other wavefront sensing observations. Many future missions plan to incorporate WFS information into their high-contrast imaging observations, and WFE optimization routines will still be necessary to improve the modeling of the PSF due to changes from WFE drift. This technique is broadly applicable across many observing modes allowing for observer flexibility based on target characteristics, and with its proven efficacy will increase the efficiency of high-contrast imaging programs.

## A.6 Conclusion

In this paper, we implemented our post-processing technique that utilizes JWST WFS information as priors to estimate the WFE of an observation with synthetic PSF models while simultaneously searching for a companion. This analysis is performed on JWST/NIRISS AMI and FP imaging simulations. For the first time, we have extract the posterior distributions for both the WFE and companion parameters simultaneously using pyMultiNest. With this technique, we found:

1) Our estimate of the WFE of the target observation is an improvement over the WFE derived from simulated WFSC data. In the AMI case, our WFE estimate improves the modeling of the PSF over all separations sampled, while in the full pupil case it improves the PSF model for separations $<$ 0.455".

2) This technique achieves contrasts close to the photon noise limit in the AMI case. This is in part due to the reduced number of degeneracies between primary mirror segments from seven sub-apertures as opposed to the 18 mirror segments in the full pupil case. However, this achievement is also due to the extended structure of the AMI PSF, more sensitive to small changes in the Hexike coefficients.

3) The derived sensitivity limit of our technique is less than a factor of two times the derived photon noise limit. Although evaluated in a different plane than our technique, the traditional interferometric technique appears sensitive to companions at roughly twice the derived photon noise limit when there is $\sim$ 5nm WFE drift from the calibrator star, displaying the comparable performances of both techniques.

4) We have proven the ability to recover a faint, close companion with a contrast of 8 magnitudes in the F430M filter and a separation of 0.2055" (1.5$\lambda$/D, 3.16 NIRISS pixels). The recovery of the companion parameters performs comparably to the traditional interferometric post-processing techniques.

5) Our approach shows the ability to perform high contrast imaging without a reference star observation, significantly reducing the total allocated time for such a program.

## A.7 Acknowledgements

This research made use of POPPY, an open-source optical propagation Python package originally developed for the James Webb Space Telescope project (Perrin et al., 2012).

Matthew De Furio benefited from support from JPL's Strategic University Research Partnership (SURP). This work was supported by NASA through the JWST NIRCam project through contract number NAS5-02195 (M. Rieke, University of Arizona, PI). This research was carried out at the Jet Propulsion Laboratory, California Institute of Technology, under a contract with the National Aeronautics and Space Administration.

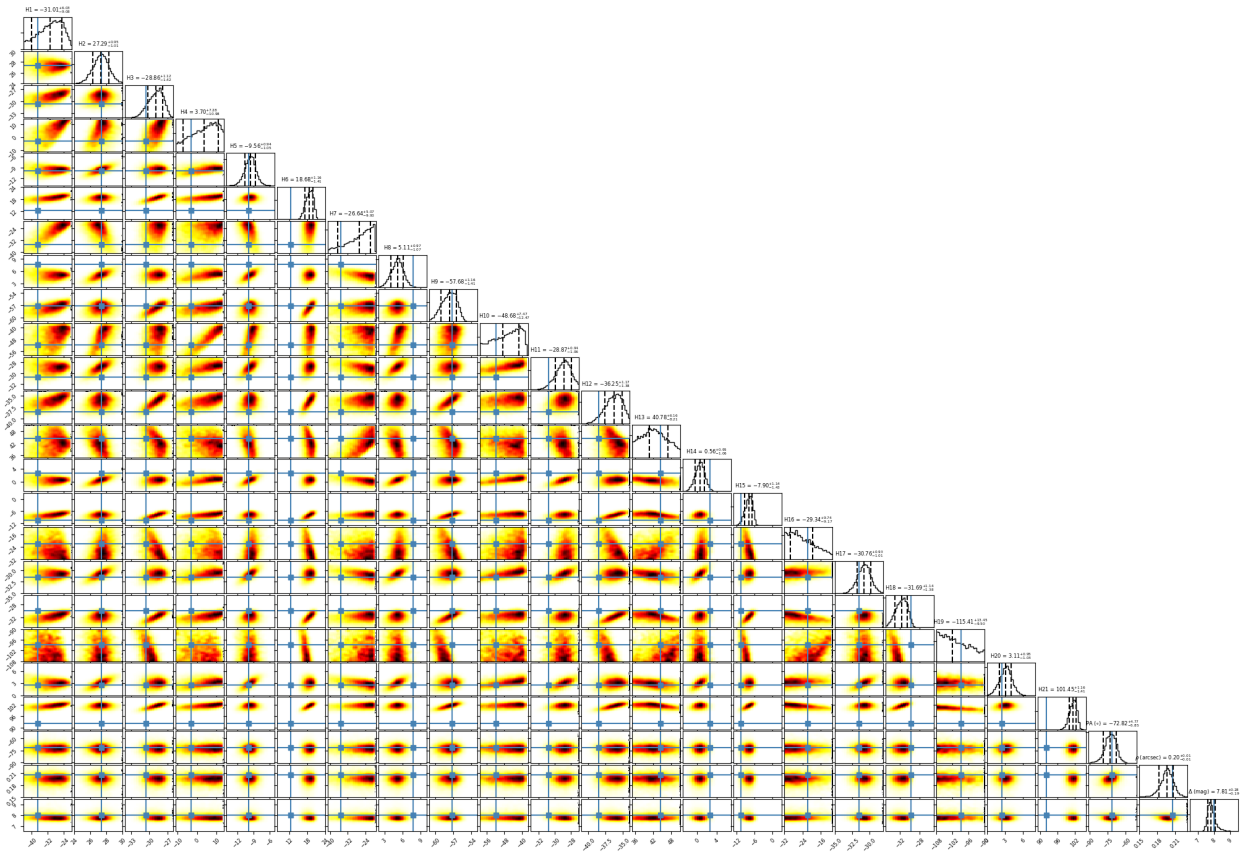

Figure A.17: Corner plot showing the estimate of the Hexike coefficients for each of the seven mirror segments used in an AMI observation (H1-H21), in addition to the companion parameters simultaneously estimated (PA, $\rho$(arcsec), $\Delta$(mag). H1-H3 represent the piston, tip, and tilt coefficients for the first mirror segment. Subsequent groups of three Hexikes correspond to the same coefficients for separate mirror segments. Blue line is known values. Black dashed lines are the median value and 68% confidence interval.

# BIBLIOGRAPHY


, 1997: *The HIPPARCOS and TYCHO catalogues. Astrometric and photometric star catalogues derived from the ESA HIPPARCOS Space Astrometry Mission*, ESA Special Publication, Vol. 1200.

Abbott, B. P., and Coauthors, 2016: Observation of Gravitational Waves from a Binary Black Hole Merger. *PhRvL*, **116 (6)**, 061102, https://doi.org/10.1103/PhysRevLett.116.061102, 1602.03837.

Abt, H. A., 1961: The Frequency of Binaries among Metalmc-Line Stars. *ApJS*, **6**, 37, https://doi.org/10.1086/190060.

Abt, H. A., 1965: The Frequency of Binaries among Normal A-Type Stars. *ApJS*, **11**, 429, https://doi.org/10.1086/190120.

Abt, H. A., 1981: Visual multiples. VII. MK classifications. *ApJS*, **45**, 437–456, https://doi.org/10.1086/190719.

Abt, H. A., A. E. Gomez, and S. G. Levy, 1990: The Frequency and Formation Mechanism of B2–B5 Main-Sequence Binaries. *ApJS*, **74**, 551, https://doi.org/10.1086/191508.

Abt, H. A., and S. G. Levy, 1985: Improved study of metallic-line binaries. *ApJS*, **59**, 229–247, https://doi.org/10.1086/191070.

Adams, F. C., S. P. Ruden, and F. H. Shu, 1989: Eccentric gravitational instabilities in nearly Keplerian disks. *ApJ*, **347**, 959–976, https://doi.org/10.1086/168187.

Adams, J. D., J. R. Stauffer, D. G. Monet, M. F. Skrutskie, and C. A. Beichman, 2001: The Mass and Structure of the Pleiades Star Cluster from 2MASS. *AJ*, **121 (4)**, 2053–2064, https://doi.org/10.1086/319965, astro-ph/0101139.

Ahmic, M., R. Jayawardhana, A. Brandeker, A. Scholz, M. H. van Kerkwijk, E. Delgado-Donate, and D. Froebrich, 2007: Multiplicity among Young Brown Dwarfs and Very Low Mass Stars. *ApJ*, **671 (2)**, 2074–2081, https://doi.org/10.1086/522875, 0708.3851.

Albert, L., and Coauthors, 2021: Multiplicity Survey of 20 Y Dwarfs with NIRCam Kernel Phase Interferometry. 2473 pp., JWST Proposal. Cycle 1, ID. #2473.

Allard, F., P. H. Hauschildt, D. R. Alexander, A. Tamanai, and A. Schweitzer, 2001: The Limiting Effects of Dust in Brown Dwarf Model Atmospheres. *ApJ*, **556 (1)**, 357–372, https://doi.org/10.1086/321547, astro-ph/0104256.

Allard, F., D. Homeier, and B. Freytag, 2011: Model Atmospheres From Very Low Mass Stars to Brown Dwarfs. *16th Cambridge Workshop on Cool Stars, Stellar Systems, and the Sun*, C. Johns-Krull, M. K. Browning, and A. A. West, Eds., Astronomical Society of the Pacific Conference Series, Vol. 448, 91, 1011.5405.

Allard, F., D. Homeier, B. Freytag, and C. M. Sharp, 2012: Atmospheres From Very Low-Mass Stars to Extrasolar Planets. *EAS Publications Series*, C. Reylé, C. Charbonnel, and M. Schultheis, Eds., EAS Publications Series, Vol. 57, 3–43, https://doi.org/10.1051/eas/1257001, 1206.1021.

Allen, P. R., 2007: Star Formation via the Little Guy: A Bayesian Study of Ultracool Dwarf Imaging Surveys for Companions. *ApJ*, **668 (1)**, 492–506, https://doi.org/10.1086/521207, 0707.2064.

Allison, R. J., S. P. Goodwin, R. J. Parker, R. de Grijs, S. F. Portegies Zwart, and M. B. N. Kouwenhoven, 2009: Dynamical Mass Segregation on a Very Short Timescale. *ApJL*, **700 (2)**, L99–L103, https://doi.org/10.1088/0004-637X/700/2/L99, 0906.4806.

Allison, R. J., S. P. Goodwin, R. J. Parker, S. F. Portegies Zwart, and R. de Grijs, 2010: The early dynamical evolution of cool, clumpy star clusters. *MNRAS*, **407 (2)**, 1098–1107, https://doi.org/10.1111/j.1365-2966.2010.16939.x, 1004.5244.

Amara, A., and S. P. Quanz, 2012: PYNPOINT: an image processing package for finding exoplanets. *MNRAS*, **427 (2)**, 948–955, https://doi.org/10.1111/j.1365-2966.2012.21918.x, 1207.6637.

Andersen, M., M. R. Meyer, J. Greissl, and A. Aversa, 2008: Evidence for a Turnover in the Initial Mass Function of Low-Mass Stars and Substellar Objects: Analysis from an Ensemble of Young Clusters. *ApJL*, **683 (2)**, L183, https://doi.org/10.1086/591473, 0807.1354.

Anderson, J., 2016: Empirical Models for the WFC3/IR PSF. 12 pp., Instrument Science Report WFC3 2016-12, 42 pages.

Anderson, J., and I. R. King, 2000: Toward High-Precision Astrometry with WFPC2. I. Deriving an Accurate Point-Spread Function. *PASP*, **112 (776)**, 1360–1382, https://doi.org/10.1086/316632, astro-ph/0006325.

Anderson, J., and I. R. King, 2006: Psfs, photometry, and astronomy for the acs/wfc. *Instrument Science Report ACS 2006-01, 34 pages*.

Anugu, N., and Coauthors, 2020: MIRC-X: A Highly Sensitive Six-telescope Interferometric Imager at the CHARA Array. *AJ*, **160 (4)**, 158, https://doi.org/10.3847/1538-3881/aba957, 2007.12320.

Aronstein, D. L., J. S. Smith, T. P. Zielinski, R. Telfer, S. C. Tournois, D. B. Moore, and J. R. Fienup, 2016: Wavefront-error performance characterization for the James Webb Space Telescope (JWST) Integrated Science Instrument Module (ISIM) science instruments. *Space Telescopes and Instrumentation 2016: Optical, Infrared, and Millimeter Wave*, H. A. MacEwen, G. G. Fazio, M. Lystrup, N. Batalha, N. Siegler, and E. C. Tong, Eds., Society of Photo-Optical Instrumentation Engineers (SPIE) Conference Series, Vol. 9904, 990409, https://doi.org/10.1117/12.2233842.

Artymowicz, P., and S. H. Lubow, 1994: Dynamics of Binary-Disk Interaction. I. Resonances and Disk Gap Sizes. *ApJ*, **421**, 651, https://doi.org/10.1086/173679.

Arzoumanian, D., and Coauthors, 2011: Characterizing interstellar filaments with Herschel in IC 5146. *A&A*, **529**, L6, https://doi.org/10.1051/0004-6361/201116596, 1103.0201.

Astropy Collaboration, and Coauthors, 2013: Astropy: A community Python package for astronomy. *A&A*, **558**, A33, https://doi.org/10.1051/0004-6361/201322068, 1307.6212.

Astropy Collaboration, and Coauthors, 2018: The Astropy Project: Building an Open-science Project and Status of the v2.0 Core Package. *AJ*, **156 (3)**, 123, https://doi.org/10.3847/1538-3881/aabc4f, 1801.02634.

Astropy Collaboration, and Coauthors, 2022: The Astropy Project: Sustaining and Growing a Community-oriented Open-source Project and the Latest Major Release (v5.0) of the Core Package. *ApJ*, **935 (2)**, 167, https://doi.org/10.3847/1538-4357/ac7c74, 2206.14220.

Azevedo, R., N. Calvet, L. Hartmann, D. F. M. Folha, F. Gameiro, and J. Muzerolle, 2006: Calcium II infrared triplet line models in classical T Tauri stars. *A&A*, **456 (1)**, 225–234, https://doi.org/10.1051/0004-6361:20054315, 0712.2971.

Babusiaux, C., and Coauthors, 2022: Gaia Data Release 3: Catalogue Validation. *arXiv e-prints*, arXiv:2206.05989, 2206.05989.

Barber, R. J., J. Tennyson, G. J. Harris, and R. N. Tolchenov, 2006: A high-accuracy computed water line list. *MNRAS*, **368 (3)**, 1087–1094, https://doi.org/10.1111/j.1365-2966.2006.10184.x, astro-ph/0601236.

Barclay, T., and Coauthors, 2013: A sub-Mercury-sized exoplanet. *Nature*, **494 (7438)**, 452–454, https://doi.org/10.1038/nature11914, 1305.5587.

Bastian, N., K. R. Covey, and M. R. Meyer, 2010: A Universal Stellar Initial Mass Function? A Critical Look at Variations. *ARA&A*, **48**, 339–389, https://doi.org/10.1146/annurev-astro-082708-101642, 1001.2965.

Bate, M. R., 2000: Predicting the properties of binary stellar systems: the evolution of accreting protobinary systems. *MNRAS*, **314 (1)**, 33–53, https://doi.org/10.1046/j.1365-8711.2000.03333.x, astro-ph/0002143.

Bate, M. R., 2012: Stellar, brown dwarf and multiple star properties from a radiation hydrodynamical simulation of star cluster formation. *MNRAS*, **419 (4)**, 3115–3146, https://doi.org/10.1111/j.1365-2966.2011.19955.x, 1110.1092.

Bate, M. R., and I. A. Bonnell, 1997: Accretion during binary star formation - II. Gaseous accretion and disc formation. *MNRAS*, **285 (1)**, 33–48, https://doi.org/10.1093/mnras/285.1.33.

Bate, M. R., I. A. Bonnell, and V. Bromm, 2002: The formation of close binary systems by dynamical interactions and orbital decay. *MNRAS*, **336 (3)**, 705–713, https://doi.org/10.1046/j.1365-8711.2002.05775.x, astro-ph/0212403.

Bate, M. R., I. A. Bonnell, and V. Bromm, 2003: The formation of a star cluster: predicting the properties of stars and brown dwarfs. *MNRAS*, **339 (3)**, 577–599, https://doi.org/10.1046/j.1365-8711.2003.06210.x, astro-ph/0212380.

Beccari, G., and Coauthors, 2017: A tale of three cities. OmegaCAM discovers multiple sequences in the color-magnitude diagram of the Orion Nebula Cluster. *A&A*, **604**, A22, https://doi.org/10.1051/0004-6361/201730432, 1705.09496.

Beichman, C., C. R. Gelino, J. D. Kirkpatrick, T. S. Barman, K. A. Marsh, M. C. Cushing, and E. L. Wright, 2013: The Coldest Brown Dwarf (or Free-floating Planet)?: The Y Dwarf WISE 1828+2650. *ApJ*, **764 (1)**, 101, https://doi.org/10.1088/0004-637X/764/1/101, 1301.1669.

Beichman, C., C. R. Gelino, J. D. Kirkpatrick, M. C. Cushing, S. Dodson-Robinson, M. S. Marley, C. V. Morley, and E. L. Wright, 2014: WISE Y Dwarfs as Probes of the Brown Dwarf-Exoplanet Connection. *ApJ*, **783 (2)**, 68, https://doi.org/10.1088/0004-637X/783/2/68, 1401.1194.

Biller, B., K. Allers, M. Liu, L. M. Close, and T. Dupuy, 2011: A Keck LGS AO Search for Brown Dwarf and Planetary Mass Companions to Upper Scorpius Brown Dwarfs. *ApJ*, **730 (1)**, 39, https://doi.org/10.1088/0004-637X/730/1/39, 1101.4934.

Boley, A. C., R. H. Durisen, Å. Nordlund, and J. Lord, 2007: Three-Dimensional Radiative Hydrodynamics for Disk Stability Simulations: A Proposed Testing Standard and New Results. *ApJ*, **665 (2)**, 1254–1267, https://doi.org/10.1086/519767, 0704.2532.

Bonnell, I. A., and M. R. Bate, 1994: Massive Circumbinary Discs and the Formation of Multiple Systems. *MNRAS*, **269**, https://doi.org/10.1093/mnras/269.1.L45.

Borgniet, S., and Coauthors, 2019: Extrasolar planets and brown dwarfs around AF-type stars. X. The SOPHIE sample: combining the SOPHIE and HARPS surveys to compute the close giant planet mass-period distribution around AF-type stars. *A&A*, **621**, A87, https://doi.org/10.1051/0004-6361/201833431, 1809.09914.

Bourges, L., G. Mella, S. Lafrasse, G. Duvert, A. Chelli, J. B. Le Bouquin, X. Delfosse, and O. Chesneau, 2017: VizieR Online Data Catalog: JMMC Stellar Diameters Catalogue - JSDC. Version 2 (Bourges+, 2017). *VizieR Online Data Catalog*, II/346.

Bowens, R., and Coauthors, 2021: Exoplanets with ELT-METIS. I. Estimating the direct imaging exoplanet yield around stars within 6.5 parsecs. *A&A*, **653**, A8, https://doi.org/10.1051/0004-6361/202141109, 2107.06375.

Bowler, B. P., 2016: Imaging Extrasolar Giant Planets. *PASP*, **128 (968)**, 102 001, https://doi.org/10.1088/1538-3873/128/968/102001, 1605.02731.

Bradley, L., and Coauthors, 2020: astropy/photutils: 1.0.0. Zenodo, Zenodo, https://doi.org/10.5281/zenodo.4044744.

Brandner, W., J. M. Alcala, M. Kunkel, A. Moneti, and H. Zinnecker, 1996: Multiplicity among T Tauri stars in OB and T associations. Implications for binary star formation. *A&A*, **307**, 121, astro-ph/9507018.

Briceño, C., and Coauthors, 2019: The CIDA Variability Survey of Orion OB1. II. Demographics of the Young, Low-mass Stellar Populations. *AJ*, **157 (2)**, 85, https://doi.org/10.3847/1538-3881/aaf79b.

Buchner, J., and Coauthors, 2014a: X-ray spectral modelling of the AGN obscuring region in the CDFS: Bayesian model selection and catalogue. *A&A*, **564**, A125, https://doi.org/10.1051/0004-6361/201322971, 1402.0004.

Buchner, J., and Coauthors, 2014b: X-ray spectral modelling of the AGN obscuring region in the CDFS: Bayesian model selection and catalogue. *A&A*, **564**, A125, https://doi.org/10.1051/0004-6361/201322971, 1402.0004.

Burgasser, A. J., J. D. Kirkpatrick, K. L. Cruz, I. N. Reid, S. K. Leggett, J. Liebert, A. Burrows, and M. E. Brown, 2006: Hubble Space Telescope NICMOS Observations of T Dwarfs: Brown Dwarf Multiplicity and New Probes of the L/T Transition. *ApJS*, **166 (2)**, 585–612, https://doi.org/10.1086/506327, astro-ph/0605577.

Burgasser, A. J., J. D. Kirkpatrick, I. N. Reid, M. E. Brown, C. L. Miskey, and J. E. Gizis, 2003: Binarity in Brown Dwarfs: T Dwarf Binaries Discovered with the Hubble Space Telescope Wide Field Planetary Camera 2. *ApJ*, **586**, 512–526, https://doi.org/10.1086/346263, astro-ph/0211470.

Burgasser, A. J., I. N. Reid, N. Siegler, L. Close, P. Allen, P. Lowrance, and J. Gizis, 2007: Not Alone: Tracing the Origins of Very-Low-Mass Stars and Brown Dwarfs Through Multiplicity Studies. *Protostars and Planets V*, B. Reipurth, D. Jewitt, and K. Keil, Eds., 427, https://doi.org/10.48550/arXiv.astro-ph/0602122, astro-ph/0602122.

Burrows, A., K. Heng, and T. Nampaisarn, 2011: The Dependence of Brown Dwarf Radii on Atmospheric Metallicity and Clouds: Theory and Comparison with Observations. *ApJ*, **736 (1)**, 47, https://doi.org/10.1088/0004-637X/736/1/47, 1102.3922.

Burrows, A., W. B. Hubbard, J. I. Lunine, and J. Liebert, 2001: The theory of brown dwarfs and extrasolar giant planets. *Reviews of Modern Physics*, **73 (3)**, 719–765, https://doi.org/10.1103/RevModPhys.73.719, astro-ph/0103383.

Caldwell, J. A. R., J. H. Spencer Jones, and J. W. Menzies, 1984: A photometric study of six nearby common-proper-motion pairs. *MNRAS*, **209**, 51–58, https://doi.org/10.1093/mnras/209.1.51.

Calissendorff, P., M. Janson, R. Asensio-Torres, and R. Köhler, 2019: Spectral characterization of newly detected young substellar binaries with SINFONI. *A&A*, **627**, A167, https://doi.org/10.1051/0004-6361/201935319, 1906.05871.

Calissendorff, P., and Coauthors, 2023: JWST/NIRCam Discovery of the First Y+Y Brown Dwarf Binary: WISE J033605.05-014350.4. *ApJL*, **947 (2)**, L30, https://doi.org/10.3847/2041-8213/acc86d, 2303.16923.

Cantalloube, F., M. Ygouf, L. Mugnier, D. Mouillet, O. Herscovici-Schiller, and W. Brandner, 2018: Status of the MEDUSAE post-processing method to detect circumstellar objects in high-contrast multispectral images. *arXiv e-prints*, arXiv:1812.04312, https://doi.org/10.48550/arXiv.1812.04312, 1812.04312.

Cardelli, J. A., G. C. Clayton, and J. S. Mathis, 1989: The Relationship between Infrared, Optical, and Ultraviolet Extinction. *ApJ*, **345**, 245, https://doi.org/10.1086/167900.

Carpenter, J. M., 2000: 2MASS Observations of the Perseus, Orion A, Orion B, and Monoceros R2 Molecular Clouds. *AJ*, **120 (6)**, 3139–3161, https://doi.org/10.1086/316845, astro-ph/0009118.

Carquillat, J. M., and J. L. Prieur, 2007: Contribution to the search for binaries among Am stars - VIII. New spectroscopic orbits of eight systems and statistical study of a sample of 91 Am stars. *MNRAS*, **380 (3)**, 1064–1078, https://doi.org/10.1111/j.1365-2966.2007.12143.x.

Carter, A. L., and Coauthors, 2023: The JWST Early Release Science Program for Direct Observations of Exoplanetary Systems I: High-contrast Imaging of the Exoplanet HIP 65426 b from 2 to 16 $\mu$m. *ApJL*, **951 (1)**, L20, https://doi.org/10.3847/2041-8213/acd93e, 2208.14990.

Ceau, A., D. Mary, A. Greenbaum, F. Martinache, A. Sivaramakrishnan, R. Laugier, and M. N'Diaye, 2019: Kernel-phase detection limits. Hypothesis testing and the example of JWST NIRISS full-pupil images. *A&A*, **630**, A120, https://doi.org/10.1051/0004-6361/201935247, 1908.03130.

Celotti, A., J. C. Miller, and D. W. Sciama, 1999: Astrophysical evidence for the existence of black holes. *Classical and Quantum Gravity*, **16 (12A)**, A3–A21, https://doi.org/10.1088/0264-9381/16/12A/301, astro-ph/9912186.

Chabrier, G., 2003: Galactic Stellar and Substellar Initial Mass Function. *PASP*, **115 (809)**, 763–795, https://doi.org/10.1086/376392, astro-ph/0304382.

Chabrier, G., I. Baraffe, F. Allard, and P. Hauschildt, 2000: Evolutionary Models for Very Low-Mass Stars and Brown Dwarfs with Dusty Atmospheres. *ApJ*, **542 (1)**, 464–472, https://doi.org/10.1086/309513, astro-ph/0005557.

Chandrasekhar, S., 1963: The Equilibrium and the Stability of the Roche Ellipsoids. *ApJ*, **138**, 1182, https://doi.org/10.1086/147716.

Charbonneau, D., T. M. Brown, D. W. Latham, and M. Mayor, 2000: Detection of Planetary Transits Across a Sun-like Star. *ApJL*, **529 (1)**, L45–L48, https://doi.org/10.1086/312457, astro-ph/9911436.

Chauvin, G., A. M. Lagrange, C. Dumas, B. Zuckerman, D. Mouillet, I. Song, J. L. Beuzit, and P. Lowrance, 2004: A giant planet candidate near a young brown dwarf. Direct VLT/NACO observations using IR wavefront sensing. *A&A*, **425**, L29–L32, https://doi.org/10.1051/0004-6361:200400056, astro-ph/0409323.

Che, X., and Coauthors, 2011: Colder and Hotter: Interferometric Imaging of $\beta$ Cassiopeiae and $\alpha$ Leonis. *ApJ*, **732 (2)**, 68, https://doi.org/10.1088/0004-637X/732/2/68, 1105.0740.

Chen, H. H.-H., and Coauthors, 2019: Droplets. II. Internal Velocity Structures and Potential Rotational Motions in Pressure-dominated Coherent Structures. *ApJ*, **886 (2)**, 119, https://doi.org/10.3847/1538-4357/ab4ce9, 1908.04367.

Choi, J., A. Dotter, C. Conroy, M. Cantiello, B. Paxton, and B. D. Johnson, 2016: Mesa Isochrones and Stellar Tracks (MIST). I. Solar-scaled Models. *ApJ*, **823 (2)**, 102, https://doi.org/10.3847/0004-637X/823/2/102, 1604.08592.

Cieza, L. A., and Coauthors, 2009: Primordial Circumstellar Disks in Binary Systems: Evidence for Reduced Lifetimes. *ApJL*, **696 (1)**, L84–L88, https://doi.org/10.1088/0004-637X/696/1/L84, 0903.3057.

Clark, J. S., I. Negueruela, P. A. Crowther, and S. P. Goodwin, 2005: On the massive stellar population of the super star cluster ¡ASTROBJ¿Westerlund 1¡/ASTROBJ¿. *A&A*, **434**, 949–969, https://doi.org/10.1051/0004-6361:20042413, astro-ph/0504342.

Close, L. M., N. Siegler, M. Freed, and B. Biller, 2003: Detection of Nine M8.0-L0.5 Binaries: The Very Low Mass Binary Population and Its Implications for Brown Dwarf and Very Low Mass Star Formation. *ApJ*, **587 (1)**, 407–422, https://doi.org/10.1086/368177, astro-ph/0301095.

Close, L. M., and Coauthors, 2007: The Wide Brown Dwarf Binary Oph 1622-2405 and Discovery of a Wide, Low-Mass Binary in Ophiuchus (Oph 1623-2402): A New Class of Young Evaporating Wide Binaries? *ApJ*, **660 (2)**, 1492–1506, https://doi.org/10.1086/513417, astro-ph/0608574.

Cummings, J. D., J. S. Kalirai, P. E. Tremblay, E. Ramirez-Ruiz, and J. Choi, 2018: The White Dwarf Initial-Final Mass Relation for Progenitor Stars from 0.85 to 7.5 $M_\odot$. *ApJ*, **866 (1)**, 21, https://doi.org/10.3847/1538-4357/aadfd6, 1809.01673.

Cushing, M. C., and Coauthors, 2011: The Discovery of Y Dwarfs using Data from the Wide-field Infrared Survey Explorer (WISE). *ApJ*, **743 (1)**, 50, https://doi.org/10.1088/0004-637X/743/1/50, 1108.4678.

Cushing, M. C., and Coauthors, 2021: An Improved Near-infrared Spectrum of the Archetype Y Dwarf WISEP J182831.08+265037.8. *ApJ*, **920 (1)**, 20, https://doi.org/10.3847/1538-4357/ac12cb, 2107.00506.

Da Rio, N., M. Robberto, L. A. Hillenbrand, T. Henning, and K. G. Stassun, 2012: The Initial Mass Function of the Orion Nebula Cluster across the H-burning Limit. *ApJ*, **748 (1)**, 14, https://doi.org/10.1088/0004-637X/748/1/14, 1112.2711.

Da Rio, N., J. C. Tan, and K. Jaehnig, 2014: The Structure, Dynamics, and Star Formation Rate of the Orion Nebula Cluster. *ApJ*, **795 (1)**, 55, https://doi.org/10.1088/0004-637X/795/1/55, 1409.2503.

Da Rio, N., and Coauthors, 2016: IN-SYNC. IV. The Young Stellar Population in the Orion A Molecular Cloud. *ApJ*, **818**, 59, https://doi.org/10.3847/0004-637X/818/1/59, 1511.04147.

Danby, J. M. A., 1988: *Fundamentals of celestial mechanics*.

Darnley, M. J., V. A. R. M. Ribeiro, M. F. Bode, R. A. Hounsell, and R. P. Williams, 2012: On the Progenitors of Galactic Novae. *ApJ*, **746 (1)**, 61, https://doi.org/10.1088/0004-637X/746/1/61, 1112.2589.

De Furio, M., C. Liu, M. R. Meyer, M. Reiter, A. Kraus, T. Dupuy, and J. Monnier, 2022a: Demographics of the M-star Multiple Population in the Orion Nebula Cluster. *ApJ*, **941 (2)**, 161, https://doi.org/10.3847/1538-4357/aca285, 2211.01897.

De Furio, M., M. R. Meyer, M. Reiter, J. Monnier, A. Kraus, and T. Dupuy, 2022b: Binary Formation in the Orion Nebula Cluster: Exploring the Substellar Limit. *ApJ*, **925 (2)**, 112, https://doi.org/10.3847/1538-4357/ac36d4, 2111.02914.

De Furio, M., M. Reiter, M. R. Meyer, A. Greenbaum, T. Dupuy, and A. Kraus, 2019: A Search for Intermediate-separation Low-mass Binaries in the Orion Nebula Cluster. *ApJ*, **886 (2)**, 95, https://doi.org/10.3847/1538-4357/ab4ae3, 1910.02092.

De Furio, M., and Coauthors, 2022c: The Small Separation A-star Companion Population: First Results with CHARA/MIRC-X. *ApJ*, **941 (2)**, 118, https://doi.org/10.3847/1538-4357/aca1ad, 2211.01465.

De Furio, M., and Coauthors, 2023: JWST Observations of the Enigmatic Y-Dwarf WISE 1828+2650. I. Limits to a Binary Companion. *ApJ*, **948 (2)**, 92, https://doi.org/10.3847/1538-4357/acbf1e, 2302.12723.

De Rosa, R. J., and Coauthors, 2014: The VAST Survey - III. The multiplicity of A-type stars within 75 pc. *MNRAS*, **437**, 1216–1240, https://doi.org/10.1093/mnras/stt1932, 1311.7141.

Dean, B. H., D. L. Aronstein, J. S. Smith, R. Shiri, and D. S. Acton, 2006: Phase retrieval algorithm for JWST Flight and Testbed Telescope. *Society of Photo-Optical Instrumentation Engineers (SPIE) Conference Series*, J. C. Mather, H. A. MacEwen, and M. W. M. de Graauw, Eds., Society of Photo-Optical Instrumentation Engineers (SPIE) Conference Series, Vol. 6265, 626511, https://doi.org/10.1117/12.673569.

Di Stefano, R., 2011: Transits and Lensing by Compact Objects in the Kepler Field: Disrupted Stars Orbiting Blue Stragglers. *AJ*, **141 (5)**, 142, https://doi.org/10.1088/0004-6256/141/5/142, 1002.3009.

Domoto, N., M. Tanaka, S. Wanajo, and K. Kawaguchi, 2021: Signatures of r-process Elements in Kilonova Spectra. *ApJ*, **913 (1)**, 26, https://doi.org/10.3847/1538-4357/abf358, 2103.15284.

Dotter, A., 2016: MESA Isochrones and Stellar Tracks (MIST) 0: Methods for the Construction of Stellar Isochrones. *ApJS*, **222 (1)**, 8, https://doi.org/10.3847/0067-0049/222/1/8, 1601.05144.

Doyle, L. R., and Coauthors, 2011: Kepler-16: A Transiting Circumbinary Planet. *Science*, **333 (6049)**, 1602, https://doi.org/10.1126/science.1210923, 1109.3432.

Duchêne, G., and A. Kraus, 2013: Stellar Multiplicity. *ARA&A*, **51 (1)**, 269–310, https://doi.org/10.1146/annurev-astro-081710-102602, 1303.3028.

Duchêne, G., S. Lacour, E. Moraux, S. Goodwin, and J. Bouvier, 2018: Is stellar multiplicity universal? Tight stellar binaries in the Orion nebula Cluster. *MNRAS*, **478**, 1825–1836, https://doi.org/10.1093/mnras/sty1180, 1805.00965.

Dupuy, T. J., and M. C. Liu, 2011: On the Distribution of Orbital Eccentricities for Very Low-mass Binaries. *ApJ*, **733 (2)**, 122, https://doi.org/10.1088/0004-637X/733/2/122, 1103.5744.

Dupuy, T. J., and M. C. Liu, 2017: Individual Dynamical Masses of Ultracool Dwarfs. *ApJS*, **231 (2)**, 15, https://doi.org/10.3847/1538-4365/aa5e4c, 1703.05775.

Dupuy, T. J., M. C. Liu, and S. K. Leggett, 2015: Discovery of a Low-luminosity, Tight Substellar Binary at the T/Y Transition. *ApJ*, **803 (2)**, 102, https://doi.org/10.1088/0004-637X/803/2/102, 1502.04707.

Duquennoy, A., and M. Mayor, 1991: Multiplicity among Solar Type Stars in the Solar Neighbourhood - Part Two - Distribution of the Orbital Elements in an Unbiased Sample. *A&A*, **248**, 485.

El-Badry, K., and H.-W. Rix, 2019: The wide binary fraction of solar-type stars: emergence of metallicity dependence at a ¡ 200 au. *MNRAS*, **482 (1)**, L139–L144, https://doi.org/10.1093/mnrasl/sly206, 1809.06860.

El-Badry, K., H.-W. Rix, H. Tian, G. Duchêne, and M. Moe, 2019: Discovery of an equal-mass 'twin' binary population reaching 1000 + au separations. *MNRAS*, **489 (4)**, 5822–5857, https://doi.org/10.1093/mnras/stz2480, 1906.10128.

Falceta-Gonçalves, D., I. Bonnell, G. Kowal, J. R. D. Lépine, and C. A. S. Braga, 2015: The onset of large-scale turbulence in the interstellar medium of spiral galaxies. *MNRAS*, **446 (1)**, 973–989, https://doi.org/10.1093/mnras/stu2127, 1410.2774.

Feigelson, E. D., and G. J. Babu, 2012: *Modern Statistical Methods for Astronomy*.

Feroz, F., M. P. Hobson, and M. Bridges, 2009a: MULTINEST: an efficient and robust Bayesian inference tool for cosmology and particle physics. *MNRAS*, **398 (4)**, 1601–1614, https://doi.org/10.1111/j.1365-2966.2009.14548.x, 0809.3437.

Feroz, F., M. P. Hobson, and M. Bridges, 2009b: MULTINEST: an efficient and robust Bayesian inference tool for cosmology and particle physics. *MNRAS*, **398 (4)**, 1601–1614, https://doi.org/10.1111/j.1365-2966.2009.14548.x, 0809.3437.

Ferraro, F. R., and Coauthors, 2006: Discovery of Carbon/Oxygen-depleted Blue Straggler Stars in 47 Tucanae: The Chemical Signature of a Mass Transfer Formation Process. *ApJL*, **647 (1)**, L53–L56, https://doi.org/10.1086/507327, astro-ph/0610081.

Fischer, D. A., and G. W. Marcy, 1992: Multiplicity among M Dwarfs. *ApJ*, **396**, 178, https://doi.org/10.1086/171708.

Fontanive, C., B. Biller, M. Bonavita, and K. Allers, 2018: Constraining the multiplicity statistics of the coolest brown dwarfs: binary fraction continues to decrease with spectral type. *MNRAS*, **479 (2)**, 2702–2727, https://doi.org/10.1093/mnras/sty1682, 1806.08737.

Fontanive, C., K. Rice, M. Bonavita, E. Lopez, Mužić, K. , and B. Biller, 2019: A high binary fraction for the most massive close-in giant planets and brown dwarf desert members. *MNRAS*, **485 (4)**, 4967–4996, https://doi.org/10.1093/mnras/stz671, 1903.02332.

Fried, D. L., 1965: Statistics of a Geometric Representation of Wavefront Distortion. *Journal of the Optical Society of America (1917-1983)*, **55 (11)**, 1427–1431.

Fusco, T., and Coauthors, 2006: High-order adaptive optics requirements for direct detection of extrasolar planets: Application to the SPHERE instrument. *Optics Express*, **14 (17)**, 7515, https://doi.org/10.1364/OE.14.007515.

Gagné, J., and Coauthors, 2018: BANYAN. XI. The BANYAN Σ Multivariate Bayesian Algorithm to Identify Members of Young Associations with 150 pc. *ApJ*, **856 (1)**, 23, https://doi.org/10.3847/1538-4357/aaae09, 1801.09051.

Gaia Collaboration, and Coauthors, 2016: The Gaia mission. *A&A*, **595**, A1, https://doi.org/10.1051/0004-6361/201629272, 1609.04153.

Gaia Collaboration, and Coauthors, 2018: Gaia Data Release 2. Summary of the contents and survey properties. *A&A*, **616**, A1, https://doi.org/10.1051/0004-6361/201833051, 1804.09365.

Gaia Collaboration, and Coauthors, 2022: Gaia Data Release 3: Stellar multiplicity, a teaser for the hidden treasure. *arXiv e-prints*, arXiv:2206.05595, 2206.05595.

Gallenne, A., and Coauthors, 2015: Robust high-contrast companion detection from interferometric observations. The CANDID algorithm and an application to six binary Cepheids. *A&A*, **579**, A68, https://doi.org/10.1051/0004-6361/201525917, 1505.02715.

Garcia, E. V., T. J. Dupuy, K. N. Allers, M. C. Liu, and N. R. Deacon, 2015: On the Binary Frequency of the Lowest Mass Members of the Pleiades with Hubble Space Telescope Wide Field Camera 3. *ApJ*, **804**, 65, https://doi.org/10.1088/0004-637X/804/1/65, 1505.02361.

Gardner, J. P., and Coauthors, 2006: The James Webb Space Telescope. *SSRv*, **123 (4)**, 485–606, https://doi.org/10.1007/s11214-006-8315-7, astro-ph/0606175.

Gardner, T., and Coauthors, 2021: ARMADA. I. Triple Companions Detected in B-type Binaries $\alpha$ Del and $\nu$ Gem. *AJ*, **161 (1)**, 40, https://doi.org/10.3847/1538-3881/abcf4e, 2012.00778.

Gaudi, B. S., M. Meyer, and J. Christiansen, 2021: The Demographics of Exoplanets. *ExoFrontiers; Big Questions in Exoplanetary Science*, N. Madhusudhan, Ed., 2–1, https://doi.org/10.1088/2514-3433/abfa8fch2.

Ghez, A. M., D. W. McCarthy, J. L. Patience, and T. L. Beck, 1997: The Multiplicity of Pre-Main-Sequence Stars in Southern Star-forming Regions. *ApJ*, **481**, 378–385, https://doi.org/10.1086/304031.

Ghez, A. M., G. Neugebauer, and K. Matthews, 1993: The multiplicity of T Tauri stars in the star forming regions Taurus-Auriga and Ophiuchus-Scorpius: A 2.2 micron speckle imaging survey. *AJ*, **106**, 2005–2023, https://doi.org/10.1086/116782.

Gieles, M., 2009: The early evolution of the star cluster mass function. *MNRAS*, **394 (4)**, 2113–2126, https://doi.org/10.1111/j.1365-2966.2009.14473.x, 0901.0830.

Gil-Pons, P., and E. García-Berro, 2001: On the formation of oxygen-neon white dwarfs in close binary systems. *A&A*, **375**, 87–99, https://doi.org/10.1051/0004-6361:20010828, astro-ph/0106224.

Gizis, J. E., I. N. Reid, G. R. Knapp, J. Liebert, J. D. Kirkpatrick, D. W. Koerner, and A. J. Burgasser, 2003: Hubble Space Telescope Observations of Binary Very Low Mass Stars and Brown Dwarfs. *AJ*, **125 (6)**, 3302–3310, https://doi.org/10.1086/374991, astro-ph/0302526.

Golomb, J., G. Rocha, T. Meshkat, M. Bottom, D. Mawet, B. Mennesson, G. Vasisht, and J. Wang, 2021: PlanetEvidence: Planet or Noise? *AJ*, **162 (6)**, 304, https://doi.org/10.3847/1538-3881/ac174e.

Goodwin, S. P., and N. Bastian, 2006: Gas expulsion and the destruction of massive young clusters. *MNRAS*, **373 (2)**, 752–758, https://doi.org/10.1111/j.1365-2966.2006.11078.x, astro-ph/0609477.

Goodwin, S. P., A. P. Whitworth, and D. Ward-Thompson, 2004a: Simulating star formation in molecular cloud cores. I. The influence of low levels of turbulence on fragmentation and multiplicity. *A&A*, **414**, 633–650, https://doi.org/10.1051/0004-6361:20031594, astro-ph/0309829.

Goodwin, S. P., A. P. Whitworth, and D. Ward-Thompson, 2004b: Simulating star formation in molecular cloud cores. I. The influence of low levels of turbulence on fragmentation and multiplicity. *A&A*, **414**, 633–650, https://doi.org/10.1051/0004-6361:20031594, astro-ph/0309829.

Goodwin, S. P., A. P. Whitworth, and D. Ward-Thompson, 2004c: Simulating star formation in molecular cores. II. The effects of different levels of turbulence. *A&A*, **423**, 169–182, https://doi.org/10.1051/0004-6361:20040285, astro-ph/0405117.

Gravity Collaboration, and Coauthors, 2018: Multiple star systems in the Orion nebula. *A&A*, **620**, A116, https://doi.org/10.1051/0004-6361/201833575, 1809.10376.

Gray, R. O., and Coauthors, 2016: LAMOST Observations in the Kepler Field: Spectral Classification with the MKCLASS Code. *AJ*, **151 (1)**, 13, https://doi.org/10.3847/0004-6256/151/1/13.

Greenbaum, A. Z., L. Pueyo, A. Sivaramakrishnan, and S. Lacour, 2015: An Image-plane Algorithm for JWST's Non-redundant Aperture Mask Data. *ApJ*, **798 (2)**, 68, https://doi.org/10.1088/0004-637X/798/2/68, 1411.3446.

Greenbaum, A. Z., and A. Sivaramakrishnan, 2016: In-focus wavefront sensing using non-redundant mask-induced pupil diversity. *Optics Express*, **24 (14)**, 15 506, https://doi.org/10.1364/OE.24.015506, 1607.01776.

Greenbaum, A. Z., and Coauthors, 2023: First Observations of the Brown Dwarf HD 19467 B with JWST. *ApJ*, **945 (2)**, 126, https://doi.org/10.3847/1538-4357/acb68b, 2301.11455.

Grison, P., and Coauthors, 1995: EROS catalogue of eclipsing binary stars in the bar of the Large Magellanic Cloud. *A&AS*, **109**, 447–469.

Großschedl, J. E., J. Alves, S. Meingast, and B. Hasenberger, 2018: 3D shape of Orion A with Gaia DR2. An informed view on Star Formation Rates and Efficiencies. *arXiv e-prints*, 1812.08024.

Hanel, R., B. Conrath, L. Herath, V. Kunde, and J. Pirraglia, 1981: Albedo, internal heat, and energy balance of Jupiter: preliminary results of the voyager infrared investigation. *J. Geophys. Res.*, **86 (A10)**, 8705–8712, https://doi.org/10.1029/JA086iA10p08705.

Haniff, C. A., C. D. Mackay, D. J. Titterington, D. Sivia, and J. E. Baldwin, 1987: The first images from optical aperture synthesis. *Nature*, **328 (6132)**, 694–696, https://doi.org/10.1038/328694a0.

He, C.-C., and M. Ricotti, 2023: Massive pre-stellar cores in radiation-magneto-turbulent simulations of molecular clouds. *MNRAS*, **522 (4)**, 5374–5392, https://doi.org/10.1093/mnras/stad1289, 2210.11629.

Herczeg, G. J., and L. A. Hillenbrand, 2014: An Optical Spectroscopic Study of T Tauri Stars. I. Photospheric Properties. *ApJ*, **786 (2)**, 97, https://doi.org/10.1088/0004-637X/786/2/97, 1403.1675.

Herschel, J. F. W., 1829: Observations with a 20-feet Reflecting Telescope - Third Series; containing a Catalogue of 384 new Double and Multiple Stars; completing a first Thousand of those Objects detected in a Course of Sweeps with that Instrument: together with Observations of some previously known. *MmRAS*, **3**, 177–213.

Herschel, J. F. W., and J. South, 1824: Observations of the Apparent Distances and Positions of 380 Double and Triple Stars, Made in the Years 1821, 1822, and 1823, and Compared with Those of Other Astronomers; Together with an Account of Such Changes as Appear to Have Taken Place in Them Since Their First Discovery. Also a Description of a Five-Feet Equatorial Instrument Employed in the Observations. *Philosophical Transactions of the Royal Society of London Series I*, **114**, 1–412.

Herschel, M., and D. Watson, 1782: Catalogue of Double Stars. By Mr. Herschel, F. R. S. Communicated by Dr. Watson, Jun. *Philosophical Transactions of the Royal Society of London Series I*, **72**, 112–162.

Herschel, W., 1803: Account of the Changes That Have Happened, during the Last Twenty-Five Years, in the Relative Situation of Double-Stars; With an Investigation of the Cause to Which They Are Owing. *Philosophical Transactions of the Royal Society of London Series I*, **93**, 339–382.

Hillenbrand, L. A., and L. W. Hartmann, 1998: A Preliminary Study of the Orion Nebula Cluster Structure and Dynamics. *ApJ*, **492 (2)**, 540–553, https://doi.org/10.1086/305076.

Hillenbrand, L. A., A. S. Hoffer, and G. J. Herczeg, 2013: An Enhanced Spectroscopic Census of the Orion Nebula Cluster. *AJ*, **146 (4)**, 85, https://doi.org/10.1088/0004-6256/146/4/85, 1307.5533.

Hills, J. G., 1980: The effect of mass loss on the dynamical evolution of a stellar system - Analytic approximations. *ApJ*, **235**, 986–991, https://doi.org/10.1086/157703.

Hinkley, S., and Coauthors, 2022a: Direct Discovery of the Inner Exoplanet in the HD206893 System. *arXiv e-prints*, arXiv:2208.04867, 2208.04867.

Hinkley, S., and Coauthors, 2022b: The JWST Early Release Science Program for the Direct Imaging & Spectroscopy of Exoplanetary Systems. *arXiv e-prints*, arXiv:2205.12972, 2205.12972.

Horton, A. J., M. R. Bate, and I. A. Bonnell, 2001: Binary formation in stellar clusters. *MNRAS*, **321**, 585–592, https://doi.org/10.1046/j.1365-8711.2001.04071.x.

Hugot, E., M. Ferrari, K. El Hadi, A. Costille, K. Dohlen, P. Rabou, P. Puget, and J. L. Beuzit, 2012: Active optics methods for exoplanet direct imaging. Stress polishing of supersmooth aspherics for VLT-SPHERE planet finder. *A&A*, **538**, A139, https://doi.org/10.1051/0004-6361/201117816.

Ilee, J. D., C. J. Cyganowski, C. L. Brogan, T. R. Hunter, D. H. Forgan, T. J. Haworth, C. J. Clarke, and T. J. Harries, 2018: G11.92-0.61 MM 1: A Fragmented Keplerian Disk Surrounding a Proto-O Star. *ApJL*, **869 (2)**, L24, https://doi.org/10.3847/2041-8213/aaeffc, 1811.05267.

Ireland, M. J., 2013: Phase errors in diffraction-limited imaging: contrast limits for sparse aperture masking. *MNRAS*, **433 (2)**, 1718–1728, https://doi.org/10.1093/mnras/stt859, 1301.6205.

Janson, M., and Coauthors, 2012: The AstraLux Large M-dwarf Multiplicity Survey. *ApJ*, **754**, 44, https://doi.org/10.1088/0004-637X/754/1/44, 1205.4718.

Jee, M. J., J. P. Blakeslee, M. Sirianni, A. R. Martel, R. L. White, and H. C. Ford, 2007: Principal Component Analysis of the Time- and Position-dependent Point-Spread Function of the Advanced Camera for Surveys. *PASP*, **119 (862)**, 1403–1419, https://doi.org/10.1086/524849, 0710.5560.

Jennison, R. C., 1958: A phase sensitive interferometer technique for the measurement of the Fourier transforms of spatial brightness distributions of small angular extent. *MNRAS*, **118**, 276, https://doi.org/10.1093/mnras/118.3.276.

Jijina, J., P. C. Myers, and F. C. Adams, 1999: Dense Cores Mapped in Ammonia: A Database. *ApJS*, **125 (1)**, 161–236, https://doi.org/10.1086/313268.

Johnson, L. C., and Coauthors, 2016: Panchromatic Hubble Andromeda Treasury. XVI. Star Cluster Formation Efficiency and the Clustered Fraction of Young Stars. *ApJ*, **827 (1)**, 33, https://doi.org/10.3847/0004-637X/827/1/33, 1606.05349.

Kaib, N. A., S. N. Raymond, and M. Duncan, 2013: Planetary system disruption by Galactic perturbations to wide binary stars. *Nature*, **493 (7432)**, 381–384, https://doi.org/10.1038/nature11780, 1301.3145.

Kammerer, J., A. Mérand, M. J. Ireland, and S. Lacour, 2020: Increasing the achievable contrast of infrared interferometry with an error correlation model. *A&A*, **644**, A110, https://doi.org/10.1051/0004-6361/202038563, 2011.01209.

Kammerer, J., and Coauthors, 2023: The Near Infrared Imager and Slitless Spectrograph for JWST. V. Kernel Phase Imaging and Data Analysis. *PASP*, **135 (1043)**, 014502, https://doi.org/10.1088/1538-3873/ac9a74, 2210.17528.

Kasdin, N. J., and Coauthors, 2020: The Nancy Grace Roman Space Telescope Coronagraph Instrument (CGI) technology demonstration. *Society of Photo-Optical Instrumentation Engineers (SPIE) Conference Series*, Society of Photo-Optical Instrumentation Engineers (SPIE) Conference Series, Vol. 11443, 114431U, https://doi.org/10.1117/12.2562997, 2103.01980.

Kervella, P., F. Arenou, F. Mignard, and F. Thévenin, 2019: Stellar and substellar companions of nearby stars from Gaia DR2. Binarity from proper motion anomaly. *A&A*, **623**, A72, https://doi.org/10.1051/0004-6361/201834371, 1811.08902.

King, R. R., S. P. Goodwin, R. J. Parker, and J. Patience, 2012: Testing the universality of star formation - II. Comparing separation distributions of nearby star-forming regions and the field. *MNRAS*, **427 (3)**, 2636–2646, https://doi.org/10.1111/j.1365-2966.2012.22108.x, 1209.2415.

Kirkpatrick, J. D., and Coauthors, 2011: The First Hundred Brown Dwarfs Discovered by the Wide-field Infrared Survey Explorer (WISE). *ApJS*, **197 (2)**, 19, https://doi.org/10.1088/0067-0049/197/2/19, 1108.4677.

Kirkpatrick, J. D., and Coauthors, 2012: Further Defining Spectral Type "Y" and Exploring the Low-mass End of the Field Brown Dwarf Mass Function. *ApJ*, **753 (2)**, 156, https://doi.org/10.1088/0004-637X/753/2/156, 1205.2122.

Kirkpatrick, J. D., and Coauthors, 2019: Preliminary Trigonometric Parallaxes of 184 Late-T and Y Dwarfs and an Analysis of the Field Substellar Mass Function into the "Planetary" Mass Regime. *ApJS*, **240 (2)**, 19, https://doi.org/10.3847/1538-4365/aaf6af, 1812.01208.

Kirkpatrick, J. D., and Coauthors, 2021: The Field Substellar Mass Function Based on the Full-sky 20 pc Census of 525 L, T, and Y Dwarfs. *ApJS*, **253 (1)**, 7, https://doi.org/10.3847/1538-4365/abd107, 2011.11616.

Köhler, R., M. G. Petr-Gotzens, M. J. McCaughrean, J. Bouvier, G. Duchêne, A. Quirrenbach, and H. Zinnecker, 2006: Binary stars in the Orion Nebula Cluster. *A&A*, **458**, 461–476, https://doi.org/10.1051/0004-6361:20054561, astro-ph/0607670.

Konopacky, Q. M., A. M. Ghez, E. L. Rice, and G. Duchêne, 2007: New Very Low Mass Binaries in the Taurus Star-forming Region. *ApJ*, **663 (1)**, 394–399, https://doi.org/10.1086/518360, astro-ph/0703567.

Könyves, V., and Coauthors, 2010: The Aquila prestellar core population revealed by Herschel. *A&A*, **518**, L106, https://doi.org/10.1051/0004-6361/201014689, 1005.2981.

Könyves, V., and Coauthors, 2020: Properties of the dense core population in Orion B as seen by the Herschel Gould Belt survey. *A&A*, **635**, A34, https://doi.org/10.1051/0004-6361/201834753, 1910.04053.

Kounkel, M., S. T. Megeath, C. A. Poteet, W. J. Fischer, and L. Hartmann, 2016: An HST Survey for 100-1000 au Companions around Young Stellar Objects in the Orion Molecular Clouds: Evidence for Environmentally Dependent Multiplicity. *ApJ*, **821**, 52, https://doi.org/10.3847/0004-637X/821/1/52, 1602.07635.

Kounkel, M., and Coauthors, 2018: The APOGEE-2 Survey of the Orion Star-forming Complex. II. Six-dimensional Structure. *AJ*, **156 (3)**, 84, https://doi.org/10.3847/1538-3881/aad1f1, 1805.04649.

Kounkel, M., and Coauthors, 2019: Close Companions around Young Stars. *AJ*, **157 (5)**, 196, https://doi.org/10.3847/1538-3881/ab13b1, 1903.10523.

Kratter, K. M., 2011: The Formation of Close Binaries. *Evolution of Compact Binaries*, L. Schmidtobreick, M. R. Schreiber, and C. Tappert, Eds., Astronomical Society of the Pacific Conference Series, Vol. 447, 47, 1109.3740.

Kratter, K. M., and C. D. Matzner, 2006: Fragmentation of massive protostellar discs. *MNRAS*, **373 (4)**, 1563–1576, https://doi.org/10.1111/j.1365-2966.2006.11103.x, astro-ph/0609692.

Kratter, K. M., C. D. Matzner, and M. R. Krumholz, 2008: Global Models for the Evolution of Embedded, Accreting Protostellar Disks. *ApJ*, **681 (1)**, 375–390, https://doi.org/10.1086/587543, 0709.4252.

Kratter, K. M., C. D. Matzner, M. R. Krumholz, and R. I. Klein, 2010: On the Role of Disks in the Formation of Stellar Systems: A Numerical Parameter Study of Rapid Accretion. *ApJ*, **708 (2)**, 1585–1597, https://doi.org/10.1088/0004-637X/708/2/1585, 0907.3476.

Kraus, A. L., and L. A. Hillenbrand, 2012: Multiple Star Formation to the Bottom of the Initial Mass Function. *ApJ*, **757 (2)**, 141, https://doi.org/10.1088/0004-637X/757/2/141, 1206.4995.

Kraus, A. L., M. J. Ireland, L. A. Hillenbrand, and F. Martinache, 2012: The Role of Multiplicity in Disk Evolution and Planet Formation. *ApJ*, **745 (1)**, 19, https://doi.org/10.1088/0004-637X/745/1/19, 1109.4141.

Kraus, A. L., M. J. Ireland, D. Huber, A. W. Mann, and T. J. Dupuy, 2016: The Impact of Stellar Multiplicity on Planetary Systems. I. The Ruinous Influence of Close Binary Companions. *AJ*, **152 (1)**, 8, https://doi.org/10.3847/0004-6256/152/1/8, 1604.05744.

Kraus, A. L., M. J. Ireland, F. Martinache, and L. A. Hillenbrand, 2011: Mapping the Shores of the Brown Dwarf Desert. II. Multiple Star Formation in Taurus-Auriga. *ApJ*, **731**, 8, https://doi.org/10.1088/0004-637X/731/1/8, 1101.4016.

Kraus, A. L., M. J. Ireland, F. Martinache, and J. P. Lloyd, 2008: Mapping the Shores of the Brown Dwarf Desert. I. Upper Scorpius. *ApJ*, **679 (1)**, 762–782, https://doi.org/10.1086/587435, 0801.2387.

Kraus, A. L., R. J. White, and L. A. Hillenbrand, 2006: Multiplicity and Optical Excess across the Substellar Boundary in Taurus. *ApJ*, **649 (1)**, 306–318, https://doi.org/10.1086/503665, astro-ph/0602449.

Kroupa, P., 1995a: Inverse dynamical population synthesis and star formation. *MNRAS*, **277**, https://doi.org/10.1093/mnras/277.4.1491, astro-ph/9508117.

Kroupa, P., 1995b: The dynamical properties of stellar systems in the Galactic disc. *MNRAS*, **277**, 1507, https://doi.org/10.1093/mnras/277.4.1507, astro-ph/9508084.

Kroupa, P., 2001: On the variation of the initial mass function. *MNRAS*, **322 (2)**, 231–246, https://doi.org/10.1046/j.1365-8711.2001.04022.x, astro-ph/0009005.

Kroupa, P., S. Aarseth, and J. Hurley, 2001a: The formation of a bound star cluster: from the Orion nebula cluster to the Pleiades. *MNRAS*, **321 (4)**, 699–712, https://doi.org/10.1046/j.1365-8711.2001.04050.x, astro-ph/0009470.

Kroupa, P., S. Aarseth, and J. Hurley, 2001b: The formation of a bound star cluster: from the Orion nebula cluster to the Pleiades. *MNRAS*, **321 (4)**, 699–712, https://doi.org/10.1046/j.1365-8711.2001.04050.x, astro-ph/0009470.

Kroupa, P., J. Bouvier, G. Duchêne, and E. Moraux, 2003: On the universal outcome of star formation: is there a link between stars and brown dwarfs? *MNRAS*, **346 (2)**, 354–368, https://doi.org/10.1046/j.1365-2966.2003.06994.x, astro-ph/0307229.

Kroupa, P., and A. Burkert, 2001: On the Origin of the Distribution of Binary Star Periods. *ApJ*, **555 (2)**, 945–949, https://doi.org/10.1086/321515, astro-ph/0103429.

Krumholz, M. R., C. F. McKee, and J. Bland-Hawthorn, 2019: Star Clusters Across Cosmic Time. *ARA&A*, **57**, 227–303, https://doi.org/10.1146/annurev-astro-091918-104430, 1812.01615.

Kuffmeier, M., C. P. Dullemond, S. Reissl, and F. G. Goicovic, 2021: Misaligned disks induced by infall. *A&A*, **656**, A161, https://doi.org/10.1051/0004-6361/202039614, 2110.04309.

Kuznetsova, A., L. Hartmann, and F. Heitsch, 2019: The Origins of Protostellar Core Angular Momenta. *ApJ*, **876 (1)**, 33, https://doi.org/10.3847/1538-4357/ab12ce, 1903.09612.

Lada, C. J., and E. A. Lada, 2003: Embedded Clusters in Molecular Clouds. *ARA&A*, **41**, 57–115, https://doi.org/10.1146/annurev.astro.41.011802.094844, astro-ph/0301540.

Lafrenière, D., R. Jayawardhana, A. Brandeker, M. Ahmic, and M. H. van Kerkwijk, 2008: A Multiplicity Census of Young Stars in Chamaeleon I. *ApJ*, **683 (2)**, 844–861, https://doi.org/10.1086/590239, 0803.0561.

Lafrenière, D., C. Marois, R. Doyon, and T. Barman, 2009: HST/NICMOS Detection of HR 8799 b in 1998. *ApJL*, **694 (2)**, L148–L152, https://doi.org/10.1088/0004-637X/694/2/L148, 0902.3247.

Lanthermann, C., and Coauthors, 2023: Multiplicity of northern bright O-type stars with optical long baseline interferometry. Results of the pilot survey. *A&A*, **672**, A6, https://doi.org/10.1051/0004-6361/202245364, 2302.03168.

Lee, A. T., S. S. R. Offner, K. M. Kratter, R. A. Smullen, and P. S. Li, 2019: The Formation and Evolution of Wide-orbit Stellar Multiples In Magnetized Clouds. *ApJ*, **887 (2)**, 232, https://doi.org/10.3847/1538-4357/ab584b, 1911.07863.

Leggett, S. K., C. V. Morley, M. S. Marley, and D. Saumon, 2015: Near-infrared Photometry of Y Dwarfs: Low Ammonia Abundance and the Onset of Water Clouds. *ApJ*, **799 (1)**, 37, https://doi.org/10.1088/0004-637X/799/1/37, 1411.2020.

Leggett, S. K., C. V. Morley, M. S. Marley, D. Saumon, J. J. Fortney, and C. Visscher, 2013: A Comparison of Near-infrared Photometry and Spectra for Y Dwarfs with a New Generation of Cool Cloudy Models. *ApJ*, **763 (2)**, 130, https://doi.org/10.1088/0004-637X/763/2/130, 1212.1210.

Leggett, S. K., P. Tremblin, T. L. Esplin, K. L. Luhman, and C. V. Morley, 2017: The Y-type Brown Dwarfs: Estimates of Mass and Age from New Astrometry, Homogenized Photometry, and Near-infrared Spectroscopy. *ApJ*, **842 (2)**, 118, https://doi.org/10.3847/1538-4357/aa6fb5, 1704.03573.

Leggett, S. K., and Coauthors, 2021a: Measuring and Replicating the 1-20 $\mu$m Energy Distributions of the Coldest Brown Dwarfs: Rotating, Turbulent, and Nonadiabatic Atmospheres. *ApJ*, **918 (1)**, 11, https://doi.org/10.3847/1538-4357/ac0cfe.

Leggett, S. K., and Coauthors, 2021b: Measuring and Replicating the 1-20 $\mu$m Energy Distributions of the Coldest Brown Dwarfs: Rotating, Turbulent, and Nonadiabatic Atmospheres. *ApJ*, **918 (1)**, 11, https://doi.org/10.3847/1538-4357/ac0cfe.

Leinert, C., H. Zinnecker, N. Weitzel, J. Christou, S. T. Ridgway, R. Jameson, M. Haas, and R. Lenzen, 1993: A systematic approach for young binaries in Taurus. *A&A*, **278**, 129–149.

Li, L.-X., and B. Paczyński, 1998: Transient Events from Neutron Star Mergers. *ApJL*, **507 (1)**, L59–L62, https://doi.org/10.1086/311680, astro-ph/9807272.

Linder, E. F., C. Mordasini, P. Mollière, G.-D. Marleau, M. Malik, S. P. Quanz, and M. R. Meyer, 2019: Evolutionary models of cold and low-mass planets: cooling curves, magnitudes, and detectability. *A&A*, **623**, A85, https://doi.org/10.1051/0004-6361/201833873, 1812.02027.

Lipatov, M., T. D. Brandt, and N. E. Batalha, 2022: Effects of rotation on the spectra of brown dwarfs. *MNRAS*, **517 (2)**, 2942–2952, https://doi.org/10.1093/mnras/stac2838, 2209.15058.

Liu, M. C., T. J. Dupuy, and K. N. Allers, 2016: The Hawaii Infrared Parallax Program. II. Young Ultracool Field Dwarfs. *ApJ*, **833 (1)**, 96, https://doi.org/10.3847/1538-4357/833/1/96, 1612.02426.

Liu, M. C., T. J. Dupuy, B. P. Bowler, S. K. Leggett, and W. M. J. Best, 2012: Two Extraordinary Substellar Binaries at the T/Y Transition and the Y-band Fluxes of the Coolest Brown Dwarfs. *ApJ*, **758 (1)**, 57, https://doi.org/10.1088/0004-637X/758/1/57, 1206.4044.

Liu, W. M., M. R. Meyer, A. S. Cotera, and E. T. Young, 2003: Hubble Space Telescope NICMOS Observations of the Embedded Cluster in NGC 2024: Constraints on the Initial Mass Function and Binary Fraction. *AJ*, **126**, 1665–1676, https://doi.org/10.1086/377620, astro-ph/0306377.

Lucas, P. W., P. F. Roche, F. Allard, and P. H. Hauschildt, 2001: Infrared spectroscopy of substellar objects in Orion. *MNRAS*, **326 (2)**, 695–721, https://doi.org/10.1046/j.1365-8711.2001.04666.x, astro-ph/0105154.

Lucas, P. W., D. J. Weights, P. F. Roche, and F. C. Riddick, 2006: Spectroscopy of planetary mass brown dwarfs in Orion. *MNRAS*, **373 (1)**, L60–L64, https://doi.org/10.1111/j.1745-3933.2006.00244.x, astro-ph/0609086.

Luhman, K. L., 2004: The First Discovery of a Wide Binary Brown Dwarf. *ApJ*, **614 (1)**, 398–403, https://doi.org/10.1086/423666, astro-ph/0407344.

Luhman, K. L., 2013: Discovery of a Binary Brown Dwarf at 2 pc from the Sun. *ApJL*, **767 (1)**, L1, https://doi.org/10.1088/2041-8205/767/1/L1, 1303.2401.

Mac Low, M.-M., and R. S. Klessen, 2004: Control of star formation by supersonic turbulence. *Reviews of Modern Physics*, **76 (1)**, 125–194, https://doi.org/10.1103/RevModPhys.76.125, astro-ph/0301093.

Mace, G. N., and Coauthors, 2013: A Study of the Diverse T Dwarf Population Revealed by WISE. *ApJS*, **205 (1)**, 6, https://doi.org/10.1088/0067-0049/205/1/6, 1301.3913.

Mallonn, M., K. Poppenhaeger, T. Granzer, M. Weber, and K. G. Strassmeier, 2022: Detection capability of ground-based meter-sized telescopes for shallow exoplanet transits. *A&A*, **657**, A102, https://doi.org/10.1051/0004-6361/202140599, 2110.14344.

Marks, M., and P. Kroupa, 2012: Inverse dynamical population synthesis. Constraining the initial conditions of young stellar clusters by studying their binary populations. *A&A*, **543**, A8, https://doi.org/10.1051/0004-6361/201118231, 1205.1508.

Marley, M. S., and Coauthors, 2021a: The Sonora Brown Dwarf Atmosphere and Evolution Models. I. Model Description and Application to Cloudless Atmospheres in Rainout Chemical Equilibrium. *ApJ*, **920 (2)**, 85, https://doi.org/10.3847/1538-4357/ac141d, 2107.07434.

Marley, M. S., and Coauthors, 2021b: The Sonora Brown Dwarf Atmosphere and Evolution Models. I. Model Description and Application to Cloudless Atmospheres in Rainout Chemical Equilibrium. *ApJ*, **920 (2)**, 85, https://doi.org/10.3847/1538-4357/ac141d, 2107.07434.

Marois, C., D. Lafrenière, R. Doyon, B. Macintosh, and D. Nadeau, 2006: Angular Differential Imaging: A Powerful High-Contrast Imaging Technique. *ApJ*, **641 (1)**, 556–564, https://doi.org/10.1086/500401, astro-ph/0512335.

Martin, E. C., and Coauthors, 2018: Y Dwarf Trigonometric Parallaxes from the Spitzer Space Telescope. *ApJ*, **867 (2)**, 109, https://doi.org/10.3847/1538-4357/aae1af, 1809.06479.

Martín, E. L., W. Brandner, J. Bouvier, K. L. Luhman, J. Stauffer, G. Basri, M. R. Zapatero Osorio, and D. Barrado y Navascués, 2000: Membership and Multiplicity among Very Low Mass Stars and Brown Dwarfs in the Pleiades Cluster. *ApJ*, **543 (1)**, 299–312, https://doi.org/10.1086/317089, astro-ph/0004174.

Martinache, F., 2010: Kernel Phase in Fizeau Interferometry. *ApJ*, **724 (1)**, 464–469, https://doi.org/10.1088/0004-637X/724/1/464, 1009.3933.

Marzari, F., S. J. Weidenschilling, M. Barbieri, and V. Granata, 2005: Jumping Jupiters in Binary Star Systems. *ApJ*, **618 (1)**, 502–511, https://doi.org/10.1086/425976.

Mawet, D., and Coauthors, 2014: Fundamental Limitations of High Contrast Imaging Set by Small Sample Statistics. *ApJ*, **792 (2)**, 97, https://doi.org/10.1088/0004-637X/792/2/97, 1407.2247.

Mayor, M., and D. Queloz, 1995: A Jupiter-mass companion to a solar-type star. *Nature*, **378 (6555)**, 355–359, https://doi.org/10.1038/378355a0.

Mazeh, T., D. Goldberg, A. Duquennoy, and M. Mayor, 1992: On the Mass-Ratio Distribution of Spectroscopic Binaries with Solar-Type Primaries. *ApJ*, **401**, 265, https://doi.org/10.1086/172058.

McCaughrean, M. J., and J. R. Stauffer, 1994: High Resolution Near-Infrared Imaging of the Trapezium: A Stellar Census. *AJ*, **108**, 1382, https://doi.org/10.1086/117160.

McElwain, M. W., and Coauthors, 2023: The James Webb Space Telescope Mission: Optical Telescope Element Design, Development, and Performance. *arXiv e-prints*, arXiv:2301.01779, https://doi.org/10.48550/arXiv.2301.01779, 2301.01779.

Meyer, M. R., N. Calvet, and L. A. Hillenbrand, 1997: Intrinsic Near-Infrared Excesses of T Tauri Stars: Understanding the Classical T Tauri Star Locus. *AJ*, **114**, 288–300, https://doi.org/10.1086/118474.

Michaud, G., 1980: The astrophysical context of diffusion in stars. *AJ*, **85**, 589–598, https://doi.org/10.1086/112716.

Michaud, G., D. Tarasick, Y. Charland, and C. Pelletier, 1983: Diffusion, meridional circulation, and mass loss in Fm-Am stars. *ApJ*, **269**, 239–249, https://doi.org/10.1086/161034.

Michell, J., 1767: An Inquiry into the Probable Parallax, and Magnitude of the Fixed Stars, from the Quantity of Light Which They Afford us, and the Particular Circumstances of Their Situation, by the Rev. John Michell, B. D. F. R. S. *Philosophical Transactions of the Royal Society of London Series I*, **57**, 234–264.

Milli, J., and Coauthors, 2017: Discovery of a low-mass companion inside the debris ring surrounding the F5V star HD 206893. *A&A*, **597**, L2, https://doi.org/10.1051/0004-6361/201629908, 1612.00333.

Moe, M., and R. Di Stefano, 2017: Mind Your Ps and Qs: The Interrelation between Period (P) and Mass-ratio (Q) Distributions of Binary Stars. *ApJS*, **230 (2)**, 15, https://doi.org/10.3847/1538-4365/aa6fb6, 1606.05347.

Moe, M., and K. M. Kratter, 2018: Dynamical Formation of Close Binaries during the Pre-main-sequence Phase. *ApJ*, **854 (1)**, 44, https://doi.org/10.3847/1538-4357/aaa6d2, 1706.09894.

Moe, M., and K. M. Kratter, 2021: Impact of binary stars on planet statistics - I. Planet occurrence rates and trends with stellar mass. *MNRAS*, **507 (3)**, 3593–3611, https://doi.org/10.1093/mnras/stab2328, 1912.01699.

Moe, M., K. M. Kratter, and C. Badenes, 2019: The Close Binary Fraction of Solar-type Stars Is Strongly Anticorrelated with Metallicity. *ApJ*, **875 (1)**, 61, https://doi.org/10.3847/1538-4357/ab0d88, 1808.02116.

Moeckel, N., and M. R. Bate, 2010: On the evolution of a star cluster and its multiple stellar systems following gas dispersal. *MNRAS*, **404 (2)**, 721–737, https://doi.org/10.1111/j.1365-2966.2010.16347.x, 1001.3417.

Monnier, J. D., 2000: An Introduction to Closure Phases. *Principles of Long Baseline Stellar Interferometry*, P. R. Lawson, Ed., 203.

Monnier, J. D., and Coauthors, 2004: First Results with the IOTA3 Imaging Interferometer: The Spectroscopic Binaries $\lambda$ Virginis and WR 140. *ApJL*, **602 (1)**, L57–L60, https://doi.org/10.1086/382213, astro-ph/0401268.

Monnier, J. D., and Coauthors, 2006: Michigan Infrared Combiner (MIRC): commissioning results at the CHARA Array. *Society of Photo-Optical Instrumentation Engineers (SPIE) Conference Series*, J. D. Monnier, M. Schöller, and W. C. Danchi, Eds., Society of Photo-Optical Instrumentation Engineers (SPIE) Conference Series, Vol. 6268, 62681P, https://doi.org/10.1117/12.671982.

Monnier, J. D., and Coauthors, 2007: Imaging the Surface of Altair. *Science*, **317 (5836)**, 342, https://doi.org/10.1126/science.1143205, 0706.0867.

Monnier, J. D., and Coauthors, 2012: Resolving Vega and the Inclination Controversy with CHARA/MIRC. *ApJL*, **761**, L3, https://doi.org/10.1088/2041-8205/761/1/L3, 1211.6055.

Monnier, J. D., and Coauthors, 2018: MYSTIC: Michigan Young STar Imager at CHARA. *Optical and Infrared Interferometry and Imaging VI*, M. J. Creech-Eakman, P. G. Tuthill, and A. Mérand, Eds., Society of Photo-Optical Instrumentation Engineers (SPIE) Conference Series, Vol. 10701, 1070122, https://doi.org/10.1117/12.2312762, 1807.11569.

Morais, M. H. M., and A. C. M. Correia, 2008: Stellar wobble caused by a binary system: Can it really be mistaken as an extra-solar planet? *A&A*, **491 (3)**, 899–906, https://doi.org/10.1051/0004-6361:200810741, 0810.0506.

Morley, C. V., J. J. Fortney, M. S. Marley, C. Visscher, D. Saumon, and S. K. Leggett, 2012: Neglected Clouds in T and Y Dwarf Atmospheres. *ApJ*, **756 (2)**, 172, https://doi.org/10.1088/0004-637X/756/2/172, 1206.4313.

Morley, C. V., M. S. Marley, J. J. Fortney, and R. Lupu, 2014a: Spectral Variability from the Patchy Atmospheres of T and Y Dwarfs. *ApJL*, **789 (1)**, L14, https://doi.org/10.1088/2041-8205/789/1/L14, 1406.0863.

Morley, C. V., M. S. Marley, J. J. Fortney, R. Lupu, D. Saumon, T. Greene, and K. Lodders, 2014b: Water Clouds in Y Dwarfs and Exoplanets. *ApJ*, **787 (1)**, 78, https://doi.org/10.1088/0004-637X/787/1/78, 1404.0005.

Murphy, S. J., T. R. Bedding, H. Shibahashi, D. W. Kurtz, and H. Kjeldsen, 2014: Finding binaries among Kepler pulsating stars from phase modulation of their pulsations. *MNRAS*, **441 (3)**, 2515–2527, https://doi.org/10.1093/mnras/stu765, 1404.5649.

Murphy, S. J., M. Moe, D. W. Kurtz, T. R. Bedding, H. Shibahashi, and H. M. J. Boffin, 2018: Finding binaries from phase modulation of pulsating stars with Kepler: V. Orbital parameters, with eccentricity and mass-ratio distributions of 341 new binaries. *MNRAS*, **474 (4)**, 4322–4346, https://doi.org/10.1093/mnras/stx3049, 1712.00022.

Nardiello, D., L. R. Bedin, A. Burgasser, M. Salaris, S. Cassisi, M. Griggio, and M. Scalco, 2022: Photometry and astrometry with JWST - I. NIRCam point spread functions and the first JWST colour-magnitude diagrams of a globular cluster. *MNRAS*, **517 (1)**, 484–497, https://doi.org/10.1093/mnras/stac2659, 2209.06547.

Niemela, V., 2001: A Short History and Other Stories of Binary Stars. *Revista Mexicana de Astronomia y Astrofisica Conference Series*, Revista Mexicana de Astronomia y Astrofisica Conference Series, Vol. 11, 23–26.

Nonino, M., and Coauthors, 2023: Early Results from GLASS-JWST. XIII. A Faint, Distant, and Cold Brown Dwarf. *ApJL*, **942 (2)**, L29, https://doi.org/10.3847/2041-8213/ac8e5f, 2207.14802.

Offner, S. S. R., K. M. Kratter, C. D. Matzner, M. R. Krumholz, and R. I. Klein, 2010: The Formation of Low-mass Binary Star Systems Via Turbulent Fragmentation. *ApJ*, **725**, 1485–1494, https://doi.org/10.1088/0004-637X/725/2/1485, 1010.3702.

Offner, S. S. R., M. Moe, K. M. Kratter, S. I. Sadavoy, E. L. N. Jensen, and J. J. Tobin, 2023: The Origin and Evolution of Multiple Star Systems. *Astronomical Society of the Pacific Conference Series*, S. Inutsuka, Y. Aikawa, T. Muto, K. Tomida, and M. Tamura, Eds., Astronomical Society of the Pacific Conference Series, Vol. 534, 275.

Offner, S. S. R., and Coauthors, 2022: Turbulence, coherence, and collapse: Three phases for core evolution. *MNRAS*, **517 (1)**, 885–909, https://doi.org/10.1093/mnras/stac2734, 2006.07325.

Opitz, D., C. G. Tinney, J. K. Faherty, S. Sweet, C. R. Gelino, and J. D. Kirkpatrick, 2016: Searching for Binary Y Dwarfs with the Gemini Multi-conjugate Adaptive Optics System (GeMS). *ApJ*, **819 (1)**, 17, https://doi.org/10.3847/0004-637X/819/1/17, 1601.05508.

Padoan, P., B. J. T. Jones, and Å. P. Nordlund, 1997: Supersonic Turbulence in the Interstellar Medium: Stellar Extinction Determinations as Probes of the Structure and Dynamics of Dark Clouds. *ApJ*, **474 (2)**, 730–734, https://doi.org/10.1086/303482, astro-ph/9603061.

Parker, R. J., 2014: Dynamics versus structure: breaking the density degeneracy in star formation. *MNRAS*, **445 (4)**, 4037–4044, https://doi.org/10.1093/mnras/stu2054, 1410.0004.

Parker, R. J., and S. P. Goodwin, 2011: The dynamical evolution of very low mass binaries in open clusters. *MNRAS*, **411**, 891–900, https://doi.org/10.1111/j.1365-2966.2010.17722.x, 1009.3110.

Parker, R. J., and S. P. Goodwin, 2012: The same, but different: stochasticity in binary destruction. *MNRAS*, **424**, 272–281, https://doi.org/10.1111/j.1365-2966.2012.21190.x, 1204.6037.

Parker, R. J., S. P. Goodwin, and R. J. Allison, 2011: The evolution of binary populations in cool, clumpy star clusters. *MNRAS*, **418 (4)**, 2565–2575, https://doi.org/10.1111/j.1365-2966.2011.19646.x, 1108.3566.

Parker, R. J., and M. R. Meyer, 2014: Binaries in the field: fossils of the star formation process? *MNRAS*, **442 (4)**, 3722–3736, https://doi.org/10.1093/mnras/stu1101, 1406.0844.

Parker, R. J., and M. M. Reggiani, 2013: The binary companion mass ratio distribution: an imprint of the star formation process? *MNRAS*, **432 (3)**, 2378–2384, https://doi.org/10.1093/mnras/stt600, 1304.3123.

Patience, J., A. M. Ghez, I. N. Reid, and K. Matthews, 2002: A High Angular Resolution Multiplicity Survey of the Open Clusters $\alpha$ Persei and Praesepe. *AJ*, **123**, 1570–1602, https://doi.org/10.1086/338431, astro-ph/0111156.

Paxton, B., L. Bildsten, A. Dotter, F. Herwig, P. Lesaffre, and F. Timmes, 2011: Modules for Experiments in Stellar Astrophysics (MESA). *ApJS*, **192 (1)**, 3, https://doi.org/10.1088/0067-0049/192/1/3, 1009.1622.

Paxton, B., and Coauthors, 2013: Modules for Experiments in Stellar Astrophysics (MESA): Planets, Oscillations, Rotation, and Massive Stars. *ApJS*, **208 (1)**, 4, https://doi.org/10.1088/0067-0049/208/1/4, 1301.0319.

Paxton, B., and Coauthors, 2015: Modules for Experiments in Stellar Astrophysics (MESA): Binaries, Pulsations, and Explosions. *ApJS*, **220 (1)**, 15, https://doi.org/10.1088/0067-0049/220/1/15, 1506.03146.

Paxton, B., and Coauthors, 2018: Modules for Experiments in Stellar Astrophysics (MESA): Convective Boundaries, Element Diffusion, and Massive Star Explosions. *ApJS*, **234 (2)**, 34, https://doi.org/10.3847/1538-4365/aaa5a8, 1710.08424.

Pecaut, M. J., and E. E. Mamajek, 2013a: Intrinsic Colors, Temperatures, and Bolometric Corrections of Pre-main-sequence Stars. *ApJS*, **208 (1)**, 9, https://doi.org/10.1088/0067-0049/208/1/9, 1307.2657.

Pecaut, M. J., and E. E. Mamajek, 2013b: Intrinsic Colors, Temperatures, and Bolometric Corrections of Pre-main-sequence Stars. *ApJS*, **208 (1)**, 9, https://doi.org/10.1088/0067-0049/208/1/9, 1307.2657.

Perrin, M. D., L. Pueyo, K. Van Gorkom, K. Brooks, A. Rajan, J. Girard, and C.-P. Lajoie, 2018: Updated optical modeling of JWST coronagraph performance contrast, stability, and strategies. *Space Telescopes and Instrumentation 2018: Optical, Infrared, and Millimeter Wave*, M. Lystrup, H. A. MacEwen, G. G. Fazio, N. Batalha, N. Siegler, and E. C. Tong, Eds., Society

of Photo-Optical Instrumentation Engineers (SPIE) Conference Series, Vol. 10698, 1069809, https://doi.org/10.1117/12.2313552.

Perrin, M. D., A. Sivaramakrishnan, C.-P. Lajoie, E. Elliott, L. Pueyo, S. Ravindranath, and L. Albert, 2014: Updated point spread function simulations for JWST with WebbPSF. *Space Telescopes and Instrumentation 2014: Optical, Infrared, and Millimeter Wave*, J. Oschmann, Jacobus M., M. Clampin, G. G. Fazio, and H. A. MacEwen, Eds., Society of Photo-Optical Instrumentation Engineers (SPIE) Conference Series, Vol. 9143, 91433X, https://doi.org/10.1117/12.2056689.

Perrin, M. D., R. Soummer, E. M. Elliott, M. D. Lallo, and A. Sivaramakrishnan, 2012: Simulating point spread functions for the James Webb Space Telescope with WebbPSF. *Space Telescopes and Instrumentation 2012: Optical, Infrared, and Millimeter Wave*, M. C. Clampin, G. G. Fazio, H. A. MacEwen, and J. Oschmann, Jacobus M., Eds., Society of Photo-Optical Instrumentation Engineers (SPIE) Conference Series, Vol. 8442, 84423D, https://doi.org/10.1117/12.925230.

Perrin, M. D., and Coauthors, 2016: Preparing for JWST wavefront sensing and control operations. *Space Telescopes and Instrumentation 2016: Optical, Infrared, and Millimeter Wave*, H. A. MacEwen, G. G. Fazio, M. Lystrup, N. Batalha, N. Siegler, and E. C. Tong, Eds., Society of Photo-Optical Instrumentation Engineers (SPIE) Conference Series, Vol. 9904, 99040F, https://doi.org/10.1117/12.2233104.

Phillips, M. M., 1993: The Absolute Magnitudes of Type IA Supernovae. *ApJL*, **413**, L105, https://doi.org/10.1086/186970.

Phillips, M. W., and Coauthors, 2020a: A new set of atmosphere and evolution models for cool T-Y brown dwarfs and giant exoplanets. *A&A*, **637**, A38, https://doi.org/10.1051/0004-6361/201937381, 2003.13717.

Phillips, M. W., and Coauthors, 2020b: A new set of atmosphere and evolution models for cool T-Y brown dwarfs and giant exoplanets. *A&A*, **637**, A38, https://doi.org/10.1051/0004-6361/201937381, 2003.13717.

Pineda, J. E., and Coauthors, 2015: The formation of a quadruple star system with wide separation. *Nature*, **518 (7538)**, 213–215, https://doi.org/10.1038/nature14166.

Pope, B., F. Martinache, and P. Tuthill, 2013: Dancing in the Dark: New Brown Dwarf Binaries from Kernel Phase Interferometry. *ApJ*, **767 (2)**, 110, https://doi.org/10.1088/0004-637X/767/2/110, 1302.6682.

Pourbaix, D., 2000: Resolved double-lined spectroscopic binaries: A neglected source of hypothesis-free parallaxes and stellar masses. *A&AS*, **145**, 215–222, https://doi.org/10.1051/aas:2000237.

Preibisch, T., and E. Mamajek, 2008: *The Nearest OB Association: Scorpius-Centaurus (Sco OB2)*, Vol. 5, 235. Reipurth, B.

Preibisch, T., T. Ratzka, T. Gehring, H. Ohlendorf, H. Zinnecker, R. R. King, M. J. McCaughrean, and J. R. Lewis, 2011: Detection of a large massive circumstellar disk around a high-mass young stellar object in the Carina Nebula. *A&A*, **530**, A40, https://doi.org/10.1051/0004-6361/201116528, 1104.3706.

Press, W. H., S. A. Teukolsky, W. T. Vetterling, and B. P. Flannery, 2007: *Numerical recipes 3rd edition: The art of scientific computing*. Cambridge university press.

Raghavan, D., and Coauthors, 2010: A Survey of Stellar Families: Multiplicity of Solar-type Stars. *ApJS*, **190**, 1–42, https://doi.org/10.1088/0067-0049/190/1/1, 1007.0414.

Reggiani, M., and M. R. Meyer, 2013: Universality of the companion mass-ratio distribution. *A&A*, **553**, A124, https://doi.org/10.1051/0004-6361/201321631, 1304.3459.

Reggiani, M., M. Robberto, N. Da Rio, M. R. Meyer, D. R. Soderblom, and L. Ricci, 2011: Quantitative evidence of an intrinsic luminosity spread in the Orion nebula cluster. *A&A*, **534**, A83, https://doi.org/10.1051/0004-6361/201116946, 1108.1015.

Reggiani, M., and Coauthors, 2022: Probing the low-mass end of the companion mass function for O-type stars. *A&A*, **660**, A122, https://doi.org/10.1051/0004-6361/202142418, 2112.10831.

Reid, I. N., E. Lewitus, P. R. Allen, K. L. Cruz, and A. J. Burgasser, 2006: A Search for Binary Systems among the Nearest L Dwarfs. *AJ*, **132 (2)**, 891–901, https://doi.org/10.1086/505626, astro-ph/0606331.

Reipurth, B., and C. Clarke, 2001: The Formation of Brown Dwarfs as Ejected Stellar Embryos. *AJ*, **122 (1)**, 432–439, https://doi.org/10.1086/321121, astro-ph/0103019.

Reipurth, B., M. M. Guimarães, M. S. Connelley, and J. Bally, 2007: Visual Binaries in the Orion Nebula Cluster. *AJ*, **134**, 2272–2285, https://doi.org/10.1086/523596, 0709.3824.

Reipurth, B., and H. Zinnecker, 1993: Visual binaries among pre-main sequence stars. *A&A*, **278**, 81–108.

Rhodes, J. D., and Coauthors, 2007: The Stability of the Point-Spread Function of the Advanced Camera for Surveys on the Hubble Space Telescope and Implications for Weak Gravitational Lensing. *ApJS*, **172 (1)**, 203–218, https://doi.org/10.1086/516592, astro-ph/0702140.

Ricci, L., L. Testi, A. Natta, A. Scholz, I. de Gregorio-Monsalvo, and A. Isella, 2014: Brown Dwarf Disks with ALMA. *ApJ*, **791 (1)**, 20, https://doi.org/10.1088/0004-637X/791/1/20, 1406.0635.

Riddick, F. C., P. F. Roche, and P. W. Lucas, 2007: An optical spectroscopic HR diagram for low-mass stars and brown dwarfs in Orion. *MNRAS*, **381 (3)**, 1077–1092, https://doi.org/10.1111/j.1365-2966.2007.12308.x, 0708.1280.

Rigby, J., and Coauthors, 2022: Characterization of JWST science performance from commissioning. *arXiv e-prints*, arXiv:2207.05632, 2207.05632.

Rizzuto, A. C., and Coauthors, 2013: Long-baseline interferometric multiplicity survey of the Sco-Cen OB association. *MNRAS*, **436 (2)**, 1694–1707, https://doi.org/10.1093/mnras/stt1690, 1309.3811.

Robberto, M., and Coauthors, 2013: The Hubble Space Telescope Treasury Program on the Orion Nebula Cluster. *ApJS*, **207**, 10, https://doi.org/10.1088/0067-0049/207/1/10, 1304.4866.

Rogers, A. E. E., and Coauthors, 1974: The structure of radio sources 3C 273B and 3C 84 deduced from the "closure" phases and visibility amplitudes observed with three-element interferometers. *ApJ*, **193**, 293–301, https://doi.org/10.1086/153162.

Russell, H. N., 1914: Relations Between the Spectra and Other Characteristics of the Stars. *Popular Astronomy*, **22**, 275–294.

Sallum, S., and A. Skemer, 2019: Comparing nonredundant masking and filled-aperture kernel phase for exoplanet detection and characterization. *Journal of Astronomical Telescopes, Instruments, and Systems*, **5**, 018001, https://doi.org/10.1117/1.JATIS.5.1.018001, 1901.01266.

Salpeter, E. E., 1955: The Luminosity Function and Stellar Evolution. *ApJ*, **121**, 161, https://doi.org/10.1086/145971.

Sana, H., and Coauthors, 2012: Binary Interaction Dominates the Evolution of Massive Stars. *Science*, **337 (6093)**, 444, https://doi.org/10.1126/science.1223344, 1207.6397.

Sana, H., and Coauthors, 2013: The VLT-FLAMES Tarantula Survey. VIII. Multiplicity properties of the O-type star population. *A&A*, **550**, A107, https://doi.org/10.1051/0004-6361/201219621, 1209.4638.

Sana, H., and Coauthors, 2014: Southern Massive Stars at High Angular Resolution: Observational Campaign and Companion Detection. *ApJS*, **215 (1)**, 15, https://doi.org/10.1088/0067-0049/215/1/15, 1409.6304.

Sandage, A. R., 1953: The color-magnitude diagram for the globular cluster M 3. *AJ*, **58**, 61–75, https://doi.org/10.1086/106822.

Satsuka, T., T. Tsuribe, S. Tanaka, and K. Nagamine, 2017: Evolution of binary seeds in collapsing protostellar gas clouds. *MNRAS*, **465 (1)**, 986–996, https://doi.org/10.1093/mnras/stw2709, 1607.06592.

Scally, A., C. Clarke, and M. J. McCaughrean, 1999: Wide binaries in the Orion nebula cluster. *MNRAS*, **306 (1)**, 253–256, https://doi.org/10.1046/j.1365-8711.1999.02513.x, astro-ph/9902156.

Schatzman, E. L., 1958: *White dwarfs*.

Schlesinger, B. M., 1975: Unresolved binaries as a source of scatter in color-magnitude diagrams. *AJ*, **80**, 1071, https://doi.org/10.1086/111841.

Shatsky, N., and A. Tokovinin, 2002: The mass ratio distribution of B-type visual binaries in the Sco OB2 association. *A&A*, **382**, 92–103, https://doi.org/10.1051/0004-6361:20011542, astro-ph/0109456.

Shu, F. H., F. C. Adams, and S. Lizano, 1987: Star formation in molecular clouds: observation and theory. *ARA&A*, **25**, 23–81, https://doi.org/10.1146/annurev.aa.25.090187.000323.

Simon, M., 1997: Clustering of Young Stars in Taurus, Ophiuchus, and the Orion Trapezium. *ApJL*, **482 (1)**, L81–L84, https://doi.org/10.1086/310678.

Simon, M., 2020: An HRD-like diagram for pre-main sequence stars. *Research Notes of the AAS*, **4 (8)**, 141, https://doi.org/10.3847/2515-5172/abae71, URL https://doi.org/10.3847%2F2515-5172%2Fabae71.

Simon, M., and Coauthors, 1995: A lunar occultation and direct imaging survey of multiplicity in the Ophiuchus and Taurus star-forming regions. *ApJ*, **443**, 625–637, https://doi.org/10.1086/175554.

Sivaramakrishnan, A., and Coauthors, 2022: The Near Infrared Imager and Slitless Spectrograph for the James Webb Space Telescope – IV. Aperture Masking Interferometry. *arXiv e-prints*, arXiv:2210.17434, 2210.17434.

Slesnick, C. L., L. A. Hillenbrand, and J. M. Carpenter, 2004: The Spectroscopically Determined Substellar Mass Function of the Orion Nebula Cluster. *ApJ*, **610 (2)**, 1045–1063, https://doi.org/10.1086/421898, astro-ph/0404292.

Smart, W. M., and E. b. R. M. Green, 1977: *Textbook on Spherical Astronomy*.

Softich, E., and Coauthors, 2022: CWISE J014611.20-050850.0AB: The Widest Known Brown Dwarf Binary in the Field. *ApJL*, **926 (2)**, L12, https://doi.org/10.3847/2041-8213/ac51d8, 2202.02315.

Soummer, R., L. Pueyo, and J. Larkin, 2012: Detection and Characterization of Exoplanets and Disks Using Projections on Karhunen-Loève Eigenimages. *ApJL*, **755 (2)**, L28, https://doi.org/10.1088/2041-8205/755/2/L28, 1207.4197.

Spiegel, D. S., A. Burrows, and J. A. Milsom, 2011: The Deuterium-burning Mass Limit for Brown Dwarfs and Giant Planets. *ApJ*, **727 (1)**, 57, https://doi.org/10.1088/0004-637X/727/1/57, 1008.5150.

Strampelli, G. M., J. Aguilar, L. Pueyo, A. Aparicio, M. Gennaro, L. Ubeda, and M. Robberto, 2020: HST Survey of the Orion Nebula Cluster in the $H_2O$ 1.4 $\mu$m Absorption Band. III. The Population of Substellar Binary Companions. *ApJ*, **896 (1)**, 81, https://doi.org/10.3847/1538-4357/ab8eb3, 2004.13924.

Struve, O., 1952: Proposal for a project of high-precision stellar radial velocity work. *The Observatory*, **72**, 199–200.

Sullivan, J. F., and Coauthors, 2016: JWST's optical telescope simulator for verification of the Integrated Science Instrument Module. *Optical System Alignment, Tolerancing, and Verification X*, J. Sasián, and R. N. Youngworth, Eds., Society of Photo-Optical Instrumentation Engineers (SPIE) Conference Series, Vol. 9951, 99510E, https://doi.org/10.1117/12.2237834.

Susemiehl, N., and M. R. Meyer, 2022: Constraints on the orbital separation distribution and binary fraction of M dwarfs. *A&A*, **657**, A48, https://doi.org/10.1051/0004-6361/202038582, 2109.05951.

Swihart, S. J., E. V. Garcia, K. G. Stassun, G. van Belle, M. W. Mutterspaugh, and N. Elias, 2017: A Catalog of Calibrator Stars for Next-generation Optical Interferometers. *AJ*, **153 (1)**, 16, https://doi.org/10.3847/1538-3881/153/1/16, 1610.04600.

ten Brummelaar, T. A., and Coauthors, 2005: First Results from the CHARA Array. II. A Description of the Instrument. *ApJ*, **628 (1)**, 453–465, https://doi.org/10.1086/430729, astro-ph/0504082.

Tobin, J. J., and Coauthors, 2015: The VLA Nascent Disk and Multiplicity (VANDAM) Survey of Perseus Protostars. Resolving the Sub-arcsecond Binary System in NGC 1333 IRAS2A. *ApJ*, **798 (1)**, 61, https://doi.org/10.1088/0004-637X/798/1/61, 1410.8134.

Tobin, J. J., and Coauthors, 2022: The VLA/ALMA Nascent Disk And Multiplicity (VANDAM) Survey of Orion Protostars. V. A Characterization of Protostellar Multiplicity. *ApJ*, **925 (1)**, 39, https://doi.org/10.3847/1538-4357/ac36d2, 2111.05801.

Todorov, K. O., K. L. Luhman, Q. M. Konopacky, K. K. McLeod, D. Apai, A. M. Ghez, I. Pascucci, and M. Robberto, 2014: A Search for Companions to Brown Dwarfs in the Taurus and Chamaeleon Star-Forming Regions. *ApJ*, **788 (1)**, 40, https://doi.org/10.1088/0004-637X/788/1/40, 1404.0213.

Tokovinin, A., and C. Briceño, 2020: Binary Stars in Upper Scorpius. *AJ*, **159 (1)**, 15, https://doi.org/10.3847/1538-3881/ab5525, 1909.12700.

Tokovinin, A., B. D. Mason, R. A. Mendez, and E. Costa, 2022: Speckle Interferometry at SOAR in 2021. *AJ*, **164 (2)**, 58, https://doi.org/10.3847/1538-3881/ac78e7, 2207.02925.

Tokovinin, A., and M. Moe, 2020: Formation of close binaries by disc fragmentation and migration, and its statistical modelling. *MNRAS*, **491 (4)**, 5158–5171, https://doi.org/10.1093/mnras/stz3299, 1910.01522.

Tokovinin, A., M. G. Petr-Gotzens, and C. Briceño, 2020: Statistics of Wide Pre-main-sequence Binaries in the Orion OB1 Association. *AJ*, **160 (6)**, 268, https://doi.org/10.3847/1538-3881/abc2d6, 2010.08543.

Tokovinin, A., S. Thomas, M. Sterzik, and S. Udry, 2006: Tertiary companions to close spectroscopic binaries. *A&A*, **450 (2)**, 681–693, https://doi.org/10.1051/0004-6361:20054427, astro-ph/0601518.

Tomkin, J., and H. Tran, 1987: The Double-Lined Eccentric Spectroscopic Binary Beta Ari. *AJ*, **94**, 1664, https://doi.org/10.1086/114598.

Toomre, A., 1964: On the gravitational stability of a disk of stars. *ApJ*, **139**, 1217–1238, https://doi.org/10.1086/147861.

Trotta, R., 2008a: Bayes in the sky: Bayesian inference and model selection in cosmology. *Contemporary Physics*, **49 (2)**, 71–104, https://doi.org/10.1080/00107510802066753, 0803.4089.

Trotta, R., 2008b: Bayes in the sky: Bayesian inference and model selection in cosmology. *Contemporary Physics*, **49 (2)**, 71–104, https://doi.org/10.1080/00107510802066753, 0803.4089.

Trueba, N., and Coauthors, 2020: A Redshifted Inner Disk Atmosphere and Transient Absorbers in the Ultracompact Neutron Star X-Ray Binary 4U 1916-053. *ApJL*, **899 (1)**, L16, https://doi.org/10.3847/2041-8213/aba9de, 2008.01083.

Tuthill, P. G., J. D. Monnier, W. C. Danchi, E. H. Wishnow, and C. A. Haniff, 2000: Michelson Interferometry with the Keck I Telescope. *PASP*, **112 (770)**, 555–565, https://doi.org/10.1086/316550, astro-ph/0003146.

Velusamy, T., and C. Beichman, 2001: Nulling interferometry for extra-solar planet detection: sensitivity & image reconstruction. *2001 IEEE Aerospace Conference Proceedings (Cat. No.01TH8542)*, Vol. 4, 4/2013–4/2025 vol.4, https://doi.org/10.1109/AERO.2001.931530.

Vogel, H. C., 1890a: Orbit and Mass of Algol. *PASP*, **2 (6)**, 27, https://doi.org/10.1086/120078.

Vogel, H. C., 1890b: Spectrographische Beobachtungen an Algol. *Astronomische Nachrichten*, **123 (19)**, 289, https://doi.org/10.1002/asna.18901231902.

von Weizsäcker, C. F., 1951: The Evolution of Galaxies and Stars. *ApJ*, **114**, 165, https://doi.org/10.1086/145462.

Ward-Duong, K., and Coauthors, 2015: The M-dwarfs in Multiples (MINMS) survey - I. Stellar multiplicity among low-mass stars within 15 pc. *MNRAS*, **449 (3)**, 2618–2637, https://doi.org/10.1093/mnras/stv384, 1503.00724.

Webbink, R. F., 1984: Double white dwarfs as progenitors of R Coronae Borealis stars and type I supernovae. *ApJ*, **277**, 355–360, https://doi.org/10.1086/161701.

Weights, D. J., P. W. Lucas, P. F. Roche, D. J. Pinfield, and F. Riddick, 2009: Infrared spectroscopy and analysis of brown dwarf and planetary mass objects in the Orion nebula cluster. *MNRAS*, **392 (2)**, 817–846, https://doi.org/10.1111/j.1365-2966.2008.14096.x, 0810.3584.

Weinberg, M. D., S. L. Shapiro, and I. Wasserman, 1987: The Dynamical Fate of Wide Binaries in the Solar Neighborhood. *ApJ*, **312**, 367, https://doi.org/10.1086/164883.

Welsh, W. F., and Coauthors, 2012: Transiting circumbinary planets Kepler-34 b and Kepler-35 b. *Nature*, **481 (7382)**, 475–479, https://doi.org/10.1038/nature10768, 1204.3955.

Werner, M. W., and Coauthors, 2004: The Spitzer Space Telescope Mission. *ApJS*, **154 (1)**, 1–9, https://doi.org/10.1086/422992, astro-ph/0406223.

Whelan, J., and J. Iben, Icko, 1973: Binaries and Supernovae of Type I. *ApJ*, **186**, 1007–1014, https://doi.org/10.1086/152565.

Willott, C. J., and Coauthors, 2022: The Near-infrared Imager and Slitless Spectrograph for the James Webb Space Telescope. II. Wide Field Slitless Spectroscopy. *PASP*, **134 (1032)**, 025002, https://doi.org/10.1088/1538-3873/ac5158, 2202.01714.

Winters, J. G., and Coauthors, 2019: The Solar Neighborhood. XLV. The Stellar Multiplicity Rate of M Dwarfs Within 25 pc. *AJ*, **157 (6)**, 216, https://doi.org/10.3847/1538-3881/ab05dc, 1901.06364.

Wizinowich, P., and Coauthors, 2000: First Light Adaptive Optics Images from the Keck II Telescope: A New Era of High Angular Resolution Imagery. *PASP*, **112 (769)**, 315–319, https://doi.org/10.1086/316543.

Wood, M. L., A. W. Mann, and A. L. Kraus, 2021: Characterizing Undetected Stellar Companions with Combined Data Sets. *AJ*, **162 (4)**, 128, https://doi.org/10.3847/1538-3881/ac0ae9, 2106.09040.

Wright, E. L., and Coauthors, 2010a: The Wide-field Infrared Survey Explorer (WISE): Mission Description and Initial On-orbit Performance. *AJ*, **140 (6)**, 1868–1881, https://doi.org/10.1088/0004-6256/140/6/1868, 1008.0031.

Wright, E. L., and Coauthors, 2010b: The Wide-field Infrared Survey Explorer (WISE): Mission Description and Initial On-orbit Performance. *AJ*, **140 (6)**, 1868–1881, https://doi.org/10.1088/0004-6256/140/6/1868, 1008.0031.

Wright, N. J., S. Goodwin, R. D. Jeffries, M. Kounkel, and E. Zari, 2022: OB Associations. *arXiv e-prints*, arXiv:2203.10007, https://doi.org/10.48550/arXiv.2203.10007, 2203.10007.

Ygouf, M., L. M. Mugnier, D. Mouillet, T. Fusco, and J. L. Beuzit, 2013: Simultaneous exoplanet detection and instrument aberration retrieval in multispectral coronagraphic imaging. *A&A*, **551**, A138, https://doi.org/10.1051/0004-6361/201220318, 1302.7045.

Ygouf, M., and Coauthors, 2016: Data processing and algorithm development for the WFIRST coronagraph: comparison of RDI and ADI strategies and impact of spatial sampling on post-processing. *Space Telescopes and Instrumentation 2016: Optical, Infrared, and Millimeter Wave*, H. A. MacEwen, G. G. Fazio, M. Lystrup, N. Batalha, N. Siegler, and E. C. Tong, Eds., Society of Photo-Optical Instrumentation Engineers (SPIE) Conference Series, Vol. 9904, 99045M, https://doi.org/10.1117/12.2231581.

Ygouf, M., and Coauthors, 2020: Data processing for high-contrast imaging with the James Webb Space Telescope. *Society of Photo-Optical Instrumentation Engineers (SPIE) Conference Series*, Society of Photo-Optical Instrumentation Engineers (SPIE) Conference Series, Vol. 11443, 114433N, https://doi.org/10.1117/12.2561628.

Young, M. D., and C. J. Clarke, 2015: Binary accretion rates: dependence on temperature and mass ratio. *MNRAS*, **452 (3)**, 3085–3091, https://doi.org/10.1093/mnras/stv1512, 1507.01850.

Zalesky, J. A., M. R. Line, A. C. Schneider, and J. Patience, 2019: A Uniform Retrieval Analysis of Ultra-cool Dwarfs. III. Properties of Y Dwarfs. *ApJ*, **877 (1)**, 24, https://doi.org/10.3847/1538-4357/ab16db, 1903.11658.

Zhao, M., and Coauthors, 2009: Imaging and Modeling Rapidly Rotating Stars: $\alpha$ Cephei and $\alpha$ Ophiuchi. *ApJ*, **701 (1)**, 209–224, https://doi.org/10.1088/0004-637X/701/1/209, 0906.2241.

Ziegler, C., A. Tokovinin, M. Latiolais, C. Briceño, N. Law, and A. W. Mann, 2021: SOAR TESS Survey. II. The Impact of Stellar Companions on Planetary Populations. *AJ*, **162 (5)**, 192, https://doi.org/10.3847/1538-3881/ac17f6, 2103.12076.